University of Southampton Research Repository

UNIVERSITY OF SOUTHAMPTON

INITIATION AND GROWTH OF SHORT CRACKS IN U-NOTCH BEND SPECIMENS OF SUPERALLOY IN718 DURING HIGH TEMPERATURE LOW CYCLE FATIGUE

By Thomas Connolley

Thesis Submitted for the Degree of Doctor of Philosophy

SCHOOL OF ENGINEERING AND APPLIED SCIENCES
MATERIALS RESEARCH GROUP

September 2001

UNIVERSITY OF SOUTHAMPTON

ABSTRACT

SCHOOL OF ENGINEERING AND APPLIED SCIENCES
MATERIALS RESEARCH GROUP

Doctor of Philosophy

INITIATION AND GROWTH OF SHORT CRACKS IN U-NOTCH BEND SPECIMENS OF SUPERALLOY IN718 DURING HIGH TEMPERATURE LOW CYCLE FATIGUE

By Thomas Connolley

Inconel 718 (IN718) is a nickel-based superalloy used extensively for gas turbine discs. Since turbine discs are safety-critical components, considerable effort is expended in determining their safe operating life. This requires a thorough understanding of the fatigue damage which can occur during service.

One type of in-service damage is low cycle fatigue cracking in the fir tree root fixtures of discs. To study this, fatigue tests at 600°C were performed on two batches of U-notch bend specimens (Batch A & B), taken from disc forgings with the same composition, heat treatment and microstructure. U-notches were machined by a broaching process similar to that used for fir tree root fixtures. Fractography and metallography were used to study the natural initiation of cracks. Dwells of 1 to 30 seconds at maximum stress were used to investigate previous findings of a beneficial effect on fatigue life under certain conditions. Selected tests were performed on polished notches to measure surface short crack growth rates using replicas. Unstressed thermal exposure experiments were also performed to study primary carbide oxidation, which is implicated in crack initiation.

Oxidation of primary carbides readily occurred in unstressed samples and fatigue tests. Localised matrix deformation was observed in the vicinity of oxidised carbides. Theoretical calculations of mismatch strains showed that oxidation of primary carbide particles caused substantial plastic deformation in the surrounding matrix. This was a common cause of crack initiation in Batch A specimens, but was less common in Batch B.

In Batch A, short crack growth was approximately constant across a wide range of crack lengths. The cracks observed were straight and transgranular at the surface. Batch B, tested at a higher stress level, exhibited the more typical behaviour of increasing growth rate with increasing crack length, and surface crack paths were more tortuous.

A difference between the batches was clearly seen in strain-life results, with Batch B exhibiting longer lifetimes than Batch A under the same experimental conditions. A beneficial effect on life of dwell at maximum stress was observed for Batch A tests. However, no such beneficial effect was observed for Batch B tested at a higher stress level. Differences in crack initiation and propagation between the two batches were investigated.

Batch A was found to have a work-hardened deformation layer in the broached notch, while Batch B did not. The effects of the deformation layer and differences in surface finish on observed fatigue behaviour are discussed.

TABLE OF CONTENTS

ACKNOWLEDGEMENTS

I am grateful to the United Kingdom Engineering and Physical Sciences Research Council and ALSTOM Power for financial support of my research. Particular thanks are owed to Dr. Steve Moss, Dr. Rob Jakeman and Martin Hughes at ALSTOM Power for their valuable technical discussions, supply of material and provision of the finite element model used in part of my work.

At Southampton I would like to thank my supervisors Dr. Philippa Reed and Dr. Marco Starink for their continuing guidance and support. For all their assistance I wish to thank the technical and support staff, David Beckett, Eric Bonner, Erik Roszkowiak, Sheila Cleary, Sue Walker, Gwyneth Skiller, Hazel Douglas and Gill Rood.

Other friends and colleagues I would particularly like to acknowledge are: Dr. Nick Hide for all his wisdom and experience regarding high temperature fatigue testing equipment; Dr. Barbara Cressey and Dr. Richard Pearce at Southampton Oceanography Centre for assistance with electron microscopy and Gwen and François Hugo for tea, sympathy and ensuring I got at least one decent meal a month!

Finally, special thanks to my parents and sister, who have always supported and encouraged me in whatever I've done.

"We are here for this - to make mistakes and to correct ourselves, to stand the blows and hand them out. We must never feel disarmed: nature is immense and complex, but it is not impermeable to the intelligence; we must circle around it, pierce and probe it, look for the opening or make it."
-Primo Levi, "The Periodic Table".

"Results! Why, man, I have gotten a lot of results. I know several thousand things that won't work."
- Thomas Edison

LIST OF SYMBOLS AND ABBREVIATIONS

SYMBOLS

B	bulk modulus
D_g	grain boundary diffusivity
E	elastic modulus
G	shear modulus
H_v	Vickers hardness
J	J-integral
J_{max}	maximum value of J-integral
ΔJ	J-integral range
K	stress intensity factor
K_c	fracture toughness
K_{max}	maximum value of stress intensity factor
ΔK	stress intensity factor range
ΔK_{th}	threshold stress intensity factor range
K_t	elastic stress concentration factor
K_ε	strain concentration factor
N	number of fatigue cycles
N_f	number of cycles to specimen fracture = fatigue life
N_i	number of cycles to crack initiation
P	load
P_{max}	maximum load
P_{min}	minimum load
R	load ratio
R_a	average deviation from the mean surface (surface roughness)
R_v	maximum valley depth below the mean surface (surface roughness)
T	temperature
V_i	molar volume of phase 'i'
Z	atomic number
a	crack depth
b	bend specimen breadth
c	crack length
d	notch depth

p	hydrostatic pressure
q	notch sensitivity factor
r_i	radius of particle or feature "i"
r_{root}	notch root radius
r_p	plastic zone radius
s	span
w	bend specimen depth

α	linear thermal expansion coefficient
δ_v	volume expansion factor
γ	engineering shear strain
γ_{ij}	i, j component of engineering shear strain (i, j = x, y or z; i ≠ j)
ε	strain
ε_{ij}	i, j component of strain (i = j = x, y or z)
$\Delta\varepsilon_{eq}$	equivalent strain range
ε_{amp}	strain amplitude
ε_m	misfit parameter
ε_{eq}^{pl}	equivalent plastic strain
ε_f'	fatigue ductility coefficient
ρ	density
σ	applied stress
σ_{ij}	i, j component of stress (i, j = x, y or z in rectangular co-ordinates)
σ_b	bending stress
σ_o	mean applied stress
σ_{min}	minimum applied stress
σ_{max}	maximum applied stress
$\Delta\sigma$	applied stress range
σ_{amp}	applied stress amplitude
σ_e	endurance limit
σ_{op}	crack opening stress
σ_y	yield stress
σ_{uts}	ultimate tensile stress

σ_f'	fatigue strength coefficient
υ	Poisson's ratio

ABBREVIATIONS

BEI	Backscattered Electron Imaging
DFM	Deterministic Fracture Mechanics
EDM	Electrostatic Discharge Machining
EDX	Energy-dispersive X-ray Spectroscopy
EPFM	Elastic-Plastic Fracture Mechanics
FCC	Face Centred Cubic
FE	Finite Element
HCF	High Cycle Fatigue
HCP	Hexagonal Close Packed
LCF	Low Cycle Fatigue
LEFM	Linear Elastic Fracture Mechanics
NDT	Non-Destructive Testing
PFM	Probabilistic Fracture Mechanics
POD	Probability of Detection
SEI	Secondary Electron Imaging
SEM	Scanning Electron Microscope
SENB	Single Edge Notch Bend
TG-DTA	thermogravimetry-differential thermal analysis
TEM	Transmission Electron Microscope
XPS	X-ray photoelectron spectroscopy
ZAF	Atomic Number (Z), Absorption, Fluorescence (in EDX analysis)

1 INTRODUCTION

Gas turbine engines were developed in the 1930-40s as an alternative to the piston engine for aircraft propulsion. Since then, gas turbine engines have evolved from their aviation origins to find applications in many areas of propulsion and power generation. Aviation is still the primary sector for gas turbine use, from small turboprop and turboshaft units for light aircraft and helicopters to the latest high-bypass turbofan engines for civil airliners like the Airbus A340 and Boeing 777. Another application of increasing economic and technical importance is power generation, where gas turbines are used in power stations generating electricity for supply to the grid, or as self-contained generators for industry, ships, oil platforms, and large public buildings.

Though individual designs vary according to the application, all gas turbines have a common layout consisting of a compressor, a combustion chamber and a turbine. A cutaway drawing of a modern turbofan engine is shown in Figure 1.1. Air entering the front of the engine is compressed and heated in the compressor. The air then passes into the combustion chamber where it is mixed with fuel and ignited. Hot, high pressure gases from the combustion process pass through the turbine. The turbine blades have an aerofoil section, so that the hot gases flowing over the blade surfaces generate lift forces acting on the blades. Turbine blades are oriented so that the lift forces cause the turbine to spin, converting the kinetic energy of the hot gas stream into rotational motion of the turbine and its shaft, which in turn drives the compressor at the front of the engine. Finally, the hot gases exit the engine at the rear via a nozzle. In turbofan engines for aircraft, the propulsive force is provided by a combination of the high velocity hot gases exiting through the nozzle and additional airflow from a fan at the front of the engine, which like the compressor is driven by the turbine. Alternatively, the turbine can be designed to convert most of the energy from the hot gas stream into rotational motion. As well as turning the compressor, such a design can be used to drive an aircraft propeller, a helicopter rotor, a ship's propeller, a pump or an electrical generator.

The widespread use of gas turbines today would not have been possible without the introduction of new materials able to withstand the harsh operating conditions within the compressor, combustor and turbine stages of the engine [1.1]. A great deal of attention has also been paid to how materials perform and deteriorate under the service conditions experienced in gas turbines. Common causes of damage to gas turbine components are:

- Creep, which is the elongation of materials under constant load at high temperatures. Creep may eventually lead to stress-rupture of components.
- High cycle fatigue (HCF) caused by low stress amplitude, high frequency vibrations during normal engine operations.
- Low cycle fatigue (LCF) caused by high stress amplitude, low frequency fluctuations in load, such as engine start-up, shut-down or changes in engine operating speed.
- Thermal fatigue, which is a form of low-cycle fatigue arising from thermal expansion and contraction of components.

Crucial to the success of gas turbines was the development of a group of alloys based on iron, nickel or cobalt known collectively as superalloys. These alloys are designed specifically for high temperature, high stress applications like gas turbines, which require long-term strength at elevated temperature, fatigue resistance, creep resistance and resistance to high temperature corrosion and erosion [1.2]. The first superalloys were used in superchargers for aircraft piston engines, but the range of applications has grown to include gas turbines, rocket motors, chemical plant, and furnaces. Certain superalloys are also used in cryogenic systems, because of their good low temperature strength and ductility.

One of the most commonly used superalloys in modern gas turbine designs is Inconel 718 (IN718), originally developed by the International Nickel Company (INCO) in the 1950s to be more resistant to post-weld cracking than existing superalloys like René 41. In addition to its good welding characteristics, IN718's combination of high strength, creep resistance and oxidation resistance made it an ideal candidate for the fabrication of turbine discs. Following considerable development work by engine manufacturers and their suppliers, IN718 has become one of the most widely used superalloys in gas turbine designs. For example, IN718 represents 34% by weight of the materials used in the General Electric CF6 turbofan engine [1.3]. Components manufactured from IN718 include spacers, shafts, support frames, seals, compressor discs, compressor blades, turbine discs, exhaust nozzles and fasteners. In polycrystalline form, IN718 is restricted to service temperatures below 650°C, but there has been recent interest in single crystal forms for blade applications at higher temperatures [1.4]. IN718 can be cast, wrought, or produced by powder metallurgy techniques. Widespread use of IN718 is enhanced by its availability in a wide variety of product forms. This versatility enables selection of the optimum manufacturing route for specific components, so that IN718 continues to be used in many gas turbine designs despite being a relatively old alloy.

This thesis is concerned with the use of wrought IN718 for turbine discs in engines used for ground-based power generation. Turbine discs are critical components, because failure of a disc will result in serious, often irreparable damage to the engine. Turbine disc integrity is even more critical for aero engines, where engine failure could lead to loss of the aircraft. Turbine blades are attached to the circumference of the disc by dovetail-like fir tree root fixtures, through which the forces on the blades are transmitted to the disc. A common type of in-service damage to discs is low cycle fatigue cracking in the fir tree root fixtures, so discs need to be inspected regularly for cracks and retired from service before the cracks reach a critical size. This damage-tolerant approach to fatigue cracking requires reliable information about how quickly cracks nucleate and grow, so that the time taken for a sub-critical crack to reach a critical size can be predicted.

The aims of the research presented in this thesis are to study the initiation and growth of short cracks in Inconel 718, paying particular attention to the following:

- The role of oxidation in crack initiation at elevated temperatures.
- High temperature short crack growth in a notched geometry representative of a turbine disc blade root fixing.
- The effect of dwell time at maximum load on the low cycle fatigue behaviour.

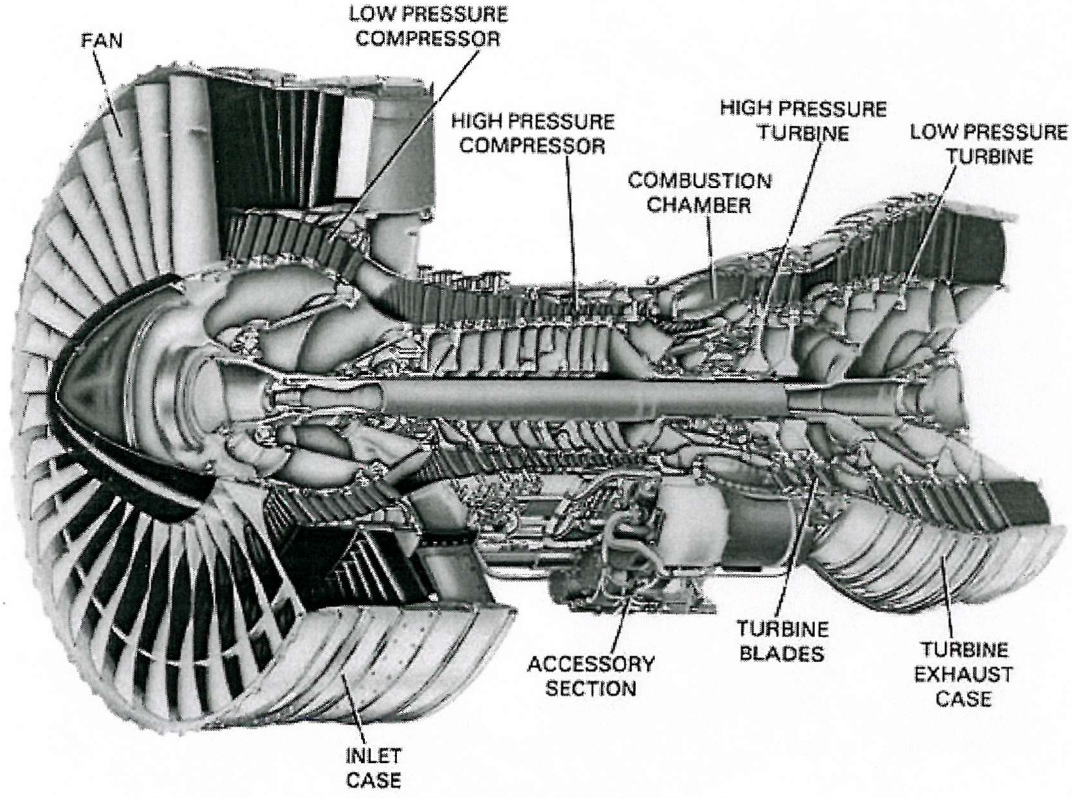

Figure 1.1: Cut-away drawing of a Pratt & Whitney PW4000 turbofan engine, showing principal components.

1.1 References

[1.1] Backman D. G. & Williams J. C. "Advanced materials for aircraft engine applications" Science, vol. 255 pp. 1082-1087 (1992)

[1.2] Bradley E.H. Superalloys: A technical guide ASM International, Ohio, USA, ISBN 0-87170-327(1988)

[1.3] Barker J. F. "The initial years of Alloy 718 - A GE perspective" Proc. Superalloy 718 - Metallurgy & Applications Ed. Loria E. A., TMS, USA, pp. 269-277 (1989)

[1.4] Mercer C., Soboyejo A. B. O. & Soboyejo W. O. "Micromechanisms of fatigue crack growth in a single crystal Inconel 718 nickel-based superalloy" Acta Mater. vol. 47 pp. 2727-2740 (1999)

2 GENERAL FATIGUE PRINCIPLES

Fatigue is the term used to describe the changes in properties which occur in materials due to the repeated application of stresses and strains, in particular those changes which lead to cracking and eventual fracture of components. Failures due to fatigue frequently occur under cyclic loads whose peaks are well below the safe load predicted by static analyses, so it is vital to understand fatigue processes in order to design products that will perform safely under fatigue conditions. It is inappropriate to conduct a detailed review of fatigue theory, since comprehensive textbooks like those of Suresh [2.1, 2.2] are available. Instead, the elements of fatigue theory most relevant to the project are discussed here.

2.1 Fatigue Cycle Terminology & Definitions

2.1.1 Fatigue Cycle Parameters

Consider the loading cycle in Figure 2.1, where applied stress is plotted against time. Basic parameters used to describe fatigue cycles are as follows:

Mean stress
$$\sigma_o = \frac{(\sigma_{\max} + \sigma_{\min})}{2} \qquad \text{Eqn. 2.1}$$

Stress amplitude
$$\sigma_{amp} = \frac{(\sigma_{\max} - \sigma_{\min})}{2} \qquad \text{Eqn. 2.2}$$

Stress range
$$\Delta\sigma = \sigma_{\max} - \sigma_{\min} \qquad \text{Eqn. 2.3}$$

Load ratio
$$R = \frac{\sigma_{\min}}{\sigma_{\max}} \qquad \text{Eqn. 2.4}$$

2.1.2 Fatigue Crack Loading Modes

There are three general ways in which cracks can be loaded relative to the orientation of the crack faces and crack front:

- Mode I : The opening mode in which the applied load is perpendicular to the crack faces and the crack faces are separated in a direction normal to the plane of the crack.
- Mode II: The in-plane sliding or shearing mode, where the loads are in the plane of the crack and the crack faces are sheared in a direction normal to the crack front.
- Mode III: The tearing or anti-plane shear mode, where the loads are in the plane of the crack and the crack faces are sheared parallel to the crack front.

These loading modes are illustrated in Figure 2.2.

2.1.3 Describing Crack Lengths

In the fatigue community, the parameters a, c or occasionally l are used to describe the length of cracks. In many cases, only crack growth in one dimension is considered, and a or c can be used interchangeably to represent crack length. However, care must be taken when crack behaviour in two dimensions is being considered, since different authors adopt different conventions in the use of a and c for labelling crack length and crack depth. In this thesis, the convention shown in Figure 2.3 will be used.

2.2 Fatigue Life Predictions

The ultimate goal of studying fatigue behaviour is to develop models for predicting the safe operating life of engineering components and structures. The overall fatigue life of a component is the sum of the time required to initiate cracks, the subsequent propagation and coalescence of short cracks to form a dominant crack or cracks, and the propagation of the dominant crack until the component fails. Thus the fatigue life consists of crack initiation, short crack growth and long crack growth. The relative time spent in the different stages of fatigue life is governed by the material, the initial defect size, the loading on the component and its operating environment. Historically, two major approaches to fatigue life prediction have developed [2.1]. These are the total-life and damage-tolerant approaches.

2.2.1 Total Life Approach

The total life approach considers how the number of cycles to failure varies with the applied cyclic stress range (the stress-life approach) or the applied strain range (the strain-life approach). The stress-life approach is generally used for high cycle fatigue (HCF) where the applied stresses are low and material deformation is predominantly elastic. In such cases, the number of cycles to failure is high, hence the term high cycle fatigue. The strain-life approach is sometimes adopted for low cycle fatigue (LCF), where stresses are high enough for significant plastic deformation, and the number of cycles to failure is low, hence the term low cycle fatigue.

Stress-life data is presented in the form of stress-life curves (commonly called S-N curves), where the applied stress amplitude σ_{amp} is plotted against the number of cycles to failure N_f. Typical curves are plotted in Figure 2.4. For a number of materials, such as low carbon steels, there is a stress amplitude below which fatigue failure does not occur, defined as the fatigue limit or endurance limit σ_e. This behaviour is shown by curve (a) in Figure 2.4. Other materials do not exhibit an endurance limit, notably aluminium alloys and other alloys which do not strain-age harden. For non-strain-age hardening materials, a fatigue strength is defined as the stress amplitude which will not cause failure for at least 10^7 cycles, shown by curve (b) in Figure 2.4.

In a similar way to stress-life data, strain-life data is usually presented as a plot of applied strain amplitude versus the number of cycles to failure. Strain-life data can be fitted to the following equation [2.1], established form the work of Coffin [2.3] and Manson [2.4].

$$\frac{\Delta\varepsilon}{2} = \varepsilon_{amp} = \frac{\sigma_f^{'}}{E}(2N_f)^{\lambda_1} + \varepsilon_f^{'}(2N_f)^{\lambda_2} \qquad \text{Eqn. 2.5}$$

where:

N_f = number of cycles to fracture

ε'_f = fatigue ductility coefficient

σ'_f = fatigue strength coefficient

E = elastic modulus

λ_1 and λ_2 are constants.

The first term on the right hand side of Eqn. 2.5 represents the elastic contribution to strain amplitude, while the second term denotes the plastic contribution.

In laboratory tests, stress-life and strain-life data are obtained from smooth, nominally defect-free specimens and much of the measured life is taken up by crack initiation rather than crack propagation. For this reason, the total life approach is useful for selecting materials where resistance to crack initiation is important, but it is of limited value when trying to determine the resistance of a material to crack propagation. In applications where resistance to crack propagation is important, the damage-tolerant approach to fatigue is adopted.

2.2.2 Damage-Tolerant Approach

With advances in the understanding of crack initiation and growth behaviour, the damage-tolerant approach is widely used in predicting fatigue life. Components are assumed to contain flaws of an initial size a_o, usually based on the crack size detectable by non-destructive testing (NDT). The useful fatigue life is determined as the number of cycles required to propagate a crack from its initial flaw size a_o to some critical size a_c. Selection of a_c is based on knowledge of the fracture toughness of the material, the limit load, the maximum allowable strain or maximum permitted compliance change for a particular component. Fatigue lives are determined by integration of equations relating the crack growth rate to some characteristic driving force. The crack driving force can be determined on the basis of linear elastic fracture mechanics (LEFM) or elastic-plastic fracture mechanics (EPFM), as discussed in the following sections.

2.3 Linear Elastic Fracture Mechanics (LEFM)

There are various ways of characterising fatigue crack growth rates, the most widely used of which is the Linear Elastic Fracture Mechanics (LEFM) approach. This approach characterises the stresses at co-ordinates near a crack tip in terms of the nominal applied stress and the flaw length. For example, consider a sharp, through thickness crack length $2a$ in a thin, elastically deforming plate (see Figure 2.5). The local stresses at co-ordinates $(r,\ \theta)$ close to the crack tip are given to a first approximation by:

$$\sigma_{xx} = \frac{K_I}{\sqrt{2\pi r}}\left[\cos\frac{\theta}{2}\left(1-\sin\frac{\theta}{2}\sin\frac{3\theta}{2}\right)\right] \qquad \text{Eqn. 2.6}$$

$$\sigma_{yy} = \frac{K_I}{\sqrt{2\pi r}}\left[\cos\frac{\theta}{2}\left(1+\sin\frac{\theta}{2}\sin\frac{3\theta}{2}\right)\right] \qquad \text{Eqn. 2.7}$$

$$\sigma_{xy} = \frac{K_I}{\sqrt{2\pi r}}\left[\sin\frac{\theta}{2}\cos\frac{\theta}{2}\cos\frac{3\theta}{2}\right] \qquad \text{Eqn. 2.8}$$

K_I is known as the stress intensity factor for Mode I loading, defined in terms of the applied stress σ and flaw length a as:

$$K_I = \sigma\sqrt{\pi a} \qquad \text{Eqn. 2.9}$$

and in general:

$$K = \alpha\sigma\sqrt{\pi a} \qquad \text{Eqn. 2.10}$$

α is a geometrical factor which varies with the specimen geometry, crack geometry and mode of loading (Mode I, Mode II or Mode III). K provides a convenient way of describing the local stress fields around a crack tip. If two cracks of different geometry have the same value of K, then in theory the stress fields around the crack tips of the two flaws are identical. Note that in Eqn. 2.6 to Eqn. 2.8, the calculated stresses tend to infinity as r tends to zero, implying a stress singularity, though this situation does not occur in reality because of plastic yielding.

The concept of K has been adopted in fatigue theory to characterise crack growth behaviour. Instead of using an applied stress range $\Delta\sigma$, the stress intensity factor range ΔK is used. Log-log plots of the crack growth rate da/dN, vs. ΔK typically show a sigmoidal relationship divided into three distinct regimes, as depicted in Figure 2.6.

Regime A describes the low ΔK region where the crack growth rate tends towards zero, defining a threshold stress intensity factor ΔK_{th} below which crack growth is arrested or imperceptible. Regime B is the region of stable crack growth described by the Paris Equation:

$$\frac{da}{dN} = C\Delta K^{m} \qquad \text{Eqn. 2.11}$$

where C and m are materials constants.

Regime C is the region of high ΔK where the crack growth rate accelerates rapidly towards final fast fracture or plastic collapse of the uncracked ligament. The onset of fast, crack growth under static loading is represented by the fracture toughness K_c for the loading mode in question (K_{Ic}, K_{IIc} or K_{IIIc}).

2.4 Short Cracks and the Limitations of LEFM

Making a distinction between short and long cracks is important because of experimentally observed differences in propagation behaviour. In general, short cracks tend to propagate at higher rates than long cracks when compared on the basis of stress intensity factor range, ΔK. In the past, this has led to overestimates of fatigue lives when long crack data alone has been used [2.5, 2.6]. Useful definitions of what constitutes a short crack are given by Suresh [2.1]:

- Microstructurally short cracks where crack length is similar to a characteristic microstructural dimension such as grain size in monolithic materials, or particle spacing in discontinuously reinforced composites.

- Mechanically short cracks where the crack length is similar to the crack tip plastic zone in smooth specimens, or where the crack is engulfed by the plastic strain field of a notch. Such situations cast doubts on the validity of using ΔK to characterise crack growth, because ΔK is based on calculations of elastic stresses only.

- Physically short cracks which may be larger than any microstructural dimensions or plastic zones, but are small in relation to the size of the component in which they occur.

- Chemically short cracks which show anomalous behaviour below a certain size as a result of an environmental factor like stress corrosion.

General characteristics of short crack growth, when characterised by LEFM are:

- Higher crack growth rates than long cracks, when compared on a *da/dN* vs. ΔK basis.
- Short crack growth at stress intensity ranges below the threshold ΔK_{th} for long cracks.
- Considerable fluctuations and scatter in short crack growth rate data.
- Retardation or arrest of short crack growth.

Explanations for the anomalous behaviour of short cracks compared to long cracks are given in terms of [2.1]:

- Absence of crack closure.
- Microstructural effects.
- The invalidity of the LEFM parameter ΔK to characterise growth rates when cracks are small relative to the size of a plastic zone.

Crack closure is a term used to describe load transfer in the wake of a growing crack, due to contact between crack faces. Load transfer reduces the effective crack driving force at the tip, with a consequent reduction in fatigue crack growth rates. Closure is promoted by shear components of deformation and crack roughness. At elevated temperatures, build-up of an oxide layer on the crack surface may aid closure. Closure is more likely for long cracks because of the greater length of crack along which closure may occur. Conversely, the closure of short cracks is limited due to their short wake.

Microstructural effects on short crack growth rates arise from interactions between cracks and microstructural features such as grain boundaries, secondary phase particles, inclusions or, in the case of composites, the reinforcing component. When cracks are of a similar scale to the grain size of a material, there can be a strong crystallographic influence on crack propagation, with crack arrest or deflection occurring at grain boundaries. Short cracks can be deflected or arrested by secondary phase particles and inclusions, or these features may promote crack growth by providing preferential paths for crack propagation. Miller [2.7] discussed two thresholds for fatigue behaviour, the first related to microstructure and the second mechanically-based. The mechanically based threshold applies where crack growth is insensitive to microstructure and depends on crack length and stress level. This is the long crack regime that is amenable to characterisation by LEFM. However, short cracks exhibit a microstructurally-based threshold, related to the microstructural barriers to crack growth that exist in a material, such as grain boundaries. Miller [2.7] distinguished between the fatigue resistance of a material, which is controlled by microstructure, and the fatigue resistance of components (including fatigue test specimens), which is affected by the presence of stress concentrators such as notches, steps or surface roughness.

Two main limits exist in using LEFM to characterise crack growth [2.8]. The first limit concerns the size of the plastic zone at the crack tip relative to the length of the crack. For a crack of length a, the elastic stress intensity factor K accurately describes the crack tip stress-strain state, providing the size of the crack tip plastic zone, r_p, is small compared to the crack length. Typically, $r_p \leq 0.02a$ is required for LEFM to be applicable [2.8]. However, LEFM breaks down when the crack is very short, typically less than two or three grain diameters, because the extent of plastic yielding at the crack tip becomes comparable to the crack length. The second limitation in applying LEFM arises for short cracks emanating from the root of a notch, where the plastic zone due to the notch stress field is larger than the crack length. In this second case, the crack is mechanically short and may exhibit the transient da/dN versus ΔK behaviour shown in Figure 2.7 [2.1, 2.9]. In typical transient behaviour, the short crack growth rate decreases with increasing ΔK, passing through a minimum before increasing again (see curve A in Figure 2.7). Occasionally, cracks may arrest completely and become non-propagating (see curve B in

Figure 2.7). The transient behaviour of mechanically short cracks growing from notches is attributed to the development of crack closure as the crack length increases. Initially, the growing crack has a small wake and the possibility of crack closure due to notch plasticity in the crack wake is limited. As the crack grows, the amount of crack closure in the notch strain field increases, reducing the effective crack driving force ΔK and as a consequence the crack growth rate reduces. Eventually, the crack is long enough to escape the plastic zone of the notch and the crack driving force becomes controlled by the far-field loading rather than local notch effects. Sometimes, the level of closure in the notch strain field may reduce ΔK below the threshold for propagation, resulting in a non-propagating crack.

An alternative and controversial explanation of short crack behaviour has been developed by Sadananda and Vasudevan [2.10, 2.11, 2.12], who expressed strong doubts about the validity of the concept of crack closure. Instead, they proposed a two parameter model of crack growth, the first parameter being the stress intensity range ΔK and the second the maximum stress intensity K_{max}. For any crack growth rate, it was stated that there exist two critical values of K_{max} and ΔK that must be exceeded for crack growth to proceed. These critical values K^*_{max} and ΔK^* reduce to the threshold values $K^*_{max,th}$ and ΔK^*_{th} at the crack growth threshold [2.12]. In Sadananda and Vasudevan's model of crack propagation, ΔK represents the cyclic plasticity and fatigue damage accumulation ahead of the crack tip, while K_{max} represents the local stress required to break bonds at the crack tip and cause the crack to advance. For short cracks, K_{max} was considered to be more important for propagation than ΔK, with $K^*_{max,th}$ greater than ΔK^*_{th}. Short crack growth behaviour such as arrest was explained by arguing that the local value of K_{max} is affected by internal stresses [2.10], such as the stress field of a notch, dislocation density gradients, or stress concentration at a slip band extrusion. At initiation, the internal stresses are high resulting in high K_{max} and high da/dN. As the crack grows it propagates out of the region of high internal stress, and K_{max} decreases, resulting in crack deceleration. If it falls below K^*_{max}, the crack arrests, even if ΔK is above the critical value ΔK^*. The authors claimed that the concept of K^*_{max} and ΔK^* was applicable to both short and long cracks, eliminating the need to invoke closure to explain differences in crack growth behaviour. The theory of Sadananda and Vasudevan is worthy of consideration because it acknowledges that the local stress-strain environment influences crack growth through K_{max}. However, it is considered to be controversial in its dismissal of closure concepts.

Whatever the arguments about closure and short crack growth, it is important not to overlook the effects of microstructure or crack deflection on cracks growing from notches. Cracks growing from a notch may be both microstructurally short and mechanically short, depending on the relative scale of the microstructure and notch strain field. Cracks will be microstructurally short relative to the grain size during initiation and propagation through the first few grains, and will also be mechanically short relative to the size of the notch plastic zone during further propagation.

2.5 Elastic-Plastic Fracture Mechanics (EPFM)

In order to overcome the limitations of LEFM, Elastic-Plastic Fracture Mechanics (EPFM) have been applied to fatigue crack characterisation. EPFM uses the concept of the *J*-Integral developed by Rice [2.13]. *J* was originally proposed to characterise non-linear elastic behaviour, but its use has been extended to elastic-plastic behaviour. *J* is calculated by taking a line integral around any path which encircles the crack tip [2.13].

$$J = \int_{\Gamma} \left(W dy - \mathbf{T} \frac{\partial \mathbf{u}}{\partial x} ds_{arc} \right) \qquad \text{Eqn. 2.12}$$

where:

Γ = contour encircling crack

W = strain energy density

y = distance along direction normal to crack plane

$\mathbf{T}$ = traction vector

$\mathbf{u}$ = displacement vector

s_{arc} = arc length along contour Γ

For non-linear elastic behaviour, *J* is a measure of the potential energy available for crack advance. In the case of linear elastic behaviour, *J* reduces to the strain energy release rate. For elastic plane stress conditions:

$$\Delta J = \frac{\Delta K^2}{E} = \text{strain energy release rate} \qquad \text{Eqn. 2.13}$$

where:

E = elastic modulus

For plastic deformation, J loses its potential energy interpretation, and the assumption of non-linear elastic behaviour does not adequately describe elastic-plastic behaviour during the unloading portion of the fatigue cycle. However, J remains useful as a way of characterising the strain field at a crack tip [2.14]. The cyclic J-Integral ΔJ is used to characterise fatigue crack growth in a similar way to ΔK, using a form of the Paris Equation:

$$\frac{da}{dN} = C' \Delta J^{m'} \qquad \text{Eqn. 2.14}$$

Various formulae exist for calculating ΔJ for different crack geometries, but much of the analytical work on cracks is now performed using computer-based finite element (FE) modelling.

When using ΔK or ΔJ to characterise the driving force for crack growth, additional parameters are introduced into models to account for anomalous short crack behaviour and the effects of plasticity on short or long crack growth. A commonly used correction proposed by Irwin [2.15], is to modify the calculation of ΔK for long cracks to include the effects of the crack tip plastic zone, producing an effective stress intensity factor range ΔK_{eff}.

$$\Delta K_{eff} = \alpha \Delta \sigma \sqrt{\pi (a + r_p)} \qquad \text{Eqn. 2.15}$$

where:
r_p = radius of the crack tip plastic zone

For short cracks, El Haddad et al. [2.14, 2.16, 2.17] proposed a correction to the crack length used when calculating ΔK or ΔJ. Instead of using the physical crack length a, the value $(a + a_o)$ was employed, where a_o is a constant for a given material and material condition. For example:

$$\Delta K = \alpha \sigma \sqrt{\pi (a + a_o)} \qquad \text{Eqn. 2.16}$$

$$a_o = \frac{1}{\pi}\left(\frac{\Delta K_{th}}{\Delta\sigma_e}\right)^2 \qquad \text{Eqn. 2.17}$$

where:

ΔK_{th} = threshold stress intensity factor range

$\Delta\sigma_e$ = endurance limit stress range

Using this modified short crack length eliminated the discrepancy between short crack and long crack data from aluminium alloy BS L65 (using ΔK) and A533 B steel (using ΔJ) [2.14]. The modified crack length approach was also applied to short fatigue cracks growing from notches [2.16], and used in combination with long crack growth data to predict fatigue lives for smooth and notched specimens [2.17]. Although attractive from the point of view of reconciling the discrepancies between short crack and long crack behaviour, no convincing explanation for the physical significance of a_o in Eqn. 2.16 and Eqn. 2.17 has been offered [2.1].

2.6 Short Crack Interactions

In real engineering components, several short fatigue cracks may initiate and grow in service and the total life of the component will depend upon how these cracks interact and coalesce to form a dominant defect [2.18]. Continuing refinements of damage-tolerant models requires more information on short crack growth and coalescence and some research has been conducted into the behaviour of multiple short fatigue cracks.

A simple case to study is the interaction between two coplanar cracks like those shown in Figure 2.8. A phenomenological study of such cracks in Q1N steel [2.19, 2.20] showed that both cracks grew independently of one another until just before coalescence. The highest crack growth rates were observed in the "a" direction during coalescence, with the growth rates decreasing again as the coalescing crack adopted an equilibrium thumbnail shape. FE modelling of stress intensity factors [2.19, 2.20]. predicted that K at the point of contact increased to a maximum at coalescence, then decreased again as the crack evolved towards its equilibrium shape.

Another case of relevance to real components is the behaviour of parallel, non-coplanar cracks. Shielding of two overlapping short cracks can occur, as shown in Figure 2.9. The longer Crack A will tend to shield the shorter Crack B from the full extent of the applied stress, resulting in lower growth rates or arrest of crack B. This shielding effect has been confirmed for arrays of non-coplanar cracks in Q1N steel [2.21]. For parallel offset cracks like those shown in Figure 2.10, Forsyth [2.22] identified three coalescence scenarios. In the first scenario, more common for high values of K, the crack-tip plastic zones of the approaching cracks overlap and the cracks coalesce by breakthrough of the intervening material as shown in Figure 2.10(a). Plastic zone overlap and breakthrough may occur before the tips are in opposition. In the second scenario described by Forsyth [2.22], the crack tip plastic zones do not overlap and the cracks propagate past each other, gradually deflecting until coalescence occurs at a point some way behind the tips, as shown in Figure 2.10(b). In the third scenario, fatigue cracks with large offsets may not deflect or coalesce, but they may affect propagation due to shielding effects. This behaviour is consistent with calculations of local values of K and plastic zone sizes at the crack tips [2.22] and examples of these types of crack coalescence have been observed experimentally [2.21, 2.22]. Post-fracture analysis [2.21] demonstrated that coalescence can also occur at depth positions without coalescence being apparent at the surface.

For arrays of many non-coplanar cracks, the shielding and coalescence behaviour can become very complex, depending upon the spatial distribution of the cracks and the applied loads. The generation of a dominant defect will be enhanced by coalescence events, but coalescence may be delayed by shielding effects. Some progress has been made with characterisation of the growth and coalescence behaviour of multi-crack arrays [2.23, 2.24]. The effect of an array of microcracks on the propagation behaviour of a dominant defect has also been analysed [2.25].

2.7 Cracks in Notched Components

Many engineering structures and components contain stress concentrators, such as holes, channels, steps, weld roots and grooves. Stress concentrators are the predominant sites for fatigue crack initiation, so studies of notched specimens yield valuable information for component life prediction. Both the total life and damage-tolerant approaches are applied to fatigue cracks emanating from notches and various notch geometries are used to simulate the mechanical conditions expected in service.

Notches are generally characterised by a theoretical elastic stress concentration factor K_t, which is a function of the loading mode and notch geometry. K_t is calculated using continuum elasticity theory and its value is the factor by which the nominal far-field stress is multiplied to give the local stress in the vicinity of the notch.

$$K_t = \frac{\text{local stress in notch root}}{\text{nominal applied stress}} \qquad \text{Eqn. 2.18}$$

In some cases, the local stress state exceeds the yield stress of the material, producing a zone of plastic deformation as well as a zone of raised elastic stresses, as shown in Figure 2.11. Since stress concentrators are sites where cracks commonly initiate, the elastic and plastic zones associated with the notch will have an effect on the growing crack. As can be seen in Figure 2.11, a short crack initiated at a plastically yielded notch has to grow through plastic and elastic zones before escaping the region of influence of the notch. In common with short cracks in smooth specimens, short cracks growing in the influence of a notch stress field frequently exhibit anomalous behaviour when characterised by an LEFM approach. Considering the idealised life history of a single crack from initiation to final fracture, growth will proceed as follows:

- Nucleation of a short crack entirely within the plastic zone of the notch.
- Growth of the crack entirely within the plastic zone of the notch.
- Growth beyond the plastic zone of the notch, but still within the elastic stress field of the notch.
- Growth of the crack under the influence of far-field stresses only.
- Crack reaches a critical length, and the component fails.

Predicting fatigue lifetimes in the situation described above is a complex problem, because no single approach or model satisfactorily describes crack behaviour at all stages.

2.7.1 Stress-Life Approach to Notch Fatigue

The stress-life approach to notch fatigue is employed for high-cycle fatigue situations where time to crack initiation is the important criterion for determining the fatigue life. The S-N data for smooth, un-notched specimens is modified to reflect the increased propensity for crack initiation in a stress concentrator. This is achieved by defining a fatigue notch factor K_f, which is the ratio of the endurance limit of a material obtained for a smooth specimen compared to the endurance limit for a notched specimen [2.26].

$$K_f = \frac{\sigma_e(\text{un - notched})}{\sigma_e(\text{notched})} \qquad \text{Eqn. 2.19}$$

K_f is either determined experimentally or from empirical relationships established for specific materials and notch geometries. It is possible to define a notch sensitivity factor q which compares the stress concentration factor K_t with the fatigue notch factor K_f:

$$q = \frac{K_f - 1}{K_t - 1} \qquad \text{Eqn. 2.20}$$

The notch sensitivity factor q determines how effective the notch is [2.26]. As q tends to 1, K_f tends to K_t and the notch is a fully effective stress concentrator. However, if q tends to zero, K_f tends to 1 and the notch has apparently no effect on the fatigue limit.

If K_f is known, S-N data obtained from un-notched specimens can be modified by dividing σ_{amp} by K_f to give predicted S-N data for notch geometries, although this can lead to very conservative results. Alternatively, the un-notched endurance limit or fatigue strength σ_e is simply reduced by a factor of K_f. The stress-life approach to notch fatigue is only valid when the stress-strain field of the notch is elastic, and breaks down when there is appreciable plastic yielding ahead of the stress concentrator. Some attempts have been made to take into account the effect of microstructure on the fatigue limit of notched structures. For blunt notches, this may be controlled by the spacing of effective microstructural barriers to short crack propagation [2.27].

2.7.2 Local Strain Approach to Notch Fatigue

In the local strain approach to notch fatigue, the local deformation in the stress concentrator relative to the applied remote stresses and strains is determined, either by finite element analysis or by physical measurement using strain gauges or other displacement measurement equipment. Strain-life data can then be estimated from smooth laboratory specimens, by applying a strain amplitude to the smooth specimen which is equivalent to that predicted or measured for the notch.

For design purposes, simple engineering approximations are frequently used to relate notch tip strain fields to the nominal applied load. It is possible to define a strain concentration factor K_ε such that:

$$K_\varepsilon = \frac{\text{local strain in notch}}{\text{nominal strain}} \qquad \text{Eqn. 2.21}$$

For elastic deformation, the strain concentration factor K_ε is equal to the stress concentration factor. Once yielding occurs, the stress and strain concentration factors adopt different values K_σ and K_ε respectively. For plastic conditions, the theoretical elastic stress concentration factor is given approximately by:

$$K_t = \sqrt{K_\sigma K_\varepsilon} \qquad \text{Eqn. 2.22}$$

In the local strain approach, some expressions for the notch fatigue reduction factor K_f have been proposed which give satisfactory predictions of fatigue behaviour for notched members in steels [2.1]:

For plastic deformation in the notch root:

$$K_f = \sqrt{K_\sigma K_\varepsilon} \qquad \text{Eqn. 2.23}$$

For elastic deformation in the notch root under fully reversed loading ($R = -1$):

$$K_f = \frac{\sqrt{\Delta\sigma\Delta\varepsilon E}}{\Delta\sigma_\infty} \qquad \text{Eqn. 2.24}$$

where:

$\Delta\sigma$ = notch tip stress range

$\Delta\varepsilon$ = notch tip strain range

$\Delta\sigma_\infty$ = nominal applied stress range

For a fixed value of $\Delta\sigma_\infty$, Eqn. 2.24 can be rearranged to give the equation of a rectangular hyperbola, as proposed by Neuber [2.28], commonly referred to as Neuber's Rule:

$$\Delta\sigma\Delta\varepsilon = \frac{(K_f\Delta\sigma_\infty)^2}{E} = \text{constant} \qquad \text{Eqn. 2.25}$$

Eqn. 2.25 represents a family of curves with different combinations of $\Delta\sigma$ and $\Delta\varepsilon$ which satisfy the equation. K_f can be solved using the cyclic stress-strain constitutive equation for the material in question. Such constitutive equations have the form:

$$\frac{\Delta\varepsilon}{2} = \frac{\Delta\sigma}{2E} + \left(\frac{\Delta\sigma}{2A'}\right)^{\frac{1}{n_f}} \qquad \text{Eqn. 2.26}$$

where:
A' = cyclic strength coefficient
n_f = cyclic strain hardening exponent

Multiplying both sides of Eqn. 2.26 by $\Delta\sigma$ gives:

$$\frac{\Delta\sigma\Delta\varepsilon}{2} = \frac{(\Delta\sigma)^2}{2E} + \Delta\sigma\left(\frac{\Delta\sigma}{2A'}\right)^{\frac{1}{n_f}} \qquad \text{Eqn. 2.27}$$

From Eqn. 2.25:

$$\frac{(K_f\Delta\sigma_\infty)^2}{2E} = \frac{(\Delta\sigma)^2}{2E} + \Delta\sigma\left(\frac{\Delta\sigma}{2A'}\right)^{\frac{1}{n_f}} \qquad \text{Eqn. 2.28}$$

Equations Eqn. 2.25 to Eqn. 2.28 can be used to determine the local values of $\Delta\sigma$ and $\Delta\varepsilon$ in the notch root for successive stress reversals. In addition to analytical approaches like Neuber's Rule, computer-based finite element analysis can be used to determine the local stress and strain amplitudes in notched geometries. With recent advances in computing power and speed, FE modelling is now extensively used as a tool for predicting stress and strain distributions in components. Note that the accuracy of FE modelling is dependent upon the constitutive equations used to describe a material's behaviour and such constitutive equations may not always be available for the system being studied.

2.7.3 LEFM & Notch Fatigue

The use of linear elastic fracture mechanics to describe the stress-strain fields at the tip of sharp cracks was discussed in Section 2.3. A sharp crack can be considered as a notch for which the tip radius r_{root} is zero. LEFM can also be applied to notch geometries where r_{root} is greater than zero, but is only valid when the deformation is elastic.

As an example of the use of LEFM to calculate local stresses near a notch, the situation of a sharp, through-thickness crack in a plate as discussed in Section 2.3 can be adapted by replacing the crack with a notch of root radius r_{root}, as depicted in Figure 2.12. The elastic stresses in the vicinity of the notch are then given by:

$$\sigma_{xx} = \frac{K_I}{\sqrt{2\pi r}}\left[\cos\frac{\theta}{2}\left(1-\sin\frac{\theta}{2}\sin\frac{3\theta}{2}\right)\right] + \frac{K_I}{\sqrt{2\pi r}}\left(\frac{r_{root}}{2r}\right)\left(-\cos\frac{3\theta}{2}\right) \qquad \text{Eqn. 2.29}$$

$$\sigma_{yy} = \frac{K_I}{\sqrt{2\pi r}}\left[\cos\frac{\theta}{2}\left(1+\sin\frac{\theta}{2}\sin\frac{3\theta}{2}\right)\right] + \frac{K_I}{\sqrt{2\pi r}}\left(\frac{r_{root}}{2r}\right)\left(\cos\frac{3\theta}{2}\right) \qquad \text{Eqn. 2.30}$$

$$\sigma_{xy} = \frac{K_I}{\sqrt{2\pi r}}\left[\sin\frac{\theta}{2}\cos\frac{\theta}{2}\cos\frac{3\theta}{2}\right] + \frac{K_I}{\sqrt{2\pi r}}\left(\frac{r_{root}}{2r}\right)\left(-\sin\frac{3\theta}{2}\right) \qquad \text{Eqn. 2.31}$$

where K_I is the stress intensity factor for a sharp crack of the same length as the notch subjected to the same loading conditions. For $r_{root} = 0$, equations Eqn. 2.29 to Eqn. 2.31 reduce to those for a sharp crack given by Eqn. 2.6 to Eqn. 2.8.

When a far-field stress range of $\Delta\sigma_\infty$ is applied, the stress intensification in the notch is a maximum at $r = r_{root}/2$ and $\theta = 0$ in Figure 2.12. The maximum local stress range $\Delta\sigma_{max}$ is given by:

$$\Delta\sigma_{\max} = \frac{2\Delta K_I}{\sqrt{\pi r_{root}}} = K_t\left(\Delta\sigma_\infty\right) \qquad \text{Eqn. 2.32}$$

ΔK_I is the stress intensity factor range at the tip of a sharp crack of the same length as the notch subjected to the same far-field applied stress range $\Delta\sigma_\infty$. Strictly, Eqn. 2.32 is only true for vanishingly small root radii, but it has been shown to be accurate to within 10% of FE model results for $r_{root} < 4.5$ mm and notch lengths significantly longer than the root radius [2.1]. In an approach similar to the stress-life approach discussed previously, the number of cycles to crack initiation in the notch root can be correlated with $\Delta\sigma_{max}$ or $\Delta K_I / \sqrt{r_{root}}$. Experimental work on double-edged notched plates in steel with different root radii showed that fatigue crack initiation exhibited a threshold value of $\Delta K_I / \sqrt{r_{root}}$ [2.1]. This threshold value can be considered as an endurance limit for notched bars when characterised by LEFM.

2.7.4 Damage-Tolerant Approach to Notch Fatigue

The approaches to notch fatigue described in the previous sections are primarily concerned with determining a modified endurance or fatigue limit, assuming that most of the fatigue life is spent in crack initiation. In a damage-tolerant approach to notch fatigue, it is acknowledged that a significant proportion of component life may be occupied by crack growth, hence it is necessary to have reliable methods of measuring and characterising crack growth behaviour. A full prediction of the fatigue lifetime of a notched component requires characterisation of the proportion of the total life spent in:

- The initiation of a dominant fatigue crack in the notch root.
- Early growth of the dominant crack within the notch plastic zone.
- Subsequent crack growth in the notch elastic stress-strain field.
- Final growth in the elastic stress-strain field of the bulk material.

For purely elastic deformation in notched components, it is possible to apply LEFM to characterise crack growth da/dN or dc/dN in terms of the stress intensity factor range ΔK. For example, Dowling [2.29] considered the case of a crack growing from a circular hole in a plate, shown in Figure 2.13. For an applied far-field stress range $\Delta\sigma_\infty$, the theoretical elastic stress concentration factor K_t can be used to determine the local value of ΔK when the crack length is small compared to the dimensions of the notch. For short crack lengths in the vicinity of the notch:

$$\Delta K_{short} = 1.12 K_t \Delta\sigma_\infty \sqrt{\pi l} \qquad \text{Eqn. 2.33}$$

As the crack grows longer, it grows out of the elastic stress field of the notch and ΔK is then given by:

$$\Delta K_{long} = \alpha \Delta \sigma_{\infty} \sqrt{\pi a} \qquad \text{Eqn. 2.34}$$

where α is a function of geometry.

The transition crack length l_t for the changeover from the short crack to the long crack solution for ΔK is given by equating Eqn. 2.33 and Eqn. 2.34:

$$l_t = \frac{r}{\left[(1.12K_t/\alpha)^2 - 1\right]} \qquad \text{Eqn. 2.35}$$

However, LEFM is not applicable when yielding occurs in the notch root. So, instead of using LEFM for the short crack stage, Dowling [2.29] proposed a local strain approach whereby strain-life tests on smooth specimens are used to determine the number of cycles N_i to initiate a crack of transition length l_t. The long crack solution for ΔK can then be used to describe the propagation of the crack beyond the influence of the notch stress-strain field, and integrated to give the crack propagation life N_p. Hence:

$$N_f = N_i + N_{p(\text{long})} \qquad \text{Eqn. 2.36}$$

This methodology assumes that the transition crack length l_t, which is based on an elastic analysis, is valid for elastic-plastic deformation as well. It also requires very specific short crack initiation data which is difficult to obtain experimentally. Dowling's predictions of total fatigue lives agreed reasonably well with experimental results for a blunt notch of radius 2.5 mm [2.29], although the actual initiation life was longer than predicted and the propagation life shorter than predicted.

Another fracture mechanics approach proposed by El Haddad et al. [2.17] uses a strain-based intensity factor for a short crack in the stress-strain field of the notch:

$$\Delta K = \alpha E \Delta\varepsilon \sqrt{\pi(a + a_o)} \qquad \text{Eqn. 2.37}$$

where:

α = geometrical constant

E = elastic modulus

a = crack length

a_o = short crack length correction given by Eqn. 2.17.

The strain range $\Delta\varepsilon$ is calculated using Neuber's Rule or by FE modelling. Once the crack has grown away from the influence of the notch, LEFM expressions are used to calculate ΔK, but El Haddad et al. [2.17] do not state how the transition from the use of short crack to long crack solutions for ΔK is determined. The short crack length correction has also been used for *da/dN* versus ΔJ characterisation of short cracks growing from notches, successfully correlating short crack and long crack behaviour [2.16]. However, the physical significance of the parameter a_o remains uncertain [2.1].

Experimental measurement of crack closure combined with FE modelling predictions of notch stress and strain concentration factors has been used [2.9] to calculate ΔK_{eff} for short cracks emanating from a plastically yielded notch:

$$\Delta K_{eff} = C K_t \Delta\sigma_{eff} \sqrt{\pi a} \qquad \text{Eqn. 2.38}$$

In Eqn. 2.38, C is a constant for a particular notch of root radius r_{root} [2.9]. K_t is calculated using Eqn. 2.22 from FE modelling predictions of K_σ and K_ε. $\Delta\sigma_{eff}$ is an effective stress range introduced to account for crack closure in the plastic zone of the notch. It assumes that only the proportion of the applied stress range for which the crack faces are not in contact contributes to crack propagation.

$$\Delta\sigma_{eff} = \sigma_{\max} - \sigma_{op} \qquad \text{Eqn. 2.39}$$

where:

σ_{op} = applied stress at which crack faces become fully separated.

Eqn. 2.38 was used to rationalise the transient behaviour of short cracks emerging from a notch in a medium carbon steel [2.9], in terms of a reduced crack driving force ΔK_{eff}. Use of ΔK_{eff} is attractive to researchers because it enables use of the well-known LEFM stress intensity factor K to describe crack stress-strain fields. However, the determination of σ_{op}, K_σ and K_ε is not always straightforward and the use of ΔK in elastic-plastic situations is open to question, even with appropriate corrections for the effects of plasticity.

To overcome some of the limitations of LEFM, the EPFM parameter J can be used to describe the stress-strain fields of notched geometries [2.13]. When employing EPFM to characterise crack growth in notched geometries on a da/dN versus ΔJ basis, ΔJ is calculated either from analytical expressions [2.30] or by FE modelling [2.31]. Like LEFM, the use of EPFM to predict fatigue lives requires estimation of the transition from mechanically short crack growth within the plastic zone of the notch to long crack growth influenced by elastic loading only. EPFM has the advantage that it can be used to characterise crack growth rates within the notch plastic zone from some initial crack length l_i to the transition length l_t [2.30]. The transition crack length using EPFM can be determined by equating the short and long crack expressions for J. A suitable long crack expression for J can then be used to characterise crack growth rates beyond l_t. The total life is obtained by integrating the short crack and long crack growth laws and adding the result to the initiation life N_i.

$$N_f = N_i + N_{p(short)} + N_{p(long)} \qquad \text{Eqn. 2.40}$$

A comparison of EPFM fatigue life predictions using ΔJ with predictions using the LEFM parameter ΔK found that the EPFM method based on the J-integral gave predictions closer to actual experimental results than LEFM [2.30]. Unfortunately, there is still the problem of obtaining data for the number of cycles N_i to initiate a short crack of length l_i. Strain-life data for smooth specimens can be used instead, but generally leads to non-conservative predictions of total life [2.30].

Another elastic-plastic model for characterising the initiation and growth of fatigue cracks in notches was proposed by Hammouda et al. [2.32, 2.33]. For the initiation stage, the model considered the plastic shear displacement ϕ_s required to initiate a crack along a persistent slip band, which must be greater than some threshold value ϕ_{th}. In practice, an empirical relationship for crack initiation based on smooth torsional tubular test specimens was used [2.33]. For the crack growth stage, propagation was considered to be controlled by the plastic shear displacement at the crack tip, ϕ_t, which has contributions from notch plasticity and from crack-tip plasticity. Beyond the notch plastic zone, a standard LEFM solution can be used to characterise crack growth behaviour. Hammouda's model produced slightly conservative predictions of actual fatigue lives [2.33], and was able to account for non-propagating cracks, which arise when ϕ_t falls below the threshold value ϕ_{th}.

Elastic-plastic FE analyses of notches can be used to study the effect of notch plasticity on short fatigue crack growth behaviour [2.34]. It was found that the extent of Stage I cracking decreased with increasing notch plastic strain. The transition to Stage II crack growth was thought to be linked to a change in the crack tip displacement from shear (Mode II) to an opening mode (Mode I). In Stage II, cracks were amenable to characterisation using ΔK. Ahmad et al. [2.34] commented that further characterisation of Stage I crack growth in notch roots was required, taking into account crack growth thresholds and the local plastic strain amplitude ahead of the notch.

2.8 Lifing of Gas Turbine Components

The different philosophies of turbine disc lifing have been reviewed by Goswami [2.35]. The lifing philosophies were originally developed for aerospace gas turbines, but they are also applicable to gas turbines used in power generation.

In the traditional predicted safe life philosophy, the life is declared based on laboratory specimen and component testing. The end point of a component test can be determined in different ways. Sometimes, 2/3 of the life to failure is used [2.36]. This ensures a known safety margin between the declared safe life and the failure life of the component. Alternatively, the test end point is determined as the number of cycles required to initiate an "engineering crack" of a pre-determined size. Typically the engineering crack has a depth of 0.75-0.8 mm [2.35, 2.36, 2.37], based on a size which can be detected reliably by NDT during engine overhaul or inspection. The test end point for an engineering crack is established either by inspection during rig testing, or by back-calculation from a larger crack size. The engineering crack approach has the disadvantage of the lack of a consistent safety margin [2.36]. Because of the statistical variability of fatigue behaviour and the limited amount of testing possible, a Gaussian distribution of life is generally assumed, and the predicted safe life is declared for the mean minus three standard deviations. Additional reduction factors are applied to determine the actual service life of a component. For example, a service life of half the predicted safe life may be cleared. Selected components are withdrawn from service and tested to confirm the initial life prediction, permitting usage up to the predicted safe life [2.36]. However, there are concerns about the statistical validity of testing only a limited number of components withdrawn from service. As an alternative, the full predicted safe life may be cleared for service. A detailed life management plan is agreed for the fleet, involving inspection of components withdrawn from service at pre-determined intervals.

Damage-tolerant approaches to lifing have arisen from the requirement to demonstrate acceptable component life assuming crack initiators are present in the components. Lifing models have been developed by different gas turbine manufacturers which take into account a number of damage processes, including fatigue, creep and thermo-mechanical fatigue [2.38]. Crack propagation lives are determined for various locations in a component using fracture mechanics. Different initial crack sizes can be used to account for the likelihood of different defects and inhomogeneities in the material. The lowest life obtained is then reduced by a safety factor to give the predicted safe life, and components are withdrawn from service once this life is reached. Fracture mechanics can also be used to back-calculate from the critical defect size at the end of life to an assumed initial or effective size [2.39]. This calculated initial defect size can be used in process control, for example in defining the maximum permitted inclusion size in a powder metallurgy disc [2.37]. Application of fracture mechanics and an expanding database of material and component behaviour has led to the development of database lifing. Providing the material and production methods do not change, database lifing can be used to predict the life of new components based on the existing materials and component database, though component testing is still required to verify the predictions. If the production route changes (for example a change in surface finishing technique), then more testing is required to validate the applicability of the existing database to the new component.

Historically, turbine discs are retired from service once they reach their predicted safe life. Although this approach minimises the risk of failure, it may lead to the unnecessary retirement of discs which are still within their useable life. The concept of retirement-for-cause was developed to enable the full life of each disc to be utilised. A critical requirement of retirement-for-cause is an NDT technique capable of reliably detecting cracks, measured in terms of a probability of detection (POD). In advocating retirement-for-cause, the risk of introducing damage during the overhaul and inspection process must also be considered. Retirement-for-cause uses either probabilistic fracture mechanics (PFM) [2.40, 2.41] or deterministic fracture mechanics (DFM) to establish safe inspection intervals for components. PFM considers a probability distribution of times to initiate cracks of a given size a_o [2.40]. Fracture mechanics are used to calculate crack propagation rates, also taking into account the statistical variability in propagation by use of a probability distribution. Probability theory is used to determine the risk of a critical defect being present, and the NDT inspection intervals are set accordingly. In DFM, an initial defect a_o is assumed to already exist at the most critical part of the component, where a_o is the maximum crack size that might be overlooked by NDT. Fracture mechanics are used to predict the worst-case scenarios of crack growth, and inspection intervals are established by applying a safety factor to the predicted time to reach the critical defect size. DFM tends to be more conservative than PFM [2.35], but PFM requires a large database of results to establish the statistical distributions used in the prediction models. PFM can be applied to life extension programmes, where there is an interest in extending the life of a fleet beyond the original predicted safe life, providing it can be demonstrated that the risk of fracture is acceptably low. It is important for the probability of detection of defects to be high to minimise risk of fracture when the disc is returned to service. Low statistical confidence in the detection of defects may make retirement-for-cause or life extension economically unviable because the required inspection intervals become too short [2.35].

2.9 Summary of General Fatigue Principles

Historically, two complementary approaches to fatigue lifing have evolved, based on total life or damage-tolerant approaches. The total life approach is most appropriate for situations where resistance to crack initiation is important, while the damage-tolerant approach is used to predict safe operating lives by considering contributions from both crack initiation and crack propagation. Continued advances in engineering designs and greater demands for high performance and reliability require improved damage-tolerant models. Such models require reliable information on crack initiation and growth behaviour, taking into account the differences between short and long cracks and the propagation of cracks in notched geometries representative of real components. Crack growth laws relating the growth rate *da/dN* to a characteristic driving force have been developed, using either linear elastic fracture mechanics (LEFM) or elastic-plastic fracture mechanics (EPFM) to derive the crack driving force ΔK (LEFM) or ΔJ (EPFM). Both LEFM and EPFM have their limitations, particularly when dealing with short cracks and the behaviour of cracks in notches. A desirable element for improved damage-tolerant models is improved information about the initiation, growth and coalescence of short cracks to form a dominant long crack defect. An expansion of the available information on crack growth is important for the lifing of components such as gas turbine discs, where there is interest in the use of retirement-for-cause philosophies and the development of life extension programmes.

2.10 Figures

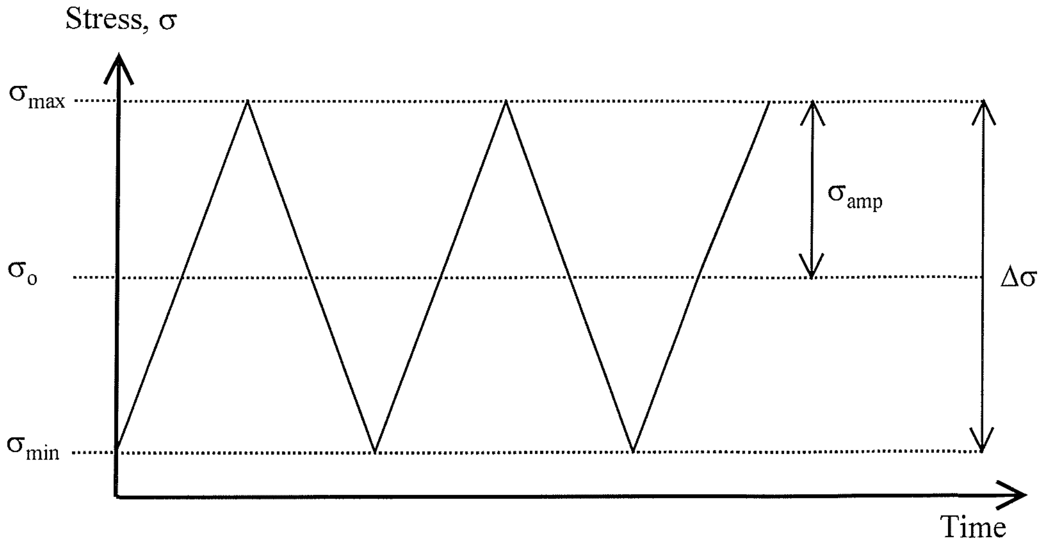

Figure 2.1: An example fatigue cycle.

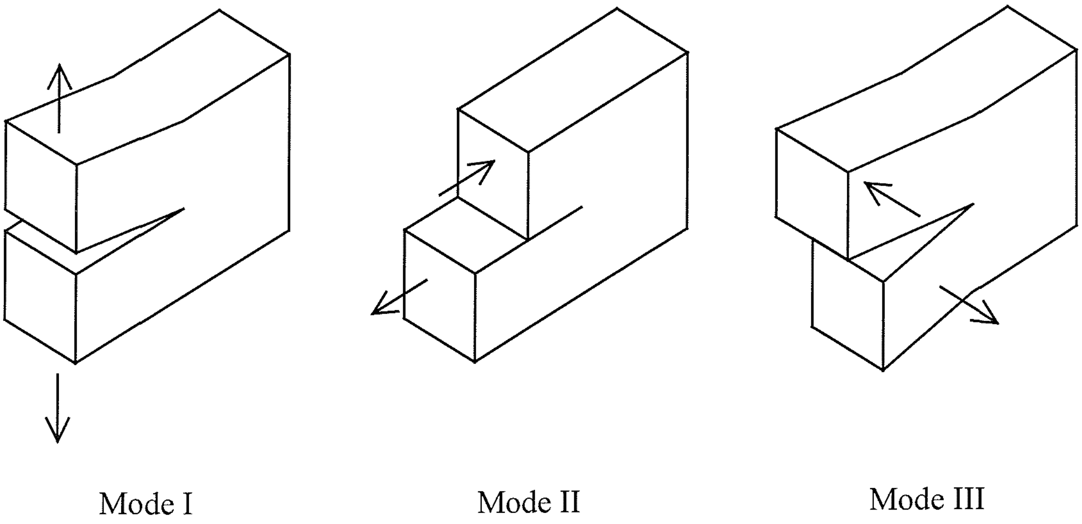

Figure 2.2: Crack loading modes.

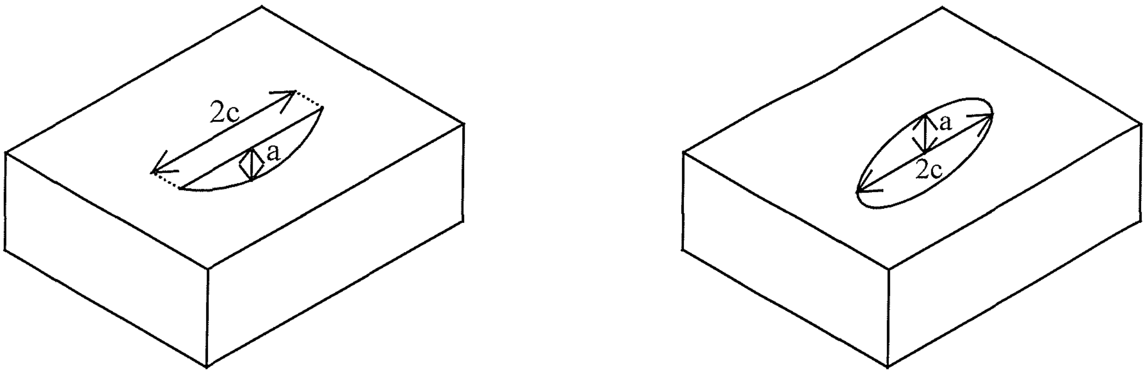

(a) Semi-elliptical surface crack. (b) Elliptical embedded crack; $c \geq a$.

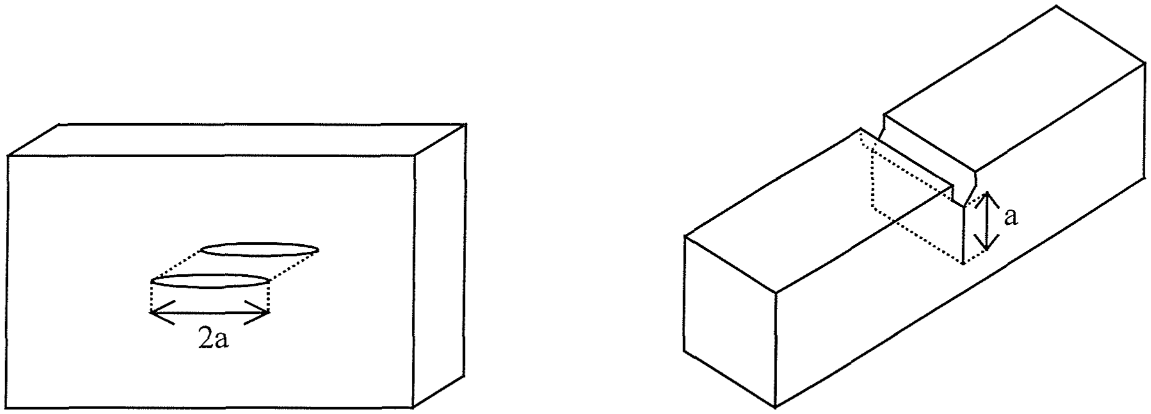

(c) Through-thickness crack in a plate. (d) Through-thickness crack from a notch.

Figure 2.3: Convention used for the geometrical description of crack lengths. The above convention will be used throughout this thesis.

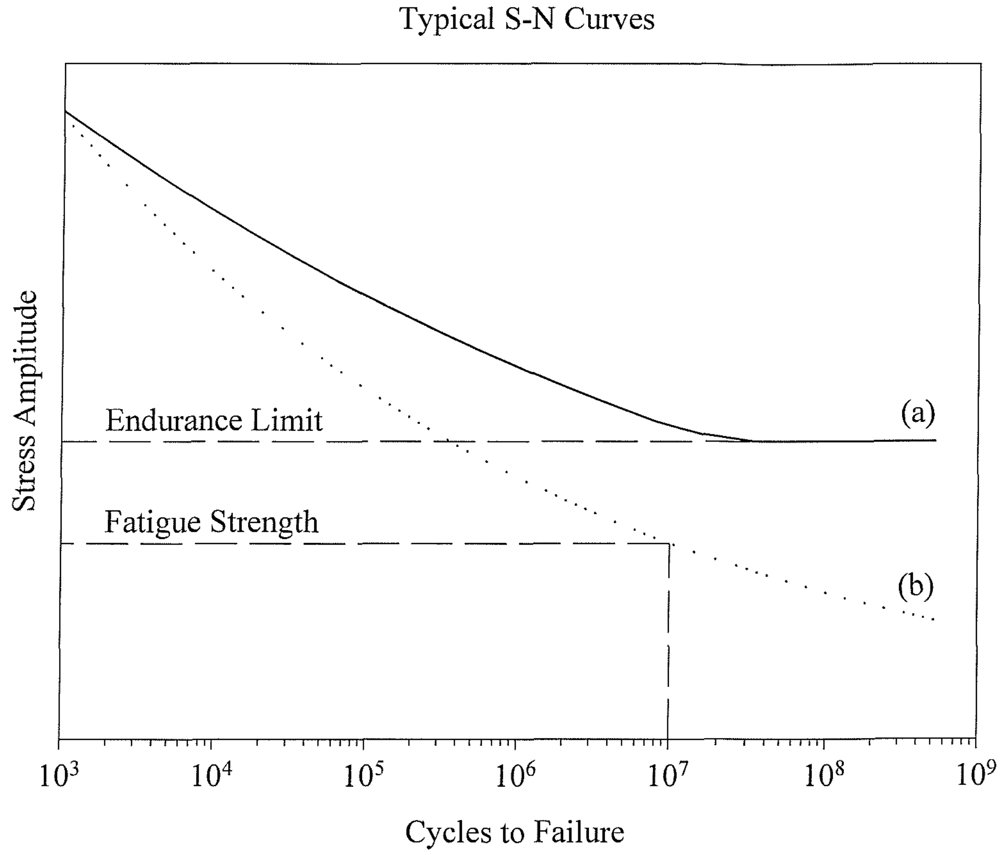

Figure 2.4: Typical S-N curves. Curve (a) is typical of strain-age hardening materials which exhibit an endurance limit. Curve (b) represents materials which do not strain-age harden, with a fatigue strength defined as the stress amplitude which will not cause failure for at least 10^7 cycles.

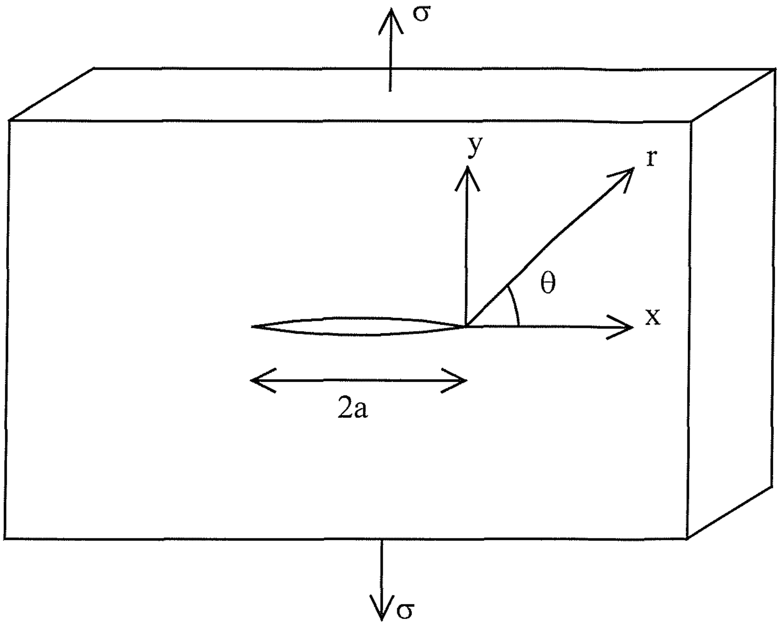

Figure 2.5: Sharp crack length $2a$ in a thin elastic plate, with a nominal applied stress σ.

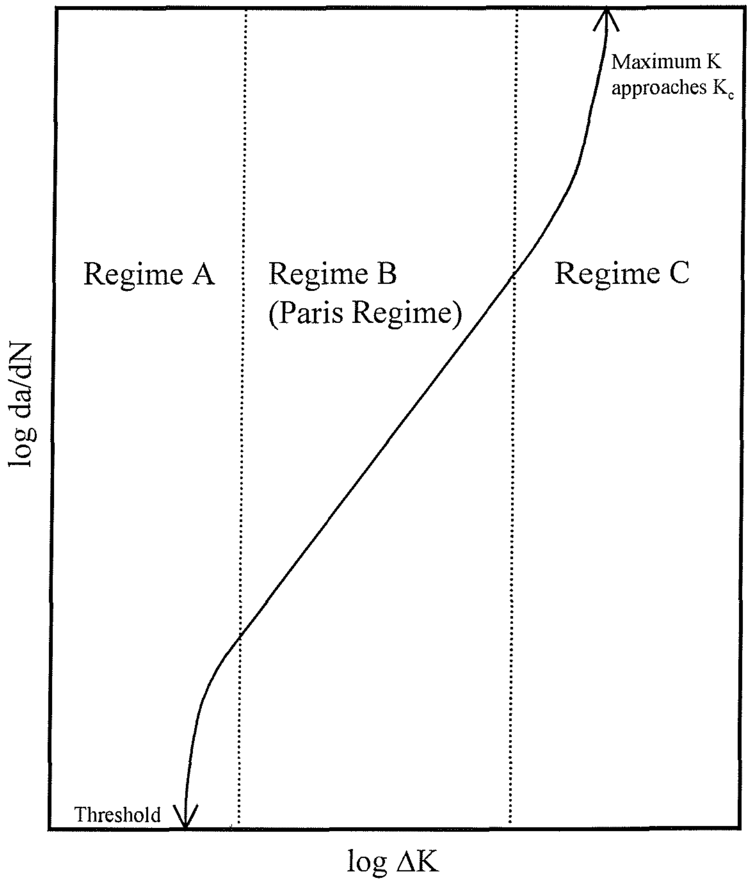

Figure 2.6: Schematic diagram showing typical variation of crack growth rate *da/dN* with ΔK. (After Suresh [2.1]).

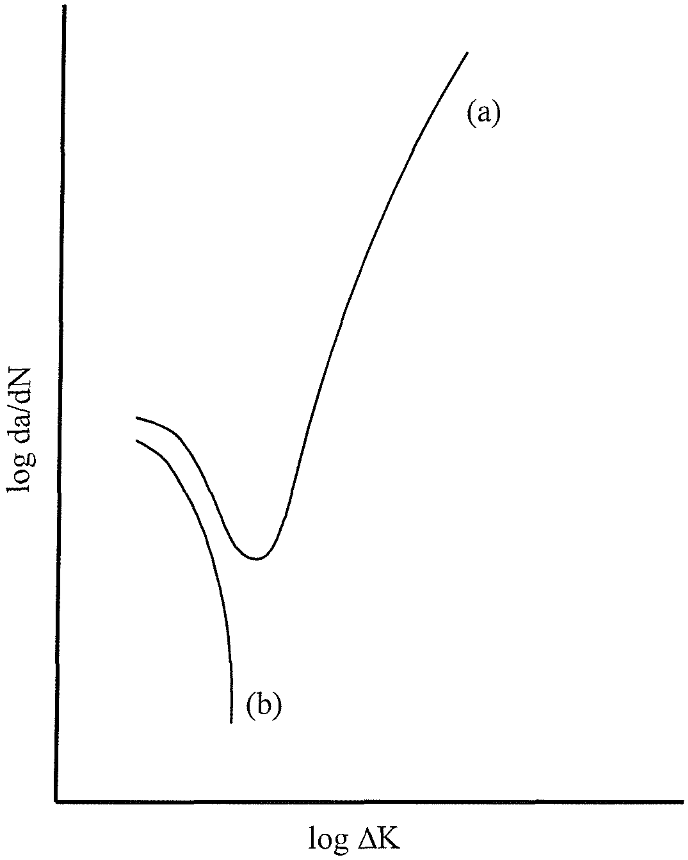

Figure 2.7: Schematic plot showing typical growth rate behaviour of short cracks growing in the plastic zone of a notch. (a): Transient behaviour; (b) Arrested growth.

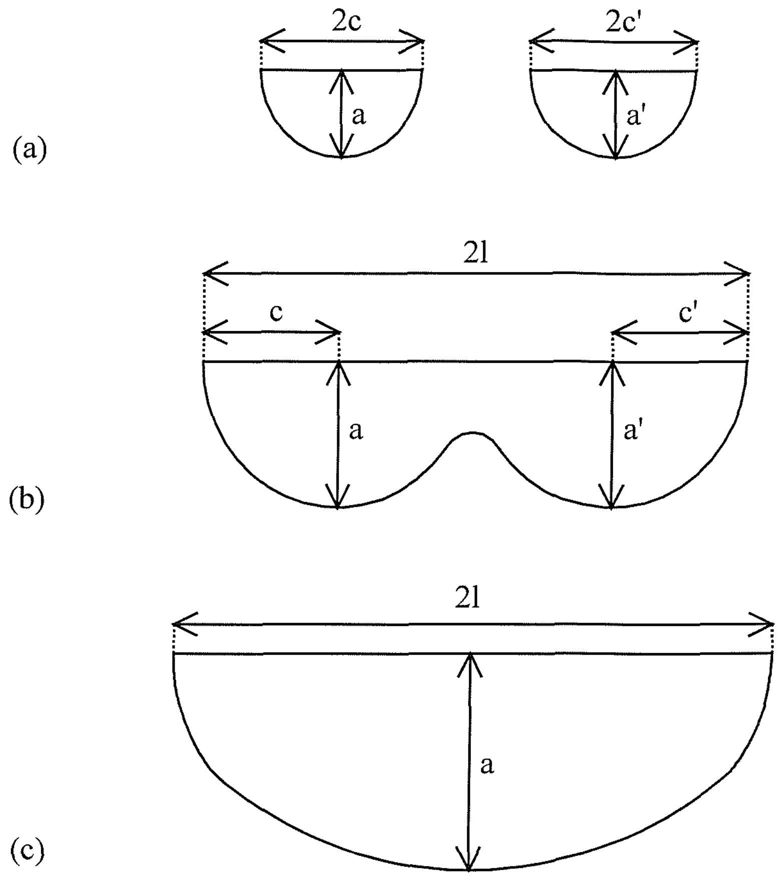

Figure 2.8: Coalescence of two coplanar, colinear short cracks. (a) Before coalescence; (b) During coalescence; (c) After coalescence.

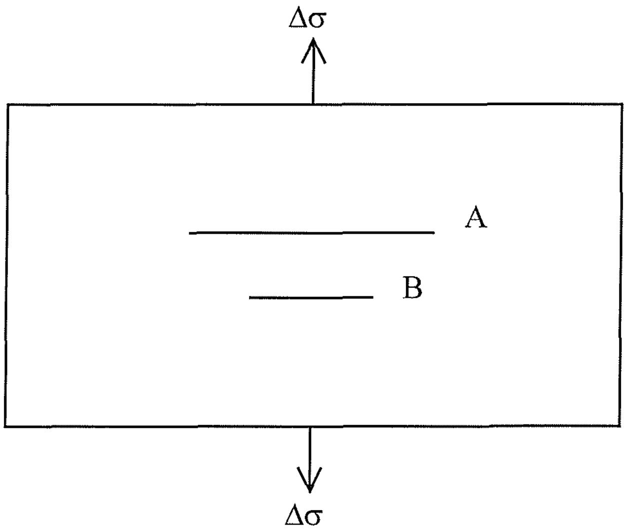

Figure 2.9: Shielding of overlapping, parallel non-coplanar surface cracks (plan view). The longer Crack A shields the shorter Crack B from the full effects of the applied load, resulting in lower growth rates or arrest for Crack B.

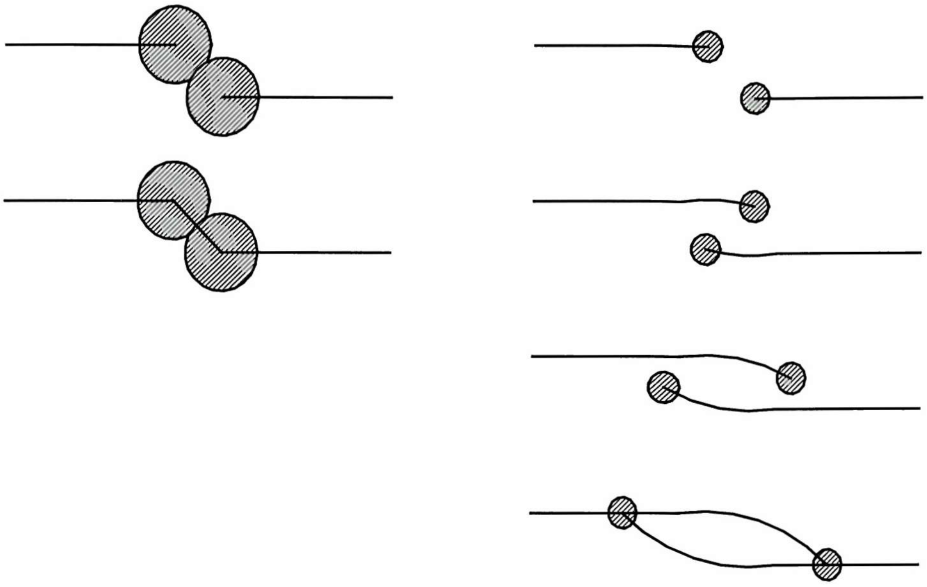

(a) (b)

Figure 2.10: Coalescence behaviour of offset, non-coplanar surface cracks (plan view). (a) Crack tip plastic zones overlap - coalescence by breakthrough of intervening material. (b) Crack tip plastic zones don't overlap - cracks by-pass each other and deflect to coalesce behind their respective tips. See Forsyth [2.22].

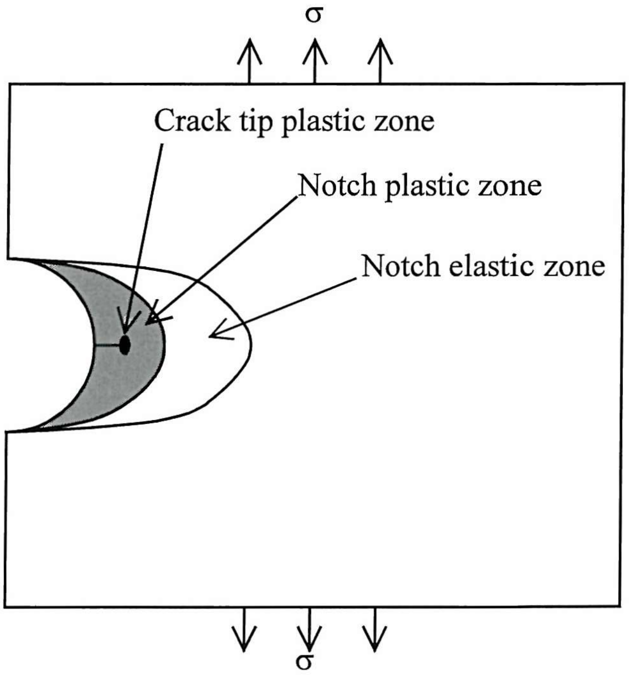

Figure 2.11 Elastic and plastic zones associated with a notch containing a small fatigue crack.

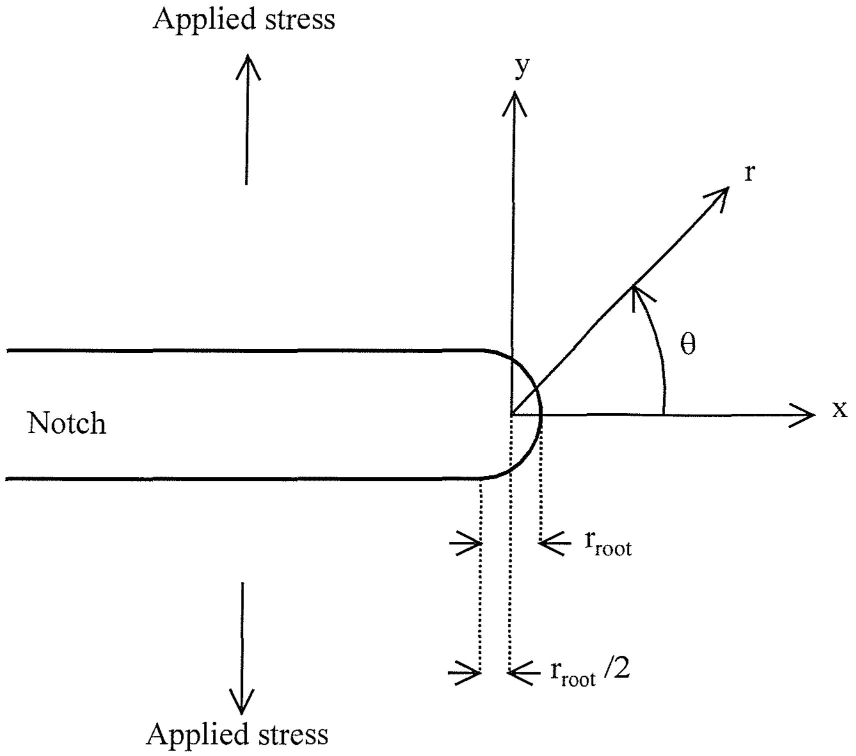

Figure 2.12: Co-ordinate system for LEFM analysis of a blunt notch of root radius r_{root} in an elastically deforming plate.

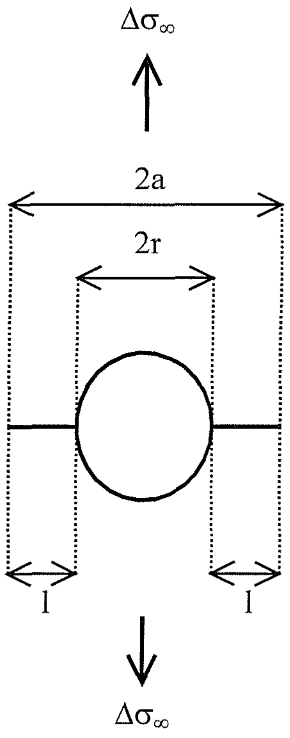

Figure 2.13: Geometry of crack growing from a hole radius r in a plate subjected to a far field stress range $\Delta\sigma_\infty$. After Dowling [2.29].

2.11 References

[2.1] Suresh S. Fatigue of Materials Cambridge Solid State Science Series, Cambridge University Press, Cambridge, UK. ISBN 0-521-43763-6 (1991)

[2.2] Suresh S. Fatigue of Materials: Second Edition Cambridge University Press, Cambridge, UK. ISBN 0-521-57847-7 (1998)

[2.3] Coffin L. F. "A study of the effects of cyclic thermal stresses on a ductile metal" Trans. ASME vol. 76 pp. 931-950 (1954)

[2.4] Manson S. S. "Behavior of materials under conditions of thermal stress" NACA Report 1170, Lewis Flight Propulsion Laboratory, Cleveland, USA (1954)

[2.5] Miller K. J. "The behaviour of short fatigue cracks and their initiation Part I - A review of two recent books" Fatigue Fract. Engng. Mater. Struct. vol. 10 pp. 75-91 (1987)

[2.6] Miller K. J. "The behaviour of short fatigue cracks and their initiation part II - A general summary" Fatigue Fract. Engng. Mater. Struct. vol. 10 pp. 92-113 (1987)

[2.7] Miller K. J. "The two thresholds of fatigue behaviour" Fat. Fract. Engng. Mater. Struct. vol. 16 pp. 931-939 (1993)

[2.8] Miller K. J. "The short crack problem" Fat. Engng. Mater. Struct. vol. 5 pp. 223-232 (1982)

[2.9] Ye T., Jiawen H. & Naisai H. "Effect of notch stress field and crack closure on short fatigue crack growth" Fatigue Fract. Engng. Mater. Struct. vol. 13 pp. 423-430 (1990)

[2.10] Sadananda K. & Vasudevan A. K. "Short crack growth and internal stresses" Int. J. Fatigue vol. 19 Supp. No. 1 pp. S99-S108 (1997)

[2.11] Sadananda K. & Vasudevan A. K. "Short Crack Growth Behavior" Fatigue and Fracture Mechanics Vol. 27, ASTM STP 1296, Eds. Piascik R. S., Newman J. C. & Dowling N. E., ASTM, USA pp. 301-316 (1997)

[2.12] Sadananda K. & Vasudevan A. K. "Analysis of small crack growth behavior using unified approach" Proc. Third International Conference Small Fatigue Cracks: Mechanics, Mechanisms & Applications, (Hawaii, Dec. 1998), Ed. Ravichandran K. S., Ritchie R. O. & Murakami Y. Elsevier Science, Oxford, UK, pp. 73-83 (1999)

[2.13] Rice J. R. "A path independent integral and the approximate analysis of strain concentration by notches and cracks" ASME J. Applied Mech. vol. 35 pp. 379-386 (1968)

[2.14] El Haddad M.H., Smith K.N. & Topper T.H. "Fatigue Crack Propagation of Short Cracks" Trans. ASME J. Engng. Mater. Tech. vol. 101 pp. 42-46 (1979)

[2.15] Irwin G. R. "Plastic zone near a crack and fracture toughness" Proc. 7th International Sagamore Ordnance Materials Conf. vol. IV, Syracuse University, New York, pp. 63-78 (1960)

[2.16] El Haddad M.H., Dowling N.E., Topper T.H. & Smith K.N. "J integral applications for short fatigue cracks at notches" Int. J. Fracture vol. 16 pp. 15-30 (1980)

[2.17] El Haddad M.H., Topper T.H. & Topper T.N. "Fatigue life predictions of smooth and notched specimens based on fracture mechanics" Trans. ASME J. Engng. Mater. Tech. vol. 103 pp. 91-96 (1981)

[2.18] Wu Z. & Sun X. "Multiple fatigue crack initiation, coalescence and growth in blunt notched specimens" Engng. Fract. Mech. vol. 59 pp. 353-359 (1998)

[2.19] Soboyejo W. O., Kishimoto K., Smith R. A. & Knott J. F. "A study of the interaction and coalescence of two coplanar fatigue cracks in bending" Fatigue Fract. Engng. Mater. Struct. vol. 12 pp. 167-174 (1989)

[2.20] Soboyejo W. O., Knott J. F., Walsh M. J. & Cropper K. R. "Fatigue crack propagation of coplanar semi-elliptical cracks in pure bending" Engng. Fract. Mech. vol. 37 pp. 323-340 (1990)

[2.21] Soboyejo W. O. & Knott J. F. "The propagation of non-coplanar semi-elliptical fatigue cracks" Fatigue Fract. Engng. Mater. Struct. vol. 14 pp. 37-49 (1991)

[2.22] Forsyth P. J. "A unified description of micro and macroscopic fatigue crack behaviour" Int. J. Fatigue vol. 5 pp. 3-14 (1983)

[2.23] Zhao Y-X., Gao Q. & Wang J-N. "Interaction and evolution of short fatigue cracks" Fatigue Fract. Engng. Mater. Struct. vol. 22 pp. 459-467 (1999)

[2.24] Chen E. Y., Lawson L. & Meshii M. "Comparison of the growth of individual and average microcracks in the fatigue of Al-SiC composites" Metall. & Mater. Trans. A vol. 26 pp. 3163-3176 (1995)

[2.25] Wu S. & Chudnovsky A. "Effect of microcrack array on stress intensity factor of main crack" Int. J. Fracture vol. 59 pp. 41-52 (1993)

[2.26] Smith R. A. "Propagation of fatigue cracks from notches" Mater. Sci. Tech., vol. 1 pp. 537-543 (1985)

[2.27] Chapetti M. D., Kitano T., Tagawa T. & Miyata T. "Fatigue limit of blunt-notched components" Fat. Fract. Engng. Mater. Struct. vol. 21 pp. 1525-1536 (1998)

[2.28] Neuber H. "Theory of stress concentration for shear-strained prismatical bodies with arbitrary non-linear stress-strain law" J. Applied Mechanics vol. 28 pp. 544-550 (1961)

[2.29] Dowling N. E. "Notched member fatigue life predictions combining crack initiation and propagation" Fatigue Engng. Mater. Struct. vol. 2 pp. 129-138 (1979)

[2.30] Sehitoglu H. "Fatigue life prediction of notched members based on local strain and elastic-plastic fracture mechanics concepts" Engng. Fract. Mech. vol. 18 pp. 609-621 (1983)

[2.31] Wang J. C. & Lu Y. Z. "Cyclic analysis of propagating short cracks at notches and short-crack growth behaviour" Engng. Fract. Mech. vol. 34 pp. 831-840 (1989)

[2.32] Hammouda M. M., Smith R. A. & Miller K. J. "Elastic-plastic fracture mechanics for initiation and propagation of notch fatigue cracks" Fatigue Engng. Mater. Struct. vol. 2 pp. 139-154 (1980)

[2.33] Hammouda M. M. & Miller K. J. "Prediction of fatigue lifetime of notched members" Fatigue Engng. Mater. Struct. vol. 2 pp. 377-386 (1980)

[2.34] Ahmad H. Y., De Los Rios E. R. & Yates J. R. "The influence of notch plasticity on short fatigue crack behaviour" Fat. Fract. Engng. Mater. Struct. vol. 17 pp. 235-242 (1994)

[2.35] Goswami T. K. "Hot section turbine disk lifing philosophies" American Society of Mechanical Engineers (Paper number: 93-GT-363) Presented at International Gas Turbine & Aeroengine Congress and Exposition ASME, New York pp. 1-13 (1993)

[2.36] Pickard A. C. "Component Lifing" Mater. Sci. Tech. vol. 3 pp. 743-749 (1987)

[2.37] Tsubota M., King J. E. & Knott J. F. "Crack propagation and threshold behaviour in Ni-base super-alloys and its implications for component life assessment" Proc. First Parsons International Turbine Conference pp. 189-196 (1984)

[2.38] Halford G.R., Meyer T.G., Nelson R.S., Nissley D.M. & Swanson G.A. "Fatigue life prediction modeling for turbine hot section materials" Trans. ASME J. Engineering for Gas Turbines & Power vol. 111 pp.279-285 (1989)

[2.39] Harrison G. F. "The role of materials modelling techniques in stress analysis and life assessment of modern aero-engine components" Proc. Inst. Mech. Engineers Part G: J. Aerospace Engng. vol. 208 pp. 19-31 (1994)

[2.40] Hanagud S. & Uppaluri B. "Reliability-based optimum inspection and maintenance procedures" J. Aircraft vol. 12, pp. 403-410 (1975)

[2.41] Yang J. N. & Chen S. "Fatigue reliability of gas turbine engine components under scheduled inspection maintenance" J. Aircraft vol. 22 pp. 415-422 (1985)

3 INCONEL 718 AND ITS FATIGUE BEHAVIOUR

This chapter begins with a description of the composition, physical metallurgy and microstructure of Inconel 718 (IN718), with reference to their influence on fatigue performance. The published literature on the fatigue characteristics of IN718 is reviewed, concentrating on the effects of high temperature environments on crack initiation and growth.

3.1 Composition and Physical Metallurgy

The limiting chemical composition for IN718 is given in Table 3.1 [3.1].

Element	**Limiting Chemical Composition (wt%)**
Ni	50.00-55.00
Cr	17.00-21.00
Fe	Balance
Nb (+Ta)	4.75-5.50
Mo	2.80-3.30
Ti	0.65-1.15
Al	0.20-0.80
Co	1.00 max
C	0.08 max
Mn	0.35 max
Si	0.35 max
P	0.015 max
S	0.015 max
B	0.006 max
Cu	0.30 max

Table 3.1: Limiting chemical composition for Inconel 718 [3.1].

The high strength of IN718 and other nickel-base superalloys arises from a combination of solid solution strengthening and precipitation hardening of the face-centred cubic (FCC) nickel-rich matrix [3.2]. Solid solution strengthening in IN718 is enabled by the presence of Fe, Cr, Al, Ti, Mo and Co. Solid solution strengthening remains effective up to about 0.6 of the melting temperature. At temperatures where creep becomes significant, the presence of Mo can help reduce creep deformation by lowering self-diffusivity. Co can also reduce creep deformation by lowering the stacking fault energy, thus hindering dislocation cross-slip and climb.

The main precipitate-forming alloy additions in IN718 are Nb, Ti and Al. Nb favours the formation of the metastable γ'' phase, whereas Ti and Al favour formation of γ'. These phases are discussed in more detail below. The major reinforcement phase in IN718 is γ'', though some γ' is also present. It has been shown that increasing the ratio of (Ti + Al):Nb increases the amount of γ' relative to γ'' [3.3]. Oxidation and corrosion resistance is enhanced by the presence of Cr, which forms a stable, non-porous Cr_2O_3 surface oxide layer.

The presence of carbon is important in the melt processing of superalloys. It significantly lowers the solidus temperature of nickel, enables better control of liquid metal properties, and can help in the removal of detrimental elements like sulphur and oxygen [3.4]. The carbon that remains in the superalloy upon casting affects the final properties of the material through the formation and transformation of a variety of carbide phases. These carbides are important microstructural constituents because of their effects on mechanical properties, fatigue resistance and creep.

3.2 Microstructure

3.2.1 Strengthening Precipitates

The principal strengthening constituent in IN718 is γ'', a metastable Ni_3Nb phase with a body-centred tetragonal crystal structure of type DO_{22} [3.5]. There is some solubility of Al and Ti in γ'' [3.6, 3.7]. The γ'' forms during ageing as coherent disk shaped particles on the {100} planes of the face-centred cubic γ matrix. Typical γ'' precipitate dimensions are 20-60nm diameter, with a thickness of 5-9nm [3.8]. The orientation relationship between γ'' and the γ matrix has been identified as [3.3, 3.9]:

$$(001)_{\gamma''} // \{001\}_{\gamma} \text{ and } [100]_{\gamma''} // <100>_{\gamma}$$

Some additional contribution to strength comes from the $Ni_3(Al,Ti,Nb)$ γ' phase, which has a face-centred cubic structure of type $L1_2$. The role of γ'' as the principal strengthening phase distinguishes IN718 from other nickel-based superalloys, in which the principal strengthening phase is mostly γ'. Investigations have been carried out into the precipitation sequence of γ' and γ'' in IN718, to determine whether γ' and γ'' appear simultaneously or sequentially during the precipitation process [3.3, 3.9]. Sundararaman et al. [3.9] studied the precipitation of γ' and γ'' in IN718, finding that the two phases precipitated predominantly by homogeneous nucleation. Systematic experiments to determine the sequence of precipitation showed that γ' did not appear before γ'', though it was not possible to confirm the alternative possibility of γ'' nucleating before γ'. Frequently, association of the precipitation of γ' and γ'' was observed, particularly for ageing at 750°C. Further evidence of close association of γ' and γ'' was observed in an atom probe field ion microscopy study [3.10].

The precipitation of γ' and γ'' is very sensitive to the ratio (Ti + Al):Nb (in atomic %), as demonstrated by the work of Cozar and Pineau [3.3]. They studied a number of model Fe-Ni-Cr-Ti-Al-Nb alloys with various (Al + Ti):Nb ratios higher than the usual (Al + Ti):Nb ratio of ~0.7 for IN718. The authors found that γ'' always nucleated on γ', and increasing the (Al + Ti):Nb ratio increased the volume fraction of γ' relative to that of γ''. When alloys with an (Al + Ti):Nb ratio greater than 0.9 were aged above a certain temperature, a "compact morphology" was obtained, consisting of cuboidal γ' particles surrounded by a shell of γ'' on all six cube faces. The critical temperature above which the compact morphology was obtained decreased as the (Al + Ti):Nb ratio was increased above 0.9. Extended ageing showed that the compact morphology was more resistant to coarsening than standard γ'/γ'' morphologies, suggesting a possible way of improving the microstructural stability of IN718-type alloys at elevated temperatures. However, the lower (Al + Ti):Nb ratio in standard IN718 does not permit the formation of the compact morphology, as confirmed by Sundararaman et al. [3.9]. Commercial interest in improving the microstructural stability of IN718 has led to investigations of modified compositions and heat treatments, which can produce the compact morphology [3.11, 3.12, 3.13], or an increased volume fraction of γ' [3.14].

3.2.2 Primary Carbides & Nitrides

For superalloys in general, primary carbides are of the form MC, where M is Ti, Nb, Ta, Hf, Th or Zr. Nitrides take the form MN, where M is Ti, Nb or Zr. Both MC and MN have the B1 (NaCl) crystal structure. In the case of IN718, the most important alloying elements that form primary carbides and nitrides are Ti and Nb. Primary carbides and nitrides form early on in the solidification of IN718 [3.15]. (Ti,Nb)N forms first in the melt, acting as nucleation sites for primary carbides of the form (Nb,Ti)C. Not all the carbon present forms carbides on solidification, so that some remains in solid solution. This carbon is then available to precipitate further MC carbide or one of the lower carbides. During subsequent heat treatment and service, primary carbides are not completely stable, and may react with the gamma matrix to form lower carbides.

It is recognised that MC carbides can initiate fatigue cracks in superalloys. Crack initiation at high temperature is attributed to the oxidation of carbides at the surface of components, creating a notch effect [3.8], though there is very little published work on the detailed mechanisms or kinetics of fatigue crack initiation at carbides.

3.2.3 Lower Carbides

There are several lower carbides which can form in superalloys, namely $M_{23}C_6$, M_6C and M_7C_3. The chemistry and morphology of the various carbides observed experimentally is summarised in Table 3.2 [3.8].

For IN718, the lower carbides M_6C and $M_{23}C_6$ are occasionally observed, usually after extended exposure at elevated temperature. Lower carbides can form from primary carbides by the following reactions:

$$MC + \gamma \rightarrow M_6C + \gamma' \qquad \text{Eqn. 3.1}$$

$$MC + \gamma \rightarrow M_{23}C_6 + \gamma' \qquad \text{Eqn. 3.2}$$

Carbide Phase	**Crystal Structure**	**Typical Formulae**	**Comments**
MC	FCC	TiC NbC HfC	Primary carbides. Composition is variable. "M" elements can be Ti, Ta, Nb, V, Hf, Th or Zr. Generally globular, irregularly shaped particles that form early on in the solidification process.
$M_{23}C_6$	FCC	$Cr_{23}C_6$ $(Cr,Fe,W,Mo)_{23}C_6$ $Cr_{21}(W,Mo)_2C_6$	Precipitates in the solid state as films, globules, platelets, lamellae or cells. Usually forms at grain boundaries. The "M" element is predominantly Cr, but Ni, Co, Fe, Mo and W can substitute.
M_6C	FCC	Fe_3Mo_3C Fe_3W_3C- Fe_4W_2C Fe_3Nb_3C Nb_3Co_3C Ta_3Co_3C	Randomly distributed carbide. It always contains at least two metallic components "M". Generally, one or more metallic element from the group Fe, Ni & Co is combined with one or more from the group W, Mo, Nb & Ta.
M_7C_3	Hexagonal	Cr_7C_3	A blocky, intergranular carbide. Only observed in certain alloys, such as Nimonic 80A after exposure above 1000°C, and some cobalt-based alloys.

Table 3.2: Summary of the carbide phases observed in superalloys. (After "Superalloys-A Technical Guide" Ed. E.F. Bradley [3.8].)

3.2.4 δ Phase

δ phase is the stable orthorhombic form of Ni_3Nb. (Note that some authors refer to orthorhombic Ni_3Nb as the β phase). It can form at grain boundaries, at primary carbides or inside grains during ageing treatments or prolonged thermal exposure [3.5, 3.16, 3.17, 3.18]. The morphology of δ tends to be acicular, though it can adopt globular forms.

Precipitation of δ occurs heterogeneously at grain and twin boundaries at low ageing temperatures (below 900°C), and by intragranular precipitation at higher ageing temperatures. Below 900°C, precipitation of δ is preceded by γ" and γ', while at higher temperatures δ can precipitate directly from the supersaturated γ matrix [3.16]. Transmission electron microscopy (TEM) showed that δ can nucleate at stacking faults in γ" particles. This is consistent with a proposed mechanism in which shearing of the DO_{22} structure of γ" by a $\frac{1}{6}\left[\bar{1}12\right]$ partial dislocation creates the same stacking sequence as the δ phase [3.16].

The orientation relationship for δ phase has been reported as [3.16]:

$$\{111\}_\gamma // (010)_\delta \text{ and } \langle 1\bar{1}0\rangle_\gamma // [100]_\delta$$

Liu et al. [3.19, 3.20] studied the effect of cold rolling solution treated IN718 on subsequent precipitation of γ" and δ phase at 860°C. For a given ageing time, it was found that the amount of δ phase formed increased with increasing prior cold reduction, while the amount of γ" decreased. This effect was attributed to the increased availability of δ nucleation sites on stacking faults in deformation bands [3.19], and enhanced diffusivity of Nb along dislocations introduced by cold rolling [3.20].

3.2.5 Laves Phase

The Laves phase is a brittle, intermetallic phase which is one of the components of the terminal eutectic reaction (liquid → γ + Laves), for the solidification of IN718 [3.21]. The phase has a hexagonal close packed (HCP) crystal structure of type C14. The chemical composition of Laves phase in IN718 is $(Nb,Mo,Ti)(Ni,Fe,Cr)_2$. The formation of Laves phase is avoided wherever possible because of its detrimental effect on tensile properties, fatigue life and creep ductility. It is present in as-cast IN718 and welds [3.22, 3.23], but where possible it is eliminated by a homogenisation treatment [3.24]. For this reason it is extremely rare to find Laves phase in wrought IN718.

3.2.6 Minor Phases

Numerous minor phases have been identified in IN718, including borides, sulphides and phosphides [3.25]. Many of these phases form during welding, where non-equilibrium solidification conditions exist [3.22].

3.2.7 Grain Sizes & Processing Routes

The microstructure of IN718 is dependent upon the way in which the material is processed to produce the final product. Grain size in IN718 varies depending upon the processing route and heat treatment. Thermo-mechanical processing can be used to control the final grain size of wrought material, with the possibility of producing fine grained, coarse grained or bimodal "necklace" microstructures through controlled recrystallisation.

Numerous hot forming routes and heat treatments have been developed by different suppliers and users of IN718 to suit different applications, and some of the most common ones are described below.

Forging of IN718 typically takes place in the temperature range 900-1120°C, starting at higher temperatures and finishing with light reductions in the range 900-954°C [3.1]. Precipitation of δ phase at the lower forging temperatures provides some grain size control through grain boundary pinning. A fine grained microstructure for components such as turbine shafts can be obtained by the "Minigrain^{TM}" process [3.26]. In this process, δ phase is precipitated in billets prior to the final forging or extrusion operation, which is performed below the δ solvus temperature (typically 980-1010°C). The δ particles pin grain boundaries, restricting grain growth during extrusion or forging. A fine grained microstructure is the result, and the δ phase morphology changes from acicular to globular.

Standard heat treatments for IN718 consist of a solution anneal, followed by a duplex ageing treatment to precipitate γ" and γ'. Performing the solution anneal below the δ solvus temperature retains the δ phase precipitated during hot forming operations. The δ prevents grain growth during the anneal, preserving the desired grain structure developed during forming. A typical heat treatment would consist of:

Anneal at 925-1010°C, followed by ageing at 720°C for 8 hours, furnace cool to 621°C then hold at 621°C for 10hours; air cool. Note that the maximum operating temperature or test temperature of the component may be higher than the minimum ageing temperature (621°C), so some overageing of the material may occur during service or fatigue testing [3.27].

The direct ageing process [3.28] was developed to produce turbine discs with improved high temperature static and fatigue strength, though there is some reduction in stress rupture life in the low stress/high temperature regime. Direct ageing is intended to produce a final microstructure with a fine grain size and small amounts of δ phase. Forging takes place at an initial upset temperature of around 1024°C, and a final upset temperature of approximately 982°C, followed by water quenching. The forging is then given a standard duplex ageing treatment without a solution anneal.

3.2.8 γ" & Slip Heterogeneity

A characteristic of plastic deformation in IN718 and other nickel-based superalloys is that slip occurs heterogeneously. This means that dislocation motion is concentrated in planar bands (known as slip bands or deformation bands), rather than occurring homogeneously throughout the material. The FCC matrix of nickel-base superalloys has a low stacking fault energy, so that dislocations dissociate into two partials with a stacking fault between them. This helps to strengthen the material by preventing cross-slip or climb of dislocations and favours the movement of dislocations along particular slip bands. The γ'' and γ' strengthening precipitates are coherent with the matrix and strengthen the material by providing a barrier to the movement of dislocations [3.29]. Coherency strains between the particle and the matrix are the first mechanism by which the precipitates impede the passage of dislocations. However, if the local stresses are high enough, the dislocations can pass through the γ'' and γ' particles, shearing them in the process. This shearing process provides another mechanism of strengthening, due to the difference in stacking fault energy between the particle and the matrix, and the energy required to create additional particle-matrix interfaces. The γ' and γ'' particles are also ordered phases. Shearing of the particles disrupts the ordering, forming an antiphase boundary which is energetically unfavourable because the atoms in the structure then have incorrect nearest neighbours. Antiphase boundary formation thus provides another obstacle to dislocation motion through the particle. Passage of a second dislocation through the particle can restore the ordering, so that the dislocations move through the structure in pairs [3.29]. This again minimises cross-slip and favours slip band formation. The degree of heterogeneity is characterised by the density of the bands for a given plastic strain. The fewer and more intense the bands are, then the more heterogeneous the slip behaviour is. Conversely, a higher density of less intense bands at a given plastic strain implies more homogeneous slip. Apart from observations of dislocation arrays, some evidence of twinning in deformation bands has been reported in IN718 [3.30, 3.31].

Another characteristic of IN718 is pronounced cyclic softening during low cycle fatigue testing, observed at both room and elevated temperatures [3.30, 3.32]. Under cyclic loading, the repeated shearing of precipitates by dislocations results in favoured paths for the glide of dislocations through the microstructure. Repeated movement of dislocations through the precipitates reduces their strengthening effectiveness. The mechanism by which this occurs in IN718 is thought to be the shear dissolution of the γ'' precipitates [3.32, 3.33]. Merrick [3.32] performed TEM examinations on IN718 fatigued at $538^{o}C$ and noticed the apparent absence of γ'' within slip bands. Cyclic softening at elevated temperatures was thus attributed to shearing and dissolution of γ''. However, in a similar TEM study Fournier & Pineau [3.30] pointed out that although γ'' was not visible in the slip bands, this did not mean the precipitates had dissolved, and that softening was due solely to the shearing of γ'' by dislocations. Supporting evidence for this conclusion came from streaks in electron diffraction patterns associated with stacking faults in sheared γ'', and an additional diffraction spot attributed to the presence of δ particles. It was proposed that δ can result from the shear of the γ'' DO_{22} structure by partial dislocations, as commented on in studies of δ precipitation [3.16]. Instead of particle dissolution, loss of order in the particle and a reduction in the mean particle area encountered by dislocations in their slip planes were proposed as the main mechanisms of cyclic softening [3.30, 3.34].

3.3 Fatigue Characteristics of Inconel 718

For materials used in gas turbine engines, a critical aspect of performance is their resistance to crack initiation and propagation caused by the combined effects of fatigue, creep and environmental degradation. Measuring and predicting crack initiation and growth has considerable commercial significance for gas turbine manufacturers and operators, who need to understand when to inspect and replace components before cracks grow beyond a critical size [3.35].

Fatigue studies of IN718 have tended to concentrate on long crack growth rates rather than initiation behaviour or the growth of short cracks. Much of the work has considered how IN718 performs at elevated temperatures where fatigue, creep and environmental effects occur. The behaviour of materials where fatigue, creep and environmental effects are involved can be divided into two broad regimes [3.36]:

Cycle-dependent behaviour, where fatigue crack growth (in terms of da/dN) is controlled by the characteristics of the loading cycle, such as the stress intensity range ΔK, the maximum stress intensity factor $K_{\max}$ and the load ratio R.
Time-dependent behaviour, where thermally activated processes of environmental degradation and creep influence crack propagation, producing a temperature and time dependence in fatigue crack growth rates.

Generally, cycle dependent behaviour is favoured by low temperatures, high fatigue frequencies and inert environments, whereas time dependent behaviour is favoured by low fatigue frequencies, high temperatures and detrimental environments [3.36, 3.37]. Note that the two regimes are not mutually exclusive. Instead, fatigue crack growth rates can be both cycle-dependent and time-dependent. Synergies between fatigue, creep and environment can accelerate or retard crack growth rates. It is also important to note that the behaviour of materials subjected to fatigue-creep-environment interactions is strongly influenced by their microstructure.

3.4 Effects of Cycle Parameters

In purely cycle-dependent fatigue crack growth, the rate of crack growth per cycle, da/dN is proportional to the stress intensity range ΔK as described by the Paris equation. However, at high temperatures where creep and oxidation may occur, cycle parameters such as load ratio, frequency and loading waveform influence the transition between purely cycle-dependent and time dependent crack growth, as discussed in the following sections.

3.4.1 Load Ratio Effects

When da/dN is plotted against ΔK, the crack growth rate at a given temperature generally increases with increasing R [3.27, 3.38, 3.39], because a higher R ratio reduces crack closure for a given level of ΔK. However, it has been observed that the R ratio effect also depends upon whether the fatigue regime is cycle-dependent, time-dependent, or a combination of the two [3.38]. For cycle-dependent conditions at constant $K_{\max}$, da/dN decreases as R increases, because the overall crack driving force ΔK is reduced. Under time-dependent conditions at constant $K_{\max}$, da/dN increases as R increases, because it is the mean stress, rather than the stress intensity range, which governs crack growth under time-dependent conditions. It has been suggested [3.40] that for time-dependent conditions where creep and oxidation processes occur, the parameter $K_{\max}$ is more important for crack growth than ΔK. Under mixed cycle- and time-dependent conditions for a fixed value of $K_{\max}$, time-dependent effects are more pronounced at high R values, while cycle-dependent effects are more pronounced at low R values. For a 3-0-3-0 (0.17 Hz) sawtooth cycle at 650°C in air, Shahinian & Sadananda [3.41] observed that da/dN increased with increasing R, when compared on the basis of ΔK. The effect of increasing R was much more pronounced at high values of R (0.5 to 0.8) than at low values, (0.05 to 0.2). A similar effect was observed for a 3-60-3-0 cycle at 650°C [3.41]. Low R values can reduce the effective crack tip driving force near the threshold ΔK_{th}, because of crack closure effects. Testing at high R values to keep the crack open can eliminate closure effects, though care must be taken to ensure this does not alter the crack growth mechanism [3.42]. Elimination of closure by testing with a high R will increase da/dN, as shown by Antunes et al. using corner crack specimens [3.39]. The effect was more pronounced at low frequencies under time-dependent conditions. This was explained by an acceleration of oxidation-assisted damage, promoted by an increase in the maximum stress and a reduction in the loading rate.

3.4.2 Frequency & Waveform Effects

Frequency effects on the fatigue of superalloys have been extensively studied because of the role cycle frequency plays in determining whether cycle-dependent or time-dependent behaviour dominates. It is now well known that frequency has a significant effect on fatigue crack growth in air at elevated temperatures [3.30, 3.38, 3.43, 3.44, 3.45].

At 550°C and $R = 0.1$, Clavel and Pineau [3.43] found that for frequencies less than 0.5 Hz, a decrease in frequency increased fatigue crack growth rates in alloy IN718. However, for frequencies greater than 0.5 Hz, fatigue crack growth rates were largely independent of frequency. Floreen and Kane [3.45] observed a similar increase in crack growth rate with decreasing frequency in air at 650°C and a recent study by Antunes et al. [3.39] also demonstrated an increase in crack growth rate with decreasing frequency at 600°C.

To investigate further the frequency effect, fatigue crack growth rates for three different waveforms were compared at 550°C [3.43] These were:

(a) 0.25-10-0.25-10 trapezoidal (0.05 Hz)
(b) 10.25-0-10.25-0 sawtooth waveform, (0.05 Hz)
(c) 0.25-0-0.25-0 sawtooth waveform (2 Hz)

Note that (a) and (b) have the same frequency but different loading/unloading rates, while (a) and (c) have the same loading/unloading rates but different frequencies. As expected, the highest frequency waveform (c) produced the lowest crack growth rates. Waveform (b) produced the highest crack growth rates, while waveform (a) produced a rate similar to (but higher than) waveform (c). Clavel & Pineau [3.43] stated that the difference between the cycles was caused by the difference in loading/unloading rates, rather than frequency *per se*, and that the 10 second hold times in cycle (a) did not significantly affect fatigue crack growth rates under their experimental conditions (550°C in air).

In their review of the effect of mechanical variables on fatigue crack growth in IN718, Ghonem et al. [3.38] describe the somewhat conflicting results of several investigations into waveform effects. The conflicts arise because of the difficulties in isolating loading/unloading rate effects from the effects of dwell time and overall cycle duration. Dwell time significantly affects the tendency towards time-dependent behaviour. The general conclusions were that for a given temperature, there is a transitional frequency below which fatigue cracking changes from cycle-dependent to time dependent behaviour. Under cycle-dependent conditions, crack growth rates are largely independent of frequency. Under time-dependent conditions where intergranular fracture occurs, crack growth rates are inversely proportional to frequency and are sensitive to dwell times imposed at minimum or maximum load. Loading rate appears to be more significant than unloading rate in affecting crack growth rates at low frequencies, but the overall cycle frequency, relative to the transitional frequency, has to be considered when trying to interpret waveform effects. The existence of a transitional frequency in IN718 was also observed by Antunes et al. [3.39] at 600°C in corner cracked specimens.

SEM fractography has been combined with TEM studies to correlate the crack propagation mode with the deformation substructure adjacent to fracture surfaces [3.43, 3.46]. At room temperature under purely cycle-dependent conditions at a frequency of 10 Hz, [3.46], transgranular, crystallographic fracture was observed, with some accommodation of plastic strain ahead of crack tip by γ'' shearing and possibly limited dislocation motion. For specimens tested in air at 550°C [3.43], cracks propagated in a transgranular mode for frequencies above 0.5 Hz. Below 0.5 Hz, a mixed transgranular/intergranular mode was observed, with the proportion of intergranular fracture increasing as the frequency decreased. TEM experiments indicated that deformation at 550°C was more heterogeneous at low frequencies. Additionally, a low loading rate sawtooth waveform showed more heterogeneous slip than a trapezoidal waveform with a faster loading rate [3.43], suggesting an influence of loading rate on slip heterogeneity. Slip was concentrated in intense slip bands having a twin orientation with the matrix and there was also evidence of shearing of γ'' particles within slip bands. A similar correlation between frequency, crack propagation mode and slip heterogeneity were made by Fournier & Pineau [3.30] for low cycle fatigue (LCF) specimens.

In considering a mechanism to explain the links between frequency, slip heterogeneity and accelerated fatigue crack growth at elevated temperatures, the role of environment has been identified as an important factor [3.45, 3.47, 3.48]. The explanations offered consider the influence that the local grain boundary stress state has on diffusion and oxidation behaviour at the crack tip. IN718 contains a high percentage of chromium, so formation of the protective oxide Cr_2O_3 at the crack tip can reduce oxygen penetration along grain boundaries. Reduced oxygen penetration limits the extent of grain boundary oxidation, thus reducing the tendency for intergranular fracture. Grain boundary diffusion can be influenced by the local stress state, with stress concentrations at grain boundaries tending to enhance grain boundary diffusivity, D_g. More homogeneous deformation, favoured by high frequencies, enhances strain accommodation and stress relief along grain boundaries, reducing the stress concentrations that can enhance D_g. In the case of heterogeneous deformation, favoured by low frequencies, intense slip lines create stress concentrations at grain boundaries, enhancing D_g and encouraging rapid oxygen transport. Ghonem and Zheng [3.48] used this frequency-sensitive oxidation mechanism to explain observed frequency interactions at high temperature in IN718. Specimens pre-fatigued at high frequency were then tested at low frequency, and the crack growth rate compared with specimens that had not been pre-fatigued. Pre-fatiguing at high frequency was found to lower the subsequent low frequency crack growth rate compared to specimens that had not been pre-fatigued. It was proposed that the more homogeneous slip induced by high frequency fatigue cycling promoted the growth of protective Cr_2O_3 oxide at the crack tip, which shielded grain boundaries in the crack tip region from further oxidation penetration. Follow-up work demonstrated that pre-straining specimens of IN718 led to a reduction in subsequent low frequency (0.05Hz) fatigue crack growth rates at 650°C compared with unstrained specimens [3.49], even when crack closure effects were taken into account. The density of slip lines and associated homogeneity of slip was greater in the pre-strained specimens. Depth profiles of fracture surface chemistry obtained by ion sputtering and Auger analysis showed that the depth of oxygen penetration was lower in pre-strained specimens, while the amount of chromium present was greater, supporting the theory of crack tip oxidation shielding by a protective layer of Cr_2O_3.

3.5 Time-Dependent Phenomena

The time-dependent processes which influence the fatigue behaviour of superalloys at elevated temperature are creep and environmental effects. Creep is the time-dependent deformation of a material under a constant applied load at elevated temperatures. It is an inherent characteristic of a material, and occurs in the absence of any environmental effects. Environmental effects are those produced by high temperature oxidation and corrosion, which are time-dependent because of the kinetics of the chemical reactions involved.

As mentioned previously, complex interactions occur between fatigue, creep and environmental processes, making it difficult to completely isolate one process for individual study. However, a common way of studying the relative effects of creep and environment on fatigue behaviour is to conduct fatigue tests in air and in vacuum. Testing in a sufficiently hard vacuum suppresses oxidation and other forms of environmental attack, so that any time-dependent behaviour can be considered to be due to creep alone. Results of vacuum tests can then be compared with air tests, where both creep and environmental processes operate.

An illustration of the relative significance of creep and environmental processes is the work of Smith and Michel [3.50], who measured fatigue crack propagation rates of IN718 in air and vacuum. Long crack propagation rates were measured in IN718 for $R = 0.05$ using two different fatigue cycles. The first baseline cycle was continuous at 0.17 Hz, whereas the second cycle had a 1 minute dwell at the maximum load so that any time-dependent effects would become apparent. For the continuous 0.17 Hz cycling at 593°C, crack propagation rates were an order of magnitude higher in air than in vacuum. When the tests were repeated with 1 minute dwells at maximum load, there was only a slight increase in the crack growth rate in vacuum compared with the baseline 0.17 Hz vacuum test, whereas the growth rate in air was approximately 10 times higher than the baseline 0.17 Hz air test. Similar trends were observed for testing at 649°C, with the increase in crack growth rate between the 0.17Hz cycle and the 1 minute dwell cycle in air being even more dramatic than the equivalent change at 593°C. It was also noted that the slope of the da/dN vs. ΔK curves for vacuum tests was greater than for the air tests, despite overall crack growth rates being lower in vacuum. This suggested that different fracture micro-mechanisms were operating in air and vacuum. SEM fractography revealed that the crack propagation mode was transgranular in vacuum under all test conditions. In air, continuous 0.17 Hz cycling produced cleavage type intergranular fracture, whereas the 1 minute dwell cycling produced mixed transgranular and intergranular fracture, with the proportion of intergranular fracture being greater at 649°C. From the results reported, it appeared that environmental effects on fatigue were far more significant than creep at temperatures up to 650°C. The authors concluded that the air environment increased crack propagation rates by inhibiting planar slip and grain boundary ductility, and that the time-dependent nature of the high temperature environmental interaction was distinctly different from the time dependence of the creep process.

3.5.1 Oxidation Effects

Observation of intergranular failure in high temperature fatigue tests in air suggests that grain boundary oxidation is a major cause of accelerated crack growth rates. As well as fatigue tests, oxidation-induced crack growth in IN718 has been observed in static load tests on pre-cracked specimens at 550 - 650°C [3.51]. Some aspects of oxidation at the tips of fatigue cracks have already been discussed above in relation to frequency effects, and this section discusses further the phenomenon of environmentally enhanced fatigue crack growth.

A distinction is made between short-range and long-range oxidation effects [3.47, 3.52]. In short-range oxidation, an oxide layer grows at the crack tip. Preferential formation of the oxide at grain boundaries leads to the formation of wedge-shaped intrusions along the crack front, which can result in high local stresses being transferred to the surrounding matrix. Cracking within the oxide intrusions or at the oxide-matrix interface produces intergranular fracture and accelerated fatigue crack growth rates. In long-range oxidation, oxygen diffuses into the material ahead of the crack tip along preferential paths, such as slip bands and grain boundaries. The oxygen is then available to react with material at the grain boundaries to form internal oxide films, or to react with precipitates and inclusions [3.53, 3.54]. The grain boundaries ahead of the crack tip are thus embrittled, creating a preferential fracture path for the propagating crack. Though both short-range and long-range oxidation can occur simultaneously, it is generally assumed that short-range oxidation is the more significant mechanism for IN718 at temperatures up to 650°C [3.52].

The effective time available for grain boundary oxidation can be extended by introducing hold periods at the maximum or minimum load in a fatigue cycle. Numerous studies have demonstrated that a hold period at maximum or minimum load significantly increases fatigue crack growth rates at elevated temperatures [3.41, 3.47, 3.53, 3.54, 3.55, 3.56, 3.57, 3.58, 3.59, 3.60]. At 650°C even a 3 second hold time at minimum load produced an increase in fatigue crack growth rate [3.57]. Increasing the hold time further produced additional increases in fatigue crack growth rate, though this effect was observed to saturate for hold times longer than 1000 seconds [3.57]. The saturation effect was attributed to the formation of a protective Cr_2O_3 oxide layer at the crack tip, which prevented further oxygen penetration. X-ray analysis of polished specimens exposed at 650°C for 10 hours confirmed the presence of a Cr-rich oxide layer along grain boundaries [3.57]. Since Cr is important in forming a protective oxide layer, then a potential way of reducing oxidation-assisted fatigue crack growth is to increase the Cr content of the alloy. This was demonstrated for laboratory melts of IN718 with 24 wt.% Cr [3.61].

The mechanism of oxidation in IN718 was investigated by Andrieu et al. [3.52, 3.62], who studied the effect of oxygen partial pressure, $p(O_2)$, on grain boundary oxide formation and tensile fracture mode at 650°C. Spinel-type $Ni(Fe,Cr)_2O_4$ oxides formed at high oxygen partial pressures, with a transition to the formation of Cr_2O_3 at low partial pressures (below 1×10^{-3} mbar). Associated with the change in preferred oxide type was a transition from intergranular fracture at high $p(O_2)$ to transgranular fracture at low $p(O_2)$. The effect of oxide type on fracture mode is related to the ability of the oxide to limit further oxygen penetration along grain boundaries. The spinel-type oxide is brittle, porous and non-protective, whereas Cr_2O_3 restricts oxygen penetration. For oxidation in air, a two-stage oxidation mechanism was proposed [3.52]. The spinel-type oxide forms first, but as it thickens, the oxygen concentration at the metal-oxide interface decreases, so that conditions become favourable for Cr_2O_3 formation. Eventually the Cr_2O_3 becomes thick enough to prevent further oxygen penetration along grain boundaries, and the material is passivated. The passivation of grain boundaries by Cr_2O_3 helps to explain the saturation effect of hold times at minimum load [3.57]. If the hold time exceeds the passivation time, then no further increase in fatigue crack growth rate will occur. The passivation time is a function of temperature, $p(O_2)$, and the local stress/strain fields, so the hold time effect varies according to the experimental conditions used.

Further evidence supporting a two-stage oxidation mechanism comes from an experiment designed to delay the formation of the protective Cr_2O_3 oxide [3.52]. A 1Hz, 0.5kN amplitude signal was superimposed on a 600s hold at minimum load, during fatigue testing of compact tension (CT) specimens. The 1Hz cycle was intended to disrupt the growing spinel oxide layer so that passivation by Cr_2O_3 formation would be prevented. To ensure no crack growth occurred due to the 1 Hz signal, the load was calculated to be below the estimated threshold for crack growth (12 $MPa.m^{1/2}$) at the longest expected crack length. As predicted, fatigue crack growth rates were increased, compared to a test without the superimposed 1Hz signal during the hold period.

Ghonem & Zheng [3.63, 3.64, 3.65, 3.66] used the two-stage oxidation mechanism to produce a theoretical model of fatigue crack growth rate. The authors proposed that the fracture criterion was determined by the balance between the local ductility of an oxidising grain boundary and the effective strain at the crack tip arising from external loading [3.63, 3.64]. As a grain boundary oxidises, its ductility is reduced because the oxide layer is less able to carry load than the parent metallic matrix. If the grain boundary ductility falls below the crack tip effective strain, the oxide fractures and the crack will advance. The extent of oxidation, and the associated reduction in grain boundary ductility, was assumed to be limited by the formation of a protective Cr_2O_3 layer. The model estimated the amount of Cr_2O_3 relative to the spinel oxides, in terms of the transport of oxygen along the grain boundary and the transport of chromium along dislocation networks. A derived oxidation parameter was then correlated with the grain boundary ductility. Application of the fracture criterion enabled the rate of crack advance to be calculated. Predictions were made for a fatigue cycle with a 300 second hold at minimum load, and a 0.05 Hz cycle without hold time, at 650°C and at a load ratio $R = 0.1$. The predictions agreed well with experimental results [3.64], though they were limited in scope and based on diffusion parameters derived from fatigue experiments, rather than a first principles approach. In an adaptation of their model, Ghonem & Zheng [3.65, 3.66]. assumed that the rate of crack advance per cycle was equal to the depth of intergranular oxygen penetration during the entire cycle. Predictions of crack growth rates for cycles of 0.05Hz, 0.02Hz and 0.01Hz at 650°C agreed best with experiment at lower values of ΔK [3.65]. The grain boundary diffusivity (D_g) of oxygen near the crack tip (inferred from crack growth data) was shown to be a function of ΔK and cyclic frequency. For a given frequency, D_g increased with increasing ΔK. For a given ΔK, D_g increased with decreasing frequency [3.66]. These findings are consistent with the theory that heterogeneous plastic deformation at the crack tip enhances grain boundary diffusivity because of the development of stress concentrations [3.47, 3.48].

In work on corner crack specimens of IN718, Antunes et al. [3.67] observed an influence of stress state on crack propagation mode at 600°C in air. At the specimen surface under plane stress conditions, crack propagation was transgranular, whereas at depth under plain strain conditions, propagation was intergranular or mixed transgranular-intergranular. The degree of intergranular fracture and the crack propagation rate increased with decreasing frequency. It was proposed that plain strain conditions in the specimen interior favoured oxidation-controlled intergranular fracture, possibly because of inhomogeneous slip and accelerated diffusion under the triaxial stress state in plain strain. Deformation at the surface was thought to be more homogeneous under plane stress, favouring transgranular fracture and slower surface crack propagation rates. This led to tunnelling of cracks into the specimen depth which could not be accounted for by the predicted variation in ΔK along the crack front. Only the proposed enhancement of intergranular fracture under plain strain conditions could explain the observed results [3.67].

So far in this review, oxidation has been regarded as detrimental to fatigue crack growth resistance. However, the build-up of an oxide layer on crack faces can produce crack closure and load transfer. Such oxide-induced crack closure may raise the threshold stress intensity range (ΔK_{th}) for fatigue crack growth, and lead to lower fatigue crack growth rates at low values of ΔK. Higher thresholds attributed to oxide induced crack closure were observed by Yuen et al. for IN718 tested at 100 Hz in air at 538°C, compared with material tested in helium [3.68]. Lynch et al. studied the effect of hold time and frequency on crack growth rates in Waspaloy and Direct-Aged IN718 at 500-700°C [3.53, 3.54]. Comparisons were made between a 2 Hz sawtooth waveform, a 0.0167 Hz sawtooth waveform and a 0.25-60-0.25-0 trapezoidal waveform (i.e. a 60 s hold time at maximum load). In the case of Waspaloy [3.53], the authors noted that at low ΔK (< 30 MPa.m$^{1/2}$), crack growth rates were lower (and ΔK_{th} higher) for the 60s hold time waveform, when compared with the 0.0167 Hz or 2 Hz waveforms. At high ΔK (>30 MPa.m$^{1/2}$), crack growth rates were highest for the 0.0167 Hz waveform, intermediate for the 60s hold time waveform and slowest for the 2 Hz waveform. The effects of frequency and hold time were relatively small at 500°C, but more pronounced at 700°C. Very similar behaviour was observed for Direct-Aged IN718 [3.54]. Metallographic observations through specimens tested at 700°C revealed that cracks produced at low ΔK were filled with thicker oxide films for the 60s hold time, when compared with cracks grown by continuous cycling at 0.0167 Hz or 2 Hz. The transition in behaviour with ΔK was attributed to the competing effects of crack closure or crack branching (which tend to reduce crack growth rates) and creep or oxidation (which tend to enhance crack growth rates). Lynch et al. [3.54] noted that the behaviour they observed for Direct Aged IN718 was not reported elsewhere in the literature for standard processed IN718, perhaps because of the lower creep resistance of standard processed material. Sadananda & Vasudevan [3.69] dispute the use of closure to account for differences in crack growth behaviour. As an alternative, they advocate a two threshold parameter (ΔK^* and K^*_{max}) model, which was described in Chapter 2 Section 2.4. K^*_{max} in particular was said to be sensitive to temperature and environment, with environmental or creep damage being explained in terms of a reduction in the value of K^*_{max} required for crack propagation.

3.5.2 Creep

Creep is a thermally activated process, so creep effects will influence fatigue behaviour at elevated temperatures. Generally, the contribution of creep to the overall deformation process increases with temperature, until it dominates material behaviour. It is beyond the scope of this review to discuss creep processes in detail, but a good analysis of creep-fatigue interactions is given by Suresh [3.70]. Creep contributes to fatigue crack growth through the formation of grain boundary cavities, which is a consequence of grain boundary sliding. Note that creep produces inelastic deformation, which means that the standard LEFM parameter, ΔK, used to characterise fatigue crack growth becomes invalid. Attempts to characterise creep-fatigue are based either on partitioning crack growth rates into fatigue and creep components, or by partitioning crack growth driving forces into elastic and inelastic contributions. Matters are further complicated by the influence creep may have on the plastic zone size ahead of the crack, possible crack-tip blunting by creep, and environmental interactions.

As discussed in the preceding sections, oxidation is the dominant time-dependent process affecting elevated fatigue crack propagation in IN718 at temperatures up to 650°C. There is also a strong environmental effect when IN718 is tested under pure creep conditions [3.71, 3.72]. In creep testing at 650°C, crack growth was found to be dominated by oxidation embrittlement of grain boundaries [3.72]. Diboine and Pineau [3.57] pointed out that creep ductility in air is time-dependent because of environmental effects, notably preferential oxidation of grain boundaries. There is also evidence of moisture accelerating creep crack growth, though the mechanism by which this occurs is not fully understood [3.73, 3.74]. At higher temperatures, creep relaxation and a reduced yield stress may cause crack tip blunting which reduces or prevents creep crack growth. For example, Liu et al. [3.72] observed that creep crack growth in IN718 was suppressed at 704°C in air. Measured crack tip radii were an order of magnitude larger at 704°C compared to 650°C, providing evidence of crack tip blunting at the higher temperature.

An extensive study of environmentally accelerated creep-crack growth in IN718 has recently been undertaken by Gao and co-workers [3.74, 3.75, 3.76, 3.77, 3.78, 3.79], the results of which may be relevant to environmentally accelerated fatigue crack growth. Preliminary creep testing in oxygen, moist argon and dry argon showed that creep crack growth rates were highest in oxygen, followed by moist argon, with the lowest growth rates in dry argon [3.74]. Subsequent studies then concentrated on the mechanism of oxygen-accelerated creep crack growth. X-ray photoelectron spectroscopy (XPS) was performed on IN718 (100) single crystals, and significant Nb enrichment of the surfaces was noted when the specimen was heated to between 302°C and 702°C. Niobium enrichment was also observed for the grain boundaries of IN718 polycrystals, possibly as a result of Ni_3Nb precipitation during heat treatment [3.75, 3.76]. In further XPS experiments, the evolution of carbon monoxide was detected when ion-cleaned IN718 specimens were heated, suggesting that oxidation of carbides was taking place [3.77]. A mechanism of creep embrittlement by niobium oxide was proposed, in which niobium released onto grain boundaries by the oxidation of carbides formed a brittle, non-protective Nb_2O_5 oxide film. Analysis of published creep data showed a positive correlation between the environmental sensitivity of creep and niobium content [3.77].

The niobium embrittlement model discussed above may be applicable to environmentally-enhanced fatigue crack growth, assuming that long-range oxidation processes are active. However, the significance of long-range oxidation relative to short-range oxidation at the crack tip is open to question [3.52]. Another question is whether the source of niobium which forms Nb_2O_5 is indeed the oxidation of MC carbides. Other sources of niobium, such as γ'', δ or niobium in solid solution may be important. In the case of creep, Gao and Wei [3.79] estimated that the number and distribution of primary MC carbides was insufficient to account for the embrittlement of IN718 by release of niobium onto grain boundaries by MC oxidation. In searching for alternative sources of niobium, the authors found a number of small niobium-rich particles on grain boundaries, which they described as niobium-rich (MC) carbide with a tetragonal structure. This observation is surprising, given that EDX analysis showed they also contained chromium, iron and nickel, which are known to be absent from primary MC carbides. The tetragonal crystal structure reported is another unexpected result, since none of the carbides previously observed in superalloys have a tetragonal crystal structure. Nb-rich particles with a tetragonal microstructure have been reported in niobium-containing stainless steels [3.80], but there is no conclusive evidence in the work of Gao and Wei [3.79], or elsewhere in the literature, that such particles are indeed carbides. No quantitative analysis of carbon content or the proportion of metallic elements present was given, probably due to the difficulties in performing light element analysis using standard EDX techniques. An alternative possibility is that the tetragonal Nb-rich particles are M_3B_2 borides, similar to those observed in the heat affected zones of welds in IN718 [3.22]. However, the reported lattice parameters are quite different in the two cases, and it is not certain how a fine grain boundary distribution of borides could form in conventionally wrought and heat treated IN718. Gao and Wei concluded that decomposition of the Nb-rich carbides they identified provided an additional source of niobium for creep-embrittlement, so the true identity of these particles is important. However more sophisticated chemical and structural analysis is required to confirm whether or not the particles are indeed carbides. Recently, attention has focussed instead on the oxidation of Ni_3Nb as a possible cause of grain boundary embrittlement in IN718 [3.81, 3.82]. In XPS studies, oxygen penetration along grain boundaries to a depth of 150 μm ahead of crack tips was detected in IN718 exposed at 700°C under sustained load [3.82].

Liu et al. [3.83] demonstrated experimentally that MC carbide distribution had an effect on creep crack growth rates in IN718 bar. Creep crack growth was fastest when the carbides were parallel to the crack growth direction, intermediate when the carbides were perpendicular to the growth direction and slowest when the carbides were homogeneously distributed. The carbides were thought to be involved in the coalescence of microcracks with the main crack during growth, via cleavage and tearing of the residual ligament between the cracks. Liu et al. did not mention the environment used for their test, so it is not known if carbide oxidation had any influence on the creep behaviour.

In a theoretical study, Lu et al. [3.84] considered oxidation of carbides within the interior of creep cavities, leading to high internal gas pressures of CO or CO_2 and consequent cavity growth. The authors concluded that such a mechanism was possible providing two conditions were met. Firstly, the ratio of grain boundary oxygen diffusivity to nickel self-diffusivity has to be sufficiently high so that cavity growth by diffusion did not outpace the increase in internal pressure. Secondly, the chromium content of the alloy has to be low, to prevent reaction of chromium with oxygen to form Cr_2O_3, rather than reacting with a carbide to evolve CO or CO_2. Given that IN718 contains 17-21 wt % of chromium, it seems unlikely that the internal gas pressure mechanism is operative in this alloy.

3.6 Initiation & Short Cracks in Superalloys

Initiation and short crack growth behaviour is technically important for superalloy components, because a large part of the overall fatigue life may be spent in the initiation and short crack growth phases [3.35]. Fournier & Pineau estimated that approximately 70% of the life in low cycle fatigue tests on IN718 at 298 & 823K was spent in initiation

[3.30]. Note that their definition of "initiation" was the number of cycles required to form cracks of 50-100μm in length.

Experimental results show that short cracks grow at faster rates than long cracks when compared on the same basis of ΔK. Short cracks can also grow at ΔK levels below the threshold stress intensity range (ΔK_{th}) determined for long cracks. Applying long crack growth predictions to short cracks can thus result in over-estimates of the total fatigue life [3.85]. Understanding initiation and short crack growth behaviour is made more complex by the variety of microstructures and service conditions which superalloys experience. For example, a study on retired turbine discs showed that cracks in slot bottoms appeared early on in the component life, but took a long time to grow [3.86]. Published information on the initiation and growth of short cracks in IN718 is limited, so relevant findings for other superalloys are included in this section of the review. Much of the published data on short cracks in superalloys refers to behaviour at room temperature, because of the complexities of measuring short crack growth rates at elevated temperatures.

At room temperature, fatigue cracks in superalloys can initiate at slip bands [3.30, 3.87, 3.88, 3.89], twin boundaries [3.89], grain boundaries [3.90] or at carbide particles [3.87, 3.90, 3.91]. Other possible initiation sites are inclusions, Laves phase and micropores. Crack initiation at carbides can occur by cracking of the carbide, or separation of the carbide-matrix interface. Cracking at carbides is thought to be due to differences in the thermal expansion coefficients and elastic moduli of the carbide and matrix [3.87]. As a result, local tensile stresses form in the matrix on cooling after manufacture, making the carbides favourable sites for crack initiation. Impingement of slip bands on a carbide may cause it to crack, and the initiation of fatigue cracks from pre-existing cracks in carbide particles has been reported [3.91].

At elevated temperatures, crack initiation has been observed at slip bands [3.30, 3.87, 3.92] and inclusions [3.93]. Initiation at pre-cracked carbide particles was observed in cast and directionally solidified MAR-M200 at 760°C and 927°C [3.94]. Crack initiation at preferentially oxidised carbides has been observed during low cycle fatigue testing of cast MAR-M 509 (Co-based) [3.95, 3.96, 3.97] , IN100 (Ni-based) [3.98, 3.99, 3.100] and alloy DZ40M (Co-based) [3.101]. Kawagoishi et al. [3.92] observed slip band initiation in IN718 at 300-600°C in air. Testing was performed at 55 Hz, which probably promoted more homogeneous slip and reduced time-dependent effects compared to low frequency testing. Crack initiation was observed to occur readily, but many cracks arrested at a length of 20-30 μm.

3.6.1 Role of Carbides in Crack Initiation

It is generally understood that carbides can act as nucleation sites for fatigue cracks at room and elevated temperatures. Oxidation of carbides is cited as one cause of fatigue crack initiation at elevated temperatures [3.8]. Experimental observations of crack initiation at preferentially oxidised carbides were made [3.95 - 3.100] during LCF testing of the cast superalloys MAR-M 509 [3.95, 3.96, 3.97] and IN100 [3.98, 3.99, 3.100]. Comparisons of LCF tests in air, conducted between 20°C and 1100°C, showed that the proportion of fatigue life required to initiate cracks of length 0.25 - 0.3mm was significantly smaller for specimens tested at high temperatures [3.95, 3.99]. Similarly, shorter initiation periods were observed in air, compared with vacuum, for LCF tests at 900°C [3.96] and 1000°C [3.100], indicating an environmental effect. Fatigue cycling was found to accelerate the kinetics of matrix oxidation, and had a slight effect on preferential oxidation of carbides in interdendritic regions [3.97, 3.98]. The effect of temperature and environment on the LCF tests was attributed to the oxidation of MC carbides, which caused early crack initiation and subsequent preferential growth along oxidised carbides, as observed by metallography. It is possible that the script-like morphology and interdendritic location of the MC carbides enhanced their influence on crack initiation and growth.

Pedron and Pineau [3.55] noted the effect of primary carbide alignment on fatigue crack growth in wrought IN718 at 650°C. They observed that the crack growth rate was faster when the main crack was parallel to the rolling direction – i.e. parallel to the primary carbide chains. Growth rates were lower when the main crack was perpendicular to the rolling direction. Retardation in crack growth rates in the latter case was attributed to crack branching along the carbide alignment direction. The authors commented on the possible role of carbide oxidation in grain boundary embrittlement, a phenomenon discussed earlier in this review for creep. Similarly, in a study of MAR-M 509 [3.96] more fatigue crack branching was observed in air compared to vacuum. This was said to be due to preferential carbide oxidation, with the potential for retarding crack growth. Though these results are interesting, it must be remembered that preferential carbide oxidation will only retard crack growth if the carbide chains are favourably oriented relative to the main crack . Note that Pedron and Pineau [3.55] were using compact tension specimens to study long crack behaviour, so the role of carbides in initiation was not evident in their study.

Some suppliers have produced experimental melts of low carbon IN718, to reduce carbide volume fraction and clustering [3.102, 3.103]. Though it is technically possible to produce low carbon IN718, large scale commercial production is difficult, because of the use of recycled material with variable carbon contents [3.102]. There is some experimental evidence that low carbon contents have a detrimental effect on stress rupture life and creep ductility [3.102]. This may be due to a lower number of carbides able to pin grain boundaries and prevent grain boundary sliding. The recycling issue and unwanted side-effects on material properties limit the scope for improving overall performance by reducing carbon content, though a future breakthrough may change this situation.

Surface eruptions as a result of the oxidation of carbides have been observed in cast [3.104] and wrought IN718 [3.105]. Oxidation of carbides at grain boundaries was responsible for increased notch-rupture sensitivity at 650°C [3.104] and recent experimental observations showed surface fatigue cracks initiating at erupted carbides for tests performed in air at 600°C [3.105]. In both cases a pronounced increase in particle volume due to oxidation was evident.

3.6.2 Short Crack Growth

Fluctuations and scatter in short crack growth rate data for superalloys are attributed to temporary crack arrests and deflections caused by the microstructure and heterogeneous slip behaviour [3.106, 3.107]. The concentration of deformation into intense slip bands means that cracks can propagate in a crystallographic manner across grains until they meet a grain boundary. The crack then arrests, until the stress intensity along a slip band in the adjacent grain becomes sufficiently high for the crack to proceed. Large deflections in crack path may occur at a grain boundary, depending on the relative orientation of adjacent grains [3.89]. Crack deflection within grains has been observed [3.107], attributed to switching of the crack between non-parallel slip bands, or a change in the direction of slip bands at twin boundaries. Kawagoishi et al. [3.92, 3.108] observed that crack initiation at slip bands occurred readily in IN718 at 300-600°C, but that some cracks arrested at a length of 20-30 μm. Note testing was performed at 55 Hz, which would have favoured more homogeneous slip and cycle-dependent rather than time-dependent crack growth behaviour. The authors attributed crack arrest to plasticity or oxide induced closure, but it is uncertain from the evidence presented if such mechanisms were operating for these very short cracks with limited wake. Kawagoishi et al. [3.92] did not discuss the possible effect of crack arrests at grain boundaries in material with a mean grain size of about 9 μm, although some microstructural influence was acknowledged for cracks less than 50 μm in length [3.108]. Short crack growth rates could not be characterised using ΔK, so instead they were characterised on the basis of da/dN vs. crack length a [3.108].

Rosenberger and Ghonem [3.109] studied short crack growth in IN718 at 650°C in air, using a strain-controlled sawtooth waveform at 0.05 Hz. These experimental conditions were used to ensure propagation was environmentally dominated. Two crack initiation methods were used. In the first case, pits were machined by electrostatic discharge machining (EDM). Cracks were initiated by pre-cracking from the pits at 25 Hz at room temperature. Alternatively, cracks were naturally initiated at 650°C under the same strain control conditions used to study crack growth. It was found that for cracks initiated at room temperature, initial short crack growth at 650°C was anomalously high compared to long crack data. Crack growth rates then decreased before merging with the long crack data. For cracks naturally initiated at 650°C, no such anomalies were observed. It was concluded that the anomalous behaviour was a transient due to the pre-cracking technique used, and not an intrinsic characteristic of short crack growth in the material [3.109].

3.7 Influence of Microstructure on Fatigue Performance of Superalloys

IN718 and other superalloys can be processed to produce various grain sizes and precipitate distributions. Some studies have been performed to assess the influence of grain size on fatigue crack initiation and propagation in various superalloys, comparing coarse grained, fine grained and necklace microstructures. Note there is no standard definition of what range of grain sizes corresponds to the terms "coarse" or "fine". The terms are instead used to identify materials of different grain sizes compared in the same study.

Microstructural effects vary according to whether fatigue occurs in a cycle-dependent or time-dependent regime. In addition, the effect of microstructure changes depending on whether short or long fatigue crack growth behaviour is being studied.

3.7.1 Cycle-Dependent Regime

For Astroloy under cycle-dependent conditions, fine grain sizes or necklace microstructures gave better resistance to crack initiation and short crack growth than coarse grain sizes [3.106]. The better short crack growth resistance of fine grained material was attributed to crack arrest and deflection at grain boundaries. In contrast, long crack growth rates were slower in coarse grained material than in fine grained material. At low values of ΔK, crack deviations within large grains may improve long crack propagation resistance, as a result of roughness-induced crack closure, [3.27, 3.42] or a reduction in the local value of ΔK [3.42]. Large grain sizes may also promote greater reversibility of slip, reducing fatigue damage accumulation [3.42]. Necklace microstructures typically give a good compromise between short crack and long crack growth resistance [3.106].

Precipitate sizes can affect cycle-dependent fatigue behaviour. Coarsening of γ' precipitates in Waspaloy reduced short crack growth rates in vacuum at 700°C [3.110]. Coarsening of γ' softened the material, so that it was more able to accommodate large changes in plastic strain with lower rates of work hardening. More homogeneous slip caused by coarser precipitates may reduce the extent of slip band cracking, as demonstrated for γ' strengthened PM Astroloy in high cycle fatigue tests [3.111]. However, a different effect of precipitate size for fatigue at low temperature was described in a review by King [3.42]. Decreasing γ' precipitate size in Waspaloy reduced fatigue crack growth rates in the low ΔK regime at $R = 0.05$, probably because the smaller γ' size raised the yield stress.

3.7.2 Time-Dependent Regime

Under time-dependent conditions, larger grain sizes and necklace microstructures exhibited reduced long crack growth rates [3.55], compared with fine grained material from the same batch tested under the same conditions. It is thought that coarse grained material is more resistant to oxidation-assisted fatigue crack growth, because there is less grain boundary area along which oxygen can diffuse. Necklace microstructures may reduce intergranular fatigue crack propagation rates by forcing the crack to follow a more tortuous path. Crack path tortuosity can be shown to reduce the effective local ΔK, compared with a straight crack of the same projected length subjected to the same nominal far-field ΔK [3.70].

Precipitate size and distribution can affect time-dependent fatigue performance. Results for IN718 [3.112] indicate that coarse precipitates promote more homogeneous slip behaviour, which may reduce the tendency for stress-assisted grain boundary oxidation.

Overall fatigue lifetimes at elevated temperatures were observed to be longer for fine grained IN718 [3.113, 3.114]. However, these results were for test frequencies above 0.5 Hz [3.113] or in the high cycle fatigue regime [3.114], where time-dependent environmental effects are not as significant. This highlights the difficulty of comparing results from different studies, because of the wide variety of test conditions and microstructural variants used. Comparisons of the long crack growth rates of different commercial batches of IN718 have been made at different temperatures [3.115]. This revealed some difference between batches, but the results were not consistent from temperature to temperature, making identification of a clear microstructural influence difficult.

3.8 Summary of Inconel 718 & Its Fatigue Behaviour

IN718 is an Ni-Cr-Fe-Nb-Ti-Al superalloy in which the principal strengthening constituent is the metastable γ'' Ni_3Nb phase. The role of γ'' as the principal strengthening phase distinguishes IN718 from other nickel-based superalloys, in which the principal strengthening phase is mostly γ'. IN718 is available in numerous product forms, and can be processed to give a variety of microstructures. Awareness of the microstructure is necessary to enable understanding of fatigue behaviour under different test conditions and in service.

It appears that long crack growth behaviour in IN718 has been more extensively studied than short crack or initiation behaviour. Complex interactions between microstructure, cycle parameters, environmental effects and creep govern the overall fatigue crack growth behaviour observed experimentally. Establishing the nature of fatigue-creep-environment interactions can be difficult because of the wide variety of test conditions and microstructural variants used. Considerable attention has been given to the effects of fatigue cycle parameters and environment on fatigue crack growth rates. Grain boundary oxidation is identified as a major cause of accelerated fatigue crack growth in air at temperatures up to 650°C.

Less is known about crack initiation and short crack growth in IN718 at elevated temperatures. Some attention has been paid to the role of carbides in elevated temperature fatigue and fracture, but there is little detail in the literature on the mechanisms of crack initiation. Work on environmentally accelerated creep suggests that oxidation of carbides and Ni_3Nb may have a role in grain boundary embrittlement. Recent work on IN718 notched bars demonstrates that oxidation of carbides may be a major cause of crack initiation in IN718 under time-dependent conditions at 600°C.

3.9 References

[3.1] Inco Alloys International INCONEL alloy 718 Information Booklet IAI-19/4M/1994 INCO Alloys International, Fourth Edition (1985)

[3.2] Hammond C. & Nutting J. "The physical metallurgy of superalloys and titanium alloys" Metal Science pp. 474-489 (1977)

[3.3] Cozar R. & Pineau A. "Morphology of γ' and γ'' precipitates and thermal stability of Inconel 718 type alloys" Metall. Trans. vol. 4 pp. 47-59 (1973)

[3.4] Holt R. T. & Wallace W. "Impurities and trace elements in nickel-base superalloys" International Metals Reviews Review 203 pp. 1-24 (1976)

[3.5] Kirman I. & Warrington D. H. "The precipitation of Ni_3Nb Phases in a Ni-Fe-Cr-Nb alloy" Metall. Trans. vol. 1 pp. 2667-2675 (1970)

[3.6] Burke M. G. & Miller M. K. "Precipitation in Alloy 718: A combined AEM & APFIM investigation" Proc. 2nd Int. Symp. Superalloy 718, 625 & Various Derivatives Ed. Loria E. A., TMS, Warrendale PA, USA, pp. 337-350 (1991)

[3.7] Miller M. K., Babu S. S. & Burke M. G. "Intragranular precipitation in alloy 718" Mater. Sci. Engng. A vol. 270 pp. 14-18 (1999)

[3.8] Bradley E. H. Superalloys: a technical guide ASM International, Ohio USA. ISBN 0-87170-327 (1988)

[3.9] Sundararaman M., Mukhopadhyay P. & Banerjee S. "Some aspects of the precipitation of metastable intermetallic phases in Inconel 718" Metall. Trans. A vol. 23A pp. 2015-2028 (1992)

[3.10] Miller M. K., Babu S. S. & Burke M. G. "Intragranular precipitation in alloy 718" Mater. Sci. Engng. A. vol. 270 pp. 14-18 (1999)

[3.11] Guo E., Xu F. & Loria E. A. "Improving thermal stability of Alloy 718 via small modifications in composition" Proc. Superalloy 718 - Metallurgy & Applications Ed. Loria E. A., TMS, Warrendale, PA, USA, pp. 567-576 (1989)

[3.12] Guo E., Xu F. & Loria E. A. "Effect of heat treatment and compositional modification on strength and thermal stability of Alloy 718" Proc. 2nd Int. Symp. Superalloy 718, 625 & Various Derivatives Ed. Loria E. A., TMS, Warrendale, PA, USA, pp. 389-396 (1991)

[3.13] Guo E., Xu F. & Loria E. A. "Comparison of γ'/γ'' precipitates and mechanical properties in modified 718 alloys" Proc. 2nd Int. Symp. Superalloy 718, 625 & Various Derivatives Ed. Loria E. A., TMS, Warrendale, PA, USA, pp. 397-408 (1991)

[3.14] Tien J. K., Collier J. P. & Vignoul G. "The role of niobium and other refractory elements in superalloys" Superalloy 718-Metallurgy & Applications Ed. Loria E. A., TMS, Warrendale, PA, USA, pp. 553-566 (1989)

[3.15] Mitchell A., Schmalz A. J., Schvezov C. & Cockcroft S. L. "The precipitation of primary carbides in alloy 718" Proc. 3rd Int. Symp. Superalloys 718, 625, 706 and Various Derivatives Ed. Loria E. A., TMS, Warrendale, PA, USA, pp. 65-78. (1994)

[3.16] Sundararaman M., Mukhopadhyay P. & Banerjee S. "Precipitation of the δ Ni_3Nb phase in two nickel base superalloys" Metall. Trans. A vol. 19A pp. 453-465 (1988)

[3.17] Dong J., Xie X., Xu Z. & Zhang S. "TEM study on microstructure behavior of Alloy 718 after long time exposure at high temperatures" Proc. 3rd Int. Symp. Superalloys 718, 625, 706 & Various Derivatives Ed. Loria E. A., TMS, Warrendale PA, USA, pp. 649-658 (1994)

[3.18] Geng L., Na Y-S. & Park N-K. "Continuous cooling transformation behaviour of Alloy 718" Mater. Lett. vol. 30 pp. 401-405 (1997)

[3.19] Liu W. C., Xiao F. R. et al. "Influence of cold rolling on the precipitation kinetics of gamma and delta phases in Inconel 718 alloy" J. Mater. Sci. Lett. vol. 17 pp. 245-247 (1998)

[3.20] Liu W. C., Chen Z. L. & Yao M. "Effect of cold rolling on the precipitation behavior of δ phase in INCONEL 718" Metall. & Mater. Trans. A vol. 30A, pp. 31-40 (1999)

[3.21] Knorovsky G. A., Cieslak M. J., Headley T. J., Romig (Jnr.) A. D. & Hammetter W. F. "Inconel 718: A solidification diagram" Metall. Trans. A vol. 20A pp. 2149-2158 (1989)

[3.22] Vincent R. "Precipitation around welds in the nickel-base superalloy, Inconel 718" Acta Metall. vol. 33 pp. 1205-1216 (1985)

[3.23] Radhakrishna C. H. & Prasad Rao K. "The formation and control of Laves phase in superalloy 718 welds" J. Mater. Sci. vol. 32 pp. 1977-1984 (1997)

[3.24] Radavich J. F. "The physical metallurgy of cast and wrought Alloy 718" Proc. Superalloy 718 - Metallurgy & Applications Ed. Loria E. A., TMS, Warrendale, PA, USA (1989)

[3.25] Nakkalil R., Richards N. L. & Chaturvedi M. C. "A study of precipitates and insolubles in an Ni-Fe based superalloy by analytical electron microscopy" Mater. Sci. Engng. vol. A157 pp. 89-100 (1992)

[3.26] Brown E. E., Boettner R. C. & Ruckle D. L. "MINIGRAIN™ processing of nickel base superalloys" Proc. 2nd. Int. Symp. on Superalloys, TMS, Warrendale, PA, USA, pp. L1-L12(1972)

[3.27] James L. A. "Fatigue Crack Propagation in Alloy 718: A Review" Proc. Superalloy 718 - Metallurgy & Applications Ed. Loria E. A., TMS, Warrendale PA, USA, pp. 499-515 (1989)

[3.28] Krueger D. D. "The development of direct age 718 for gas turbine engine disk applications" Proc. Superalloy 718 - Metallurgy & Applications Ed. Loria E. A., TMS, Warrendale, PA, USA (1989)

[3.29] Chaturvedi M. C. & Han Y-F. "Strengthening Mechanisms in Inconel 718 superalloy" Metal Science vol. 17 pp. 145-149 (1983)

[3.30] Fournier D. & Pineau A. "Low cycle fatigue behavior of Inconel 718 at 298K and 823K" Metall. Trans. A vol. 8A pp. 1095-1105 (1977)

[3.31] He J., Fukuyama S. & Yokogawa K. "Deformation bands in Inconel 718" Mater. Sci. Tech. vol. 11 pp. 914-919 (1995)

[3.32] Merrick H. F. "The low cycle fatigue of three wrought nickel-base alloys" Metall. Trans. vol. 5 pp. 891-897 (1974)

[3.33] Worthem D. W., Robertson I. M., Leckie F. A., Socie D.F. & Altstetter C. J. "Inhomogeneous deformation of INCONEL 718 during monotonic and cyclic loadings" Metall. Trans. A vol. 21A pp.3215-3220 (1990)

[3.34] Kalluri S., Rao K. B. S., Halford G. R. & McGaw M. A." Deformation and damage mechanisms in Inconel 718 superalloy" Proc. 3rd. Int. Symp. Superalloys 718, 625, 706 & Various Derivatives, Ed. Loria E. A., TMS, Warrendale, PA, USA, pp. 593-606 (1994)

[3.35] Halford G. R., Meyer T. G., Nelson R. S., Nissley D. M. & Swanson G. A. "Fatigue life prediction modeling for turbine hot section materials" Trans. ASME: J. Engineering for Gas Turbines & Power vol. 111 pp. 279-285 (1989)

[3.36] Sadananda K. & Shahininan P. "Creep-fatigue crack growth" Fatigue at High Temperature Ed. Skelton R. P. Elsevier Applied Science, London, pp. 109-195 (1983)

[3.37] Pineau A. "High temperature fatigue of Ni-base superalloys: Microstructural and environmental effects" Proc. Conf. Engineering Against Fatigue 17-21 March 1997, Sheffield, UK (1997)

[3.38] Ghonem H., Nicholas T. & Pineau A. "Elevated temperature fatigue crack growth in alloy 718-Part I: Effects of mechanical variables" Fatigue Fract. Engng. Mater. Struct. vol. 16 pp. 565-576 (1993)

[3.39] Antunes F. V., Ferreira J. M., Branco C. M. & Byrne J. "High temperature fatigue crack growth in Inconel 718" Materials at High Temperatures vol. 17 no. 4 pp. 439-448 (2000)

[3.40] Sadananda K. & Vasudevan A. K. "Analysis of high temperature fatigue crack growth behavior" Int. J. Fatigue vol. 19 Supp. No. 1 pp. S183-S189 (1997)

[3.41] Shahinian P. & Sadananda K. "Effects of stress ratio and hold-time on fatigue crack growth in Alloy 718" Trans. ASME J. Engng. Mater. & Tech. vol. 101 pp. 224-230 (1979)

[3.42] King J. E. "Fatigue crack propagation in nickel-base superalloys-effects of microstructure, load ratio and temperature" Mater. Sci. & Tech. vol. 3 pp. 750-764 (1987)

[3.43] Clavel M. & Pineau A. "Frequency and wave-form effects on the fatigue crack growth behavior of alloy 718 at 298K and 823K" Metall. Trans. A vol. 9A pp. 471-480 (1978)

[3.44] Clavel M., Levaillant C. & Pineau A. "Influence of micromechanisms of cyclic deformation at elevated temperature on fatigue behaviour" Proc. Conf. Creep-Fatigue Environment Interactions, Milwaukee, Wisconsin, TMS/AIME, USA, pp. 24-45 (1979)

[3.45] Floreen S. & Kane R. H. "An investigation of the creep-fatigue-environment interaction in a Ni-base superalloy" Fatigue Engng. Mater. Struct. vol. 2 pp. 401-412 (1980)

[3.46] Mercer C. & Soboyejo W. O. "Fatigue crack growth mechanisms in a forged IN718 Nickel-based superalloy" Proc. 4th Int. Symp. Superalloys 718, 625, 706 & Various Derivatives Ed. Loria E. A., TMS, Warrendale PA, USA, pp. 577-586 (1997)

[3.47] Ghonem H., Nicholas T. & Pineau A. "Elevated temperature fatigue crack growth in alloy 718-Part II: Effects of environmental and material variables" Fatigue Fract. Engng. Mater. Struct. vol. 16 pp. 577-590 (1993)

[3.48] Ghonem H. & Zheng D. "Frequency interactions in high-temperature fatigue crack growth in Superalloys" Metall. Trans. A vol. 23A pp. 3067-3072 (1992)

[3.49] Zheng D., Rosenberger A. & Ghonem H. "Influence of prestraining on high temperature, low frequency, fatigue crack growth in superalloys" Mater. Sci. Engng. vol. A161 pp. 13-21 (1993)

[3.50] Smith H. H. & Michel D. J. "Effect of environment on fatigue crack propagation behaviour of Alloy 718 at elevated temperatures" Metall. Trans. A vol. 17A pp. 370-374 (1986)

[3.51] Pfaendtner J. A. & McMahon Jr. C. J. "Oxygen-induced intergranular cracking of a Ni-base alloy at elevated temperatures - an example of dynamic embrittlement" Acta Mater. vol. 49 pp. 3369-3377 (2001)

[3.52] Andrieu A., Molins R., Ghonem H. & Pineau A. "Intergranular crack tip oxidation mechanism in a nickel-based superalloy" Mater. Sci. Engng. A vol. 154 pp. 21-28 (1992)

[3.53] Lynch S. P., Radtke T. C., Wicks B. J. & Byrnes R. T. "Fatigue crack growth in nickel-based superalloys at 500-700C. I: Waspaloy" Fatigue Fract. Engng. Mater. Struct. vol. 17 pp. 297-311 (1994)

[3.54] Lynch S. P., Radtke T. C., Wicks B. J. & Byrnes R. T. "Fatigue crack growth in nickel-based superalloys at 500-700C. II: Direct-aged alloy 718" Fatigue Fract. Engng. Mater. Struct. vol. 17 pp. 313-325 (1994)

[3.55] Pedron J. P. & Pineau A. "The effect of microstructure and environment on the crack growth behaviour of Inconel 718 alloy at 650°C under fatigue, creep and combined loading" Mater. Sci. Engng. vol. 56 pp. 143-156 (1982)

[3.56] Andrieu E., Cozar R. & Pineau A. "Effect of environment and microstructure on the high temperature behavior of Alloy 718" Proc. Superalloy 718 - Metallurgy & Applications Ed. Loria E. A., TMS, Warrendale PA, USA, pp. 241-256 (1989)

[3.57] Diboine A. & Pineau A. "Creep crack initiation and growth in Inconel 718 alloy at 650C" Fatigue Fract. Engng. Mater. Struct. vol. 10 pp. 141-151 (1987)

[3.58] James L. A. "The effect of grain size upon the fatigue-crack propagation behavior of alloy 718 under hold-time cycling at elevated temperature" Engng. Fract. Mech. vol. 25 pp. 305-314 (1986)

[3.59] Coles A., Johnson R. E. & Popp H. G. "Utility of surface-flawed tensile bars in cyclic life studies" Trans. ASME J. Engng. Mater. & Tech. vol. 98 pp. 305-315 (1976)

[3.60] Bache M. R., Evans W. J. & Hardy M. C. "The effects of environment and loading waveform on fatigue crack growth in Inconel 718" Int. J. Fatigue vol. 21 supplement pp. S69-S77 (1999)

[3.61] Chang K-M. "Metallurgical control of fatigue crack propagation in Alloy 718" Proc. 2nd Int. Symp. Superalloy 718, 625 & Various Derivatives Ed. Loria E. A., TMS, Warrendale PA, USA, pp. 447-456 (1991)

[3.62] Andrieu E., Hochstetter G., Molins R. & Pineau A. "Oxidation mechanisms in relation to high temperature fatigue crack growth properties of alloy 718" Proc. 3rd Int. Symp. Superalloys 718, 625, 706 and Various Derivatives Ed. Loria E. A., TMS, Warrendale, PA, USA, pp. 619-631(1994)

[3.63] Ghonem H. & Zheng D. "Oxidation-assisted fatigue crack growth behaviour in Alloy 718-Part 1. Quantitative Modeling" Fatigue Fract. Engng. Mater. Struct. vol.14 pp. 749-760 (1991)

[3.64] Zheng D. & Ghonem H. "Oxidation-assisted fatigue crack growth behaviour in Alloy 718-Part II. Applications" Fatigue Fract. Engng. Mater. Struct. vol.14 pp. 761-768 (1991)

[3.65] Ghonem H. & Zheng D. "Characterisation of environment-dependent fatigue crack growth in alloy 718 at 650C" Proc. 2nd Int. Symp. Superalloy 718, 625 & Various Derivatives Ed. Loria E. A., TMS, Warrendale, PA, USA, pp. 477-490 (1991).

[3.66] Ghonem H. & Zheng D. "Depth of intergranular oxygen diffusion during environment-dependent fatigue crack growth in Alloy 718" Mater. Sci. Engng. A vol. 150 pp. 151-160 (1992)

[3.67] Antunes F. V., Ferreira J. M., Branco C. M. & Byrne J. "Influence of stress state on high temperature fatigue crack growth in Inconel 718" Fatigue Fract Engng. Mater. Struct. vol. 24, 127-135 (2001)

[3.68] Yuen J. L., Schmidt C. G. & Roy P. "Effects of air and inert environments on the near threshold fatigue crack growth behaviour of Alloy 718" Fatigue Fract. Engng. Mater. Struct. vol. 8 pp. 65-76 (1985)

[3.69] Sadananda K. & Vasudevan A. K. "Analysis of high temperature fatigue crack growth behavior" Int. J. Fatigue vol. 19 Supp. No. 1 pp. S183-S189 (1997)

[3.70] Suresh S. Fatigue of Materials Cambridge Solid State Science Series, Cambridge University Press, UK. ISBN 0-521-43763-6 (1991)

[3.71] Sadananda K. & Shahinian P. "The effect of environment on the creep crack growth behavior of several structural alloys" Mater. Sci. Engng. vol. 43 pp. 159-168 (1980)

[3.72] Liu J., Lyons J., Sutton M. & Reynolds A. "Experimental characterization of crack tip deformation fields in Alloy 718 at high temperatures" Trans. ASME. J. Engng. Mater. Tech. vol. 120 pp. 71-78 (1998)

[3.73] Hayes R. W., Smith D. F., Wanner E. A. & Earthman J. "Effect of environment on the rupture behaviour of alloys 909 and 718" Mater. Sci. Engng. A vol. 177 pp. 43-53 (1993)

[3.74] Valerio P., Gao M. & Wei R. P. "Environmental enhancement of creep crack growth in Inconel 718 by oxygen and water vapour" Scripta Metall. & Mater. vol. 30 pp. 1269-1274 (1994)

[3.75] Pang X. J., Dwyer D. J., Gao M., Valerio P. & Wei R. P. "Surface enrichment and grain boundary segregation of Niobium in Inconel 718 single- and poly-crystals" Scripta Metall. & Mater. vol. 31 pp. 345-350. (1994)

[3.76] Gao M., Dwyer D. J. & Wei R. P. "Chemical and microstructural aspects of creep crack growth in Inconel 718 alloy" Proc. 3rd Int. Symp. Superalloys 718, 625, 706 and Various Derivatives Ed. Loria E. A., TMS, Warrendale, PA, USA, pp. 581-592 (1994)

[3.77] Gao M., Dwyer D. J. & Wei R. P. "Niobium enrichment and environmental enhancement of creep crack growth in nickel-base superalloys" Scripta Metall. & Mater. vol. 32 pp. 1169-1174. (1995)

[3.78] Gao M., Chen S-F., Chen G. S. & Wei R. P. "Environmentally enhanced crack growth in nickel-based alloys at elevated temperatures" Elevated Temperature Effects on Fatigue and Fracture ASTM STP 1297, Eds. R. S. Piascik, R. P. Gangloff & A. Saxena, ASTM, USA, pp. 74-84 (1997)

[3.79] Gao M. & Wei R. P. "Grain boundary niobium carbides in Inconel 718" Scripta Mater. vol. 37 pp. 1843-1849 (1997)

[3.80] O'Hara M. J., Wilkinson D. & Allsop R. T. "A new phase in silicon bearing 17 per cent chromium, 8 per cent nickel and 1 per cent niobium steel" Nature vol. 187 (July 30 1960) pp. 407-408 (1960)

[3.81] Miller C. F., Simmons G. W. & Wei R. P. "High temperature oxidation of Nb, NbC and Ni3Nb and oxygen enhanced crack growth" Scripta Mater. vol. 42 pp. 227-232 (2000)

[3.82] Miller C. F., Simmons G. W. & Wei R. P. "Mechanism for oxygen enhanced crack growth in Inconel 718" Scripta Mater. vol. 44 pp. 2405-2410 (2001)

[3.83] Liu C. D., Han Y. F., Yan M. G. & Chaturvedi M. C. "Creep crack growth behaviour of Alloy 718" Proc. 2nd Int. Symp. Superalloys 718, 625 & Various Derivatives Ed. Loria E. A., TMS, Warrendale, PA, USA pp. 537-548 (1991)

[3.84] Lu H. M., Delph T. J., Dwyer D. J., Gao M. & Wei R. P. "Environmentally enhanced cavity growth in nickel and nickel-based alloys" Acta Mater. vol. 44 pp. 3259-3266 (1996)

[3.85] Lankford J. & Hudak (Jr.) S.J. "Relevance of the small crack problem to lifetime prediction in gas turbines" Int. J. Fatigue vol. 9 pp. 87-93 (1987)

[3.86] Xie J. Z. "Low cycle fatigue and fatigue crack growth behaviours of alloy IN718" Proc. 2nd Int. Symp. Superalloys 718, 625 & Various Derivatives Ed. Loria E. A., TMS, Warrendale, PA, USA, pp. 491-500 (1991)

[3.87] Healy J. C., Grabowski L. & Beevers C. J. "Short-fatigue-crack growth in a nickel-base superalloy at room and elevated temperature" Int. J. Fatigue vol. 13 pp. 133-138 (1991)

[3.88] Yates J. R., Zhang W. & Miller K. J. "The initiation and propagation behaviour of short fatigue cracks in Waspaloy subjected to bending" Fatigue Fract. Engng. Mater. Struct. vol. 16 pp. 351-362 (1993)

[3.89] Boyd-Lee A. & King J. E. "Short fatigue crack path determinants in polycrystalline Ni-Base superalloys" Fatigue Fract. Engng. Mater. Struct. vol. 17 pp. 1-14 (1994)

[3.90] Mei Z., Krenn C. R. & Morris J. W. "Initiation and growth of small fatigue cracks in a Ni-base superalloy" Metall. & Mater. Trans. A vol. 26 pp. 2063-2073 (1995)

[3.91] Gell M. & Leverant G. R. "The fatigue of the nickel-base superalloy, MAR-M200, in single crystal and columnar-grained forms at room temperature" Trans. Metall. Soc. of AIME vol. 242 pp. 1869-1879 (1968)

[3.92] Kawagoishi N., Chen Q. & Nisitani H. "Fatigue strength of Inconel 718 at elevated temperatures" Fatigue Fract. Engng. Mater. Struct. vol. 23 pp. 209-216 (2000)

[3.93] Denda T., Bretz P. L. & Tien J. K. "Inclusion size effect on the fatigue crack propagation mechanism and fracture mechanics of a superalloy" Metall. Trans. A vol. 23 pp. 519-526 (1992)

[3.94] Leverant G. R. & Gell M. "The elevated temperature fatigue of a nickel base superalloy, MAR-M200, in conventionally cast and directionally-solidified forms" Trans. Metall. Soc. of AIME vol. 245 pp. 1167-1173 (1969)

[3.95] Reuchet J. & Remy L. "High temperature low cycle fatigue of MAR-M 509 Superalloy I: The influence of temperature on the low cycle fatigue behaviour from 20 to 1100°C" Mater. Sci. Engng. vol. 58 pp. 19-32 (1983)

[3.96] Reuchet J. & Remy L. "High temperature low cycle fatigue of MAR-M 509 Superalloy II: The influence of oxidation at high temperatures" Mater. Sci. Engng. vol. 58 pp. 33-42 (1983)

[3.97] Reuchet J. & Remy L. "Fatigue oxidation interaction in a superalloy - Application to life prediction in high temperature low cycle fatigue" Metall. Trans. A Vol.14 pp. 141-149 (1983)

[3.98] Reger M. & Remy L. "Fatigue oxidation interaction in IN100 superalloy" Metall. Trans. A vol. 19 pp. 2259-2268 (1988)

[3.99] Reger M. & Remy L. "High temperature, low cycle fatigue of IN 100 superalloy I: Influence of temperature on the low cycle fatigue behaviour" Mater. Sci. Engng. A vol. 101 pp. 47-54 (1988)

[3.100] Reger M. & Remy L. "High temperature, low cycle fatigue of IN 100 superalloy II: Influence of frequency and environment at high temperatures" Mater. Sci. Engng. A vol. 101 pp. 55-63 (1988)

[3.101] Jiang W. H., Yao X. D., Guan H. R. & Hu Z. Q. "Carbide behaviour during high temperature low cycle fatigue in a cobalt-base superalloy" J. Mater. Sci. vol. 34 pp. 2859-2864 (1999)

[3.102] Banik T., Keefe P. W., Maurer G. E. & Petzold L. "Ultra fine grain/ ultra low carbon 718" Proc. 2nd Int. Symp. Superalloy 718, 625 & Various Derivatives Ed. Loria E. A., TMS, Warrendale, PA, USA, pp. 913-924 (1991)

[3.103] Jackman L. A., Boldy M. D. & Coffey A. L. "The influence of reduced carbon on Alloy 718" Proc. 2nd Int. Symp. Superalloy 718, 625 & Various Derivatives Ed. Loria E.A., TMS, Warrendale, PA, USA, pp. 261-270 (1991)

[3.104] Sjoberg G., Ingesten N-G. & Carlson R. G. "Grain boundary δ phase morphologies, carbides and notch rupture sensitivity of cast Alloy 718" Proc. 2nd Int. Symp. Superalloy 718, 625 & Various Derivatives Ed. Loria E. A., TMS, Warrendale, PA, USA, pp. 603-620 (1991)

[3.105] Reed P. A. S., Hachette F., Thakar D., Connolley T. & Starink M. J. "Creep-fatigue initiation and early crack growth in Inconel 718" Proc. 8th Int. Conf. Mechanical Behaviour of Materials (ICM8) Eds. Ellyin F. & Provan J.W., Fleming Printing Ltd. Victoria, BC, Canada, vol. 1 pp. 418-423 (1999)

[3.106] Brown C. W., King J. E. & Hicks M. A. "Effects of microstructure on long and short crack growth in nickel base superalloys" Metal Science vol. 18 pp. 374-380 (1984)

[3.107] Grabowski L. & King J. E. "Modelling short crack growth behaviour in nickel-base superalloys" Fatigue Fract. Engng. Mater. Struct. vol. 15 pp. 595-606 (1992)

[3.108] Chen Q., Kawagoishi N. & Nisitani H. "Evaluation of fatigue crack growth rate and life prediction of Inconel 718 at room and elevated temperatures" Mater. Sci. Engng. A vol. A277 pp. 250-257 (2000)

[3.109] Rosenberger A. H. & Ghonem H. "High temperature elastic-plastic small crack growth behaviour in a nickel-base superalloy" Fatigue Fract. Engng. Mater. Struct. vol. 17, pp. 509-521 (1994)

[3.110] Stephens R. R., Grabowski L., & Hoeppner D. W. "The effect of temperature on the behaviour of short fatigue cracks in Waspaloy using an in situ SEM fatigue apparatus" Int. J. Fatigue vol. 15 pp. 273-282 (1993)

[3.111] Isomoto T. & Stoloff N. S. "Effect of microstructure and temperature on high cycle fatigue of powder metallurgy Astroloy" Mater. Sci. Engng. A vol. 124 pp. 171-181 (1990)

[3.112] Zheng D. & Ghonem H. "Influence of prolonged thermal exposure on intergranular fatigue crack growth behaviour in alloy 718 at 650°C" Metall. Trans. A vol. 23 pp. 3169-3171 (1980)

[3.113] Pieraggi B. & Uginet J. F. "Fatigue and creep properties in relation with Alloy 718 microstructure" Proc. 3rd Int. Symp. Superalloys 718, 625, 706 and Various Derivatives Ed. Loria E. A., TMS, Warrendale, PA, USA, pp. 535-544 (1994)

[3.114] Korth G. E. "Effects of various parameters on the fatigue life of Alloy 718" Superalloys 718, 625 and Various Derivatives Ed. Loria E. A., TMS, Warrendale, PA, USA, pp. 457-476 (1991)

[3.115] James L. A. & Mills W. J. "Effect of heat-treatment and heat-to-heat variations in the fatigue-crack growth response of alloy 718" Engng. Fract. Mech. vol. 22 pp. 797-817 (1985)

4 EXPERIMENTAL METHODS

This chapter describes the materials, experimental methods and techniques used during the course of the research programme. Some preliminary fatigue experiments were performed on plain bend bar specimens at room temperature and elevated temperature. The main body of experimental work concentrated on the study of crack initiation and growth in U-notch specimens at elevated temperatures. In support of the U-notch fatigue experiments, finite element (FE) modelling was performed to aid understanding of the stress-strain state in the specimens. Thermal exposure experiments were also conducted to study the oxidation behaviour of the IN718 material in stress-free samples. Materials characterisation, metallography and the investigation of crack initiation and growth phenomena were conducted with the aid of optical microscopy, scanning electron microscopy (SEM) and energy-dispersive X-ray spectroscopy (EDX).

4.1 Materials

4.1.1 Disc Material

Most of the experimental work was performed on IN718 material extracted from two turbine disc forgings provided by ALSTOM Power. Both forgings came from the same cast of material and were manufactured at the same time. When manufactured, each forging was solution treated at 955°C for 1 hour followed by an air cool. They were then aged at 720°C for 8 hours, cooled at 50°C/h to 620°C, then aged at 650°C for a further 8 hours, finishing with an air cool. The composition of the disc material is given in Table 4.1. Restricted availability of material prevented supply of specimens solely from a single disc. Specimens cut from the two discs were kept separate and labelled Batch A and Batch B respectively.

The disc material was supplied by ALSTOM Power in the form of single edge U-notch specimens. These specimens were designed by Reed et al. [4.1] for a previous project on IN718 performed at the University of Southampton. The specimen geometry is shown in Figure 4.1. The dimensions of the U-notch were originally chosen to achieve a stress concentration factor of 2.23, using predictions based on the work of Neuber [4.2]. Finite element (FE) modelling of the specimen was performed as part of the present work to provide an alternative prediction of the stress concentration factor. The FE modelling for this project is described in Section 4.5 below.

Element	**Composition**	
	(wt%)	**(at%)**
B	0.003	0.016
C	0.031	0.15
N	0.006	0.024
O	0.0006	0.002
Mg	0.002	0.004
Al	0.46	0.99
Si	0.08	0.17
P	0.01	0.02
S	0.0004	0.001
Ti	1.02	1.24
Cr	18.0	20.08
Mn	0.06	0.063
Fe	18.6	19.37
Co	0.43	0.42
Ni	52.9	52.28
Cu	0.1	0.09
Mo	3.02	1.83
Nb + Ta	5.22	3.26

Table 4.1: Chemical composition of IN718 turbine disc material.

Fatigue specimens were extracted from locations close to the rim of the disc forgings, as shown in Figure 4.2. Twenty four U-notch specimens were supplied in Batch A, and twenty two in Batch B. The longitudinal axes of the specimens were tangential to the disc circumference, and the notch axis in each specimen was parallel to the disc axis. Notches were machined using a broaching process similar to that used for machining fir tree root fixings in production discs. In the broaching process a cutting tool with multiple shaped teeth is drawn through a hole or over a surface to remove material by axial cutting [4.3]. Figure 4.3 shows a schematic diagram of a broaching tool and its application in machining of a U-notch. Many complex profiles can be cut by a broaching process, the only restrictions being that there must be adequate clearance for passage of the tool over the surface being cut, and the component itself must be strong enough to withstand the high machining forces required. With appropriate tool design, complex profiles can be machined with the single pass of a tool, though in some cases multiple passes with separate tools may be required. Broach tooling is expensive, but it is suitable for mass production and generally produces a better finish than alternative processes such as milling or reaming. Further information on broaching processes, tooling and applications can be found in the ASM Handbook, Volume 16 [4.3].

4.1.2 Extruded Material

Due to initial constraints on availability of disc material, a small amount of extruded IN718 remaining from a previous study [4.1] was used for some preliminary fatigue experiments. Like the disc material, this was supplied in the form of U-notch bend specimens. These specimens were machined with their longitudinal axes parallel to the extrusion direction of the bar (Figure 4.4). No detailed composition or heat treatment information is available for the extruded bar, but it was supplied by ALSTOM Power on the understanding that it was of a similar specification to the disc material which was used for the majority of this work.

4.2 Materials Characterisation

4.2.1 Metallography & Microscopy

Metallographic samples for optical microscopy and SEM examination were prepared using standard techniques. If required, samples were nickel plated first to provide edge retention and protection for surface features. Nickel plating was performed in Watt's solution (500ml Distilled water; 150g Nickel Sulphate; 30g Nickel Chloride; 20g Boric Acid) at a temperature of 55-60°C and a voltage of 3V, using a 99.9% pure Ni anode in the apparatus shown in Figure 4.5. Specimens were then mounted in conducting phenolic resin and polished to a 1 μm diamond finish on an automatic polisher. The polishing route is summarised in Table 4.2. Specimens were thoroughly cleaned with water and methanol between each preparation step.

Specimens were etched using either modified Kalling's Reagent (80 ml HCl; 40 ml CH_3OH & 40g $CuCl_2$) or Nimonic etch (10 ml HNO_3, 50 ml HCl, 40 ml H_2O & 2.5g $CuCl_2$). Typical etching times were 4-10 seconds. Both etches produced similar results on Inconel 718, though Nimonic etch was more controllable and gave more consistent etching of specimens.

Paper/ Cloth	**Abrasive size**	**Lubricant**	**Wheel speed (rpm)**	**Head direction (opposite or same as wheel)**	**Force (lbf)***	**Time (minutes)**
SiC	120 grit	Water	150	Opposite	20	Until planar
SiC	600 grit	Water	150	Opposite	20	2
SiC	1200 grit	Water	150	Opposite	20	2
SiC	4000 grit	Water	150	Opposite	20	2 (Change after 1 min.)
Struers DP-Plus	3 μm suspension	Struers Blue	70	Same	20	6
Struers DP-Nap	1 μm suspension	Struers Blue	70	Same	20	4

Table 4.2: Polishing route for IN718 microsections. * The force control on the polishing machine used was labelled in lbf, not Newtons. 20lbf = 88.9 N.

Microsections were examined under an Olympus BH-2 optical microscope in the as-polished condition and after etching. A Zeiss KS300 image analysis system was used to determine the combined area fraction of primary carbide and primary nitride particles present in the IN718 materials. Measurements were performed on as-polished specimens using 12 fields selected at random at a magnification of 100x. Grain size measurements were performed on etched specimens using a mean linear intercept method in accordance with ASTM Standard E 112-96 [4.4]. Selected specimens received additional examination in a JEOL T300 or JEOL JSM6400 SEM using accelerating voltages of 15kV or 20kV. The microscopes were operated in secondary electron imaging (SEI) mode to obtain topographical contrast or the backscattered electron imaging (BEI) mode to obtain atomic number contrast. BEI was used to assist in identifying different microstructural phases. Contrast in BEI mode is determined by the electron backscattering coefficient of the atoms present, which is proportional to their atomic number Z. Hence, heavier elements appear brighter in backscatter than lighter elements. The JSM6400 was equipped with a PGT energy-dispersive X-ray (EDX) spectrometer for chemical compositional analysis. Quantitative analysis of EDX spectra was performed using atomic number, absorption and fluorescence (ZAF) correction algorithms.

4.2.2 Hardness Testing

To identify any gross variations or changes in material properties that might affect fatigue test results, Vickers hardness measurements using a mass of 30 kg were performed on specimens in the as-received condition. The average of four measurements was taken. Care was taken to locate hardness indents well outside the loaded region of specimens, so that the indentations could not initiate fatigue cracks. Post-test hardness measurements were performed on selected high temperature fatigue test specimens to check for any changes in materials properties as a result of thermal exposure.

4.2.3 Surface Roughness Measurements

The broaching process used to machine the U-notches in fatigue specimens produced long machining marks parallel to the notch axis. After preliminary fatigue testing, it was decided to perform surface roughness measurements on the remaining U-notch specimens to confirm that no severe variations in surface roughness were present that might affect the fatigue performance of specimens tested in the as-broached condition. Surface roughness measurements were made on 15 out of the 24 U-notch specimens from Batch A (Nos. 10 to 24), and all 22 specimens from Batch B. A Talysurf instrument was used to obtain the following measures of surface roughness:

R_a = average deviation from the mean surface.
R_v = maximum valley depth below the mean surface detected in a measurement run.

For each specimen, three measurement runs (t1-t3) were made perpendicular to the notch axis. Measurement locations are shown in Figure 4.6. The runs were spaced at 5mm intervals, acquired using a data length of 1.04mm and a cut-off length of 0.08mm. The notch depth meant this was the longest data length possible without risk of damage to the Talysurf stylus. The instrument was programmed to account for the curvature of the U-notch.

Metallographic sections were taken through selected untested U-notch specimens to check for any microstructural changes that may have occurred as a result of the broaching process.

4.3 Thermal Exposure Experiments

It is known from previous work [4.1, 4.5] and published literature [4.6, 4.7, 4.8, 4.9, 4.10, 4.11] that oxidation of primary carbides can play a role in high temperature fatigue crack initiation in IN718 and other superalloys. Prior to performing fatigue tests, a series of thermal exposure experiments were performed to study the oxidation behaviour of primary carbides in unstressed samples of IN718. It was intended that examination of the oxidation behaviour in the absence of applied stresses would assist understanding of crack initiation at primary carbides in subsequent fatigue tests.

Samples of IN718 disc material from Batch A were prepared so that oxidation on two surfaces could be compared; the original as-machined surface and the polished surface. The sample preparation and examination procedure is shown schematically in Figure 4.7. Samples were mounted in phenolic resin so one surface could be polished to 1μm diamond finish. After polishing, the specimens were broken out of the resin, cleaned then thermally exposed for between 1 and 256 hours. Two sets of thermal exposure experiments were performed; one set at 550°C and a second set at 600°C, corresponding to the test temperatures planned for the high temperature fatigue experiments. After thermal exposure, the surfaces of the specimens were examined by SEM to investigate features produced by oxidation. Selected samples were nickel plated, mounted in conducting phenolic resin and polished to a 1μm diamond finish, so that the thermally exposed faces could be examined in cross-section. An optical microscope was used to look for evidence of surface and sub-surface carbide oxidation in the cross-sections. Additional examination was conducted using SEM and EDX.

4.4 Fatigue Testing of Plain Bend Bar Specimens

4.4.1 Room Temperature Testing

Previous work indicated that surface eruptions due to the oxidation of (Nb,Ti)C primary carbides might play a role in crack initiation, possibly as the result of a micro-notch effect [4.1, 4.5]. Prior to high temperature testing, a small group of room temperature tests on plain bend bars was performed to establish if surface eruptions would act as crack initiators. The intention was to compare fatigue lives and fatigue crack growth rates in specimens exposed in air at 600°C with unexposed specimens. If erupted carbides play a role in crack initiation through a notch effect, then this would be expected to influence the lifetimes of exposed specimens compared with as-polished specimens. Due to restricted availability of IN718 disc material, these tests were performed on plain bend bars machined from extruded bar material remaining from the previous study [4.1]. Four plain bars were machined out of the supplied U-notch specimens, with their long axes parallel to the extrusion direction. The top surface of each bar was polished to a 1 μm diamond finish to facilitate surface crack replication. They were then given additional treatments as listed in the test matrix in Table 4.3. Etched specimens were included in the test matrix to enable observation of crack interactions with microstructural features like grain boundaries.

Test Number	**Length (mm)**	**Breadth, *b* (mm)**	**Depth, *w* (mm)**	**Surface Condition**	**Thermal Exposure**
P1	39.31	7.36	7.26	Polished	None
P2	38.47	7.42	7.31	Polished & etched	None
P3	38.53	7.04	5.04	Polished	4hrs @ 600°C
P4	39.25	8.08	5.02	Polished & etched	4hrs @ 600°C

Table 4.3: Test matrix for extruded bar material plain bend specimens fatigue tested at room temperature. The surface condition and thermal exposure treatments for each specimen are stated.

All specimens were tested under load control on an Instron 8501 servo-hydraulic testing machine in 3 point bend. Loads were calculated using Eqn. 4.1 and Eqn. 4.2 so that the maximum stress in the cycle was 1126 MPa. This was 95% of an assumed yield stress of 1185 MPa for IN718 bar, obtained from the ASM Handbook [4.12]. A 10 Hz sinusoidal waveform was used, at a load ratio $R = 0.1$.

$$P_{\max} = \frac{\sigma_{\max} b w^2}{3s} \qquad \text{Eqn. 4.1}$$

$$P_{\min} = R P_{\max} \qquad \text{Eqn. 4.2}$$

where:

P_{max} = Maximum applied load

P_{min} = Minimum applied load

σ_{max} = desired nominal maximum stress = 1126 MPa

b = specimen breadth

w = specimen depth

s = span

R = load ratio = 0.1

Acetate replicas of each specimen surface were taken at intervals of 10000 cycles until crack initiation was detected, then at intervals of 5000 cycles until specimen fracture. Crack length measurements were obtained from photomicrographs of the acetate replicas, enabling calculation of crack growth rates. Surface crack growth rates dc/dN were characterised in terms of the stress intensity range ΔK at the surface. ΔK at the surface was calculated using the model of Scott & Thorpe [4.13].

Analysis of acetate replicas was used to identify crack initiation sites. Each replica was surveyed under an optical microscope and a cumulative count taken of the number of cracks observed and the nature of the initiation site.

4.4.2 High Temperature Testing

At the start of the project, it was not certain whether high temperature short crack growth measurements could successfully be obtained from U-notch specimens. Therefore, some preliminary acetate replica studies on plain bend bars of IN718 disc material were performed. Four tests were conducted on plain bend bars of disc material, identified as Test PB1 to Test PB4. The specimens used were machined from U-notch specimens, each U-notch bar yielding two plain bend bars of approximate dimensions 6 x 11.5 x 80 mm. The top surface of each plain bend bar was polished to a 1μm diamond finish in an automatic polishing jig. All tests were performed in three point bend at an R-ratio of 0.1. Two high temperature tests, labelled PB1 and PB2, were performed at 600°C in air. Two further tests, labelled PB3 and PB4, were performed at room temperature. Individual specimen dimensions and test conditions are listed in Table 4.4. Further details about each test are given below.

Test Number	**Length (mm)**	**Breadth, *b* (mm)**	**Depth, *w* (mm)**	**σ_{max} (MPa)**	**Waveform**	**Test Temperature (°C)**
PB1	80.00	6.02	11.56	930.00	1-1-1-1	600
PB2	80.00	6.77	11.55	962.36 to 1180	10Hz & 1-1-1-1	600
PB3	80.00	6.07	11.74	1080.00	10Hz	20
PB4	80.00	6.56	11.91	1080.00 to 1125.63	10Hz	20

Table 4.4: Specimen numbers and dimensions for plain bend bar tests on disc material.

For Test PB1, a 1-1-1-1 trapezoidal waveform was applied in 3 point bend at 600°C in air. The test was conducted with σ_{max} = 930 MPa at a load ratio R = 0.1. The value of σ_{max} was based on 95% of the yield stress of 982 MPa at 600°C [4.14].

In test PB2 a sinusoidal 10 Hz waveform was applied in 3 point bend at 600°C in air. Initially, the maximum stress level σ_{max} was set at 962 MPa (98% of the yield stress at 600°C), with R = 0.1. After 50000 cycles, the test was stopped and an acetate replica taken. If no crack initiation was observed, the maximum stress level was increased and the test run for another 50000 cycles. This process was continued up to a maximum stress level of 1180 MPa (95% of the estimated UTS at 600°C). The maximum stress levels used are summarised in Table 4.5.

σ_{max}	σ_{max} (MPa)	P_{max} (kN)	P_{min} (kN)	P_{amp} (kN)	Waveform	Cycles	Total Cycles
98% σ_y	962.36	9.66	0.97	4.35	Sine, 10Hz	50000	50000
100% σ_y	982	9.85	0.99	4.43	Sine, 10Hz	50000	100000
105% σ_y	1031.1	10.35	1.03	4.66	Sine, 10Hz	50000	150000
110% σ_y	1080.2	10.84	1.08	4.88	Sine, 10Hz	50000	200000
114% σ_y	1120	11.24	1.12	5.06	Sine, 10Hz	50000	250000
116% σ_y	1140	11.44	1.14	5.15	Sine, 10Hz	50000	300000
118% σ_y	1160	11.64	1.16	5.24	Sine, 10Hz	50000	350000
Approx. 95% σ_{UTS}	1180	11.84	1.18	5.33	Sine, 10Hz	50000	400000
Approx. 95% σ_{UTS}	1180	11.84	1.18	5.33	1-1-1-1	81750	481750

Table 4.5: Summary of test conditions for plain bend bar Test PB2. The values of $\sigma_y = 982$ MPa and $\sigma_{UTS} = 1240$ MPa at 600°C are taken from the available tensile test data for the disc material [4.14].

For the room temperature test PB3 a 10 Hz sinusoidal waveform was applied with $\sigma_{max} = 1080$ MPa (95% σ_y at 20°C) and $R = 0.1$. An accidental overload to 1184 MPa occurred during set-up, but it was decided to continue with the test. No acetate replicas were taken.

In test PB4 a 10 Hz sinusoidal waveform was applied at room temperature, with $\sigma_{max} = 1080$ MPa (95% σ_y at 20°C) and $R = 0.1$. Acetate replicas were taken to monitor crack initiation and growth. After 100000 cycles σ_{max} was increased to 1126 MPa (99% σ_y at 20°C).

4.5 Finite Element Modelling of U-notch Specimens

To support the experimental fatigue testing performed at the University of Southampton, an elastic-plastic three-dimensional finite element (FE) model of the U-notch specimen was constructed by Dr. S. J. Moss of ALSTOM Power [4.15]. After verification testing, the model was passed to the University of Southampton for use as a research tool, to enable the prediction of stress and strain in the notch root region for different applied load levels. These predictions were used to compare the strain-life behaviour of the U-notch specimens with existing data provided by ALSTOM Power. An elastic-only version of the model was also used to predict the theoretical elastic stress concentration factor of the U-notch. The elastic-plastic model used a constitutive model for IN718 developed in-house by ALSTOM Power using commercially sensitive data. For this reason, the model is subject to an intellectual property agreement between ALSTOM Power and the University of Southampton, as stated in Appendix A.

The FE model of the U-notch specimen contained 2070 hexahedral elements, with a total of 9754 nodes. A view of the meshed model is shown in Figure 4.8. Symmetry permitted modelling of just one quarter of the specimen, significantly reducing the amount of computational effort required. To represent the test conditions, the model was loaded in three point bend at 600°C, using point contact to simplify computation.

The material constitutive model for IN718 was time-independent, taking into account the effects of cyclic softening, but not creep. The model was set to run for 10 load-unload cycles, representing 20 modelling steps in all. The model was run using the ABAQUS/Standard 5.8 finite element analysis package, with post-processing performed using ABAQUS Post and PATRAN. The output of the model contained the following stress and strain parameters:

- 6 components of stress.
- 6 components of total engineering strain.
- 6 components of plastic engineering strain.
- 6 components of elastic engineering strain.

4.5.1 Prediction of Strain Amplitude

The FEM model was used to predict the strain range at the centre of the notch root for the different nominal stress levels employed for U-notch testing. The six total engineering strain components in the notch root were predicted for different load levels and used to calculate an equivalent total strain range $\Delta\varepsilon_{eq}$ given by:

$$\Delta\varepsilon_{eq} = \frac{\sqrt{2}}{3}\left[\left(\Delta\varepsilon_{xx} - \Delta\varepsilon_{yy}\right)^2 + \left(\Delta\varepsilon_{yy} - \Delta\varepsilon_{zz}\right)^2 + \left(\Delta\varepsilon_{zz} - \Delta\varepsilon_{xx}\right)^2 + \frac{3}{2}\left((\Delta\gamma_{xy})^2 + (\Delta\gamma_{yz})^2 + (\Delta\gamma_{xz})^2\right)\right]^{\frac{1}{2}}$$

Eqn. 4.3

where: $\Delta\varepsilon_{ij}$ and $\Delta\gamma_{ij}$ are the difference between each respective total strain component ε_{ij} or γ_{ij} at maximum load (step 19) and minimum load (step 20).

The total strain amplitude is:

$$\varepsilon_{amp} = \frac{\Delta\varepsilon_{eq}}{2} \qquad \text{Eqn. 4.4}$$

4.5.2 Prediction of Stress Concentration Factor

An elastic-only FE model was run to predict the elastic stresses in the notch root for a given nominal applied stress. Loads in the model were defined to achieve a net section bending stress of 750 MPa. The FE model was interrogated to find the maximum predicted value of σ_{xx} in the elastic case. σ_{xx} was chosen because it was in the direction parallel to the longitudinal axis of the specimen, and hence parallel to the axis of maximum nominal bending stress. The predicted elastic stress concentration factor K_t was obtained from:

$$K_t = \frac{\sigma_{xx}\ \text{predicted by FEM}}{750\text{MPa}} \qquad \text{Eqn. 4.5}$$

Using this method, an elastic stress concentration factor of 2.08 was predicted.

4.5.3 Estimate of Plastic Zone Depth

Another use of the FE model was to predict the plastic zone depth in the U-notch. A constraint of the ABAQUS 5.8 code when using user-defined material models was that equivalent plastic strain could not be automatically calculated during execution of the model. This also meant that a yielding flag was not generated by the ABAQUS code. However, it was possible to calculate equivalent plastic strain for selected nodes using the plastic strain components ε_{ij}^{pl} and γ_{ij}^{pl} predicted using the material constitutive model. For simplicity, just the centreline of the model below the notch root was considered. This is shown by the shaded region in Figure 4.9. For each node in this region, the equivalent plastic strain was calculated using the following equation:

$$\varepsilon_{eq}^{pl} = \frac{\sqrt{2}}{3}\left[\left(\varepsilon_{xx}^{pl}-\varepsilon_{yy}^{pl}\right)^2+\left(\varepsilon_{yy}^{pl}-\varepsilon_{zz}^{pl}\right)^2+\left(\varepsilon_{zz}^{pl}-\varepsilon_{xx}^{pl}\right)^2+\frac{3}{2}\left(\gamma_{xy}^{pl^2}+\gamma_{yz}^{pl^2}+\gamma_{xz}^{pl^2}\right)\right]^{\frac{1}{2}} \qquad \text{Eqn. 4.6}$$

where: ε_{ij}^{pl} and γ_{ij}^{pl} are the plastic components of strain.

Knowing the co-ordinates of each node, contours of equivalent plastic strain were plotted.

4.6 High Temperature Fatigue Testing of U-notch Specimens

Fatigue testing was conducted inside an ESH high temperature chamber mounted on an Instron 8501 servo-hydraulic testing frame. The chamber was equipped with a Balzers turbo-molecular pumping system to enable testing of specimens in vacuum. For all vacuum tests, pressures between 2.5×10^{-3} Pa and 3.2×10^{-4} Pa (2.5×10^{-5} mbar and 3.2×10^{-6} mbar) were achieved. Specimens were heated using four high intensity quartz lamps and the temperature was monitored and controlled via an R-type thermocouple attached to the front face of each specimen. For all tests the recorded temperature was within +/- 2°C of the target temperature of 550°C or 600°C. Specimens were heated to the target temperature at a rate of 20°C per minute, with a 10 minute soak at the target temperature before commencing fatigue cycling. Tests were conducted in three point bend under load control using 1-1-1-1, 1-20-1-1 or 1-30-1-1 trapezoidal waveforms. An example of a trapezoidal waveform is shown in Figure 4.10 and the specimen set-up is shown in Figure 4.11. Initially, Nimonic 80A rollers were used, but these were later changed to IN718 rollers to avoid deformation of the rollers at the higher stresses used for some tests. Applied loads were calculated to give the desired nominal value of σ_{max} (i.e. ignoring the stress concentrating effect of the notch) in the net specimen cross section, according to the equations:

$$P_{\max} = \frac{\sigma_{\max} b(w-d)^2}{3s} \qquad \text{Eqn. 4.7}$$

$$P_{\min} = RP_{\max} \qquad \text{Eqn. 4.8}$$

where:

P_{max} = Maximum applied load

P_{min} = Minimum applied load

σ_{max} = desired nominal maximum stress

b = specimen breadth = 16 mm

w = specimen depth = 16 mm

d = U-notch depth = 4 mm

s = span = 30 mm

R = load ratio = 0.1

Maximum stresses from 750 MPa to 1000 MPa were employed. All tests were performed at a load ratio $R = 0.1$

Each U-notch test was assigned a unique code containing information about the experimental conditions used. The meaning of each element of the code is set out in Table 4.6 below, using the example A600-750-1-PR-01. A summary of all the tests performed is given in Table 4.7.

A	600	-	750	-	1	-	PR	-	01
Batch Code A or B	Temperature (°C)		σ_{max} (MPa)		Dwell at σ_{max} (s)		Special test details. P = Polished Notch R = Replicas taken V = test in vacuum		Sequential number for duplicate tests

Table 4.6: Definition of test codes used to label U-notch specimens.

The long duration of the fatigue tests resulted in some of them being interrupted before failure, due to test machine time constraints. In such cases, the opportunity was taken to examine unfailed specimens for cracks using an SEM. Table 4.8 contains a summary of when each U-notch test was interrupted.

Detailed Code	**Batch**	**Temp. (^{o}C)**	**Environment & Special Conditions**	**Cycle**	**σ_{max} (MPa)**
A550-750-1-01	A	550	Air	1-1-1-1	750
A550-750-1-V-01	A	550	Vacuum	1-1-1-1	750
A600-750-1-01	A	600	Air	1-1-1-1	750
A600-750-1-02	A	600	Air	1-1-1-1	750
A600-750-1-V-01	A	600	Vacuum	1-1-1-1	750
A600-750-20-01	A	600	Air	1-20-1-1	750
A600-750-30-01	A	600	Air	1-30-1-1	750
A600-770-1-01	A	600	Air	1-1-1-1	770
A600-790-1-01	A	600	Air	1-1-1-1	790
A600-810-1-01	A	600	Air	1-1-1-1	810
A600-870-1-01	A	600	Air	1-1-1-1	870
A600-750-1-P-01	A	600	Air, polished notch	1-1-1-1	750
A600-750-1-PR-01	A	600	Air, polished notch, replicas	1-1-1-1	750
A600-790-1-PR-01	A	600	Air, polished notch, replicas	1-1-1-1	790
A600-790-1-P-01	A	600	Air, polished notch	1-1-1-1	790
A600-790-1-P-02	A	600	Air, polished notch	1-1-1-1	790
A600-790-1-P-03	A	600	Air, polished notch	1-1-1-1	790
B600-790-1-01	B	600	Air	1-1-1-1	790
B600-790-1-02	B	600	Air	1-1-1-1	790
B600-790-1-P-01	B	600	Air, polished notch	1-1-1-1	790
B600-870-1-01	B	600	Air	1-1-1-1	870
B600-870-1-02	B	600	Air	1-1-1-1	870
B600-885-1-01	B	600	Air	1-1-1-1	885
B600-885-1-02	B	600	Air	1-1-1-1	885
B600-885-1-03	B	600	Air	1-1-1-1	885
B600-900-1-01	B	600	Air	1-1-1-1	900
B600-1000-1-01	B	600	Air	1-1-1-1	1000
B600-885-20-01	B	600	Air	1-20-1-1	885
B600-885-20-02	B	600	Air	1-20-1-1	885
B600-885-1-R-01	B	600	Air, replicas	1-1-1-1	885
B600-885-1-P-01	B	600	Air, polished notch	1-1-1-1	885
B600-885-1-PR-01	B	600	Air, polished notch, replicas	1-1-1-1	885
B600-885-1-PR-02	B	600	Air, polished notch, replicas	1-1-1-1	885

Table 4.7: Test codes and summary of test conditions for all U-notch fatigue tests.

Test Code	Lifetime (cycles)	Notes on Interruptions
A550-750-1-01	137819	SEM inspection after 125500 cycles.
A600-750-1-01	25311	SEM inspection after 19884 cycles.
A550-750-1-V-01	160938	Uninterrupted.
A600-750-20-01	50756	SEM inspections after 11761 cycles, 19590 cycles & 48261 cycles.
A600-750-30-01	71768	SEM inspections after 15400 cycles, 59870 cycles & 65595 cycles.
A600-750-1-PR-01	51279	Replicas every 2000 cycles.
A600-750-1-P-01	169413	One replica after 110000 cycles.
A600-750-1-02	20802	Uninterrupted.
A600-870-1-01	3886	Uninterrupted.
A600-810-1-01	4329	Uninterrupted.
A600-770-1-01	27538	Uninterrupted.
A600-750-1-V-01	53412	Uninterrupted.
A600-790-1-01	8792	Uninterrupted.
A600-790-1-PR-01	51687	First replica after 1000 cycles, then every 2000 cycles thereafter.
A600-790-1-P-01	123100 unfailed	SEM inspection after 123100 cycles. (overloaded during set-up).
A600-790-1-P-02	13420	Uninterrupted.
A600-790-1-P-03	87327	Inspected after 86000 cycles.
B600-790-1-01	90327	Uninterrupted.
B600-790-1-02	40440	Uninterrupted.
B600-790-1-P-01	28510	Uninterrupted.
B600-870-1-01	19856	Uninterrupted.
B600-870-1-02	19010	Stopped after 146 cycles to re-weld thermocouple. Not inspected.
B600-1000-1-01	2153	Uninterrupted.
B600-900-1-01	4475	Uninterrupted.
B600-885-1-01	5016	Uninterrupted.
B600-885-1-02	9889	Uninterrupted.
B600-885-1-03	3000 Unfailed	Stopped after 3000 cycles. SEM inspection.
B600-885-20-01	4541	Uninterrupted.
B600-885-20-02	4321	Uninterrupted.
B600-885-1-R-01	5157	Replicas every 500 cycles to 2000 cycles. Then every 1000 cycles thereafter.
B600-885-1-P-01	19605	Uninterrupted.
B600-885-1-PR-01	13591	Replicas every 1000 cycles.
B600-885-1-PR-02	7939	Replicas every 1000 cycles.

Table 4.8: Summary of when U-notch tests were interrupted.

The following sections describe the experiments performed to study different aspects of the fatigue behaviour of the U-notch specimens.

4.6.1 Temperature and Environment Effects

At the start of the project, it was intended to perform tests at 550°C and 600°C, similar to the service temperatures experienced by IN718 disc rims. Time-dependent behaviour due to oxidation was anticipated, so a comparison was made between tests conducted in air and in vacuum at 550°C and 600°C, using a 1-1-1-1 waveform. A maximum stress of 750 MPa was selected, based on experience gained with specimens of extruded IN718 tested in a previous study [4.1]. The tests were conducted with notches in the as-broached condition and are summarised in Table 4.9.

Detailed Code	**Batch**	**Temp. (°C)**	**Environment**	**Cycle**	**σ_{max} (MPa)**
A550-750-1-01	A	550	Air	1-1-1-1	750
A600-750-1-01	A	600	Air	1-1-1-1	750
A550-750-1-V-01	A	550	Vacuum	1-1-1-1	750
A600-750-1-V-01	A	600	Vacuum	1-1-1-1	750

Table 4.9: Preliminary tests performed to study the effect of temperature and environment on fatigue life to specimen fracture.

Following analysis of results from these preliminary tests, it was decided to concentrate on testing at 600°C in air, this being the more severe operating environment for the material.

4.6.2 Effect of Stress Level

Preliminary tests on U-notch specimens were performed with $\sigma_{max} = 750$ MPa and $R = 0.1$. It was found that these loading conditions resulted in specimen lifetimes considerably longer than anticipated. In order to conduct further tests to study the effect of dwell and measure short crack growth rates, a shorter specimen lifetime was desirable. Based on ALSTOM Power's operational experience with turbine disc components, a target lifetime of 10000 cycles to fracture was set, for a 1-1-1-1 waveform at 600°C in air using an as-broached specimen. Elastic-plastic FE modelling of the U-notch specimen was performed to predict the strain range in the notch root for different nominal applied stress levels. This is described in detail in Section 4.5. These strain range predictions were used in conjunction with existing strain-life data provided by ALSTOM Power to identify suitable applied stress levels to achieve a target life of 10000 cycles. Tests were then performed on as-broached U-notch specimens to verify the prediction, and the stress level revised again if necessary. A mean strain-life curve was obtained by fitting the available U-notch strain-life data to the Coffin-Manson equation:

$$\frac{\Delta\varepsilon}{2} = \left(\frac{\sigma_f'}{E}\right)(2N_f)^{\lambda_1} + \varepsilon_f'(2N_f)^{\lambda_2} \qquad \text{Eqn. 4.9}$$

where:

$\Delta\varepsilon$ = strain range

σ_f' = fatigue strength coefficient (≈ the uniaxial true fracture stress)

E = elastic modulus

N_f = number of cycles to failure

ε_f' = fatigue ductility coefficient (material-dependent)

λ_1, λ_2 = material-dependent constants.

Eqn. 4.9 was fitted to the fatigue life data using a least squares fitting procedure. In the analysis the parameters σ_f', ε_f' and λ_1 were allowed to vary. The parameter λ_2 was kept fixed at a value of -0.01.

The 1-1-1-1 tests performed at the original and higher stress levels are summarised in Table 4.10.

Detailed Code	**Batch**	**Temp. (°C)**	**Environment**	**Cycle**	**σ_{max} (MPa)**
A600-750-1-01	A	600	Air	1-1-1-1	750
A600-750-1-02	A	600	Air	1-1-1-1	750
A600-770-1-01	A	600	Air	1-1-1-1	770
A600-790-1-01	A	600	Air	1-1-1-1	790
A600-810-1-01	A	600	Air	1-1-1-1	810
A600-870-1-01	A	600	Air	1-1-1-1	870
B600-790-1-01	B	600	Air	1-1-1-1	790
B600-790-1-02	B	600	Air	1-1-1-1	790
B600-870-1-01	B	600	Air	1-1-1-1	870
B600-870-1-02	B	600	Air	1-1-1-1	870
B600-885-1-01	B	600	Air	1-1-1-1	885
B600-885-1-02	B	600	Air	1-1-1-1	885
B600-900-1-01	B	600	Air	1-1-1-1	900
B600-1000-1-01	B	600	Air	1-1-1-1	1000

Table 4.10: Tests performed to assess different values of applied σ_{max}.

4.6.3 Tests on Effect of Dwell at Maximum Load

Results from a previous study on U-notch specimens of extruded IN718 demonstrated that a dwell of 30 seconds at σ_{max} significantly increased the lifetime relative to a one second dwell under the same conditions [4.1, 4.5]. To see if this effect was also observed in IN718 disc material, tests were performed with 20 second or 30 second dwell at σ_{max}, as summarised in Table 4.11. Two tests were performed on Batch A specimens, the first with a dwell of 20 seconds and the second with a dwell of 30 seconds at σ_{max} = 750 MPa. In order to achieve a shorter specimen lifetime, two additional tests were performed on Batch B specimens, using a 20 second dwell at σ_{max} = 885 MPa. The results of these tests were compared with results for a 1-1-1-1 waveform under the same temperature and loading conditions. These are also summarised in Table 4.11.

Detailed Code	**Batch**	**Temp. (°C)**	**Environment**	**Cycle**	σ_{max} **(MPa)**
A600-750-20-01	A	600	Air	1-20-1-1	750
A600-750-30-01	A	600	Air	1-30-1-1	750
B600-885-20-01	B	600	Air	1-20-1-1	885
B600-885-20-02	B	600	Air	1-20-1-1	885
A600-750-1-01	A	600	Air	1-1-1-1	750
A600-750-1-02	A	600	Air	1-1-1-1	750
B600-885-1-01	B	600	Air	1-1-1-1	885
B600-885-1-02	B	600	Air	1-1-1-1	885

Table 4.11: Tests performed to assess the effect of dwell at σ_{max}.

4.6.4 U-notch Tests with Surface Replication

A group of tests was performed to monitor short crack initiation and growth in the U-notch root, using a cellulose acetate replication technique. The tests were performed at 600°C in air using 1-1-1-1 waveforms. Tests were interrupted every 500, 1000 or 2000 cycles to enable replicas to be taken. Each specimen was set up in three point bend and heated to 600°C at 20°C/min, followed by a 10 minute soak at 600°C. To minimise thermal stresses and prevent creep effects, all heating and cooling was performed with a small load of -1kN applied to the specimen. After the soak period, the load was increased to the required mean level for the test and 1-1-1-1 fatigue cycling was started. Once each block of cycles (500, 1000 or 2000 cycles) was complete, the applied load was reduced to -1kN and the specimen was cooled to room temperature. A surface replica of the notch root was taken using a pre-shaped piece of 3.5 mm thick cellulose acetate sheet softened in acetone (Figure 4.12). To enable better resolution of cracks on the replica, the specimen was held at an applied load of -10kN to produce some elastic crack opening. With an elastic stress concentration factor of 2.08, this produced a stress in the notch root of 812.5 MPa, approximately 325 MPa below the uniaxial yield stress of the material at room temperature. After taking a replica, the specimen was thoroughly cleaned to remove any traces of cellulose acetate, before heating back to 600°C for the next block of fatigue cycles. Preliminary trials demonstrated that it was extremely difficult to resolve cracks on replicas taken from as-broached U-notches. It was therefore necessary to polish the U-notch surface prior to testing. Specimens were mechanically polished to a 1 μm diamond finish. To minimise enlargement of the notch, which can occur during manual polishing, the specimens were clamped in a specially-designed jig and polished using soft 4mm diameter x 8mm long cylindrical dental felts mounted in a pillar drill.

In addition to the tests performed with replicas, uninterrupted tests were also performed on polished specimens under the same experimental conditions. The replica and polished notch tests are summarised in Table 4.12. Some duplicate tests were performed to evaluate experimental scatter.

Detailed Code	**Batch**	**Temp. (°C)**	**Environment & Special Conditions**	**Cycle**	σ_{max} **(MPa)**
A600-750-1-P-01	A	600	Air, polished notch	1-1-1-1	750
A600-750-1-PR-01	A	600	Air, polished notch, replicas	1-1-1-1	750
A600-790-1-P-01	A	600	Air, polished notch	1-1-1-1	790
A600-790-1-P-02	A	600	Air, polished notch	1-1-1-1	790
A600-790-1-P-03	A	600	Air, polished notch	1-1-1-1	790
A600-790-1-PR-01	A	600	Air, polished notch, replicas	1-1-1-1	790
B600-790-1-P-01	B	600	Air, polished notch	1-1-1-1	790
B600-885-1-R-01	B	600	Air, broached, replicas	1-1-1-1	885
B600-885-1-P-01	B	600	Air, polished notch	1-1-1-1	885
B600-885-1-PR-01	B	600	Air, polished notch, replicas	1-1-1-1	885
B600-885-1-PR-02	B	600	Air, polished notch, replicas	1-1-1-1	885

Table 4.12: Summary of U-notch tests performed with polished notches and those for which replicas were taken.

Replicas were analysed to quantify the number of cracks initiated with increasing fatigue cycles, to determine short crack growth rates and to study crack coalescence behaviour. Crack length measurements from replicas were made with the aid of a calibrated image analysis system connected to the microscope via a high resolution digital camera. These length measurements were then used to determine short crack growth rates.

4.7 Fractography on U-notch Specimens

4.7.1 Examination of Fracture Surfaces

Optical macro-scale examination of fracture surfaces was performed using a WILD Zoom macroscope. Simple observations were made of crack initiation and coalescence sites in support of the detailed SEM studies described in Section 4.7.2. Macroscopic observations were also used to measure crack aspect ratios and to examine the shape and area of the final fatigue fracture. Further examination of crack propagation paths and propagation modes was performed using an SEM.

4.7.2 Initiation Site Examination & Quantification

For those tests interrupted prior to fracture, the notch surface was systematically surveyed at 1000x magnification to detect and quantify initiated cracks. For all fractured specimens, the main fracture face was examined macroscopically and surveyed at 500x to 7500x magnification in an SEM to identify and quantify crack initiation sites. The number and type of crack initiation sites on the final fracture surfaces were recorded, using EDX where necessary to establish the chemical composition of particles and other features observed at crack initiation sites. To supplement the results available from study of acetate replicas, additional post-fracture SEM fractography was performed to examine crack initiation sites, crack coalescence sites and the paths taken by surface cracks in the notch root.

4.7.3 Fracture Surface Cross-Sections

Fracture surface cross-sections were prepared from selected specimens. One half of a fractured fatigue specimen was nickel plated to protect the surfaces and provide edge retention during metallographic polishing. (The other half of the specimen was retained in case further fractography was required on the as-tested surfaces). Vertical slices perpendicular to the main fracture face were cut using Electrostatic Discharge Machining (EDM). Typically, 6 slices per specimen were obtained using this technique. The orientation of the slices is shown in Figure 4.13. Slices were mounted in conducting phenolic resin to view the fracture face and U-notch in vertical cross-section. Each microsection was polished to 1μm diamond finish as described in Section 4.2.1. When required, microsections were etched. Microsections were examined in the as-polished and etched conditions, using optical microscopy, SEM and EDX.

4.8 Figures

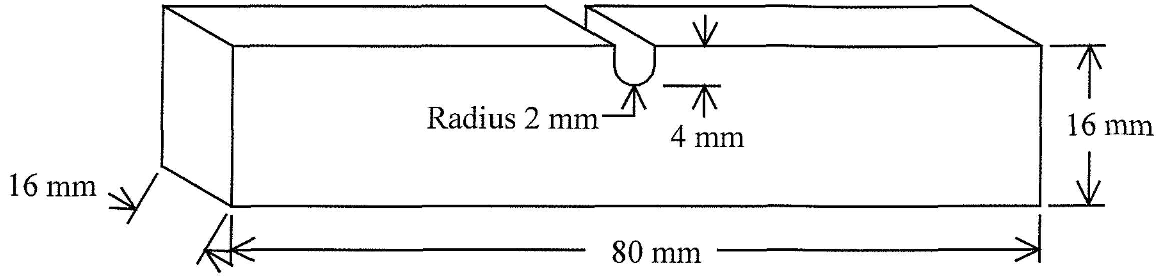

Figure 4.1: U-notch specimen geometry.

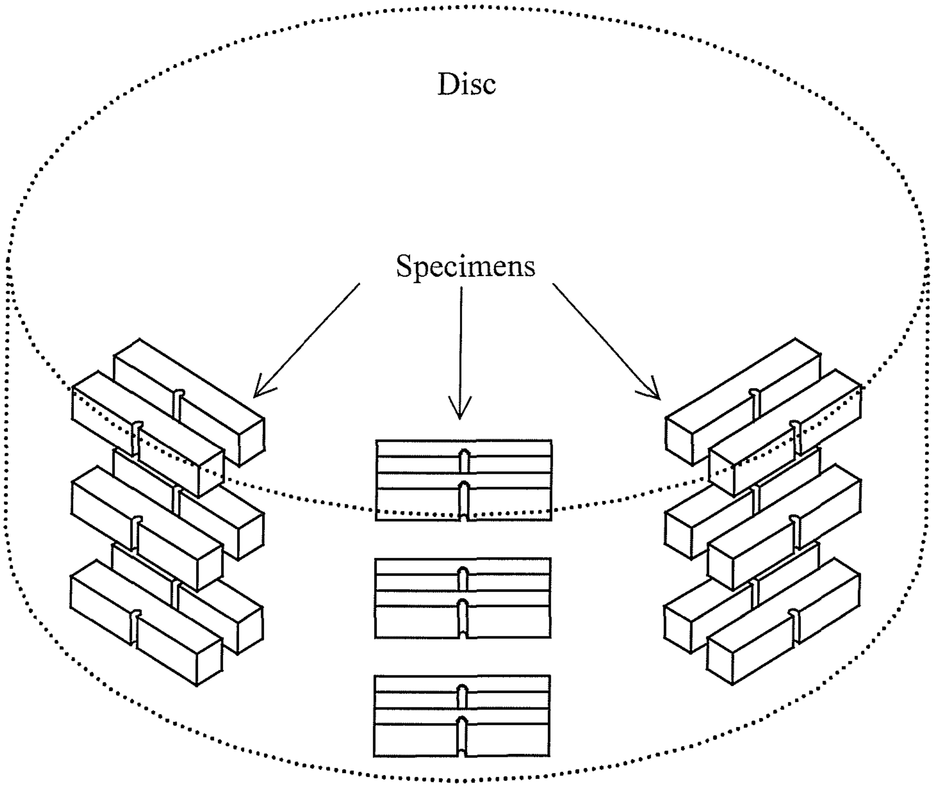

Figure 4.2: Orientation of U-notch specimens extracted from IN718 disc forging.

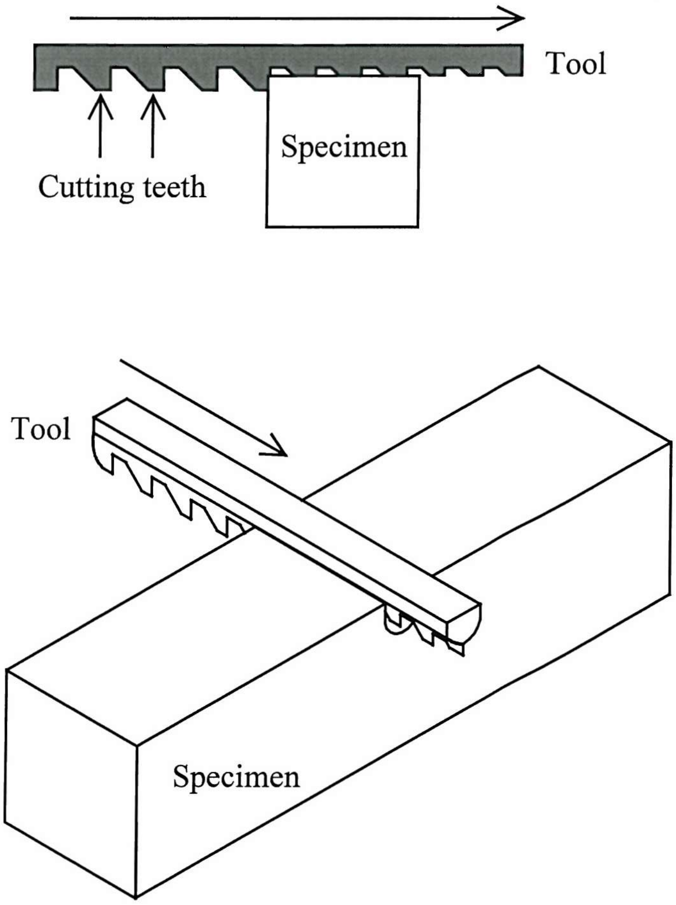

Figure 4.3: Schematic diagram of the broaching process used to produce the U-notches. A similar process is used for the fir tree root fixings in gas turbine disc rims.

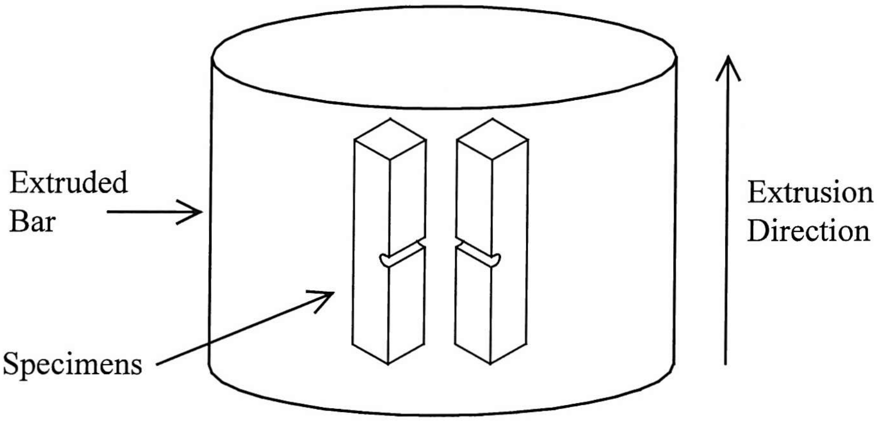

Figure 4.4: Orientation of U-notch specimens extracted from extruded bar of IN718.

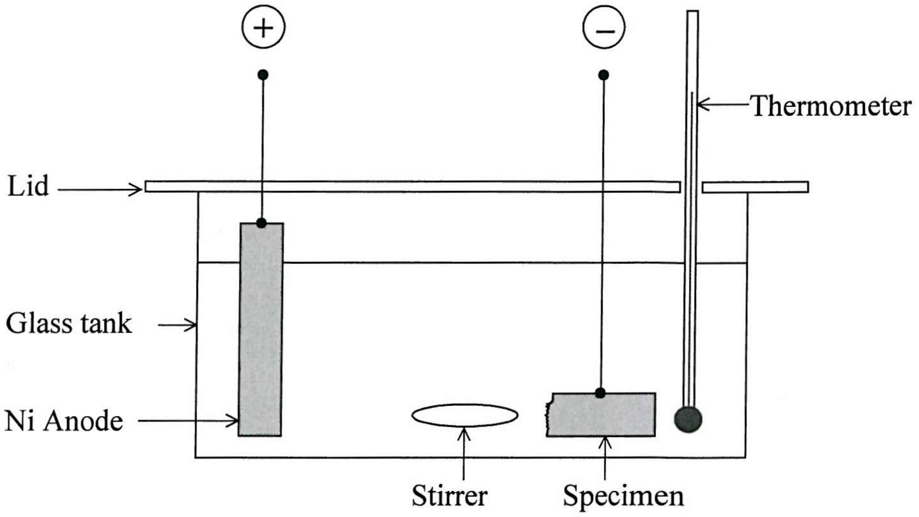

Figure 4.5: Nickel plating apparatus.

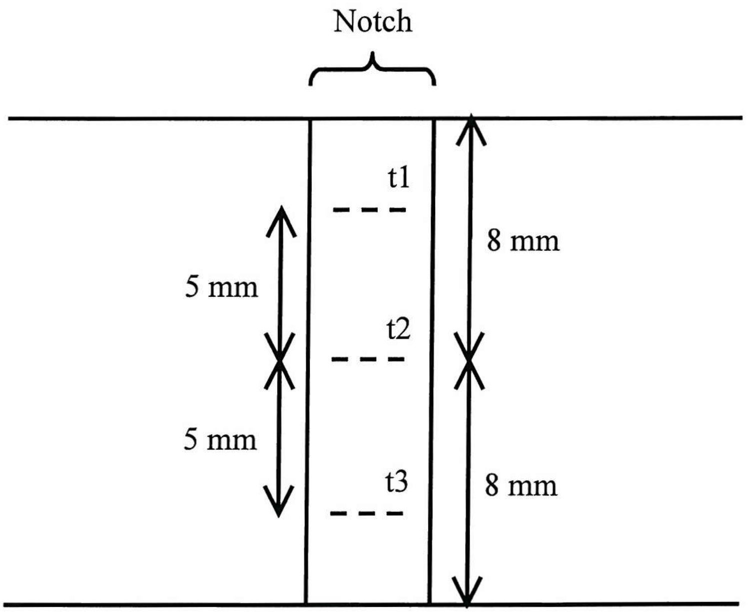

Figure 4.6: Surface roughness measurement locations.

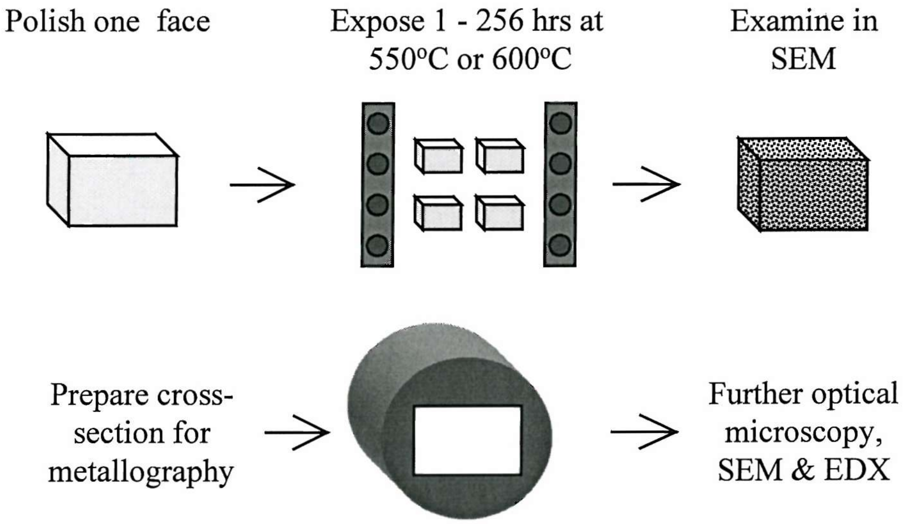

Figure 4.7: Schematic diagram of procedure for preparation and examination of thermal exposure samples.

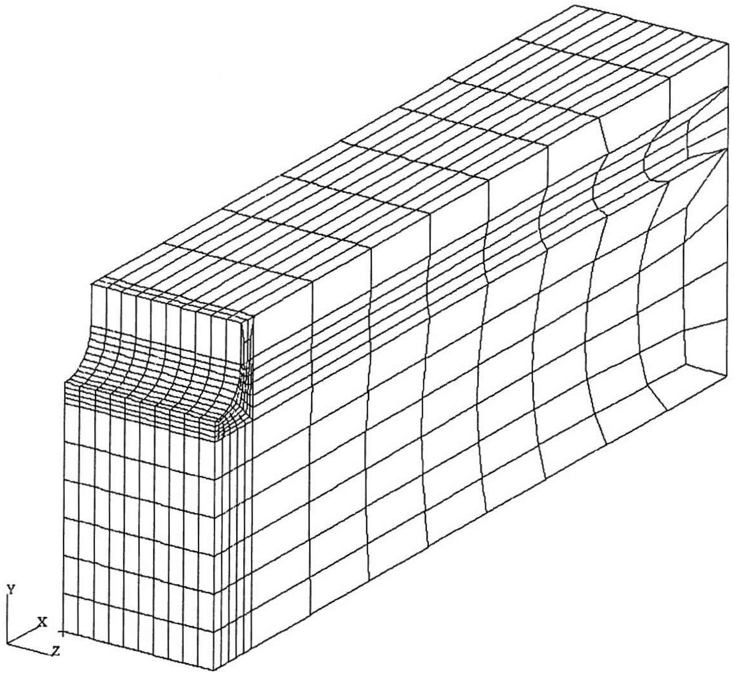

Figure 4.8: FE model of U-notch specimen.

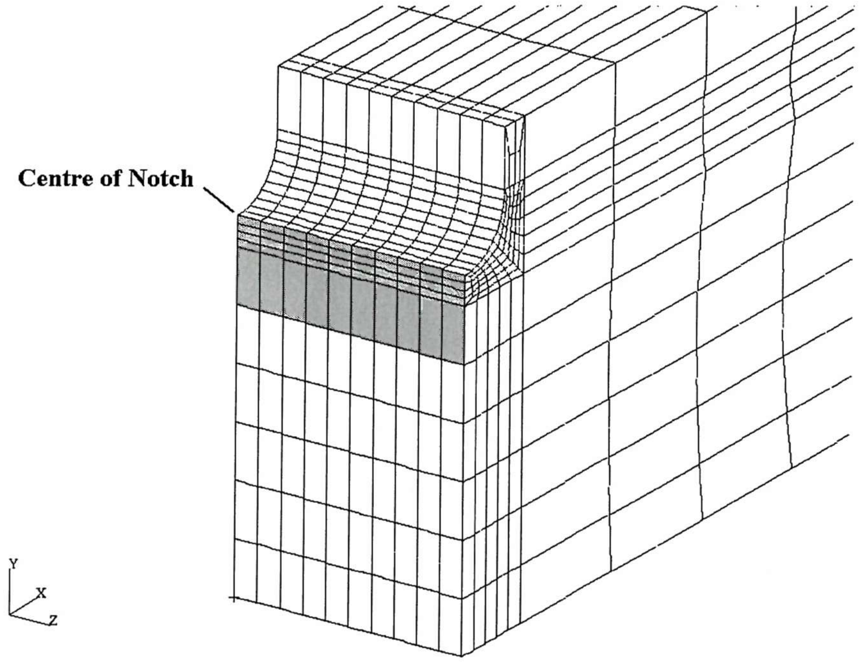

Figure 4.9: Detail of U-notch FE model. The shading shows the area considered for plastic zone size estimates.

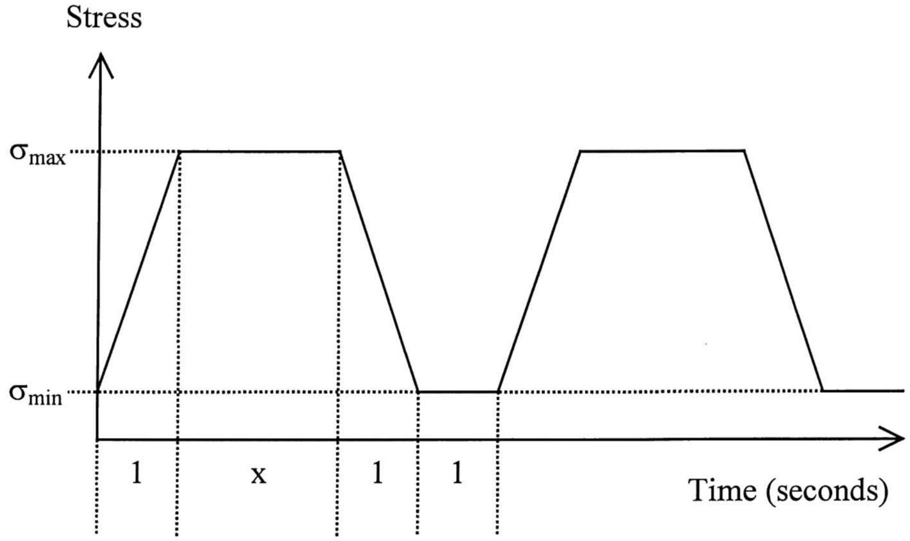

Figure 4.10: Trapezoidal waveform used for U-notch specimens. Dwell at maximum load x = 1, 20 or 30 seconds.

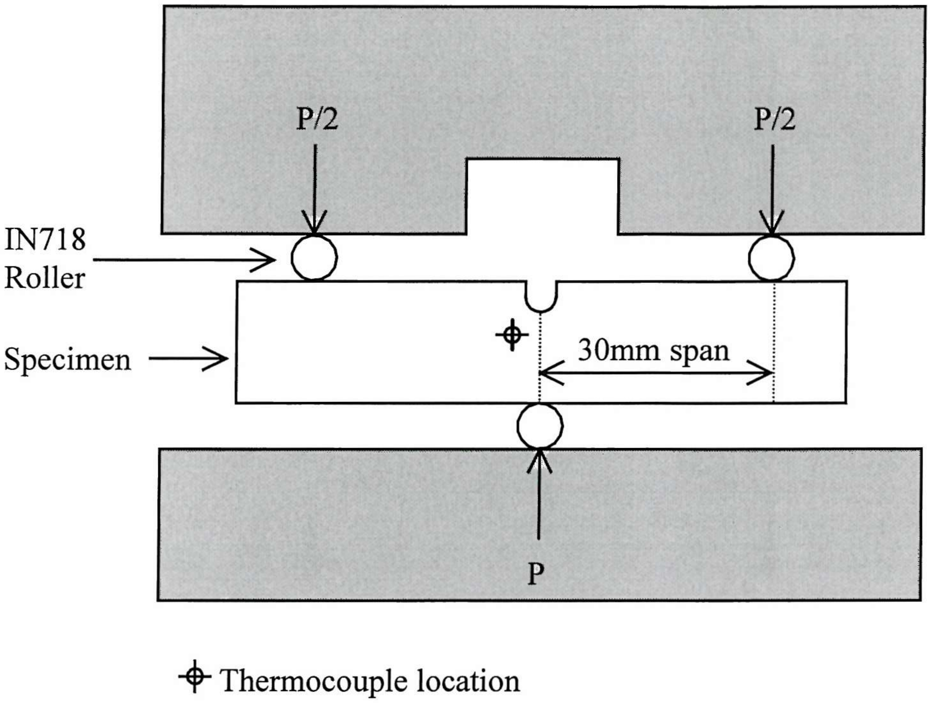

Figure 4.11: U-notch bend test specimen set-up.

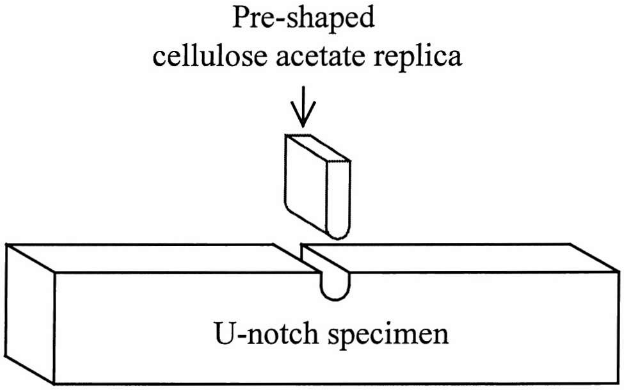

Figure 4.12: Shape of acetate replicas used for monitoring cracks in U-notch specimens.

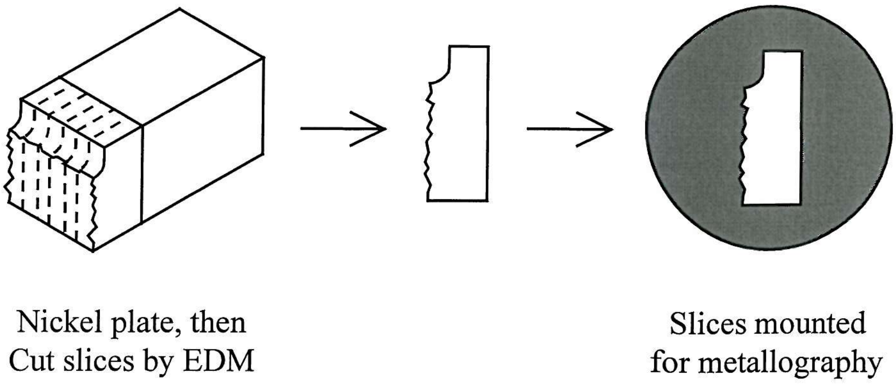

Figure 4.13: Slices taken from a fractured U-notch specimen for preparation of cross-sections.

4.9 References

[4.1] Reed P. A. S., Hachette F. & Thakar D. "Pump-priming project on crack initiation in Inconel 718" University of Southampton Department of Engineering Materials Report No. PR/RA/FH,DT/98/01/244 (1998)

[4.2] Neuber, H., Kerbspannungslehre, Springer, Berlin (1937) translated as: Theory of notch stresses, Edwards J. W., Ann Arbor, Michigan (1946)

[4.3] ASM Handbook, 10th Edition, Volume 16, Machining, Second printing, ASM International, Metals Park, Ohio, USA pp. 194-211 (1995)

[4.4] ASTM Standard E 112-96 "Standard test methods for determining Average Grain Size" American Society for Testing and Materials, West Conshohocken, PA, USA (1996)

[4.5] Reed P. A. S. Hachette F. Thakar D. Connolley T. & Starink M. J. "Creep-fatigue initiation and early crack growth in Inconel 718" Proc. 8th International Conference on Mechanical Behaviour of Materials (ICM8), Eds. Ellyin F. & Provan J. W., Fleming Printing Ltd. Victoria, BC, Canada, vol. 1 pp. 418-423 (1999)

[4.6] Reuchet J. & Remy L. "High temperature low cycle fatigue of MAR-M 509 Superalloy I: The influence of temperature on the low cycle fatigue behaviour from 20 to 1100°C" Mater. Sci. Engng. vol. 58 pp. 19-32 (1983)

[4.7] Reuchet J. & Remy L. "High temperature low cycle fatigue of MAR-M 509 Superalloy II: The influence of oxidation at high temperatures" Mater. Sci. Engng. vol. 58 pp. 33-42 (1983)

[4.8] Reuchet J. & Remy L. "Fatigue oxidation interaction in a superalloy - Application to life prediction in high temperature low cycle fatigue" Metall. Trans. A Vol.14 pp. 141-149 (1983)

[4.9] Reger M. & Remy L. "Fatigue oxidation interaction in IN100 superalloy" Metall. Trans. A vol. 19 pp. 2259-2268 (1988)

[4.10] Reger M. & Remy L. "High temperature, low cycle fatigue of IN 100 superalloy I: Influence of temperature on the low cycle fatigue behaviour" Mater. Sci. Engng. A vol. 101 pp. 47-54 (1988)

[4.11] Reger M. & Remy L. "High temperature, low cycle fatigue of IN 100 superalloy II: Influence of frequency and environment at high temperatures" Mater. Sci. Engng. A vol. 101 pp. 55-63 (1988)

[4.12] ASM Handbook, 10th Edition, Vol. 1 Properties and selection: Irons, steels and high-performance alloys, ASM International, Metals Park, Ohio, USA, p. 960 (1990)

[4.13] Scott P. M. & Thorpe T. W. "A critical review of crack-tip stress intensity factors for semi-elliptic cracks" Fatigue of Engng. Mater. & Struct. vol. 4 pp. 291-309 (1981)

[4.14] Moss S. J. Private Communication, ALSTOM Power (1998)

[4.15] Moss S. J., Private Communication, ALSTOM Power (2000)

5 RESULTS

The results presented in this chapter begin with the characterisation of the IN718 materials and specimens used in the study. Results of thermal exposure experiments are described next, followed by the results of the preliminary fatigue testing on plain bend bars. The main part of the study on U-notch specimens is then presented, starting with the FE modelling and moving on to the detailed description of fatigue lifetimes, crack initiation, short crack growth and coalescence at elevated temperatures.

5.1 Materials Characterisation

5.1.1 Microstructure

Optical microscopy, SEM and EDX on as-polished and etched specimens were used to characterise the microstructures of the two batches of disc material and the extruded bar material. Optical micrographs of the as-polished and etched microstructures are displayed in Figure 5.1 to Figure 5.3. In as-polished microsections of the two disc materials, the primary carbide particles were observed grouped in clusters (Figure 5.1a & Figure 5.2a). When viewed under an optical microscope, the primary carbides had a pale lilac colour. A small number of primary nitride particles were also observed. Primary nitrides were distinguishable from carbides by their gold colour and more angular morphology. Qualitative EDX showed the primary carbides in Batch A and Batch B material to be rich in Nb with some Ti, while primary nitrides were rich in Ti with some Nb present. Figure 5.4(a) shows an example EDX spectrum from a primary carbide in the Batch A disc material. The two disc materials had a non-equiaxed grain structure (Figure 5.1b & Figure 5.2b), with larger elongated grains (longest dimension approximately 20-70 μm) surrounded by extensive regions of small, more equiaxed grains (diameter approximately 5-10 μm). The larger grains were elongated in the tangential and radial directions, as would be expected for a forged disc. Grain boundaries were extensively decorated with δ (Ni_3Nb) phase particles of various morphologies, ranging from globular to almost continuous films. An EDX spectrum from a δ phase particle is shown in Figure 5.5, though due to the small size of the particle the spectrum contained a large contribution from the matrix as well. A reference spectrum from the adjacent matrix is plotted as the blue line in Figure 5.5. The morphology of the δ phase particles and primary carbides can be more clearly seen in the backscattered electron image in Figure 5.6(a). The bright particles along grain boundaries are δ phase. The larger particles are primary (Nb,Ti)C carbides. Both δ phase and (Nb,Ti)C appear bright in backscatter because they are rich in

Nb ($Z = 41$), resulting in a higher intensity of backscattered electrons than the surrounding Ni-rich matrix ($Z = 28$ for Ni). The mean linear intercept grain sizes for the tangential, radial and axial directions are listed in Table 5.1 and displayed as a chart in Figure 5.7(a). The elongation of the grains in the radial and tangential directions produced larger mean linear intercept grain sizes compared to the axial direction. There was no significant difference in grain size between Batch A and Batch B.

Direction	**Batch A**		**Batch B**	
	Mean Linear Intercept (μm)	**Standard Deviation***	**Mean Linear Intercept (μm)**	**Standard Deviation***
Tangential	10.8	1.4	9.6	0.6
Radial	10.8	0.4	11.5	0.8
Axial	6.3	0.6	6.7	0.8

Table 5.1: Mean linear intercept grain sizes, disc material. *Note the standard deviation is between the different areas assessed.

In the extruded bar material, primary carbides were observed running in bands along the original extrusion direction (see Figure 5.3a). Like the disc material, EDX studies indicated that the primary carbides were rich in Nb, with some Ti present, while the primary nitrides were rich in Ti, with some Nb present. The extruded bar material had an equiaxed grain structure (see Figure 5.3b) with a random distribution of small globular δ phase particles. The δ phase particles and primary carbides can be seen in the backscattered electron image Figure 5.6(b). The mean linear intercept grain sizes for the longitudinal, radial and transverse directions are listed in Table 5.2 and displayed as a chart in Figure 5.7(b).

Direction	**Mean Linear Intercept (μm)**	**Standard Deviation**[*]
Longitudinal (Extrusion Direction)	9.9	0.7
Radial	8.5	1.5
Transverse	9.7	0.7

Table 5.2: Mean linear intercept grain sizes, extruded bar material. [*]Note the standard deviation is between the different areas assessed.

The results of image analysis on polished microsections to determine the combined area fraction and sizes of primary carbide and nitride particles are given in Table 5.3. The volume fraction of primary nitrides was not separately determined, their occurrence being much less frequent than the primary carbides. Cumulative frequency size distributions of the particles for Batch A, Batch B and Extruded Bar material are displayed in Figure 5.8. The Batch A and Batch B disc materials exhibited very similar size distributions, while the cumulative frequency curve for the extruded bar material was shifted to smaller particle areas relative to the disc materials. This is consistent with the smaller mean particle diameter determined for the extruded bar material.

	Disc Batch A	**Disc Batch B**	**Extruded Bar**
Combined Area % of (Nb,Ti)C + (Ti,Nb)N particles	0.37	0.33	0.29
Mean equivalent circle particle diameter (μm)	7.8	7.6	6.7

Table 5.3: Combined area fraction and mean particle size of (Nb,Ti)C and (Ti,Nb)N particles in the IN718 materials studied.

5.1.2 Mechanical Properties

The available mean room temperature and high temperature mechanical property data for the IN718 disc material are given in Table 5.4. The tensile property data was provided by

ALSTOM Power, while the Vickers Hardness results are those measured on receipt of the U-notch specimens.

	Batch A			Batch B		
Temperature	**20 °C**	**600 °C**	**650 °C**	**20 °C**	**600 °C**	**650 °C**
σ_y **(MPa)**	1137	982	942	-	969	-
σ_{UTS} **(MPa)**	1411	-	1149	-	1219	-
Elongation (%)	19.3	-	30.92	-	21.9	-
$H_{v(30\ kg)}$	441	-	-	434	-	-

Table 5.4: Available tensile property data for the IN718 disc material.

No tensile property data were available for the IN718 extruded bar material. Its mean Vickers hardness was $H_{v\,(30kg)} = 443$.

Hardness checks on selected U-notch specimens after high temperature fatigue testing showed there was no change in hardness as a result of the time spent at test temperature.

5.1.3 Surface Roughness of U-notches

Mean R_a and R_v data for Batch A and Batch B of the U-notch specimens are given in Table 5.5. Batch A data are the average of 45 measurement runs (3 runs per specimen on 15 specimens). Batch B data are the average of 66 measurement runs (22 specimens). The polished specimen data are the average of 3 measurement runs (1 specimen). Maximum R_v values are also listed, to give an indication of the maximum broaching mark depth in each batch. The data show that the notches in Batch B specimens were rougher than those in Batch A. This can be seen in the plot of R_a values for individual specimens displayed in Figure 5.9. Polishing of the U-notches achieved a large reduction in surface roughness.

	Batch A	**Batch B**	**Polished Specimen (Batch B no. 15)**
Mean R_a **(μm)**	0.1607 (0.0202)	0.4011 (0.0803)	0.0053 (0.0004)
Mean R_v **(μm)**	0.7960 (0.1567)	1.7574 (0.4369)	0.0258 (0.0086)
Max. R_v **(μm)**	2.1582	3.1157	0.0357

Table 5.5: Mean surface roughness data for as-broached notch surfaces. Standard deviations are given in brackets.

Metallographic sections through the notches of as-broached specimens revealed a difference in the sub-surface microstructure of the notch between Batch A and Batch B. The micrographs in Figure 5.10 illustrate this. In Batch A, a sub-surface layer was observed which had the appearance of a zone of heavy localised deformation (Figure 5.10a). This extended all the way round the surface of the U-notch. The thickness of the layer was between 10-16 μm in the notch root and up to 40 μm on the notch sides. No deformation layer was observed on the other machined surfaces of the Batch A specimens, only the broached notch surface. In Batch B, a deformation layer was not observed in the broached notch (Figure 5.10b) or on the other machined surfaces. Examination of polished specimens showed that the deformation layer was still present in Batch A after polishing, though its depth in the notch root was reduced to approximately 7-10 μm.

Following discovery of the deformation layer in Batch A specimens, microhardness measurements were performed on cross-sections to establish if the layer exhibited signs of work hardening. This proved difficult because of the requirement to produce an indent small enough to be entirely within the deformation layer, but with a test mass large enough to give a true representation of hardness. A compromise was found by using a test mass of 200 g. Twenty near-surface measurements were performed with indents located 20 μm below the notch surface. For the Batch A specimen, indents were located in the deformation layer on the notch sides. These were compared with measurements made on bulk material several millimetres below the surface, and with measurements made in similar locations on a Batch B specimen. The results of the microhardness tests are given in Table 5.6 and plotted in Figure 5.11. The error bars in Figure 5.11 represent the 95% confidence intervals. The mean Vickers microhardness in the surface layer of the Batch A specimen was approximately 15% higher than that for the bulk material, indicating that the material had been work hardened by the broaching process. This may be an underestimate, due to the effect on hardness readings of the reduced constraint near the specimen surface. No evidence of work hardening was found in the Batch B specimen. The apparently softer Batch B surface hardness relative to the bulk value was probably due to reduced constraint near the specimen surface.

	Batch A		**Batch B**	
	Mean Vickers Microhardness	**Standard deviation**	**Mean Vickers Microhardness**	**Standard deviation**
Near surface	454	23	371	15
Bulk material	394	8	391	9

Table 5.6: Results of Vickers Microhardness tests to determine if work hardening had occurred in deformation layer observed in Batch A U-notch specimens.

5.2 Thermal Exposure Experiments

Oxidation of (Nb,Ti)C primary carbides occurred readily in the unstressed samples exposed at 550°C and 600°C. Oxidation of the carbides resulted in the formation of characteristic surface eruptions, which were clearly visible using an SEM. On the surfaces polished prior to exposure, the eruptions were often tower-like in appearance when viewed side-on. Examples of such towers are shown in Figure 5.12(a) & (b), where the eruptions appear to consist of a series of stacked layers or flakes. Other more irregular eruptions (Figure 5.13) were observed on polished and as-machined faces of specimens. EDX showed that the eruptions were rich in Nb, confirming that the eruptions were oxidised primary carbides. The results of quantitative EDX analysis of one of the eruptions in Figure 5.13(a) are listed in Table 5.7 and the EDX spectrum is shown in Figure 5.14. The results in Table 5.7 and the spectrum show the eruption to be rich in Nb, confirming it was formed by oxidation of an (Nb,Ti)C particle. The presence of Cr, Fe, Co and Ni in the spectrum probably arises from a contribution from the surface oxide layer of the alloy, usually a mixture of Cr_2O_3 and spinel-type $Ni(Fe,Mo,Cr)_2O_4$ [5.1, 5.2].

Element	Atomic %
C	21.5
O	51.5
Al	0.2
Ti	2.7
Cr	5.3
Fe	2.2
Co	0.1
Ni	4.7
Mo	1.6
Nb	10.2

Table 5.7: Quantitative EDX analysis of a surface eruption formed on an IN718 sample exposed in air for 32 hours at 550°C.

Metallographic sections through the thermal exposure specimens enabled observation of the sub-surface oxidation behaviour using optical and scanning electron microscopy. Under BEI conditions, unoxidised primary carbides appeared bright relative to the matrix because of their high niobium content, and hence higher atomic number contrast relative to the nickel-based matrix. Oxidised primary carbides appeared dark grey in BEI, because of the lower number of Nb atoms per unit volume after incorporation of oxygen to form the oxide. This clear BEI contrast difference aided identification of unoxidised and oxidised primary carbide particles. BEI also revealed the location of δ (Ni_3Nb) phase particles. In most cases, only primary carbides which intersected the surface underwent oxidation. The size of carbides observed ranged from 3-17 μm. For short exposure times up to 16 hours, some partial oxidation of primary carbides was seen. The depth to which the particles were oxidised increased with increasing exposure times. For exposure times longer than 16 hours, complete oxidation of surface-intersecting carbides was observed. It was not possible to reliably determine the oxidation kinetics of the primary carbides in terms of a rate equation, primarily because of the low frequency with which partially oxidised carbides were observed in microsections.

Sometimes, localised matrix deformation was observed in the vicinity of the oxidised particles, as shown in Figure 5.15(a) and (b). This deformation was most noticeable on surfaces polished prior to exposure, where the polishing provided a flat reference plane against which any localised deformation due to thermal exposure stood out. Occasionally, partial or complete oxidation of sub-surface primary carbides was observed. This was only observed in specimens exposed for 128 hours or more at 550°C or 600°C. Bulges in the matrix were seen above the oxidised particles, examples of which are shown in Figure 5.15(c)-(e). However, other sub-surface carbides at the same depth below the surface (2-3μm) remained unoxidised, as shown in Figure 5.15(f). The results of quantitative EDX analysis of the oxidised sub-surface particle shown in Figure 5.15(c) are listed in Table 5.8. For comparison purposes, an analysis taken from the nearby matrix under the same conditions is also listed in the table. The particle and matrix spectra are plotted together in Figure 5.16. The oxidised particle was rich in Nb, indicating it was originally an (Nb,Ti)C primary carbide. The presence of oxygen in the particle spectrum but not the matrix spectrum shows the particle had oxidised. EDX is not very reliable for the quantification of light elements like carbon and oxygen, but the results confirm the oxidation of the primary carbide to some form of niobium-rich oxide, possibly Nb_2O_5.

Element	**Oxidised Particle at. %**	**Matrix at. %**
C	46.1	25.4
O	35.6	0
Al	0.1	0.5
Ti	3.2	0.8
Cr	0.4	13.9
Fe	0.6	15.3
Co	0.1	0.1
Ni	1.3	41.1
Mo	1.4	1.2
Nb	11.2	1.6

Table 5.8: EDX analysis of an oxidised sub-surface (Nb,Ti)C primary carbide particle. An analysis from the nearby matrix is included for comparison purposes.

5.3 Fatigue Testing of Plain Bend Bars

5.3.1 Room Temperature Testing

The results in Table 5.9 show that thermal exposure to promote the oxidation and eruption of carbides had no significant effect on fatigue lifetimes at room temperature. For all the specimens, cracks were first observed on the replicas taken after 20000 cycles. Generally, it was the cracks which initiated early on in the fatigue life (15 - 30% N_f) which grew to form the dominant cracks leading to final fracture.

Specimen Code	**Prior Treatment**	**Fatigue Life N_f (cycles)**	**No. of cycles N_i, to first observed crack**
P1	Polished	121221	20000
P2	Etched	Not available. Test malfunctioned	Not available
P3	Polished, exposed 4hrs at 600°C	104921	20000
P4	Etched, exposed 4hrs at 600°C	128158	20000

Table 5.9: Summary of extruded IN718 plain bend bar fatigue lifetimes.

In the case of the as-polished specimens, initiation was characterised as occurring either at a particle (i.e. a carbide or nitride) or intrinsically due to slip band cracking. For the thermally exposed specimens, three types of initiation site were characterised; either an erupted particle, a non-erupted particle or intrinsic initiation along a slip band. There was a marked contrast in initiation site type between the as-polished specimen P1 and the thermally exposed specimen P3. Figure 5.17 shows the cumulative number of cracks counted on acetate replicas, grouped by initiation site type. In the as-polished specimen, the majority of cracks initiated at carbide or nitride particles. An example of this type of initiation can be seen in Figure 5.18. For the thermally exposed specimen, most of the cracks counted appeared to nucleate intrinsically (see Figure 5.19), with only a few initiating at carbide eruptions (see Figure 5.20). This behaviour indicates that for these plain bend bars tested at room temperature, erupted carbides were not effective as fatigue crack initiators.

For both specimens the number of cracks counted fluctuated later in the fatigue life, due to crack coalescence. For example, two cracks counted on one replica may have coalesced to form a single crack on the next replica in the sequence.

There was some concern about possible damage to erupted carbides caused by the acetate replication technique. Study of the sequence of replicas taken from specimens P3 and P4 showed that eruptions were consistently reproduced on the replicas, despite the large number of replicas taken. In the process of each fatigue test, up to thirty replicas were taken on each specimen. If replica quality was poor due to air bubbles or slippage, the process was repeated. SEM examination of specimen P3 and P4 showed there was some damage to eruptions, consisting mostly of removal of the more friable material standing proud of the surface.

The convention used for describing the length of surface cracks is shown in Figure 5.21. Surface cracks were defined as having a total length 2*c*, divided into two segments c_1 and c_2. Segment c_1 was the distance from the first crack tip to the middle of the initiation site and c_2 the distance from the second crack tip to the middle of the initiation site, so that $2c = c_1 + c_2$.

Although it is known that linear elastic fracture mechanics are not strictly applicable to short cracks, it is still useful to derive a crack growth driving force in terms of the stress intensity factor range ΔK so that short crack growth rates can be compared with long crack data. For semi-elliptical crack geometries like that shown in Figure 5.21, the analytical solutions reviewed by Scott & Thorpe [5.3] were used. Scott & Thorpe considered the case of a semi-elliptical crack of length *2c* and depth *a* in a plate of thickness *t*. For the case of pure bending the two main expressions used to calculate the Mode I stress intensity factors at the surface ($\theta = 0$) and at maximum depth ($\theta = \pi/2$) are:

$$K_{surface} = \left[\left[M_{f(0)}\left(1-0.3\frac{a}{t}\right)\left(1-\left(\frac{a}{t}\right)^{12}\right)\right]+\left[0.394\cdot E(k)\left(\frac{a}{t}\right)^{12}\sqrt{\frac{c}{a}}\right]\right]\frac{\sigma_b}{E(k)}\sqrt{\pi a} \qquad \text{Eqn. 5.1}$$

$$K_{depth} = M_{f(\pi(2)}\left[1-1.36\left(\frac{a}{t}\right)\left(\frac{a}{c}\right)^{0.1}\right]\frac{\sigma_b}{E(k)}\sqrt{\pi a} \qquad \text{Eqn. 5.2}$$

where σ_b is the bending stress. $M_{f(0)}$ and $M_{f(\pi/2)}$ are front face correction factors given by:

$$M_{f(0)} = \left[1.21 - 0.1\left(\frac{a}{c}\right) + 0.1\left(\frac{a}{c}\right)^4\right]\sqrt{\frac{a}{c}}$$ Eqn. 5.3

$$M_{f(\pi/2)} = 1.13 - 0.07\left(\frac{a}{c}\right)^{0.5}$$ Eqn. 5.4

E(k) is an approximation of an elliptical integral of the second kind given by:

$$E(k) = \left[1 + 1.47\left(\frac{a}{c}\right)^{1.64}\right]^{0.5}$$ Eqn. 5.5

Short crack growth rates measured from acetate replicas are displayed in Figure 5.22. Here, the average surface crack growth rate *dc/dN* is plotted against the surface stress intensity factor range calculated from Eqn. 5.1. No long crack growth rate data are available for the extruded bar material, but as a comparison, typical IN718 long crack data (*da/dN* vs. ΔK) from Mercer et al. [5.4] are also plotted on the graph. There was no appreciable difference in short crack growth rate between the unexposed and exposed specimens. The extruded bar crack growth rates exhibited behaviour typical of short cracks, namely growth at ΔK values below the threshold for long crack growth and fluctuations/arrests in growth rate. Crack propagation was transgranular, with deflections occurring at grain boundaries. The fluctuations in crack growth rate became less pronounced at higher ΔK values, suggesting a transition to Stage II crack growth at longer crack lengths. At low ΔK, the short crack growth rates were higher than the long crack rate, while at higher ΔK, the short crack growth rates converged with the long crack behaviour.

5.3.2 High Temperature Testing

Crack initiation was not observed in either of the two polished plain bend bars of disc material tested at 600°C. Test PB1 ran for 100000 cycles using a 1-1-1-1 waveform at 600°C, with a maximum stress of 930 MPa. No crack initiation was observed. No further testing was performed on this specimen, as it was decided to try and establish the lifetime using a shorter duration, high frequency test at 600°C, using Test PB2.

Test PB2 reached 400000 cycles at 10 Hz without any signs of crack initiation, despite incrementing σ_{max} to 1180 MPa. The waveform was then changed to a trapezoidal 1-1-1-1 cycle. It was decided not to increase the maximum stress above 1180 MPa because this was close to the estimated ultimate tensile strength at 600°C. The test ran for an additional 81750 cycles using the 1-1-1-1 waveform without any signs of crack initiation.

Bearing in mind the lack of crack initiation in Tests PB1 and PB2 tested at 600°C, two room temperature tests, labelled PB3 and PB4 were performed to see if residual surface compressive stresses arising from machining and polishing were preventing crack initiation at high temperature.

Test PB3 suffered an accidental overload to 1184 MPa during set-up and fractured after 69234 cycles at 10 Hz, with σ_{max} = 1080 MPa (95% σ_y at 20°C). Strong slip bands were observed on the specimen surface after fracture. The main crack which caused failure initiated at one edge of the specimen, rather than on the polished surface.

Test PB4 failed after a total of 139,253 cycles. The first 100000 cycles were performed at a σ_{max} of 1080 MPa (95% σ_y), with the remainder at a higher σ_{max} of 1126 MPa (99% σ_y). The main crack which caused failure initiated between 120000 and 125000 cycles at one edge of the specimen, rather than on the polished surface. This limited the value of the test for the observation of crack initiation at microstructural features. However, back-checking of replicas showed that a small crack had initiated at a carbide on the polished surface after 10000 cycles.

The high temperature plain bend bar tests were primarily intended as a back-up in case the U-notch tests were unsuccessful. Following successful completion of a number of U-notch tests, it was considered unnecessary to conduct further experiments on plain bend bars.

5.4 FE Modelling Results

The FE modelling was performed to support the high temperature U-notch test programme. The results of FE modelling will be described first before going on to describe the U-notch tests themselves.

5.4.1 General Observations

Contour plots of the von Mises stress in the notch root after the first loading step are shown in Figure 5.23(a) & (b). (a) shows the elastic case and (b) shows the elastic-plastic case for an applied nominal σ_{max} of 750 MPa. The stress concentration effect of the notch is evident in both the elastic and elastic-plastic cases. IN718 is a material which cyclically softens and this was taken into account by the elastic-plastic FE model. The predicted cyclic softening effect can be seen by comparing the von Mises stress after the first loading step with the von Mises stress after the tenth loading step, shown in Figure 5.24(a) & (b).

5.4.2 Predicted Strain Amplitudes

The variation in predicted total strain amplitude ε_{amp} with applied stress amplitude σ_{amp} after 10 cycles is displayed in Figure 5.25. A linear regression fit to the data follows the equation:

$$\varepsilon_{amp} = 0.001202\sigma_{amp} - 0.08386 \qquad \text{Eqn. 5.6}$$

The largest contribution to the strain amplitude in the notch root came from elastic deformations.

5.4.3 Predicted Elastic Stress Concentration Factor

Figure 5.26 shows the predicted σ_{xx} component of stress in the notch root for the elastic model at a maximum nominal stress of 750 MPa. The maximum predicted value of σ_{xx} was 1560 MPa at the centre of the notch surface, resulting in a theoretical elastic stress concentration factor of 2.08. This compares with a value of 2.23 estimated by Reed et al. [5.5] when the specimens were first designed, and a value of 2.05 estimated using curves published in ESDU Data Item No. 69020 [5.6]. A stress concentration factor of 2.08 will be assumed for all subsequent discussion in this thesis.

5.4.4 Predicted Plastic Zone Depths

Contour plots of equivalent plastic strain in the U-notch root are displayed in Figure 5.27 (a) & (b) for a maximum nominal applied stress of 750 MPa and 885 MPa respectively. The plots show the results after 10 cycles. The contours illustrate a substantial increase in plastic zone depth at the higher stress level. Using the 0.2% plastic strain contours, the plastic zone depth at the notch centre is approximately 0.185 mm for σ_{max} = 750 MPa, 0.24 mm for σ_{max} = 790 MPa (not illustrated) and 0.41 mm for σ_{max} = 885 MPa. Note the predicted decrease in plastic zone depth near the free surface at the side of the specimen (6-8 mm from the notch centre).

5.5 High Temperature Fatigue Lives of U-notch Specimens

5.5.1 Temperature and Environment Effects

Fatigue lifetimes (N_f = life to fracture) are listed in Table 5.10. Testing at 550°C with a 1-1-1-1 waveform in air produced a modest reduction in fatigue lifetime compared with testing in vacuum. Increasing the test temperature to 600°C with a 1-1-1-1 waveform reduced the fatigue lifetime in air considerably compared with the 550°C air test. Testing in vacuum at 600°C also reduced the fatigue life substantially compared to the 550°C vacuum test.

Detailed Code	**Batch**	**Temp. (°C)**	**Environment**	**Cycle**	σ_{max} **(MPa)**	N_f **(cycles)**
A550-750-1-01	A	550	Air	1-1-1-1	750	137819
A600-750-1-01	A	600	Air	1-1-1-1	750	25311
A550-750-1-V-01	A	550	Vacuum	1-1-1-1	750	160938
A600-750-1-V-01	A	600	Vacuum	1-1-1-1	750	53412

Table 5.10: Fatigue lifetimes for preliminary tests studying effect of temperature and environment.

5.5.2 Effect of Stress Level

Fatigue life results for 1-1-1-1 tests at 600°C in air on as-broached specimens are listed in Table 5.11. The results are also displayed as stress-life and strain-life curves in Figure 5.28(a) & (b). In Figure 5.28(b), lifetimes are plotted against the total strain amplitude predicted by the FE model. The data for each Batch have been fitted to the Coffin-Manson relationship given in Eqn. 4.9.

It is apparent from the graphs in Figure 5.28 that the Batch B specimens exhibited longer fatigue lives than Batch A samples under similar test conditions. Figure 5.28(b) also includes Coffin-Manson curves representing aggregate data provided by ALSTOM Power [5.7]. Note the ALSTOM data were not for U-notch specimens, but were from a variety of tests at 600°C on IN718 disc material. They are included in Figure 5.28(b) to show how the Southampton U-notch results compare with ALSTOM's database of IN718 fatigue performance. The mean curve and statistical minimum curve (mean minus three standard deviations) are shown. The Coffin-Manson curves for the U-notch specimens are shallower than the ALSTOM mean curves and show shorter lifetimes at high values of ε_{amp} but tend towards similar lifetimes at lower ε_{amp}.

Detailed Code	**Batch**	**Temp. (^oC)**	**Environment**	**Cycle**	σ_{max} **(MPa)**	σ_{amp} **(MPa)**	N_f **(cycles)**
A600-750-1-01	A	600	Air	1-1-1-1	750	337.5	25311
A600-750-1-02	A	600	Air	1-1-1-1	750	337.5	20802
A600-770-1-01	A	600	Air	1-1-1-1	770	346.5	27538
A600-790-1-01	A	600	Air	1-1-1-1	790	355.5	8792
A600-810-1-01	A	600	Air	1-1-1-1	810	364.5	4329
A600-870-1-01	A	600	Air	1-1-1-1	870	391.5	3886
B600-790-1-01	B	600	Air	1-1-1-1	790	355.5	90327
B600-790-1-02	B	600	Air	1-1-1-1	790	355.5	40440
B600-870-1-01	B	600	Air	1-1-1-1	870	391.5	19856
B600-870-1-02	B	600	Air	1-1-1-1	870	391.5	19010
B600-885-1-01	B	600	Air	1-1-1-1	885	398.25	5016
B600-885-1-02	B	600	Air	1-1-1-1	885	398.25	9889
B600-900-1-01	B	600	Air	1-1-1-1	900	405	4475
B600-1000-1-01	B	600	Air	1-1-1-1	1000	450	2153

Table 5.11: Fatigue lifetimes for 1-1-1-1 tests at 600°C in air performed to assess the effect of σ_{max}.

5.5.3 Effect of Dwell on Fatigue Life

Results showing the effect of dwell at maximum load at 600°C in air are listed in Table 5.12 and displayed graphically in Figure 5.29. For Batch A specimens tested with σ_{max} = 750 MPa, there was a beneficial effect on fatigue life of increasing dwell at maximum load. A 1-20-1-1 cycle increased the fatigue life by a factor of 2 compared to a 1-1-1-1 cycle and a 1-30-1-1 cycle increased the fatigue life by a factor of 3. These results show the same trend as that found in a study of U-notch specimens of extruded IN718 under the same conditions [5.5, 5.8]. In that study, a 1-30-1-1 cycle gave a life to fracture of 11891 cycles compared with 4603 cycles for a 1-1-1-1 waveform. However, no such beneficial effect of dwell was observed for Batch B specimens tested at a substantially higher load level of σ_{max} = 885 MPa (see Table 5.12 and Figure 5.29). Here, a 20 second dwell was detrimental to the fatigue life.

Detailed Code	**Batch**	**Temp. (°C)**	**Environment**	**Cycle**	σ_{max} **(MPa)**	N_f **(cycles)**
A600-750-1-01	A	600	Air	1-1-1-1	750	25311
A600-750-1-02	A	600	Air	1-1-1-1	750	20802
A600-750-20-01	A	600	Air	1-20-1-1	750	50756
A600-750-30-01	A	600	Air	1-30-1-1	750	71768
B600-885-1-01	B	600	Air	1-1-1-1	885	5016
B600-885-1-02	B	600	Air	1-1-1-1	885	9889
B600-885-20-01	B	600	Air	1-20-1-1	885	4541
B600-885-20-02	B	600	Air	1-20-1-1	885	4321

Table 5.12: Effect of dwell at maximum load on fatigue lifetime.

5.5.4 Polished Notch and Replica Tests

Lifetimes to fracture of tests performed with polished notches and those tests for which replicas were taken are listed in Table 5.13. Note test A600-790-1-P-01 was accidentally overloaded during test set-up. It was decided to continue with the test to see what the effect of the overload would be. The specimen reached 123100 cycles without any signs of crack initiation. No further fatigue testing was performed on this specimen.

For uninterrupted tests on Batch A specimens at σ_{max} = 750 MPa or σ_{max} = 790 MPa, polished notches produced longer lifetimes to fracture than as-broached notches under the same test conditions. This is illustrated in the bar chart in Figure 5.30(a). Where results of two tests under the same conditions were available, the average value has been plotted. The beneficial effect of notch polishing was also observed for Batch B specimens tested at σ_{max} = 885 MPa, as shown in Figure 5.30(b). However, Figure 5.30(b) shows that test B600-790-1-P-01 performed at σ_{max} = 790 MPa had a shorter life than as-broached Batch B specimens performed under the same conditions. Fractographic examination of test B600-790-1-P-01 showed that a crack had initiated at a sub-surface (Ti,Nb)N particle.

The fatigue life results in Table 5.13 and Figure 5.30 indicate that interrupting the tests to take replicas may have reduced the fatigue life compared to uninterrupted tests at σ_{max} = 750 MPa and 885 MPa, though this effect was not apparent for Batch A at σ_{max} = 790 MPa.

Detailed Code	**Batch**	**Temp. (°C)**	**Environment & Special Conditions**	**Cycle**	**σ_{max} (MPa)**	**N_f (cycles)**
A600-750-1-P-01	A	600	Air, polished notch	1-1-1-1	750	169413
A600-750-1-PR-01	A	600	Air, polished notch, replicas	1-1-1-1	750	51279
A600-790-1-P-01	A	600	Air, polished notch	1-1-1-1	790	over-loaded
A600-790-1-P-02	A	600	Air, polished notch	1-1-1-1	790	13420
A600-790-1-P-03	A	600	Air, polished notch	1-1-1-1	790	87327
A600-790-1-PR-01	A	600	Air, polished notch, replicas	1-1-1-1	790	51687
B600-790-1-P-01	B	600	Air, polished notch	1-1-1-1	790	28510
B600-885-1-R-01	B	600	Air, broached, replicas	1-1-1-1	885	5157
B600-885-1-P-01	B	600	Air, polished notch	1-1-1-1	885	19605
B600-885-1-PR-01	B	600	Air, polished notch, replicas	1-1-1-1	885	13591
B600-885-1-PR-02	B	600	Air, polished notch, replicas	1-1-1-1	885	7939

Table 5.13: Fatigue lifetimes for tests with polished notches and tests for which replicas were taken.

5.5.5 Strain-Life Results: All Specimens

Selected strain-life data has already been presented in Figure 5.28(b), comparing Batch A and Batch B U-notch specimens tested under the same conditions of waveform (1-1-1-1), temperature (600°C), environment (air) and notch surface condition (as-broached). For completeness, a strain-life plot for all U-notch tests at 600°C is shown in Figure 5.31. The Batch A and Batch B results for all specimens were re-fitted to the Coffin-Manson relationship, and aggregate IN718 data from ALSTOM are shown for comparison. Considering the variety of experimental conditions used, the majority of the U-notch results lie within the scatter band bounded by the ALSTOM mean and statistical minimum life curves (mean minus three standard deviations). However, as previously described in Section 5.5.2, the U-notch Coffin-Manson curves are shallower than the ALSTOM curves, showing shorter lives than the ALSTOM data at high strain amplitudes but tending to similar lives as the ALSTOM data at lower strain amplitudes.

5.6 Crack Initiation in U-notch Specimens

Selected tests were interrupted, because the end of the available test machine time had been reached. In such cases, the unfailed specimens were examined for cracks using an SEM before resuming testing. All specimens were examined after fracture to investigate crack initiation. The replica studies performed on polished specimens enabled study of crack initiation behaviour as the tests progressed. The results of crack initiation observations on Batch A and Batch B specimens are described separately in Sections 5.6.1 and 5.6.2 below.

5.6.1 Crack Initiation: Batch A U-notch Specimens

The first test to be performed (Test A550-750-1-01) was interrupted after 125500 cycles (91% of the life to fracture). SEM examination showed numerous small cracks in the notch root. Examples of crack initiation sites in Batch A specimens are shown in Figure 5.32. The initiation sites were categorised into three main types:

(i) Sites where oxidised primary carbides had erupted out of the notch surface (Figure 5.32a & b).
(ii) Sites with split, bulge-like features on the notch surface (Figure 5.32 c, d & e)
(iii) Sites with no distinct surface feature.

Although some cracks initiated at surface eruptions and bulge-like features, there were also numerous surface eruptions where no crack initiation was apparent, like those shown in Figure 5.32(f).

Test A600-750-1-01 was interrupted at 19884 cycles (79% of the life to fracture). Like Test A550-750-1-01, SEM examination detected numerous cracks in the notch root which were associated with bulge-like features. Other cracks appeared to have initiated from full oxide eruptions, while the remainder had no noticeable surface feature at the initiation site.

Following the observations of different crack initiation sites in Tests A550-750-1-01 and A600-750-1-01, it was decided to quantify the sites when Test A600-750-20-01 was interrupted after 19590 cycles (23% of the total life). The notch surface was systematically surveyed in an SEM at 1000x magnification. The following quantitative results were obtained:

- 17 cracks initiated from bulge like features;
- 1 crack initiated at a fully erupted oxidised primary carbide;
- 8 cracks with no noticeable surface feature at the initiation site.

The quantification exercise was also performed for Test A600-750-30-01 when it was interrupted after 15400 cycles (21% of the life to fracture):

- 6 cracks were observed at bulge-like features;
- 0 cracks were observed at erupted particles;
- 1 crack was observed with no surface feature at the initiation site.

Test A600-750-30-01 was inspected again after 50150 cycles (70% of the life to fracture):

- 13 cracks were observed at bulge-like features;
- 0 cracks were observed at erupted particles;
- 3 cracks were observed with no surface feature at the initiation site.

It became apparent from the above observations on interrupted U-notch tests that multi-site crack initiation along the root of the U-notch was occurring in all the fatigue tests and that crack initiation was probably beginning quite early on in the overall fatigue life. Further SEM fractography and initiation site quantification was performed on the U-notch specimens after fracture. It was found that the bulge-like initiation sites on the main fracture face had sub-surface particles associated with them, such as those shown in Figure 5.33(a) & (b). When EDX analysis of the particles was performed, they were found to be rich in niobium, with some titanium present as well. Their size (approximately 10-15 μm in diameter), globular shape and composition confirmed that the particles associated with the bulge-like initiation sites were oxidised primary carbides. The striking appearance of some of these bulges can be seen in the side views of the notch root in Figure 5.33 (c) & (d). Other examples of cracks initiated at bulges above oxidised sub-surface particles were found in metallographic sections through notch roots. For example Figure 5.33(e) is an optical micrograph of a crack initiated at a bulge, and Figure 5.33(f) shows an initiation site observed using BEI in an SEM. The surface deformation layer due to broaching described in Section 5.1.3 can be discerned in these two images.

The results of post-fracture quantification of crack initiation sites on the main fracture faces are displayed in Table 5.14 for Batch A specimens. Wherever possible, quantification was performed on both specimen halves. The data in Table 5.14 quantifies just those sites whose cracks coalesced to form the final main fracture path along the notch root. Other secondary cracks elsewhere in the notch root were not counted. These results show that in air, crack initiation was frequently associated with oxidised primary carbides, either as bulge-like features or surface eruptions. In vacuum, primary carbide oxidation was suppressed and no crack initiation was observed at oxidised particles. In Test A550-750-1-V-01 small bulges were found at 2 out of 17 crack initiation sites, but EDX analysis showed that they were not linked to oxidised primary carbides. In Test A600-750-1-V-01 a small bulge was found at 1 out of 18 sites. This too was not associated with an oxidised primary carbide. In just one case, Test A600-790-1-P-03, initiation was observed at a primary (Ti,Nb)N nitride particle.

Specimen Code	N_f **(cycles)**	**Left Hand Side**					**Right Hand Side**				
		(Nb,Ti)C Bulge	**Other Bulge**	**(Nb,Ti)C eruption**	**(Ti,Nb)N particle**	**No feature**	**(Nb,Ti)C Bulge**	**Other Bulge**	**(Nb,Ti)C eruption**	**(Ti,Nb)N particle**	**No feature**
A550-750-1-01	137819	23	0	1	0	12	20	0	1	0	10
A600-750-1-01	25311	n/a	0	n/a	n/a	n/a	12	0	0	0	14
A550-750-1-V-01	160938	0	2	0	0	15	0	1	0	0	13
A600-750-20-01	50756	16	0	3	0	9	11	0	4	0	13
A600-750-30-01	71768	14	0	4	0	10	12	0	4	0	11
A600-750-1-PR-01	51279	20	0	7	0	11	21	0	10	0	9
A600-750-1-P-01	169413	10	0	8	0	6	7	0	10	0	6
A600-750-1-02	20802	24	0	3	0	7	20	0	1	0	9
A600-870-1-01	3886	16	0	4	0	18	16	0	3	0	19
A600-810-1-01	4329	11	0	4	0	13	10	0	7	0	15
A600-770-1-01	27538	18	0	4	0	10	16	0	5	0	13
A600-750-1-V-01	53412	0	1	0	0	17	0	0	0	0	17
A600-790-1-01	8792	10	0	8	0	8	12	0	7	0	8
A600-790-1-PR-01	51687	22	0	13	0	5	23	0	18	0	7
A600-790-1-P-02	13420	17	0	13	0	4	20	0	9	0	8
A600-790-1-P-03	87327	16	0	17	0	6	17	0	18	1	6

Table 5.14: Results of post-fracture initiation site quantification on Batch A U-notch specimens.

Additional information about the crack initiation process was obtained from the replica records of tests A600-750-1-PR-01 and A600-790-1-PR-01. Examination of surface replicas showed that cracks began to initiate within the first 10% of the overall fatigue life.

The evolution of the number of cracks present in the notch root as tests progressed is shown in Figure 5.34 (a) & (b) for σ_{max} = 750 MPa and σ_{max} = 790 MPa respectively. For both tests, the majority of cracks initiated at bulge-like features, with the remainder starting at surface eruptions or intrinsically. A common feature in both tests was an incubation period at the beginning of the test in which no cracks were observed. This incubation period was 2000 cycles at σ_{max} = 750 MPa and 5000 cycles at σ_{max} = 790 MPa. After the initial incubation period and a period of low rate of crack initiation, the number of cracks increased at a steady rate. The initiation rate then decreased. Eventually, major coalescence of cracks led to rapid reduction in the number of individual cracks observed in the notch root.

5.6.2 Crack Initiation: Batch B U-notch Specimens

Only Test B600-885-1-03 was interrupted for SEM inspection. After 3000 cycles a number of fatigue cracks were found. However, it proved difficult to quantify them due to the roughness of the broached U-notch surface. No further fatigue cycling beyond 3000 cycles was performed on Test B600-885-1-03.

Full post-fracture quantification of crack initiation sites in the Batch B specimens was performed using the same procedure as Batch A. The results of post-fracture quantification of crack initiation sites on the main fracture faces of Batch B specimens are listed in Table 5.15.

For as-broached specimens, it was observed that the total number of initiation sites per specimen was much lower for Batch B specimens than Batch A specimens tested under the same conditions. It was also observed that unlike Batch A, the most numerous crack initiation sites were not oxidised primary carbides (eruptions or bulge-like sites). Instead, the most numerous sites were the sites with no feature such as a particle on them. Sometimes, small bulge-like features were observed, but they were not associated with sub-surface (Nb,Ti)C particles. EDX analysis of these bulges showed there was some slight enrichment in Nb relative to the matrix, but not the very high enrichment in Nb indicative of the presence of an (Nb,Ti)C particle. Examples of these bulges without associated particles are shown in Figure 5.35(a). These small bulges were not evident elsewhere on the notch surface, unlike the prominent bulges associated with (Nb,Ti)C carbide particles observed on Batch A specimens. Where an (Nb,Ti)C particle was present at an initiation site in a Batch B specimen, this was easily confirmed by the high Nb signal detected using EDX. Occasionally, initiation at (Ti,Nb)N particles was observed, such as test B600-790-1-01. One of these sites is shown in Figure 5.35(b). The (Ti,Nb)N particles in the material were known to be Ti rich and this was used to confirm the identity of the particles at initiation sites.

Specimen Code	N_f **(cycles)**	**Left Hand Side**					**Right Hand Side**				
		(Nb,Ti)C Bulge	**Other Bulge**	**(Nb,Ti)C eruption**	**(Ti,Nb)N particle**	**No feature**	**(Nb,Ti)C Bulge**	**Other Bulge**	**(Nb,Ti)C eruption**	**(Ti,Nb)N particle**	**No feature**
B600-790-1-01	90327	0	3	1	1	6	0	4	1	1	5
B600-790-1-02	40440	1	2	1	0	7	0	4	1	0	8
B600-790-1-P-01	28510	0	0	0	1	4	0	0	0	1	4
B600-870-1-01	19856	0	3	0	0	5	0	4	0	0	5
B600-870-1-02	19010	0	2	0	1	3	0	2	0	1	3
B600-1000-1-01	2153	1	0	2	0	7	1	0	2	0	7
B600-900-1-01	4475	0	0	1	0	7	0	0	1	0	7
B600-885-1-01	5016	1	0	0	0	8	1	0	0	0	8
B600-885-1-02	9889	0	0	0	0	4	0	0	0	0	4
B600-885-20-01	4541	1	2	1	0	3	0	2	0	0	2
B600-885-20-02	4321	0	3	2	0	5	0	3	1	0	5
B600-885-1-R-01	5157	0	0	1	1	6	0	0	1	0	6
B600-885-1-P-01	19605	0	4	4	1	6	0	3	3	0	7
B600-885-1-PR-01	13591	1	0	4	0	1	1	0	6	0	0
B600-885-1-PR-02	7939	0	0	2	0	7	0	0	3	0	10

Table 5.15: Results of post-fracture initiation site quantification on Batch B U-notch specimens.

The replica records of tests B600-885-1-PR-01 and B600-885-1-PR-02 were used to quantify the number of cracks in the U-notch root as each test progressed. The results are displayed in Figure 5.36. For test B600-885-1-PR-01 the dominant crack initiated at a surface eruption and was first observed after 1000 cycles. This was the only crack to grow significantly. Most of the other cracks which initiated did so late in the fatigue life ahead of the main crack tip and in the residual ligaments. In test B600-885-1-PR-02, the dominant and only significant crack was first observed after 1000 cycles at a (Ti,Nb)N particle. In a similar way to test B600-885-1-PR-01, the majority of cracks initiated late in the fatigue life ahead of the main crack tips of the dominant crack. This was different from the behaviour at σ_{max} = 750 MPa and 790 MPa where cracks initiated and grew from several sites and later coalesced to form the final dominant crack. Crack propagation and coalescence behaviour is described in more detail in Section 5.7.

The difference in initiation characteristics between the Batch A and Batch B tests can be seen in Figure 5.37 (a) and (b), where the total number of cracks observed is plotted against number of cycles (a) or percentage of life (b). In all four tests, crack initiation rates were low at first, up to 5000 cycles. The tests at σ_{max} = 750 MPa and 790 MPa then exhibited crack initiation at a fairly constant rate before reaching a plateau, with a decrease in crack numbers at the end of the life due to coalescence. However, the two σ_{max} = 885 MPa tests showed very rapid crack initiation with no plateau and no significant crack coalescence, followed shortly by specimen fracture. Comparing crack initiation behaviour plotted against percentage of fatigue life, the difference in initiation behaviour between the lower stress levels (σ_{max} = 750 & 790 MPa) and σ_{max} = 885 MPa is also apparent. The lives of the tests at 750 and 790 MPa therefore appeared to be initiation dominated, whereas the tests at 885 MPa were propagation dominated.

5.7 Short Crack Growth and Coalescence in U-notch Specimens

Projected surface crack lengths parallel to the notch root were measured from acetate replicas. The convention for labelling crack segments is shown in Figure 5.21. It was decided to characterise surface crack growth rates by plotting them against crack length $2c$. This was because of the lack of a suitable driving force parameter to describe the growth of short cracks in a plastically yielded notch. In such a situation the LEFM parameter ΔK was clearly not applicable. ΔJ may not be a suitable representation of crack driving force either, since it strictly only applies for non-linear elasticity. An alternative driving force, such as crack tip plastic strain range or strain energy density [5.9] for each crack configuration might be appropriate, but it was considered beyond the scope of this thesis. Specific results for each stress level are described in the following sections.

5.7.1 σ_{max} = 750 MPa (Test A600-750-1-PR-01)

As described in Section 5.6.1 on crack initiation, numerous cracks initiated in the notch root throughout the fatigue life. Analysis of replicas taken from test A600-750-1-PR-01 showed that many of the cracks which initiated either propagated very slowly or became non-propagating. Significant rates of crack growth were confined to just a few cracks and it is the growth rates of these cracks which are described in detail here. However, the other non-propagating or very slowly propagating cracks may have influenced the growth of the propagating cracks due to shielding effects or coalescence. In the later stages of the fatigue life, there was a transition from steady short crack growth to very rapid growth and coalescence of cracks, eventually forming a single crack along the entire notch root which resulted in specimen fracture. Crack length information for the main propagating cracks is presented in Figure 5.38(a). Total crack growth rates $d(2c)/dN$ are plotted against total crack length $2c$ in Figure 5.38(b). An interesting feature of these short crack growth rates is that unlike long crack behaviour, there was not a general increase in crack growth rate with increasing crack length.

Crack I was first observed after 6000 cycles, at a large, shallow bulge-like feature. It temporarily arrested at a length $2c = 48$ μm. Grain diameters in the IN718 material tested ranged from 5-70 μm, so the temporary arrest of this crack may have been due to the presence of grain boundaries. Alternatively, the arrest of this crack may have been related to the presence of the deformation layer in the notch root. Assuming $a{:}c = 1$, Crack I arrested at a depth of 24 μm, more than the observed depth of the deformation layer in the notch root, but possibly still within a region affected by the presence of the layer.

Crack II initiated at a small surface eruption after 6000 cycles and was the fastest growing of all the cracks observed in this test, averaging $d(2c)/dN = 2.1 \times 10^{-8}$ m/cycle. Crack II reached a length of $2c = 840$ μm at 44000 cycles, after which coalescence with other cracks occurred and a dominant through-thickness crack formed. An absence of shielding, at least in the early stages of propagation, may have contributed to the rapid growth of Crack II. However, beyond 28000 cycles, Crack II became asymmetric about its origin, with segment c_1 growing more slowly than c_2. This could be attributed to the shielding effects of other cracks, as shown in Figure 5.39.

Crack III was first observed after 16000 cycles and initiated at a bulge-like feature. The development of this bulge and the initiation of the crack can be seen in the sequence of images in Figure 5.40. Segment c_2 of Crack III arrested completely after 28000 cycles, while segment c_1 continued to grow. The arrest of segment c_2 appeared to be due to interaction with the crack tip plastic zone of another crack, as can be seen in Figure 5.41. The continued growth of segment c_1 was assisted by coalescence with an adjacent small crack, though the presence of other surrounding cracks may have shielded this crack from the full effects of the applied stress. Segment c_2 of Crack III remained arrested until it coalesced with the adjacent crack after 48000 cycles.

Crack IV was first observed at a small bulge-like feature after 4000 cycles and grew until coalescence with other cracks after 48000 cycles. The rapid coalescence of these cracks between 48000 and 50000 cycles can be seen in Figure 5.42. Notice from Figure 5.42(a) how the tips of parallel cracks grew past each other before coalescence, resulting in the formation of small islands of material after coalescence in Figure 5.42(b).

The surface cracks in the U-notches were all remarkably straight, with no deflections except those occurring during crack coalescence. Surface crack propagation was therefore transgranular, though SEM fractography indicated that propagation in the "*a*" direction into the bulk of the specimen became mixed transgranular-intergranular beyond a distance of 30-50 μm below the notch surface, shown in Figure 5.43.

5.7.2 σ_{max} = 790 MPa (Test A600-790-1-PR-01)

The initiation and propagation behaviour at σ_{max} = 790 MPa was similar to that at σ_{max} = 750 MPa. Numerous cracks initiated in the notch root. Some did not propagate to any great extent, while others grew substantially, eventually coalescing with other cracks to form a final dominant defect along the length of the U-notch. The growth of the three main cracks in test A600-790-1-PR-01 will be described in detail here. The cracks are labelled A, B and C. Crack length information is presented in Figure 5.44(a). Total crack growth rates $d(2c)/dN$ are plotted against total crack length $2c$ in Figure 5.44(b). As observed for σ_{max} = 750 MPa, crack growth rates remained relatively constant across a wide range of crack lengths.

Crack A initiated at a bulge-like feature and was first observed after 5000 cycles. Crack A soon became asymmetric about its initiation site, with segment c_1 propagating more quickly than segment c_2, as can be seen in the plot of crack lengths against number of cycles in Figure 5.44(a). Figure 5.45 shows an image of Crack A after 15000 cycles showing this crack asymmetry. The cause of the retardation of segment c_2 was not readily apparent, though it could have been due to the shielding effect of nearby surface eruptions. Segment c_1 of Crack A was arrested beyond 29000 cycles, probably due to the shielding effect of the small crack shown in Figure 5.46.

Crack B also initiated at a bulge-like feature and was first observed after 5000 cycles. This crack remained relatively symmetrical about its initiation point for most of the fatigue life, and grew stably to a length of $2c = 301$ μm at 43000 cycles. Beyond 43000 cycles there was a transition to very rapid growth. By 45000 cycles it had reached a length of $2c = 660$ μm. Beyond 45000 cycles accelerating propagation and coalescence resulted in the formation of a crack along the entire length of the notch.

Crack C was another crack which initiated at a bulge-like feature and was first observed after 5000 cycles. Its proximity to another small crack, as shown in Figure 5.47 probably resulted in shielding and crack-tip plastic zone interactions which retarded the growth of Crack C and the adjacent crack as well.

As in Test A600-750-1-PR-01, all the cracks were remarkably straight with no deflections except at crack coalescence, indicating transgranular propagation.

5.7.3 $\sigma_{max} = 885$ MPa (Tests B600-885-1-PR-01 & B600-885-1-PR-02)

In both tests performed at $\sigma_{max} = 885$ MPa, there was only one crack which grew to any significant extent following initiation. Crack length information for the tests is presented in Figure 5.48(a). Total crack growth rates $d(2c)/dN$ are plotted against total crack length $2c$ in Figure 5.48(b). The cracks from test B600-885-1-PR-01 and test B600-885-1-PR-02 are labelled Crack X and Crack Y respectively.

Crack X from test B600-885-1-PR-01 initiated at a surface eruption, while Crack Y initiated at an (Ti,Nb)N particle, as shown in Figure 5.49. This image also shows the presence of slip bands on the notch surface, which were not observed in the Batch A tests performed at $\sigma_{max} = 750$ MPa and 790 MPa. The slip bands can be seen more clearly in Figure 5.50. There was a difference in surface crack propagation path between the cracks at $\sigma_{max} = 885$ MPa and the Batch A tests at lower stress levels. As already described in the previous sections, at $\sigma_{max} = 750$ MPa and 790 MPa in Batch A, the surface cracks were straight and parallel to the notch root, except where deflections occurred during crack coalescence. However, at $\sigma_{max} = 885$ MPa in Batch B, the crack path was more tortuous, either following slip bands or grain boundaries, producing mixed transgranular-intergranular propagation at the notch surface (Figure 5.51). This was confirmed by SEM fractography.

To check whether the appearance of slip bands was a consequence of the high strain range at σ_{max} = 885 MPa, an uninterrupted test was performed on a Batch B specimen with a polished notch at σ_{max} = 790 MPa (test B600-790-1-P-01), for comparison with the equivalent Batch A tests (tests A600-790-1-P-02 and A600-790-1-P-03). Upon examination optically and in an SEM, it was found that the polished Batch B specimen exhibited slip bands on the notch surface, while the polished Batch A specimens did not. In the Batch B specimen, the surface crack paths underwent numerous microscopic deflections along slip bands or grain boundaries, while in the Batch A specimens the cracks were straight and transgranular at the surface.

5.7.4 Additional Examples of Crack Coalescence

Apart from the observation of crack coalescence on replicas, examples of crack coalescence phenomena were observed in the U-notches of fractured specimens. Crack coalescence was discussed for Crack IV (test A600-750-1-PR-01) in Section 5.7.1. There, coalescence behind the crack tips occurred, forming an island of material. Another example of coalescence in the same specimen is shown in Figure 5.52. This plan view SEM image of the notch surface shows a crack coalescence site in plan view. It is interesting because it shows two types of crack coalescence. To aid description, the crack tips in the image are labelled c_w, c_x, c_y and c_z. On the left of the image, crack tips c_w and c_x coalesced by breakthrough of the material between them, without any crack tip overlap. There is some slight crack tip curvature on c_x. Figure 5.52 also enables one to see the sub-surface step on the main fracture face formed where the cracks coalesced. On the right of the image, the crack tips c_y and c_z grew past each other. Note how c_y and c_z curved towards the other crack, before coalescence by breakthrough of the remaining material.

Figure 5.53 is a BEI image of a cross-section through test A600-750-1-01 after fracture, showing two secondary cracks in the notch root. Note how the cracks have coalesced below the surface.

5.7.5 Comparison of Crack Growth Rates

Crack growth rates obtained from all the U-notch tests are plotted together in Figure 5.54 in terms of $d(2c)/dN$ vs. $2c$. The graph shows that for σ_{max} = 750 MPa and 790 MPa in Batch A specimens, the crack growth rates remained approximately constant with increasing crack length until there was a transition to accelerating crack growth and coalescence leading to specimen fracture. For example, Crack II at σ_{max} = 750 MPa reached $2c$ = 840 μm, before accelerating crack growth and coalescence took over.

Similarly, Crack B at σ_{max} = 790 MPa reached $2c$ = 660 μm before exhibiting a transition to increasing crack growth rate with increasing crack length. However, for Batch B material at σ_{max} = 885 MPa, crack propagation followed the trend of increasing crack growth rate with increasing crack length, except for the early stages of growth of Crack X.

Little work has been published elsewhere on crack propagation in U-notch geometries in IN718 material. An exception is Bache et al. [5.10] who studied the growth of pre-initiated semi-elliptical cracks of initial surface length $2c \approx 1$ mm growing in a double-edged U-notch specimen with a quoted stress concentration factor of 2.23. Very rapid, accelerating crack propagation rates were observed at 600°C in air, producing critical crack lengths within 2000 cycles. Data from Bache et al. [5.10] are plotted in Figure 5.54 for comparison with growth rates in the current study. Note that Bache et al.'s data was obtained under different loading conditions, using 17.5-1-17.5-1 and 17.5-30-17.5-1 waveforms at σ_{max} = 613 MPa and R = 0.05. Parabolic loading and unloading was used to represent the conditions in a gas turbine spin rig test, and some tests were performed at a reduced air pressure of 150 MPa. Though the loading conditions were different, it is interesting to compare the results of Bache et al. [5.10] with the growth rates in the Batch B U-notch tests, which were of a similar order of magnitude at similar crack lengths.

Despite the reservations expressed at the beginning of Section 5.7 about using ΔK to characterise short crack growth, it was decided to calculate ΔK for the short cracks in the U-notches. This was done in order to compare their behaviour at different stress levels with long crack data obtained for similar IN718 material tested at 600°C in air using a 1-1-1-1 waveform at R = 0.1, i.e. the same conditions used for the U-notch tests. The long crack data were provided by ALSTOM Power [5.7].

According to the convention shown in Figure 5.21, long crack data represents crack growth in the "a" direction. The cracks in the U-notch roots were assumed to be semi-elliptical in shape with an a/c value of 1. The crack growth rate da/dN was then taken to be half the surface crack growth rate $d(2c)/dN$. ΔK at maximum depth for the short cracks was calculated using Eqn. 5.2. Instead of using the nominal far-field bending stress range to calculate ΔK, the local tensile range of σ_{xx} in the notch root predicted by the elastic-plastic FE model was used. The resulting comparison on the basis of ΔK of the U-notch short crack data with long crack data is displayed in Figure 5.55. It is clear from Figure

5.55 that ΔK alone is not a suitable parameter for characterising the U-notch short crack growth rates since it does not successfully collapse the data onto a single curve. The U-notch short cracks also exhibit the apparently "anomalous" behaviour of short cracks, namely growth at ΔK values below the long crack threshold, higher crack growth rates than long cracks for the same value of ΔK and crack arrest events. There is also the fact that the data for σ_{max} = 750 MPa and σ_{max} = 790 MPa exhibit relatively constant growth rates with increasing ΔK. However, the growth rates of Cracks B, X and Y do tend towards the long crack data at higher ΔK, suggesting typical Stage II type crack growth behaviour at longer crack lengths for these relatively isolated cracks.

5.8 Influence of Broaching Marks on Crack Propagation

Fatigue life results showed that polished specimens usually had longer lifetimes than as-broached specimens tested under the same conditions. Since the broaching marks were parallel to the notch root and hence the direction of surface crack propagation, it was possible that the broaching marks were accelerating either crack initiation, crack propagation or both, resulting in shorter fatigue lives than polished specimens. In the Batch A tests, the cracks observed were straight and parallel to the notch axis on both as-broached and polished specimens. Hence it was not possible to determine conclusively if the broaching marks affected crack propagation. However, for the Batch B tests at σ_{max} = 885 MPa, there was some evidence that the broaching marks were influencing crack propagation. SEM fractography was performed on tests B600-885-1-02 and B600-885-1-P-01. These were both uninterrupted run to fracture tests performed under the same conditions, except B600-885-1-02 had an as-broached notch, and B600-885-1-P-01 had a polished notch. Comparisons of the surface crack path in the notch root near the main crack initiation site are shown in Figure 5.56. In the as-broached notch, the surface crack path was essentially straight and parallel to the broaching marks, whereas in the polished notch the crack path deviated along slip bands or grain boundaries.

5.9 Crack Propagation in the "*a*" Direction

Obtaining detailed information about short crack propagation rates in the sample depth direction (the "*a*" direction in Figure 5.21) was not a major part of this study. However, some qualitative observations were obtained by examination of the fracture surfaces. As already described for Batch A specimens, crack propagation in the "*a*" direction was initially transgranular at the surface, changing to mixed transgranular/intergranular propagation at a depth of 30-50 μm (see Figure 5.43). The characteristic flat appearance of the fracture surface near initiation sites was not so apparent in Batch B specimens.

On a macroscopic scale, the position of crack initiation sites in the notch root influenced the appearance of the fatigue fracture faces in both Batch A and Batch B specimens. Selected examples will now be discussed. Figure 5.57 is a macro photograph of the fracture face of Test A600-790-1-PR-01. What became the dominant crack initiated near the notch centre, coalescing with other short cracks in the notch root to form the large thumbnail crack visible in the image. In other cases, the main crack developed away from the notch centre, as shown in Figure 5.58 for Test A600-790-1-P-03. (This test was performed under the same conditions as A600-790-1-PR-01 except no replicas were taken). The development of the dominant crack occurred from a point to the right of the notch centre in Figure 5.58, resulting in the final fatigue crack having an asymmetric shape. Small steps on the fracture face can be seen where coalescence of parallel cracks occurred. Similar symmetric and asymmetric crack shapes were observed on different Batch B specimens tested under the same conditions, such as B600-790-1-01 and B600-790-1-02 shown in Figure 5.59(a) & (b). In total, 11 specimens had roughly symmetrical fracture face profiles, 12 were asymmetric with the deepest part to the left of centre, and 8 were asymmetric with the deepest part to the right of centre.

Periods of dwell at maximum stress had an effect on the macroscopic appearance of the fatigue fracture surfaces. Fissures running parallel to the crack propagation direction were observed on the lower parts of the fatigue fracture surface for Tests A600-750-20-01 & A600-750-30-01, shown in Figure 5.59(c) & (d). In these regions with the fissures, instead of a pure fatigue fracture surface, some dimpled rupture-like fracture was observed as well suggesting some creep or localised ductile overload failure in the latter stages of fatigue crack propagation before final fracture of the specimen as a whole. In Figure 5.59(c) & (d) it is also possible to see the multiple crack initiation sites in the notch root.

On some specimens, beachmarking on the fatigue fracture surfaces made it possible to measure macroscopic crack aspect ratios. In total, 30 cracks were measured. Aspect ratios a:c ranged from 0.62 to 1.55. Of those cracks it was possible to measure, 18 cracks had a:c ratios less than 1, and only four cracks had aspect ratios greater than 1.1. The a:c value of 1.55 was an extreme example from test B600-885-20-01. An a:c ratio greater than 1 indicates some degree of crack tunnelling, in which crack propagation into the specimen depth occurred more rapidly than at the surface of the notch.

Another parameter measured from the fracture faces was the percentage of the specimen cross-sectional area covered by the fatigue fracture. There was a lot of scatter in the data, but the general trend was for a decrease in area of the fatigue fracture with increasing σ_{max}. This is plotted in Figure 5.60 for tests performed with a 1-1-1-1 cycle in air at 600°C. The decrease in fatigue crack area with increasing applied stress was expected, because at higher maximum stresses the residual cross-sectional area could not support the applied peak loads, resulting in earlier collapse of the specimen.

5.10 Figures

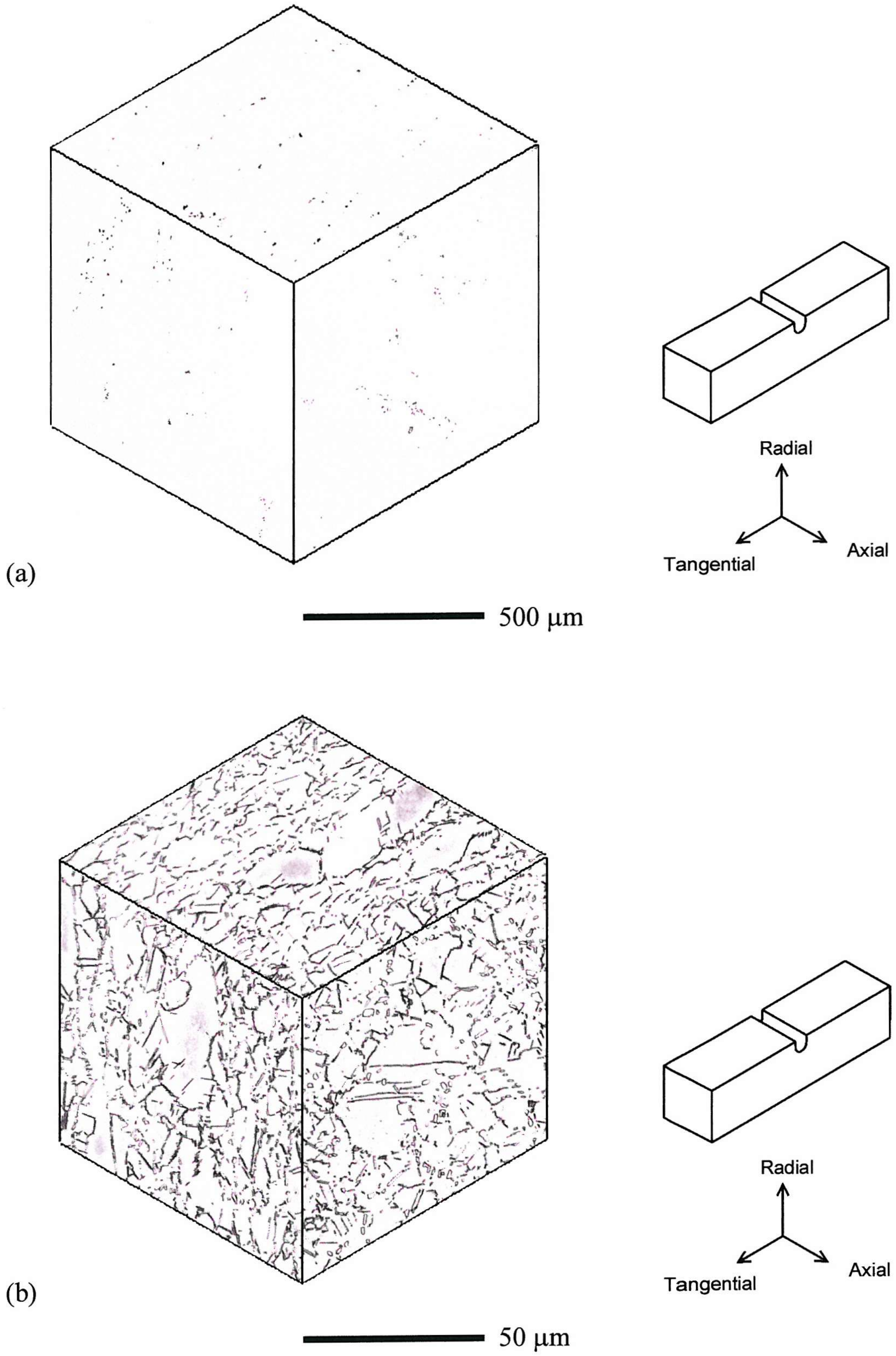

Figure 5.1: Microstructure of Batch A disc material. (a) as-polished, showing primary carbides; (b) etched, showing grain structure and δ phase distribution. (Optical).

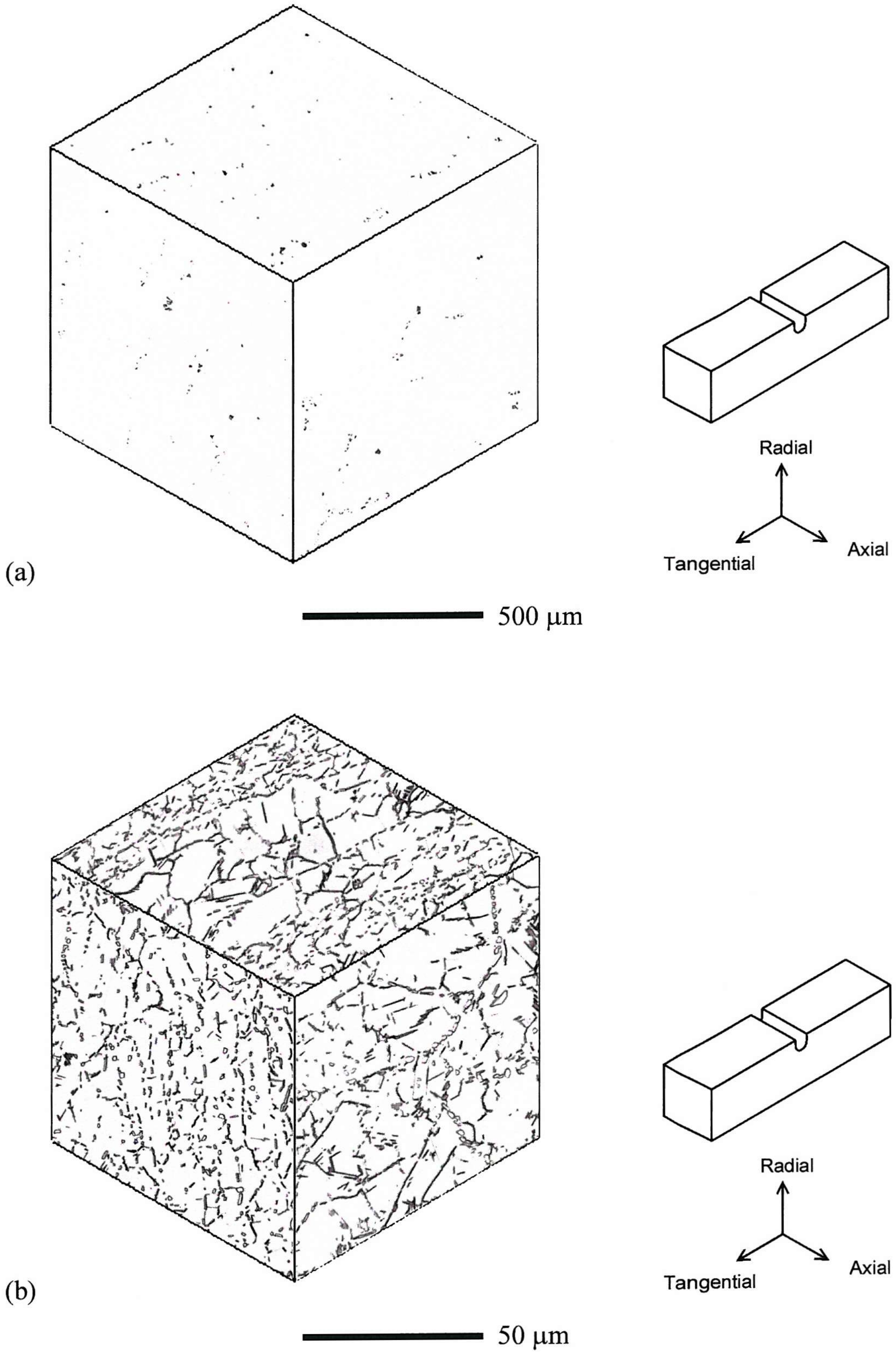

Figure 5.2: Microstructure of Batch B disc material. (a) as-polished, showing primary carbides; (b) etched, showing grain structure and δ phase distribution. (Optical).

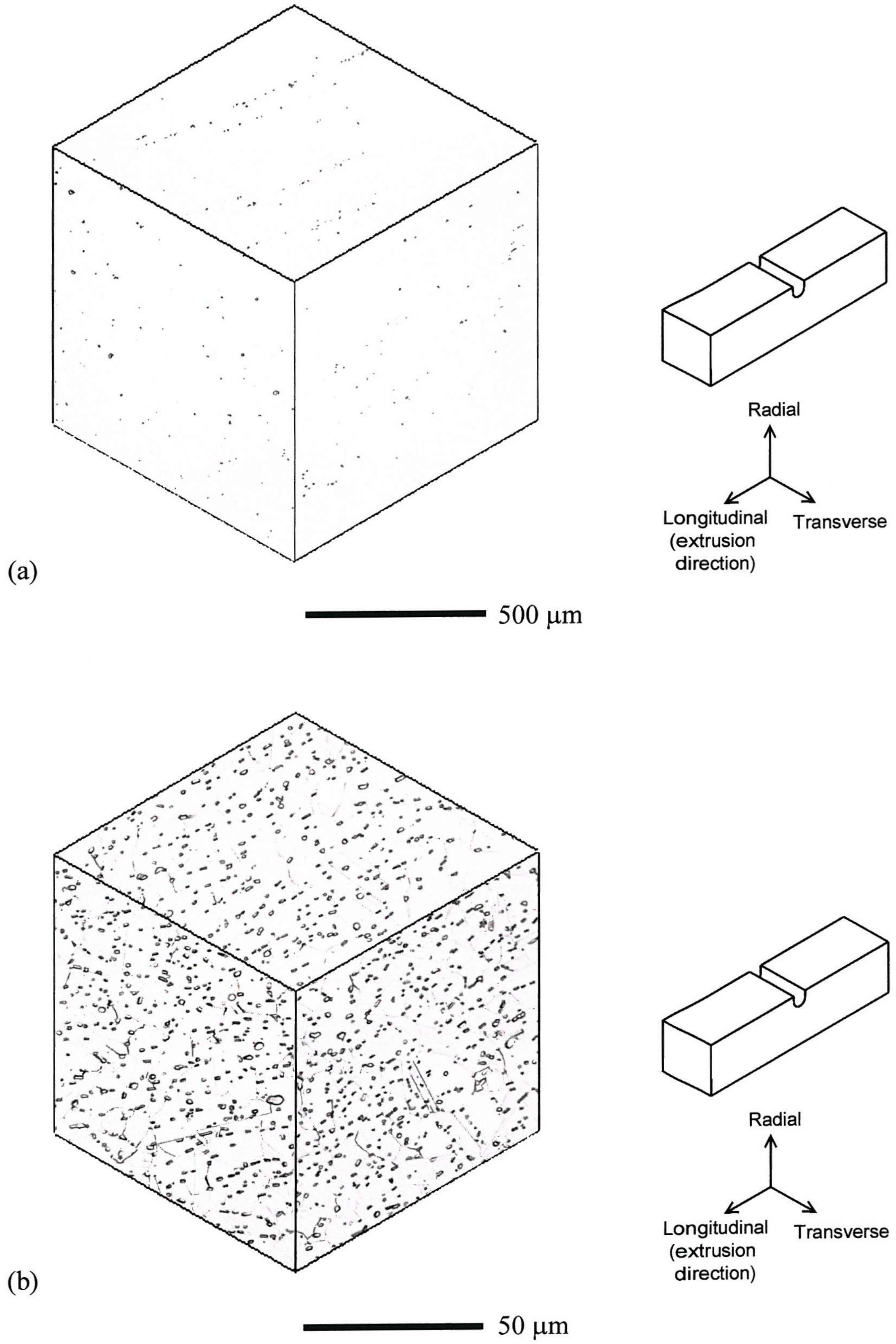

Figure 5.3: Microstructure of extruded bar material. (a) as-polished, showing primary carbides; (b) etched, showing grain structure and δ phase distribution. (Optical).

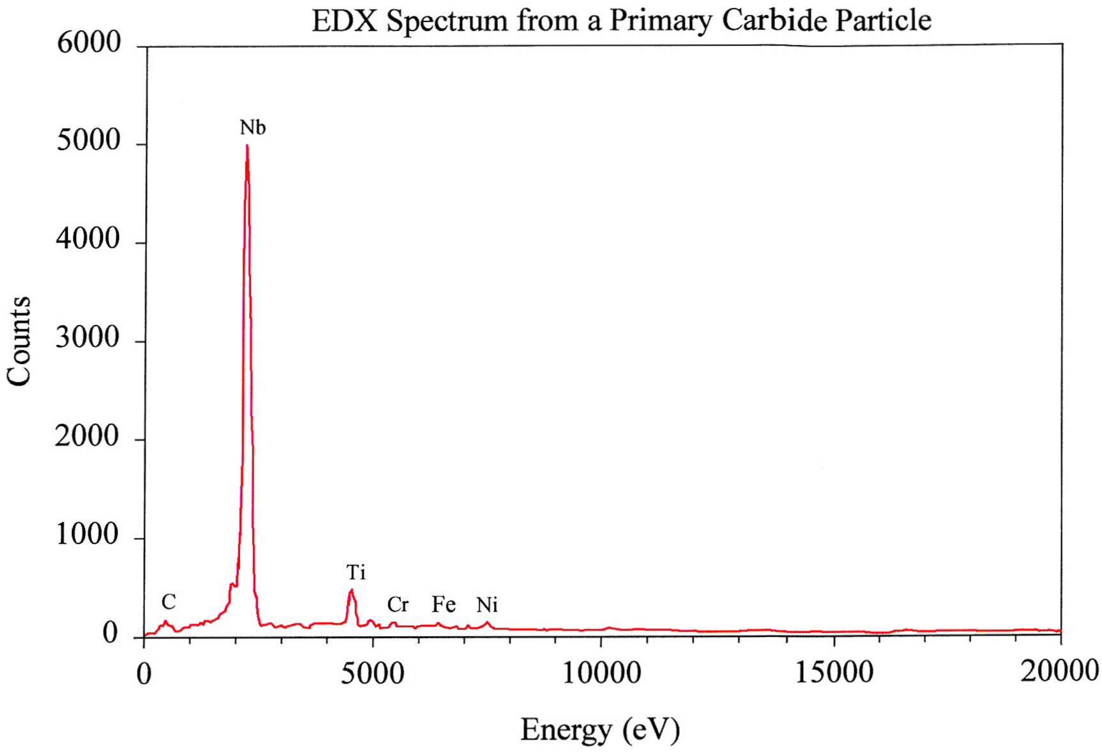

Figure 5.4: Example of an EDX spectrum from a primary (Nb,Ti)C carbide in Batch A disc material.

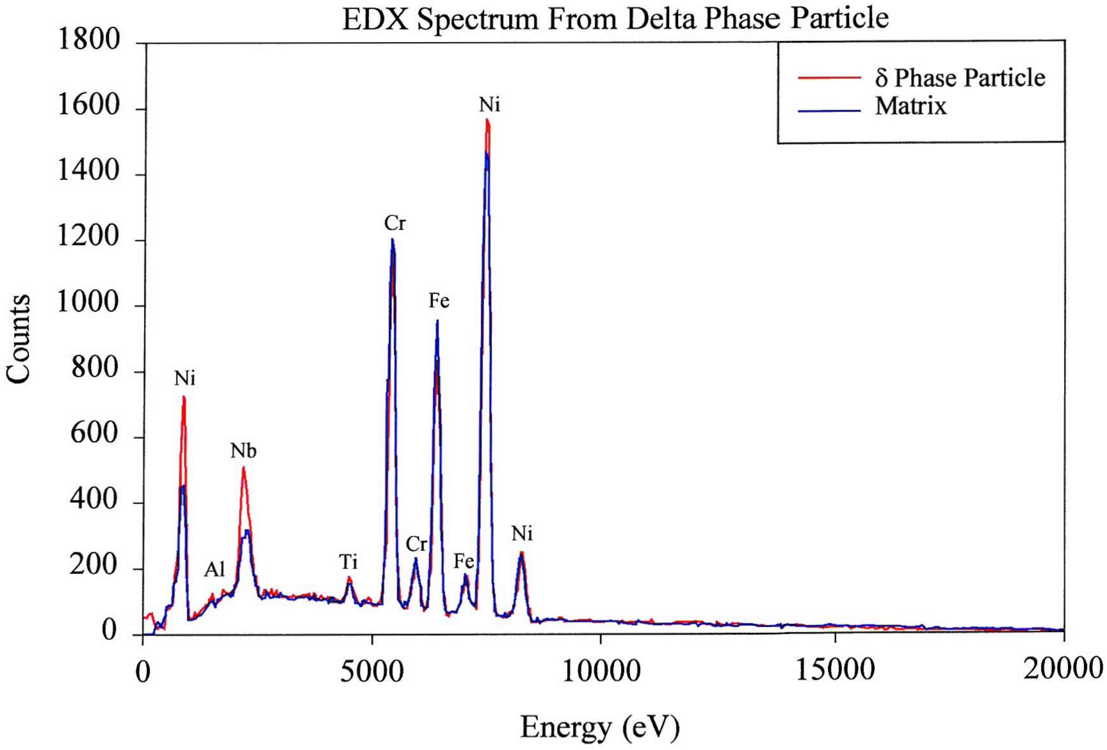

Figure 5.5: EDX spectrum from a δ phase particle in Batch A disc material. A reference spectrum from the adjacent matrix is also shown.

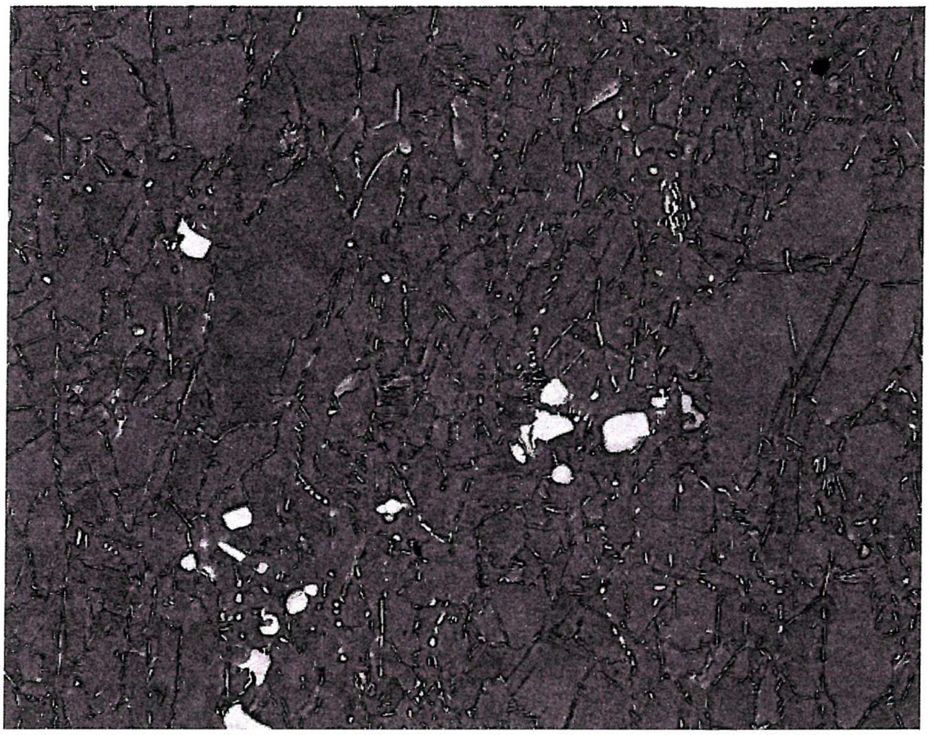

(a)

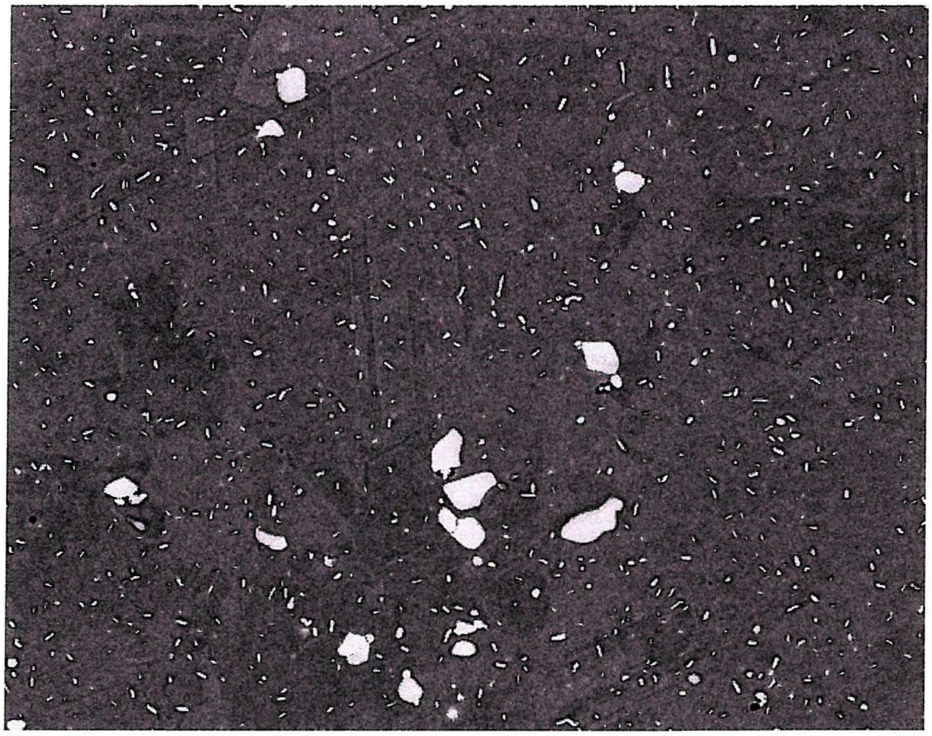

(b)

Figure 5.6: Backscattered electron images of Inconel 718 microstructures. (a) disc material; (b) extruded bar.

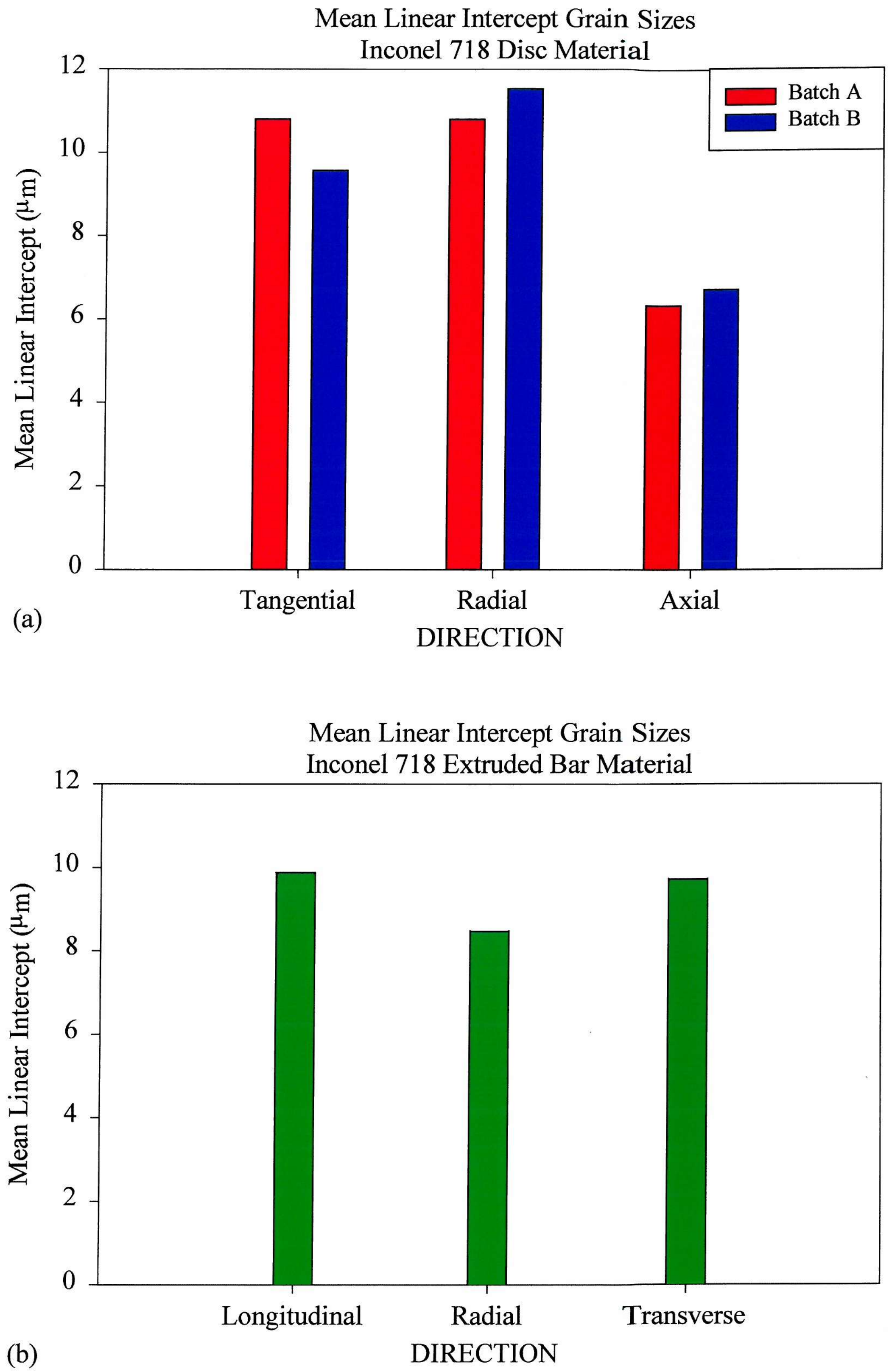

Figure 5.7: Mean linear intercept grain size measurements. (a) disc materials; (b) extruded bar material.

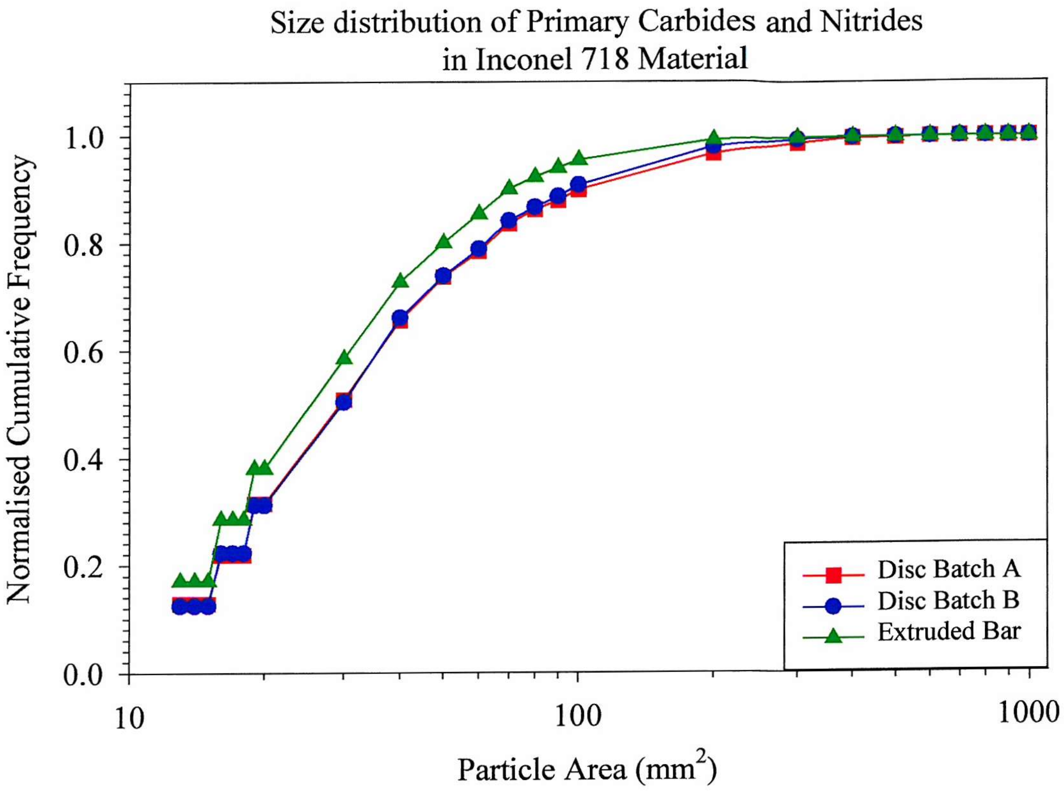

Figure 5.8: Cumulative frequency size distribution of primary carbide and nitride particles.

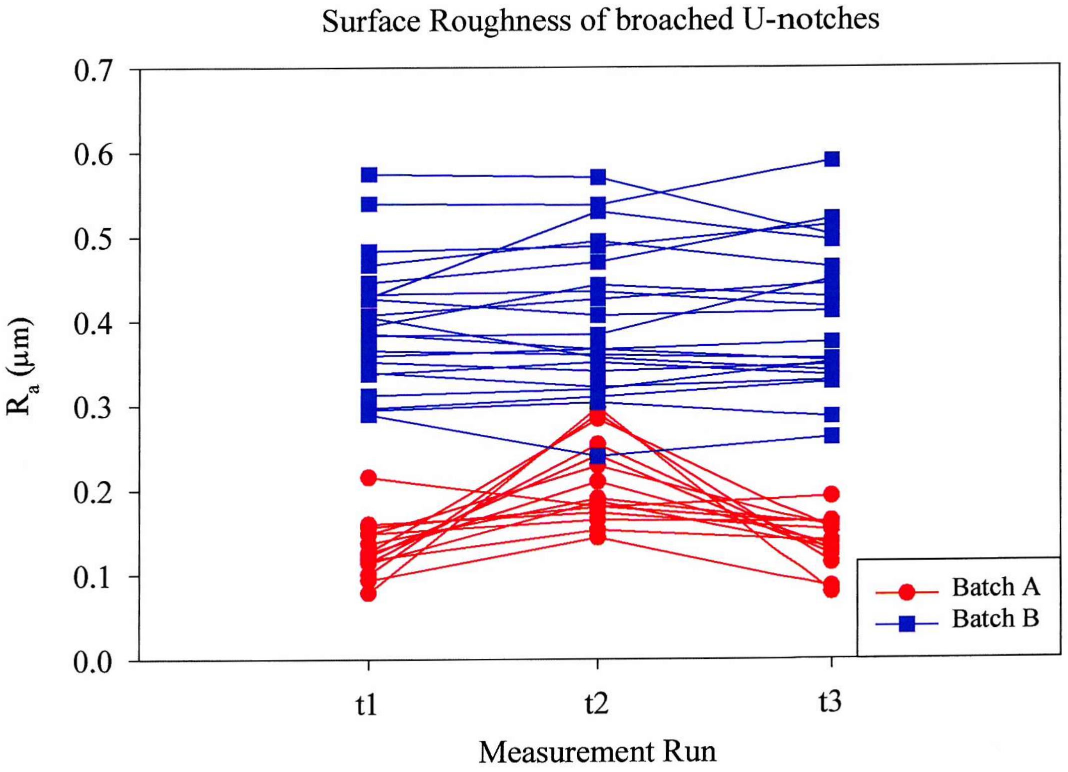

Figure 5.9: Surface roughness measurements in U-notch roots. Values of R_a for Batch A and Batch B.

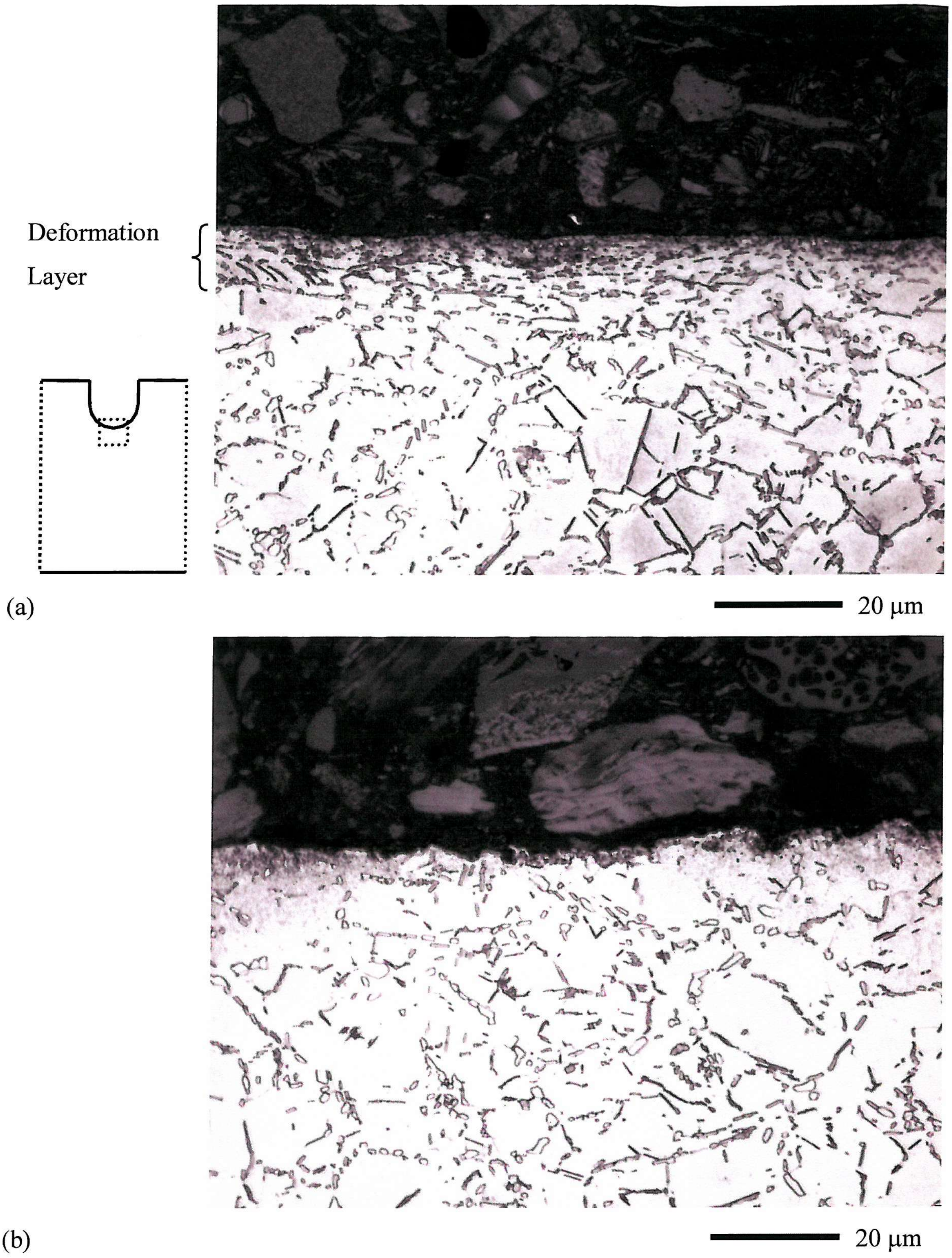

Figure 5.10: Optical micrographs of sections through U-notch root. (a) Batch A specimen, showing presence of a deformation layer at the surface. (b) Batch B specimen, with no deformation layer in the notch root. The higher surface roughness of the Batch B specimen can be seen.

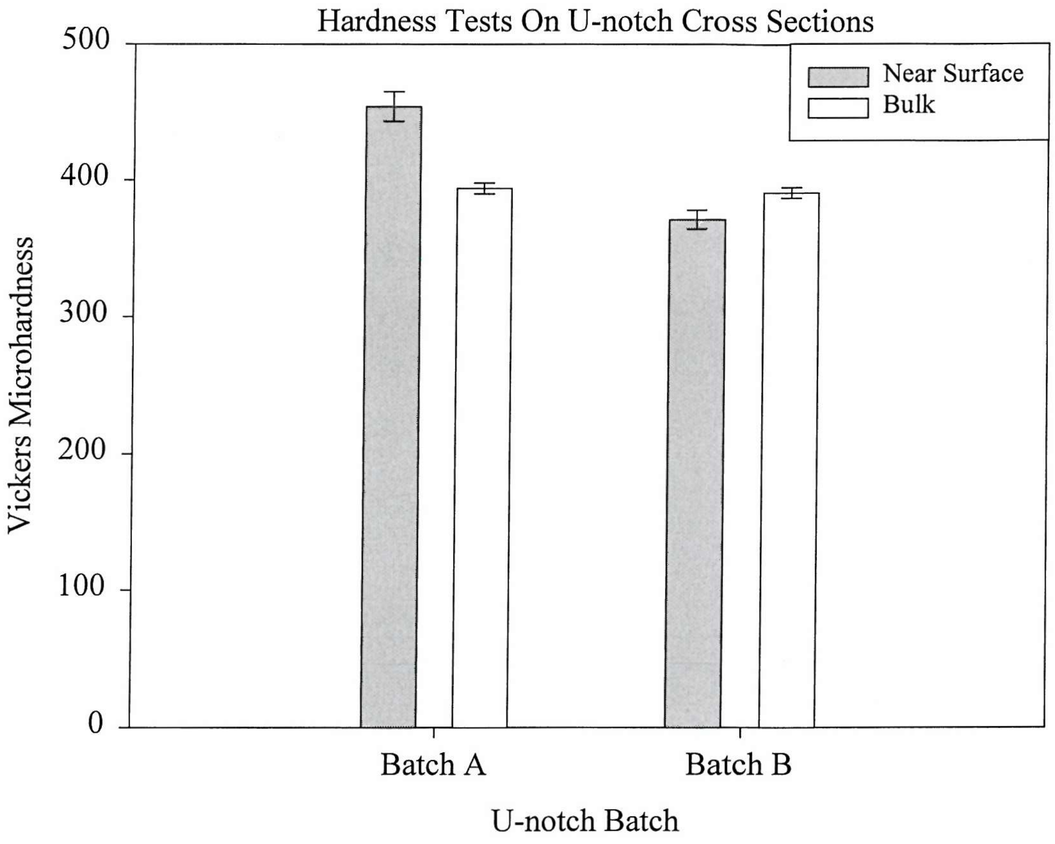

Figure 5.11: Results of microhardness tests on cross-sections through U-notches to determine if work hardening had occurred as a result of broaching. The error bars indicate the 95% confidence intervals.

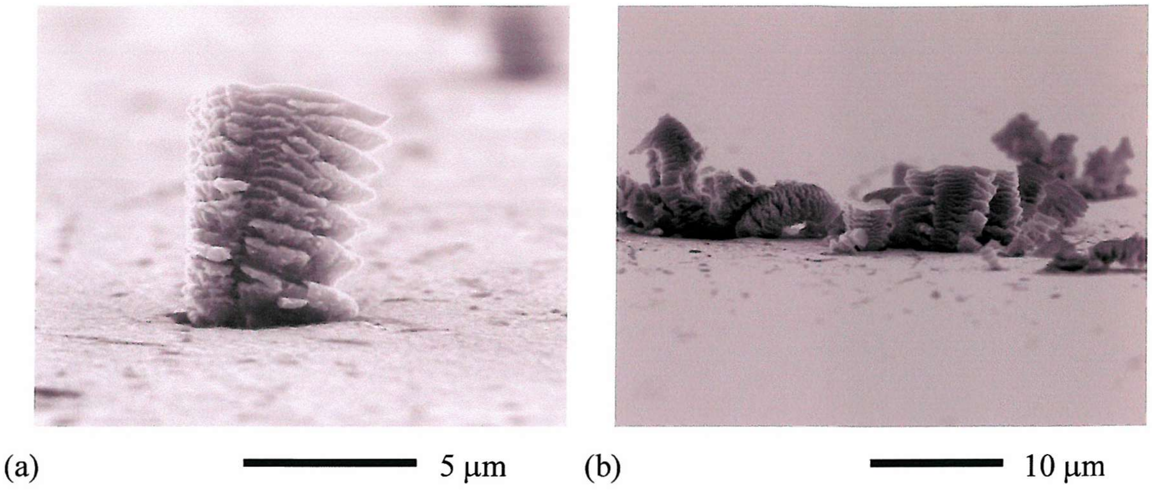

Figure 5.12: Tower-like eruptions on the polished surface of a thermal exposure specimen. (SEM, SEI).

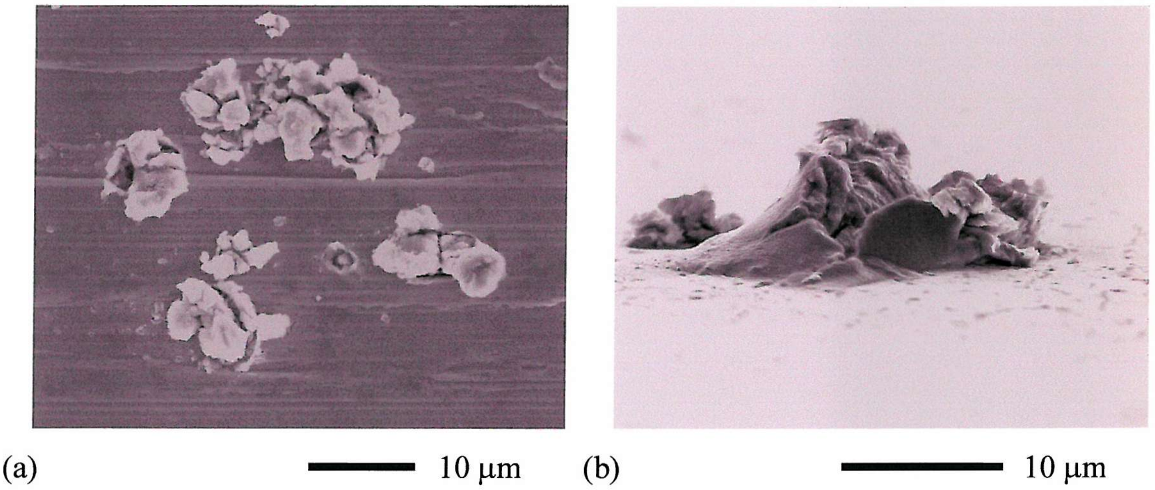

Figure 5.13: Irregularly shaped eruptions on the surface of a thermal exposure specimen. (a) plan view of machined surface; (b) An example viewed from the side. (SEM, SEI).

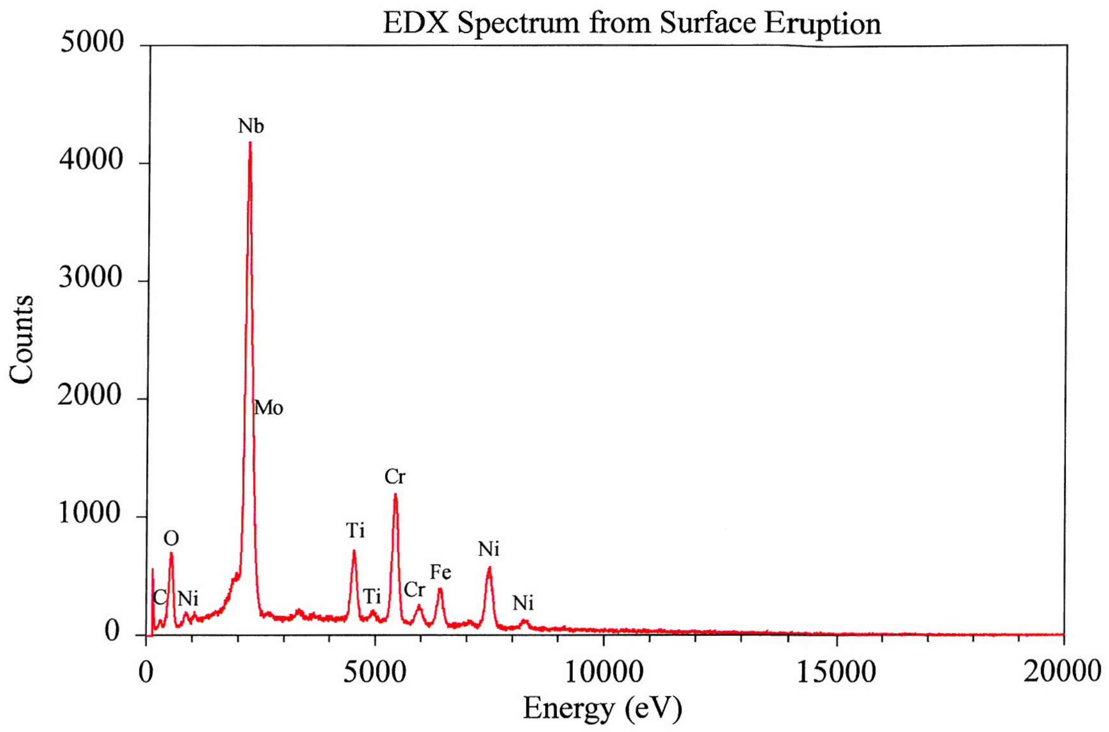

Figure 5.14: EDX spectrum from surface eruption formed by the oxidation of an (Nb,Ti)C primary carbide.

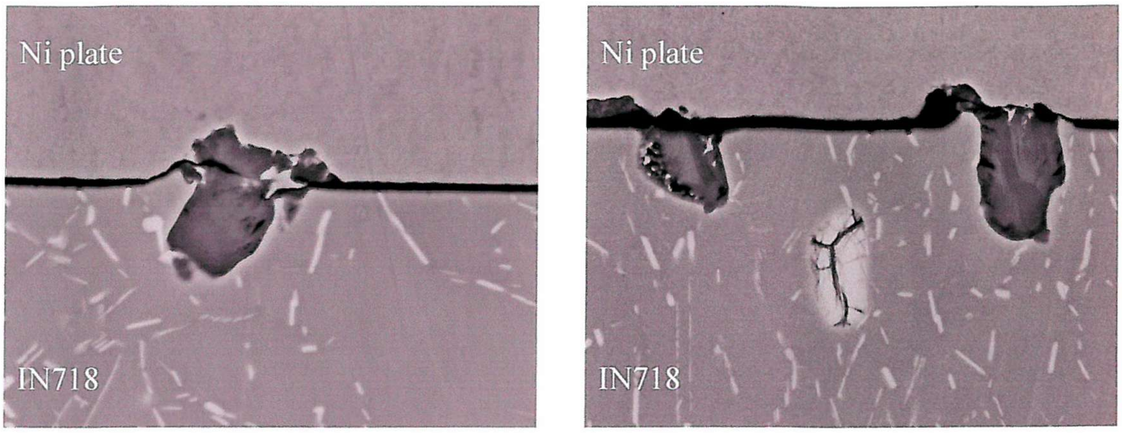

(a) 128 h at 550°C 5 µm (b) 128 h at 550°C 5 µm

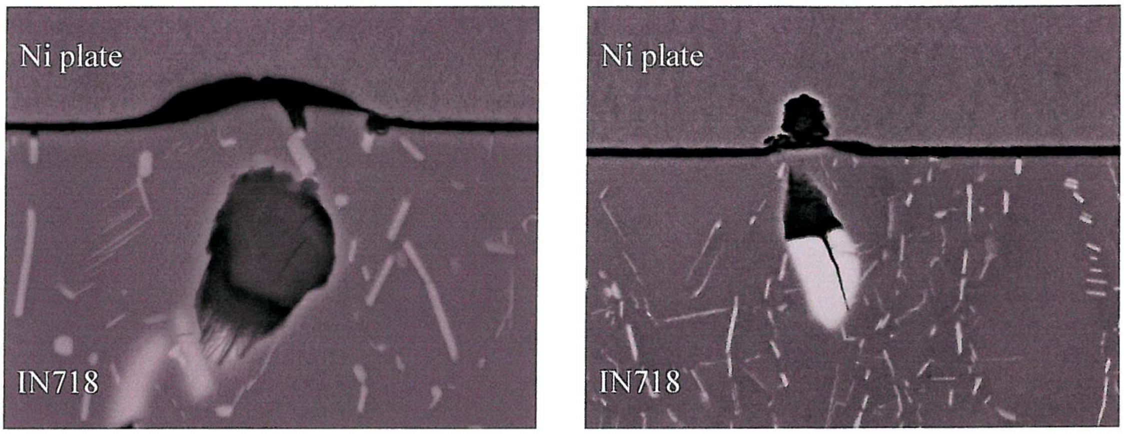

(c) 128 h at 550°C 5 µm (d) 8 h at 600°C 5 µm

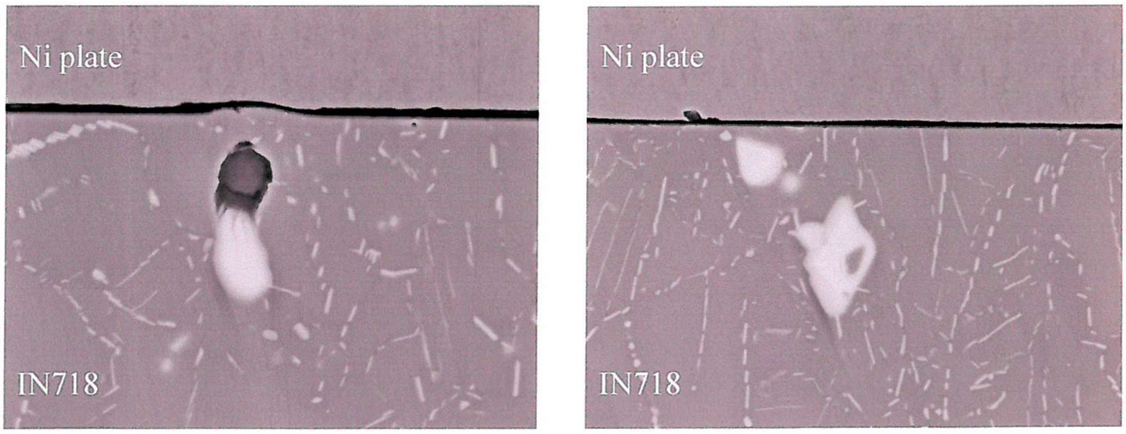

(e) 128 h at 550°C 5 µm (f) 128 h at 550°C 5 µm

Figure 5.15: Backscattered electron images showing examples of matrix deformation near oxidised surface and sub-surface primary carbide particles.

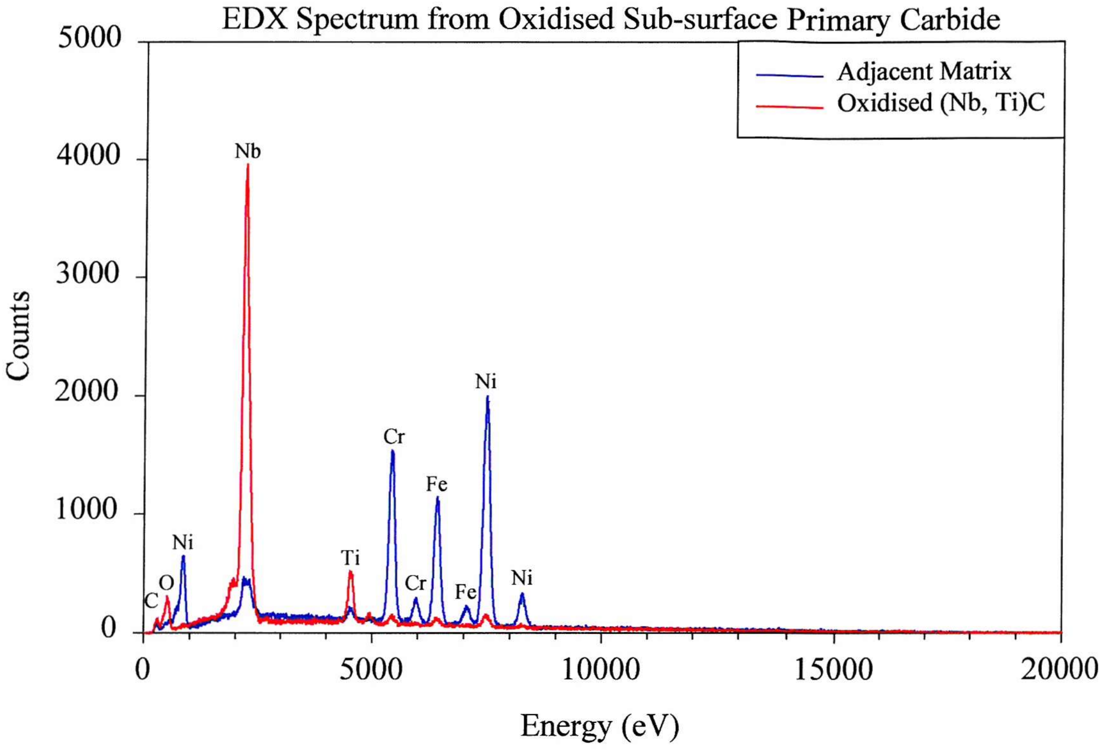

Figure 5.16: EDX spectrum from the oxidised sub-surface particle shown in Figure 5.15(c). A spectrum from the adjacent matrix is included for comparison.

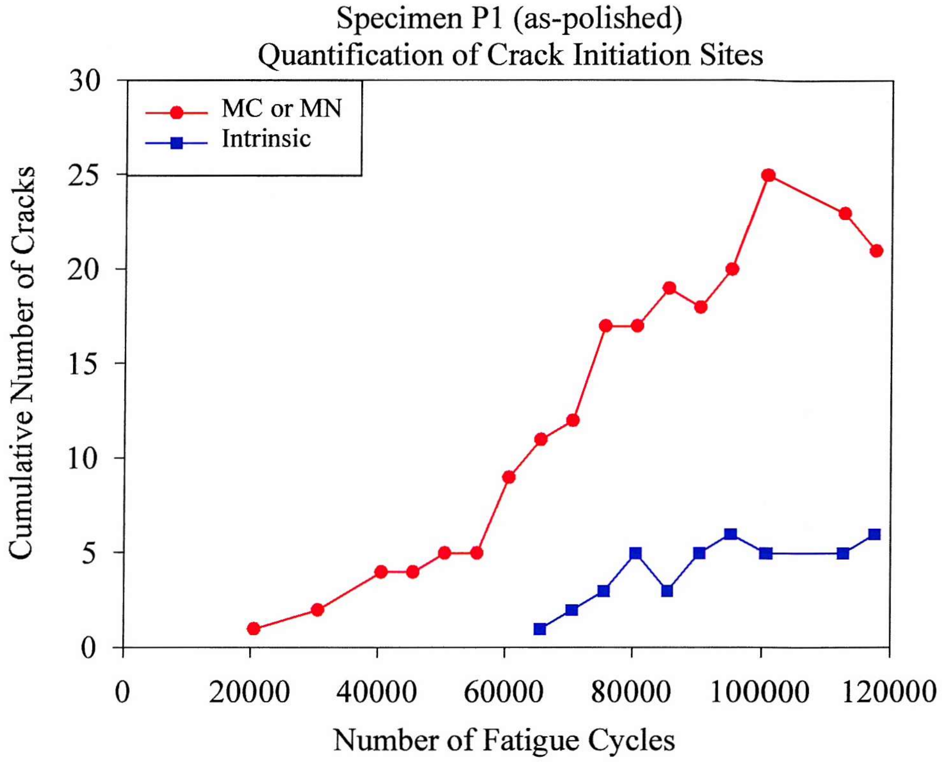

(a)

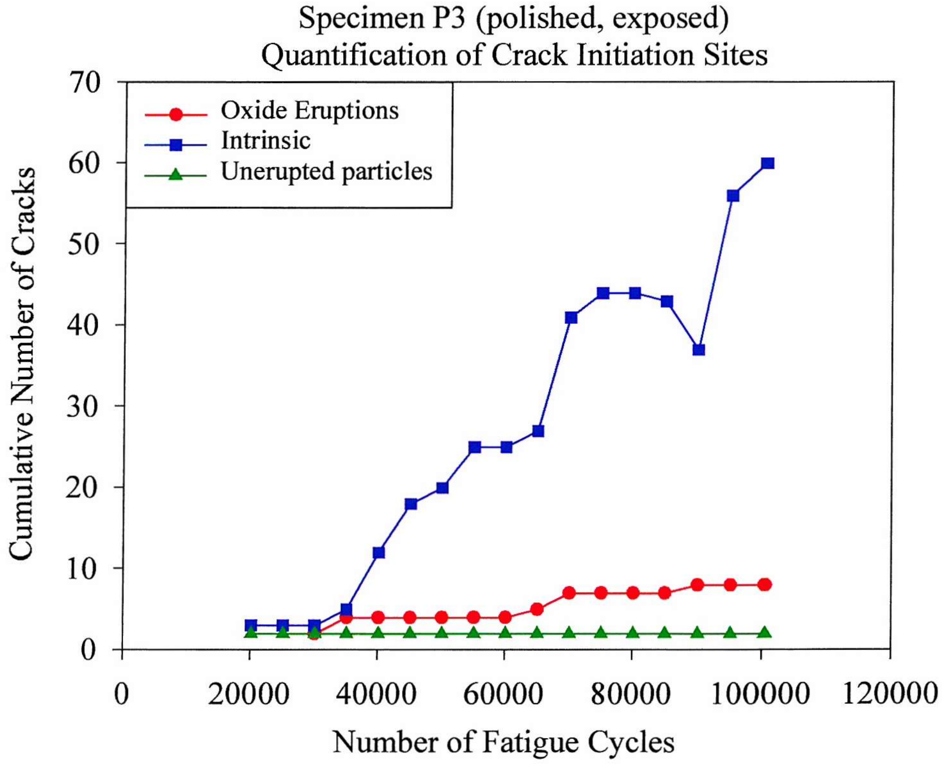

(b)

Figure 5.17: Quantification of crack initiation sites in plain bend specimens of extruded IN718. (a) As-polished specimen; (b) polished & exposed 4hrs at 600°C.

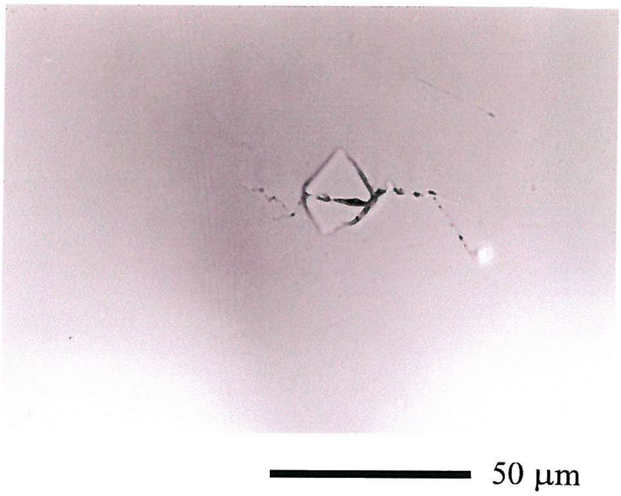

Figure 5.18: Room temperature crack initiation at a primary carbide particle in an unexposed specimen of extruded bar material. (Optical).

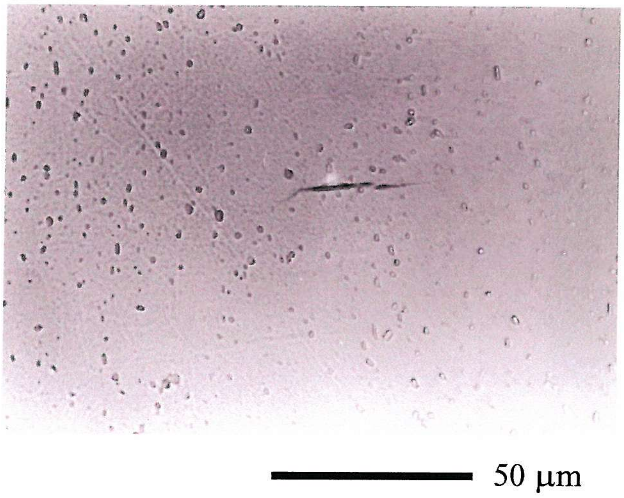

Figure 5.19: Intrinsic room temperature crack initiation in a thermally exposed specimen of extruded bar material. (Optical).

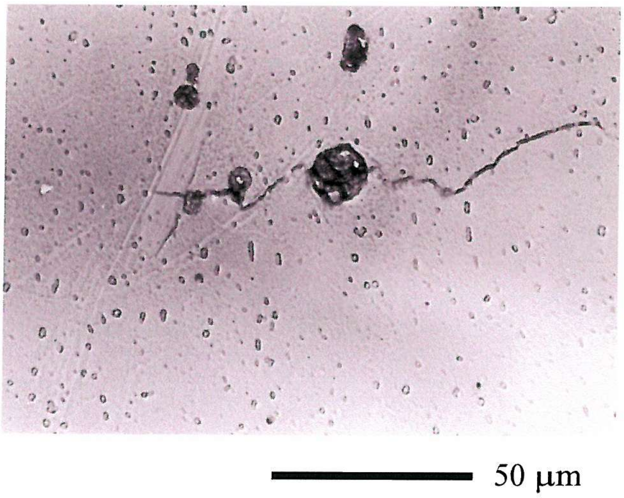

Figure 5.20: Room temperature initiation at an erupted oxidised primary carbide. (Optical)

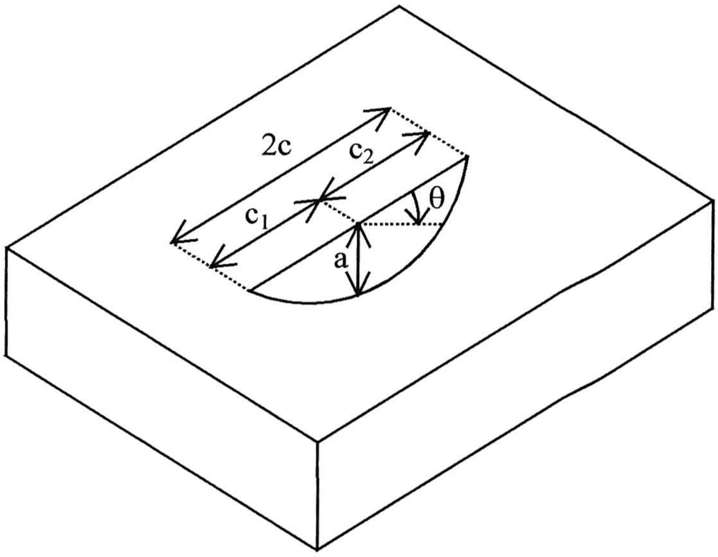

Figure 5.21: Convention used for describing short crack lengths.

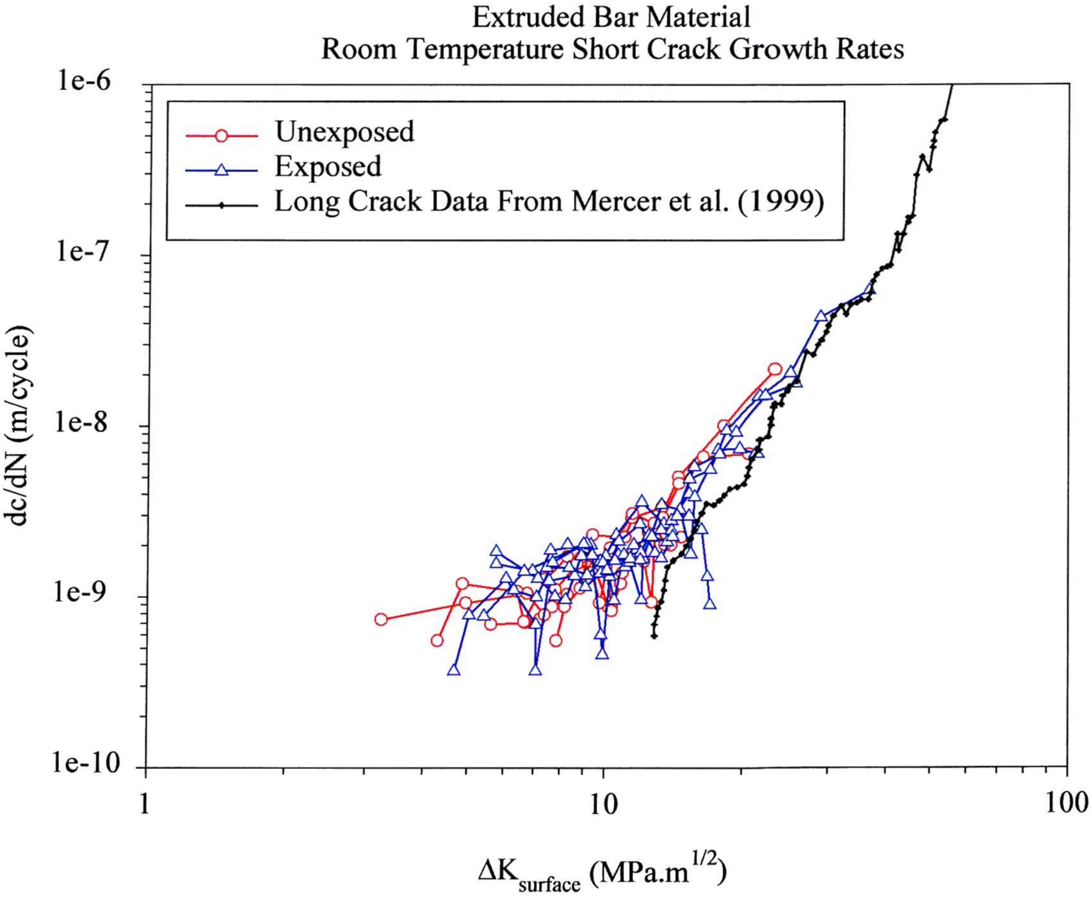

Figure 5.22: Room temperature short crack growth rates in extruded bar material.

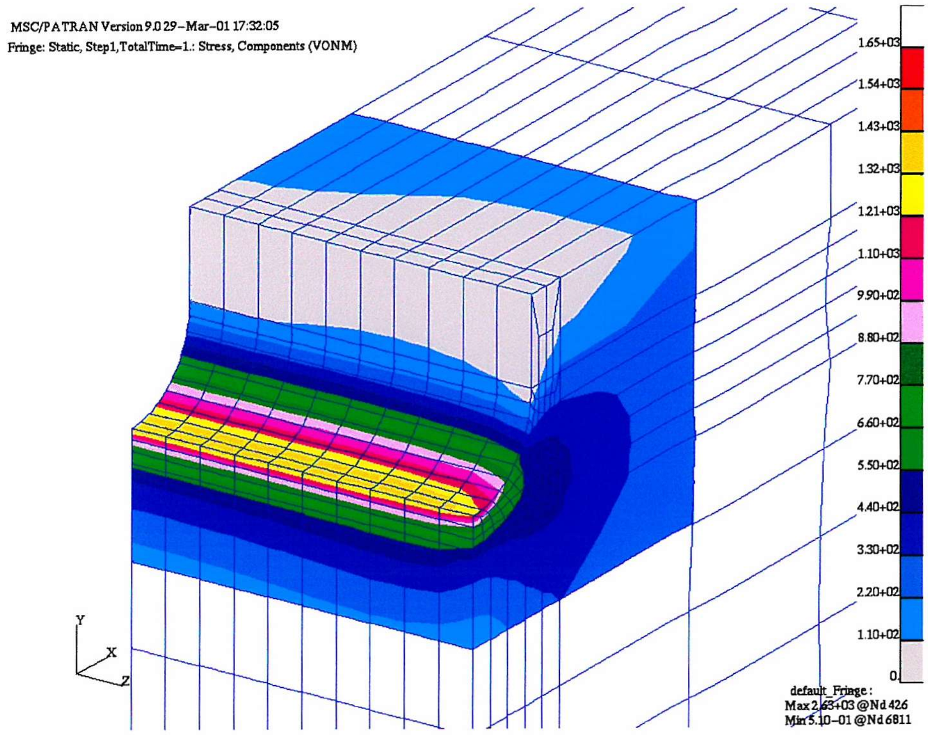

(a) Elastic

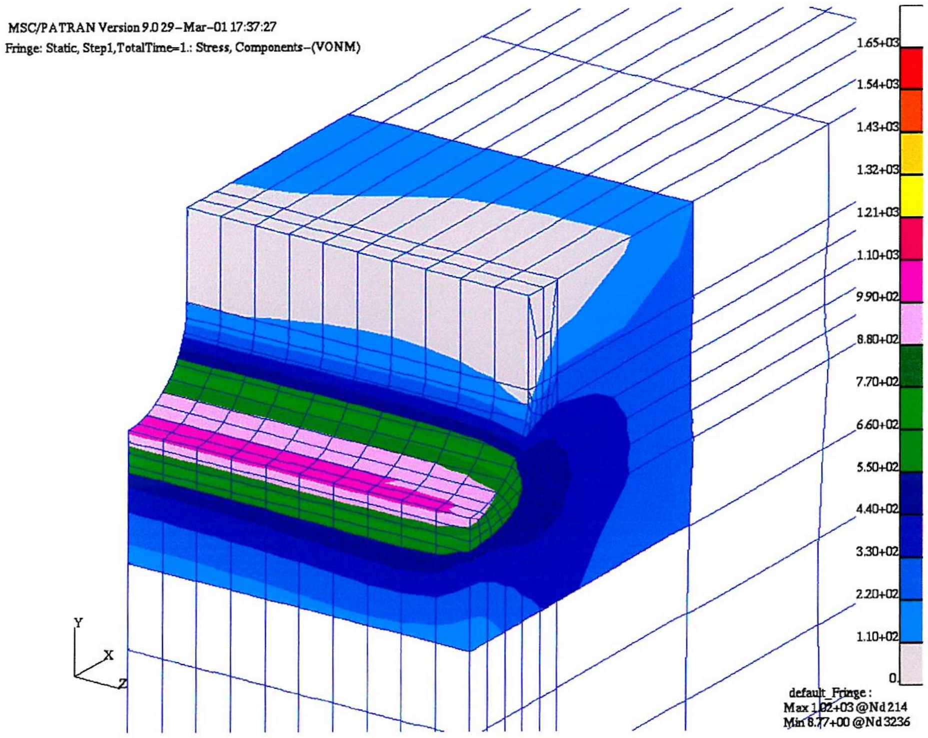

(b) Elastic-plastic

Figure 5.23: Von Mises stress in the notch root predicted by the FE model after the first loading step at σ_{max} = 750 MPa.

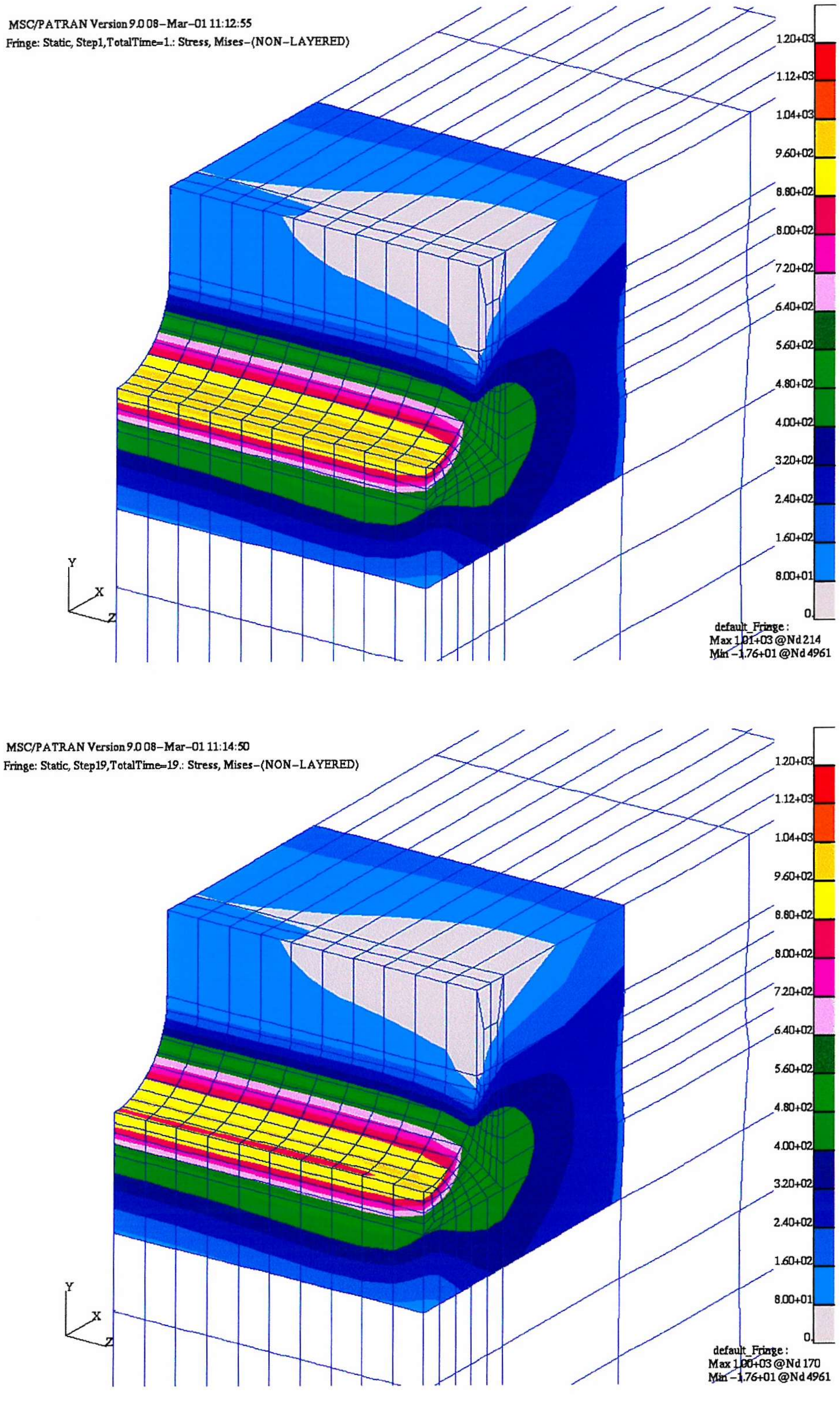

(a)

(b)

Figure 5.24: Cyclic softening in the notch root predicted by the elastic-plastic material model. (a) von Mises stress after the first loading step; (b) von Mises stress after the tenth loading step. σ_{max} = 750 MPa.

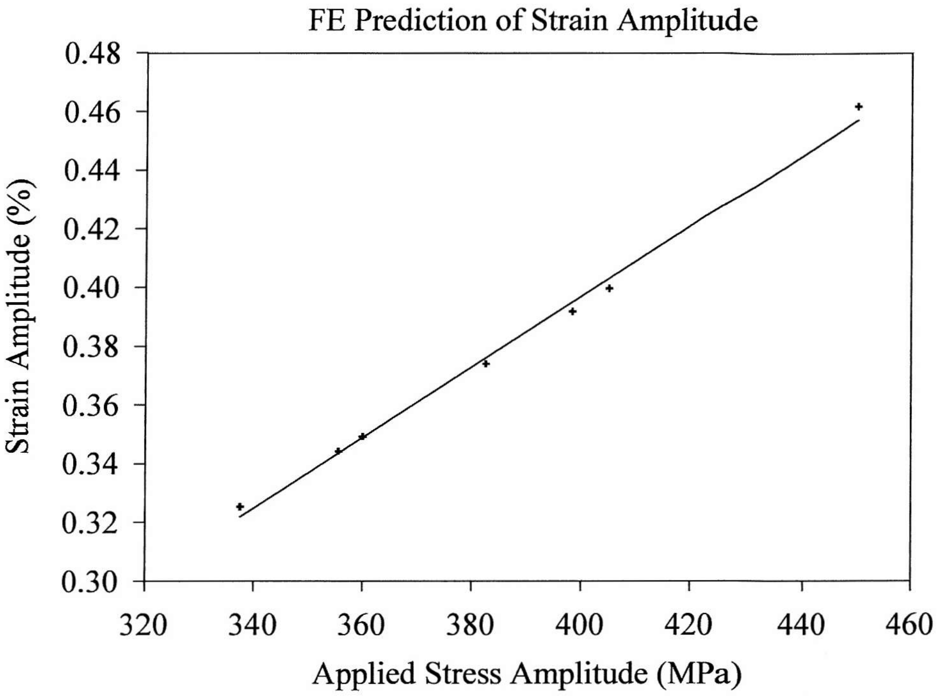

Figure 5.25: Variation in predicted strain amplitude, ε_{amp}, with applied nominal stress amplitude σ_{amp}. (After 10 complete fatigue cycles of model).

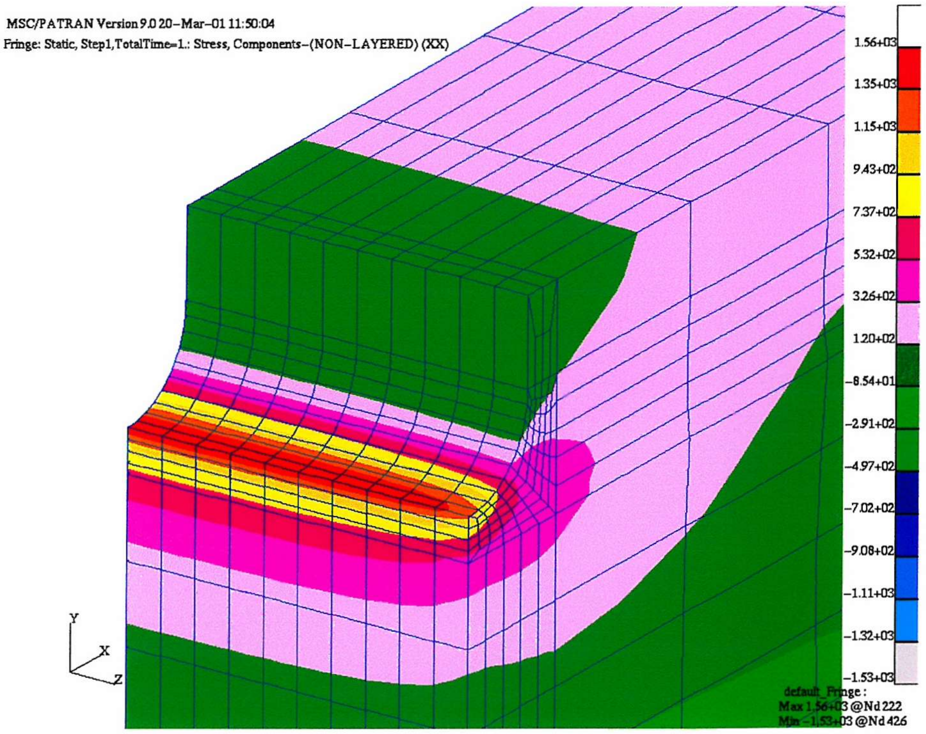

Figure 5.26: Results from an elastic-only FE model of U-notch specimen, showing contours of the σ_{xx} component of stress (i.e. the component parallel to the x axis). The nominal applied bending stress along the x axis was 750 MPa.

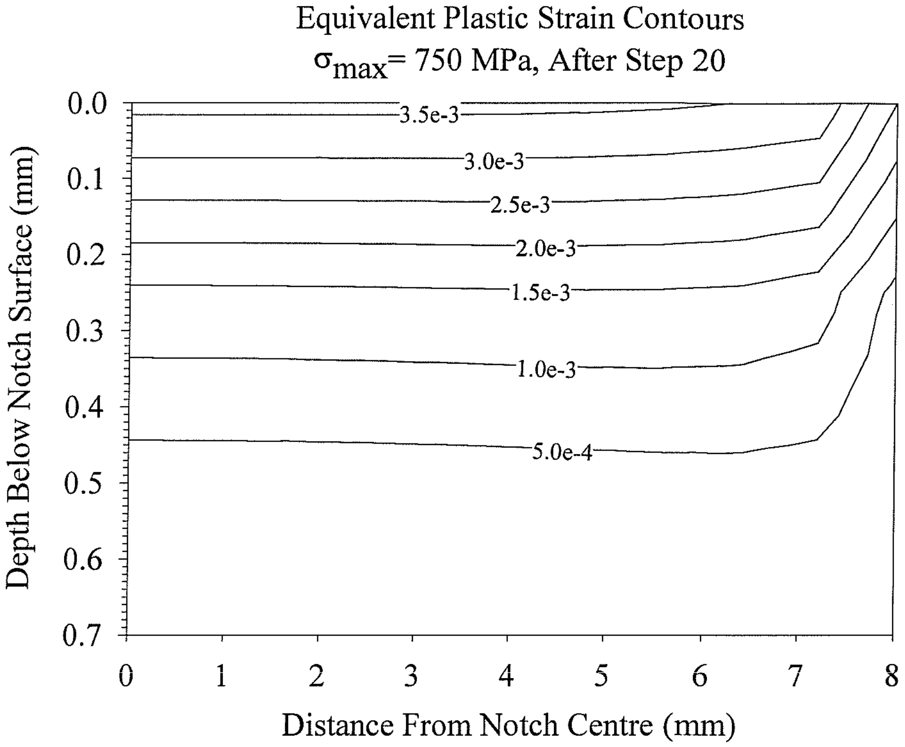

(a)

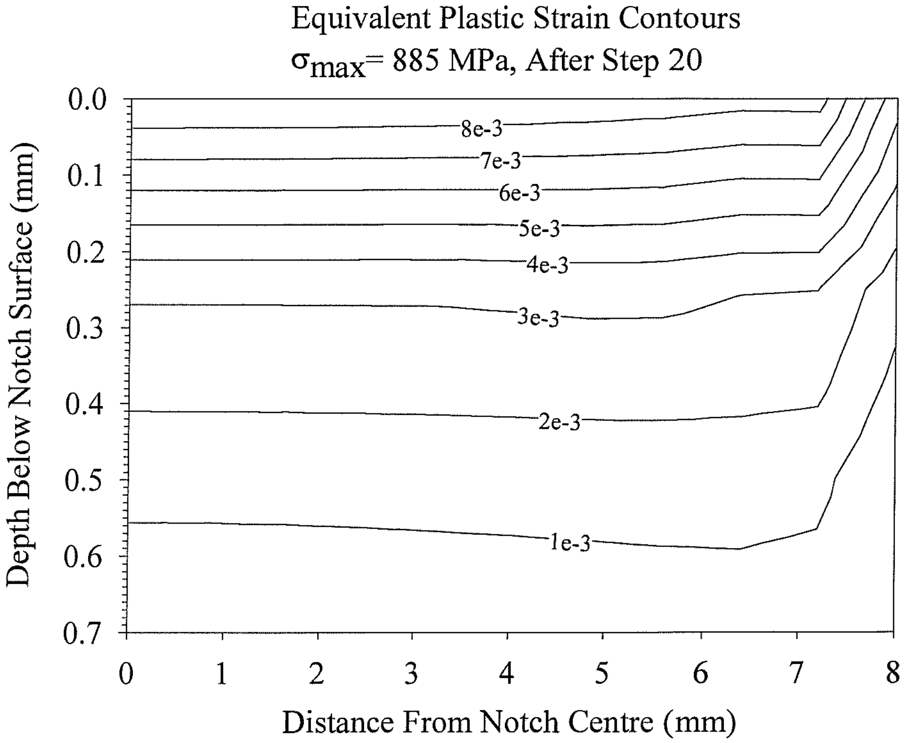

(b)

Figure 5.27: Contour plots of equivalent plastic strain in the notch root. (a) σ_{max} = 750 MPa; (b) σ_{max} = 885 MPa.

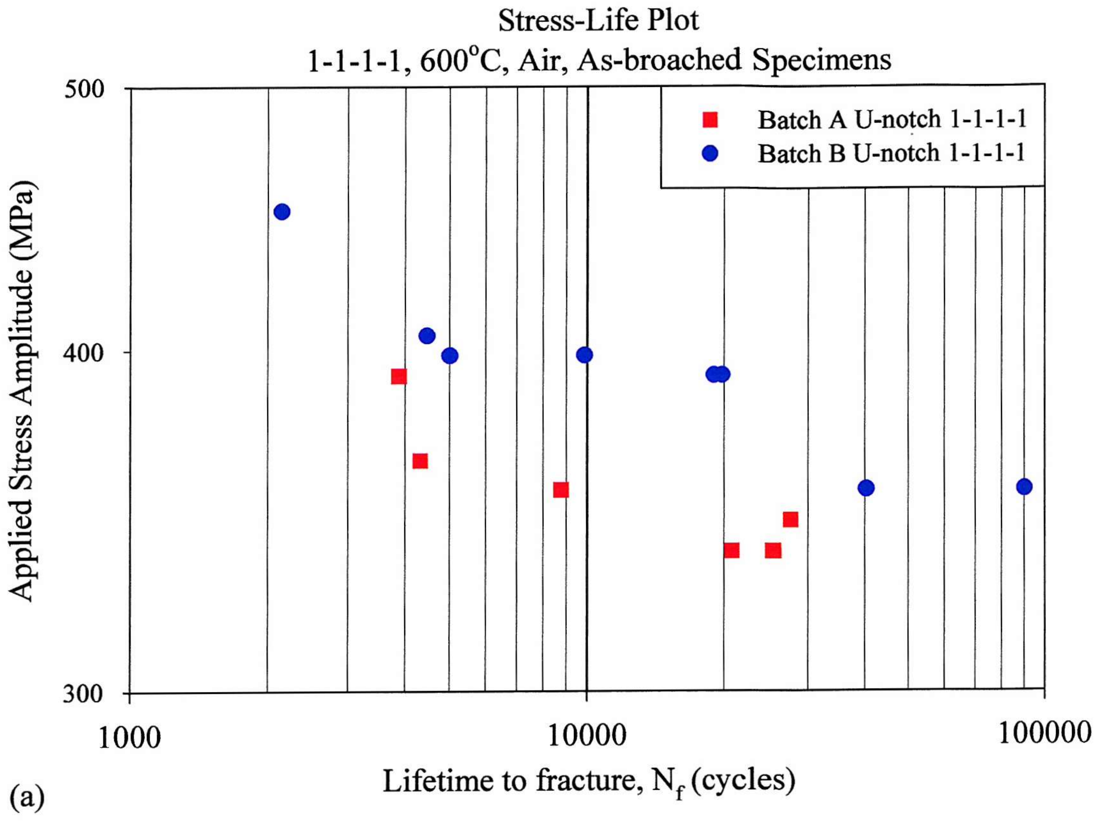

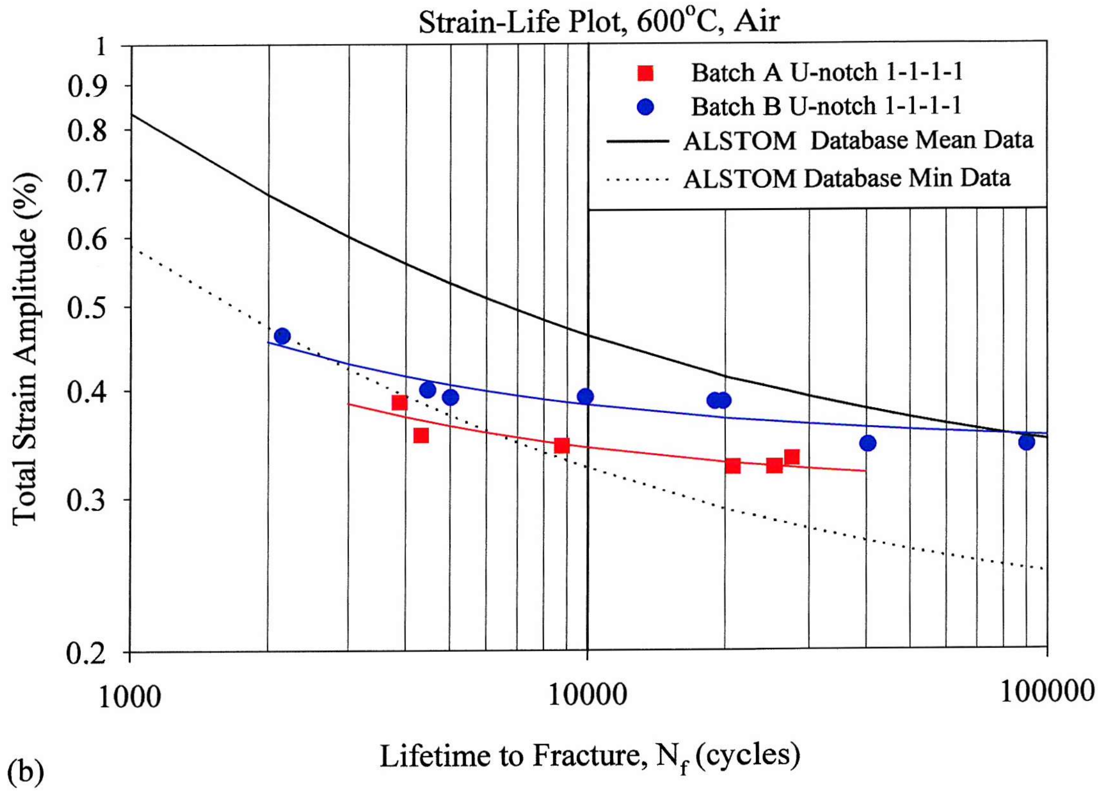

Figure 5.28: Stress-life and strain-life curves for as-broached Batch A and B U-notch specimens, 1-1-1-1, 600°C, Air. (b) also shows aggregate ALSTOM test data from a variety of specimens.

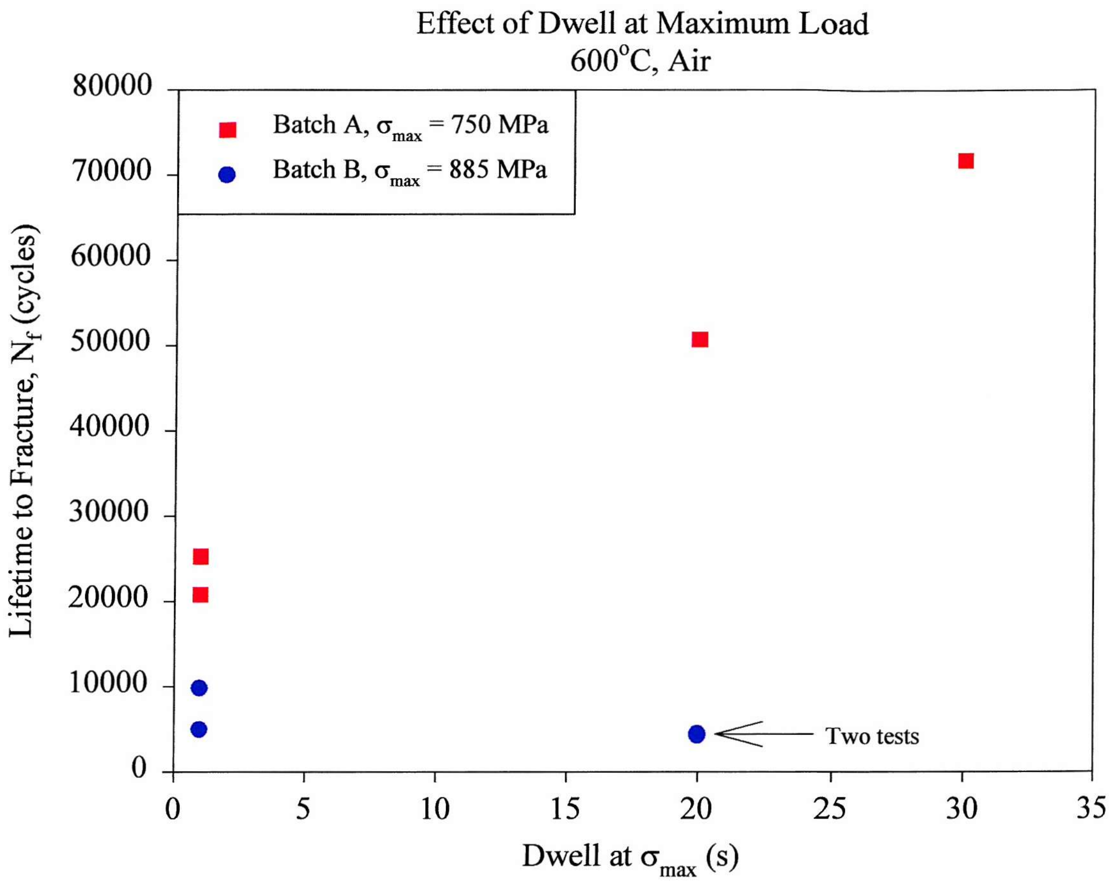

Figure 5.29: Effect of dwell at maximum load on fatigue life of as-broached U-notch specimens.

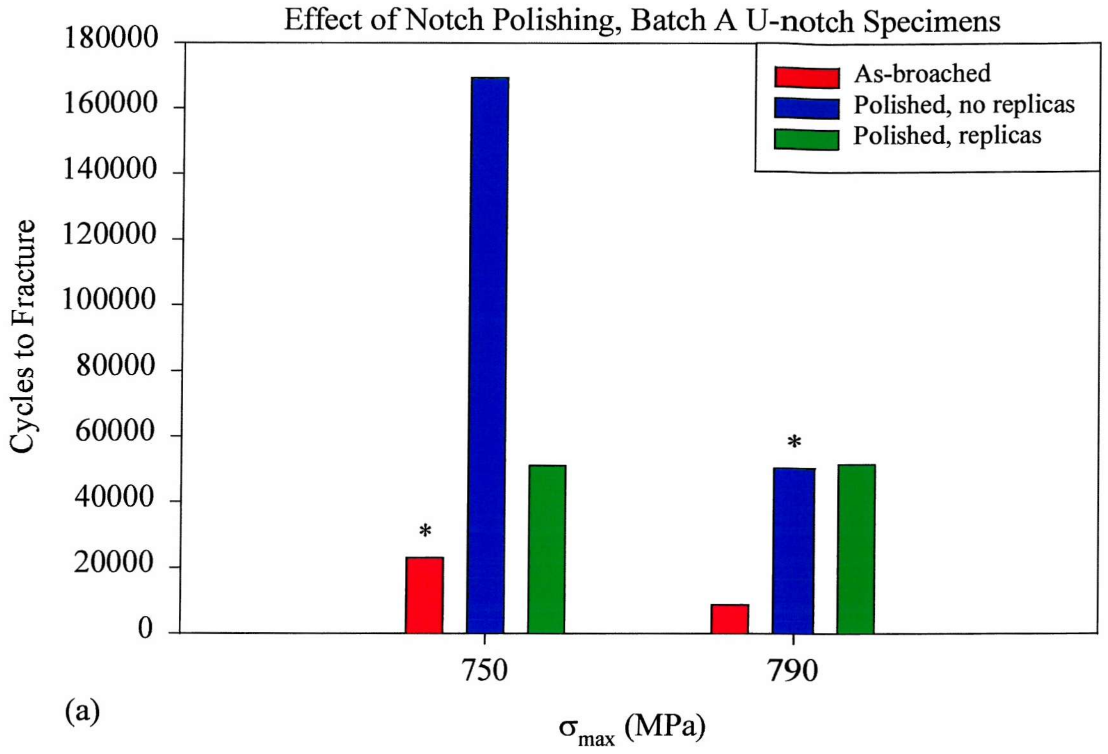

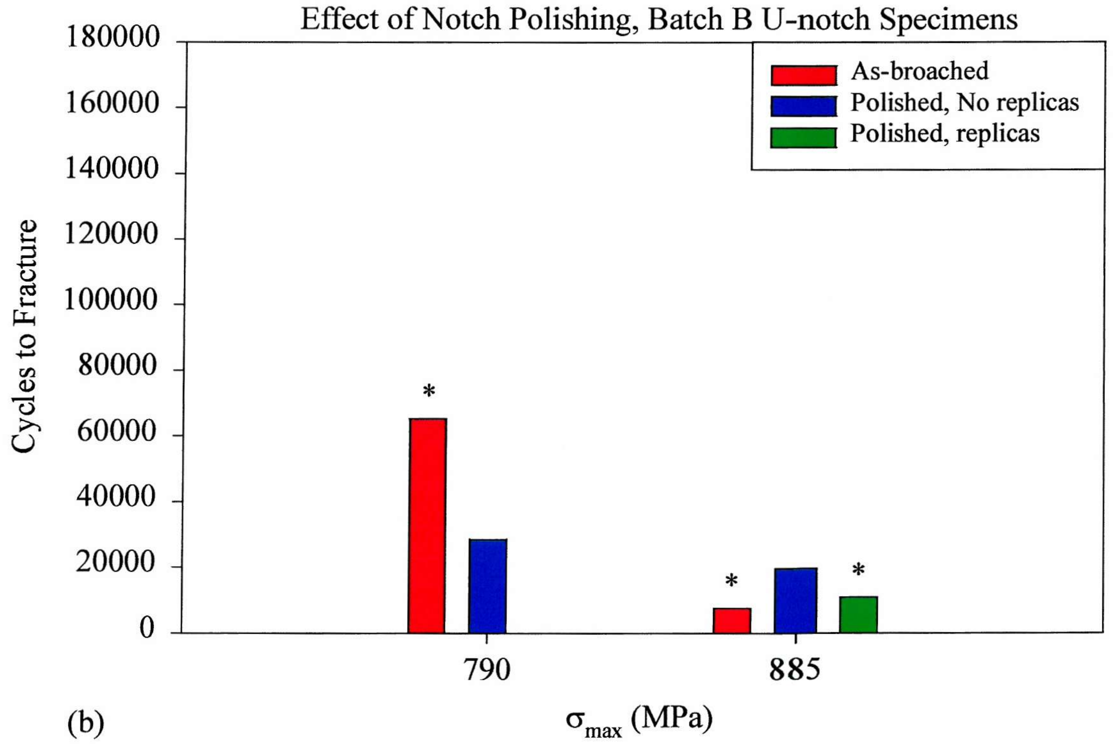

Figure 5.30: Effect of U-notch surface finish and the taking of replicas on specimen lifetime. (a) Batch A specimens; (b) Batch B specimens. * denotes average of two test results.

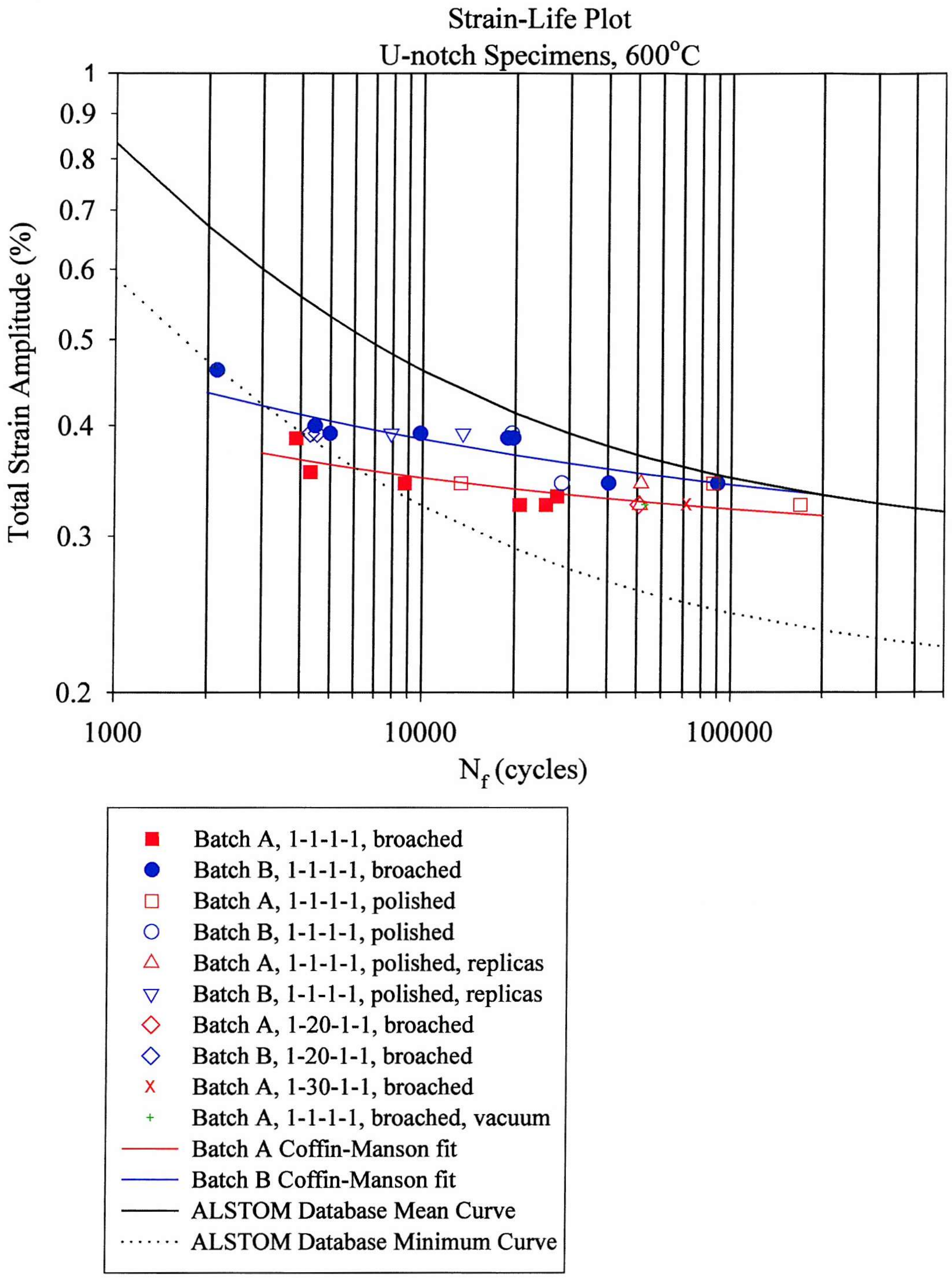

Figure 5.31: Strain-life data for all U-notch tests performed at 600°C.

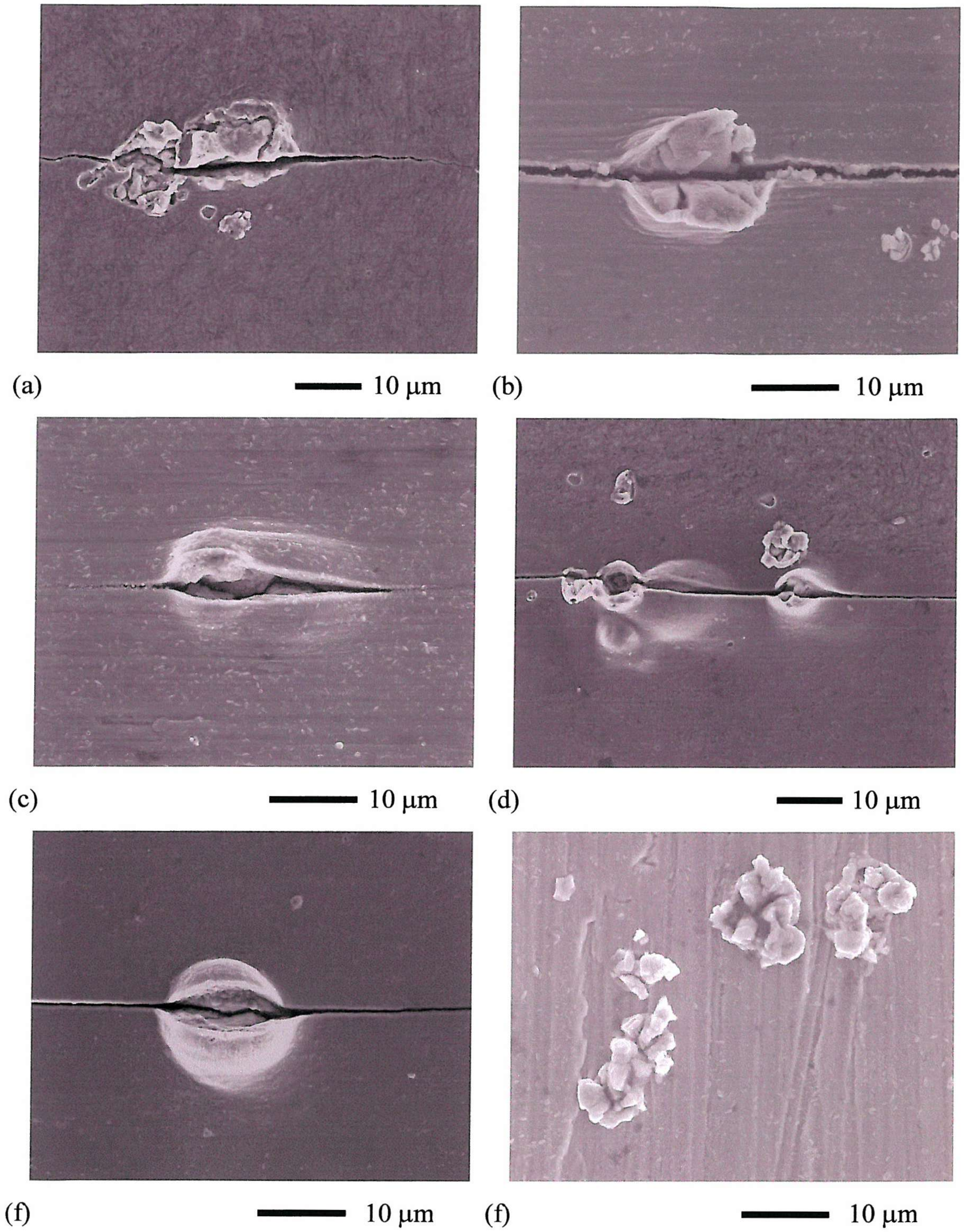

Figure 5.32: Examples of short crack initiation sites and eruptions observed in the notch root of Batch A specimens tested in air. Images (a) & (b) show cracks initiated from surface eruptions, with some deformation visible in (b). Images (c), (d) and (e) show the bulged sites commonly seen in the notch root. Image (f) shows surface eruptions with no crack initiation. (SEM, SEI).

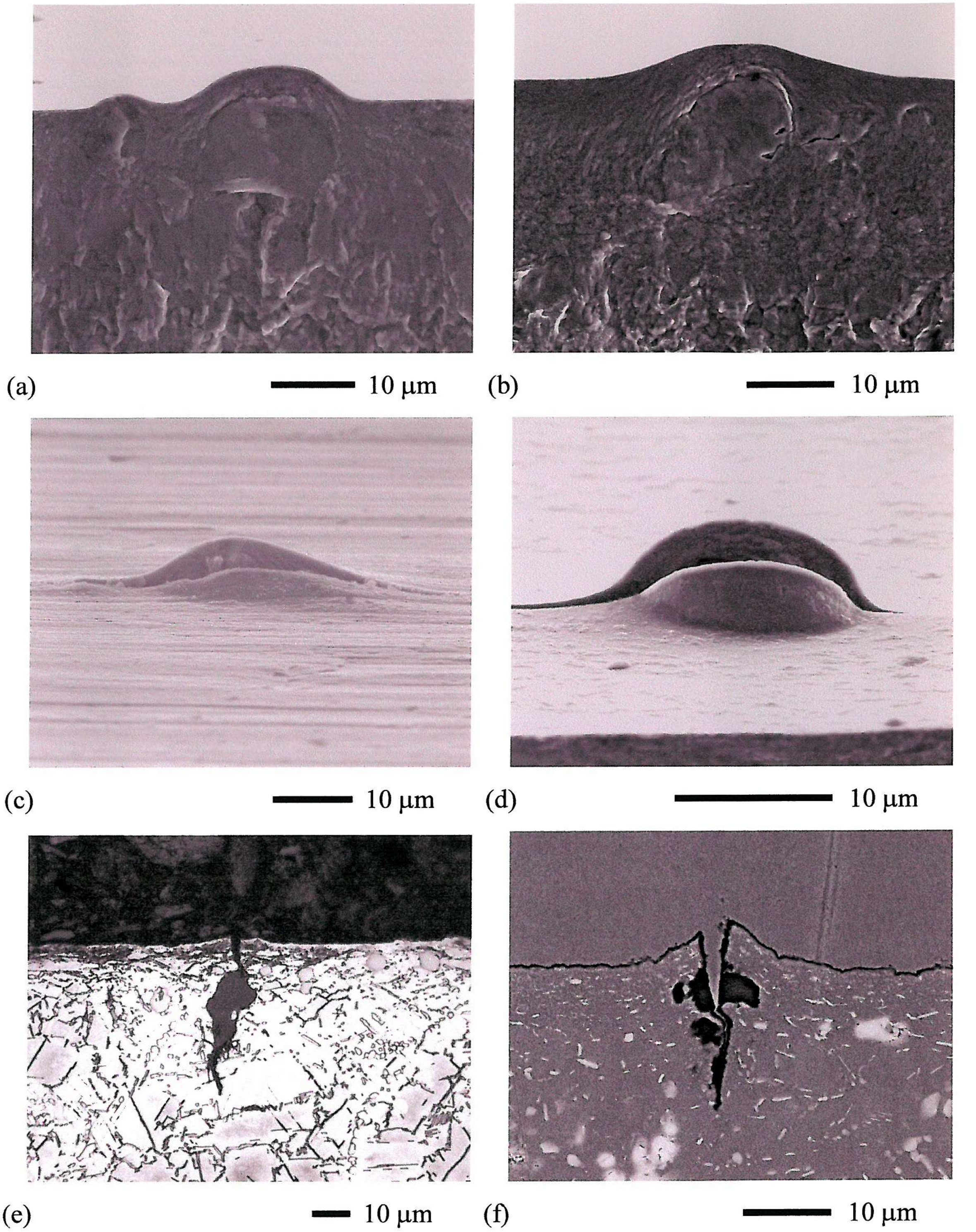

Figure 5.33: Post-fracture images of crack initiation sites at bulge-like features associated with sub-surface oxidised primary carbides. All images are from Batch A U-notch specimens tested in air. (a)-(d) SEM, SEI; (e) Optical micrograph; (f) SEM, BEI.

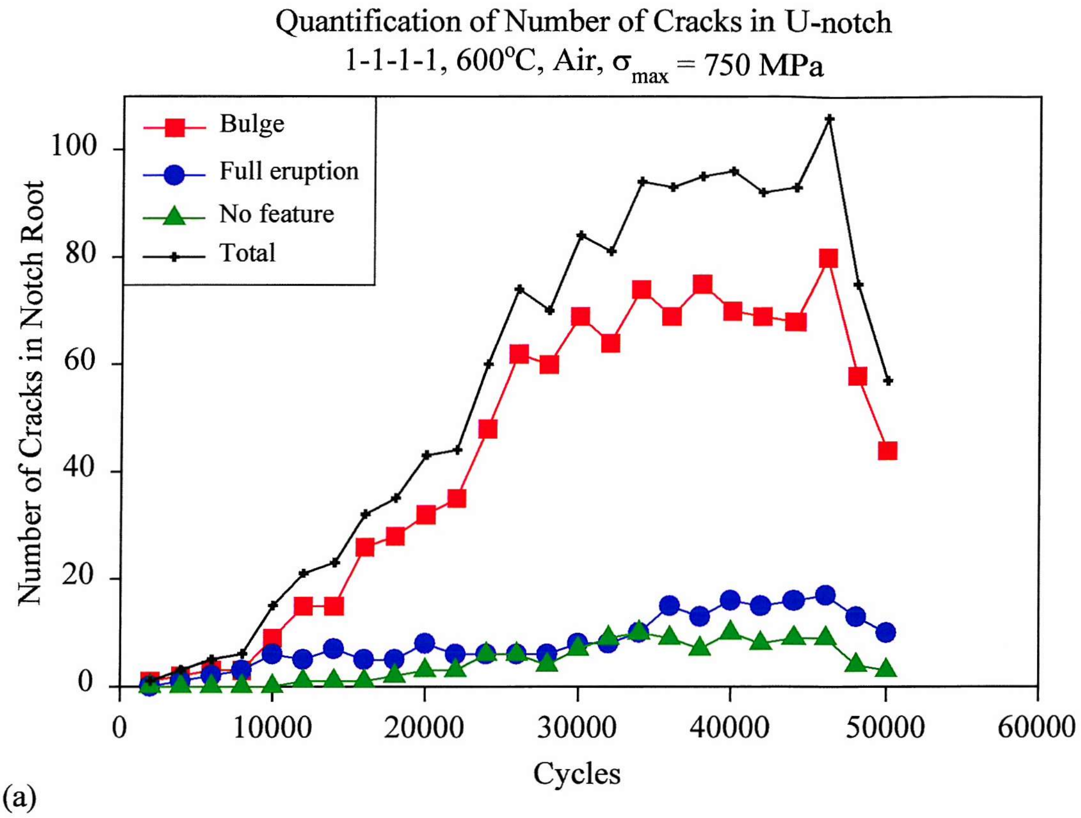

(a)

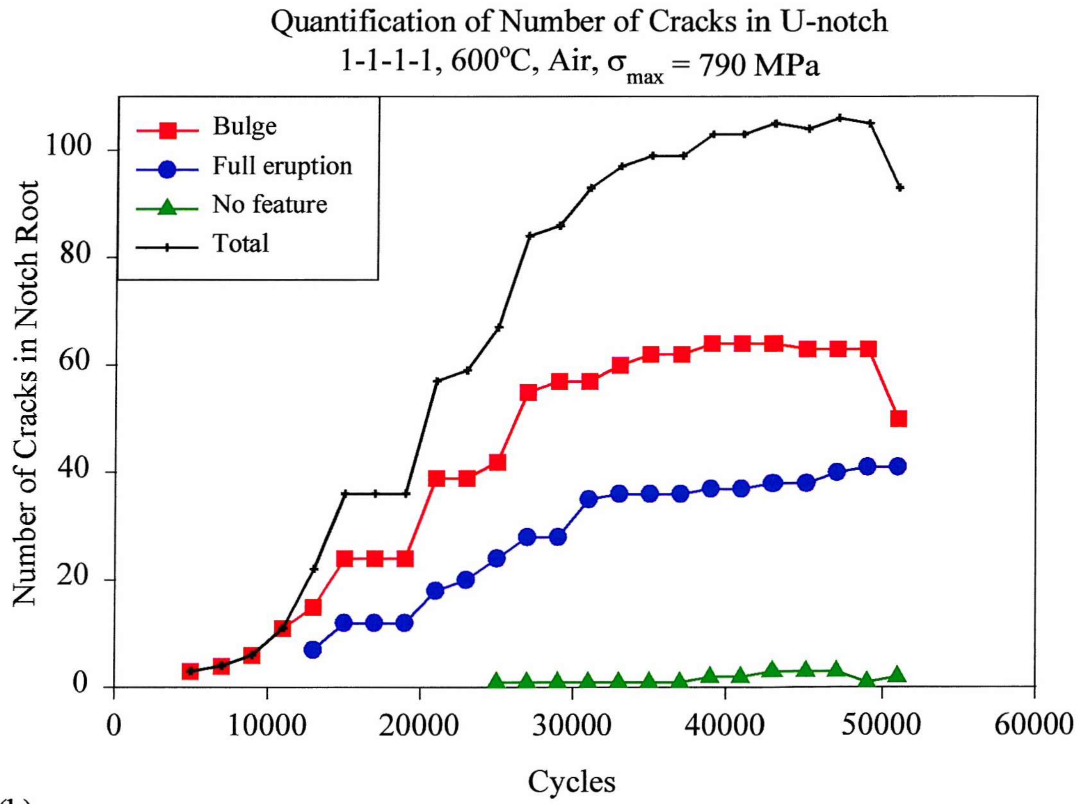

(b)

Figure 5.34: Quantification of number of cracks observed on replicas from polished Batch A U-notch specimens: (a) σ_{max} = 750 MPa; (b) σ_{max} = 790 MPa.

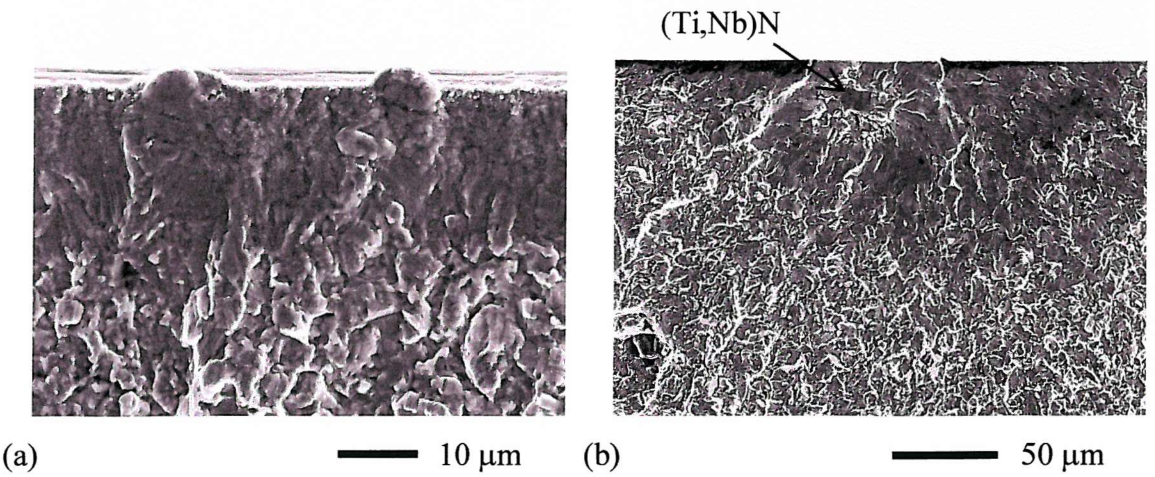

Figure 5.35: Examples of crack initiation sites in Batch B U-notch specimens tested in air at 600°C. (a) Small bulge-like features, but NOT associated with an oxidised (Nb,Ti)C particle. (b) Initiation at a sub-surface (Ti,Nb)N particle (arrowed). (SEM, SEI).

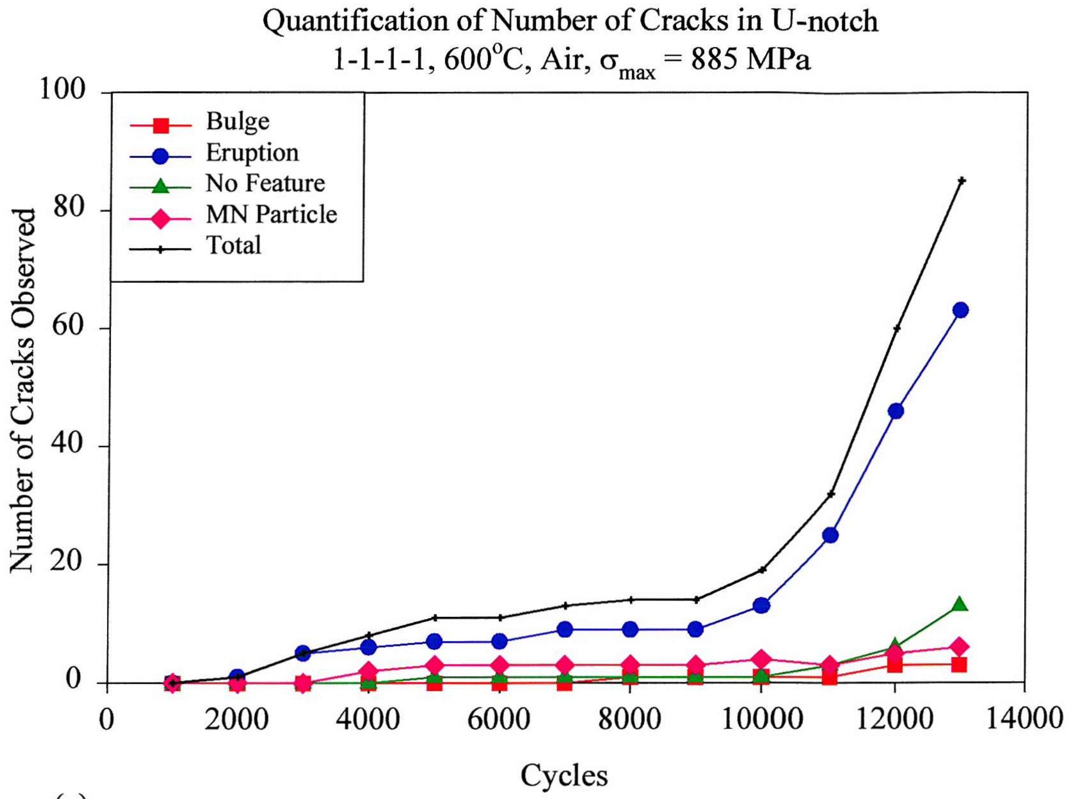

(a)

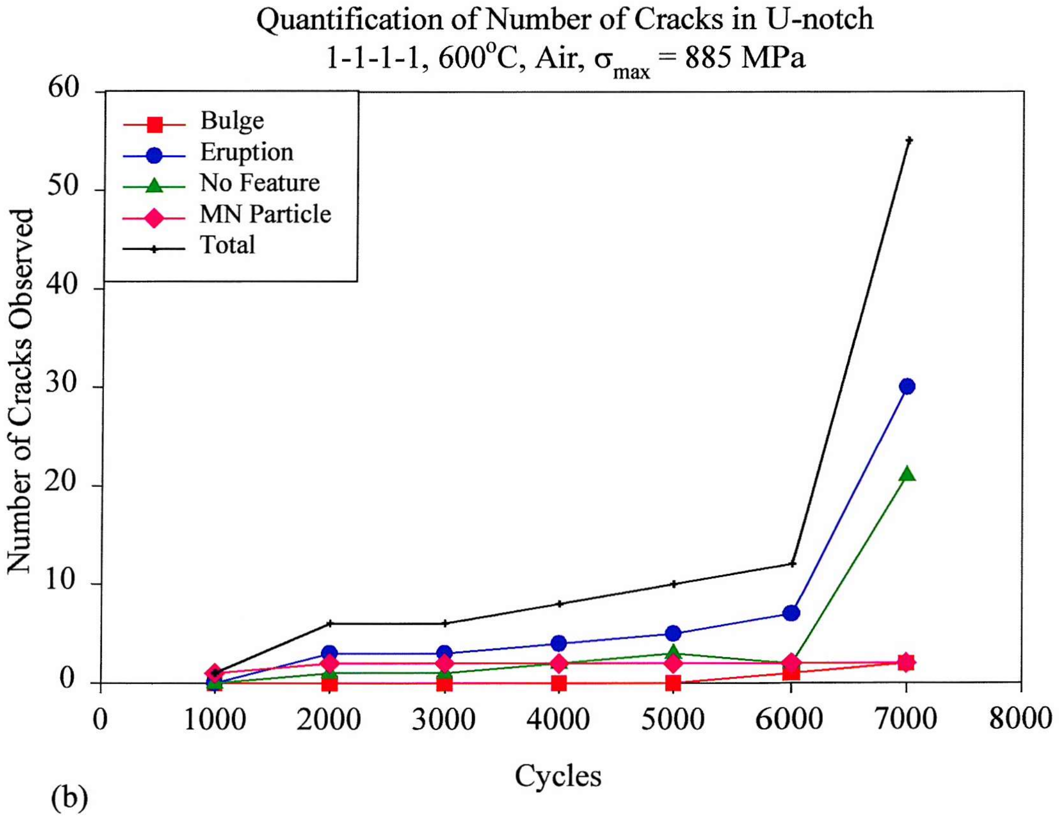

(b)

Figure 5.36: Quantification of number of cracks observed on replicas from polished Batch B U-notch specimens: (a) test B600-885-1-PR-01; (b) test B600-885-1-PR-02.

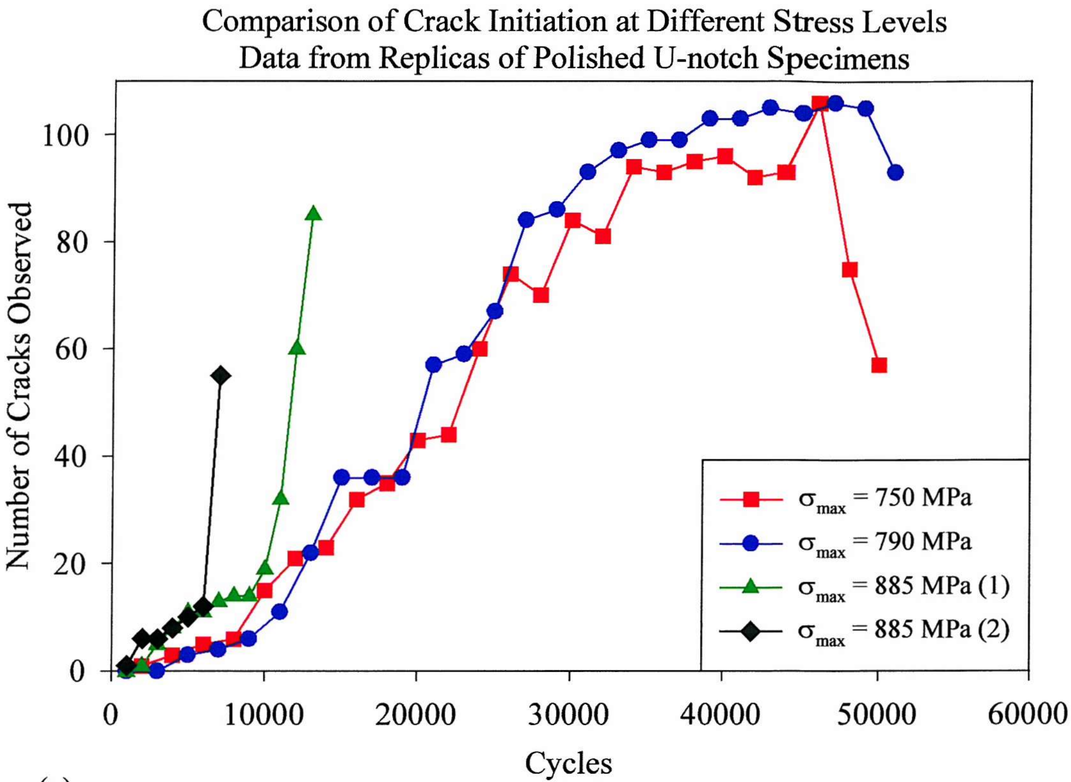

(a)

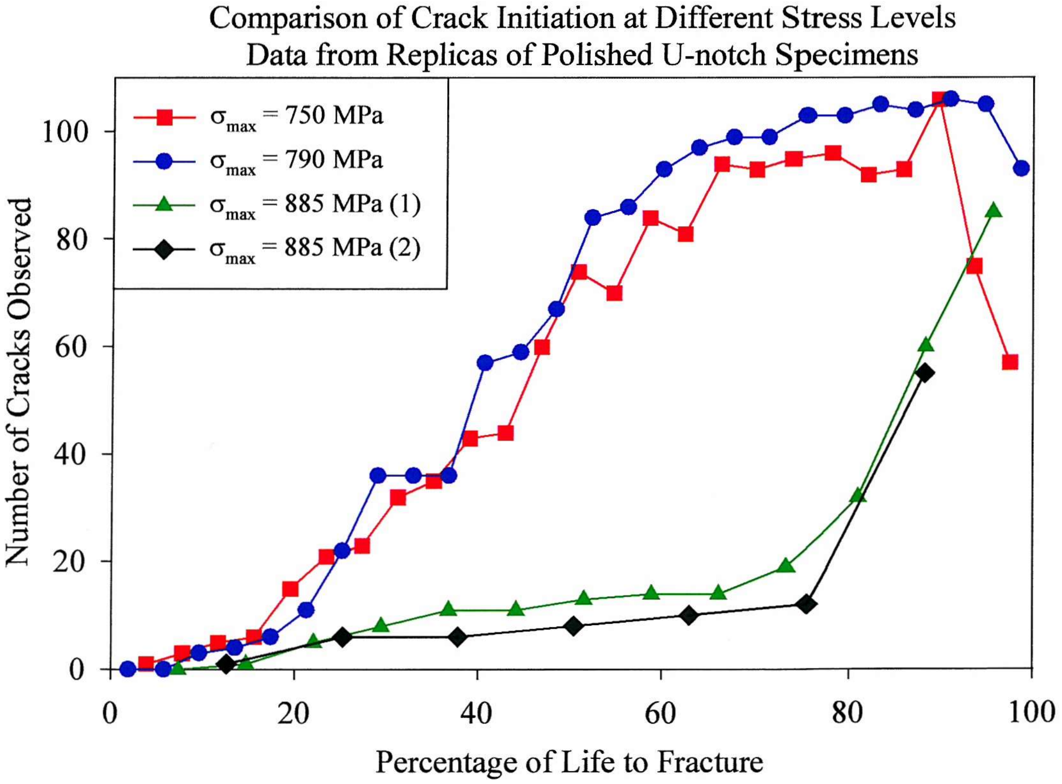

(b)

Figure 5.37: Comparison of crack initiation behaviour for tests at different stress levels. (a) in terms of cycles; (b) in terms of percentage of life to fracture.

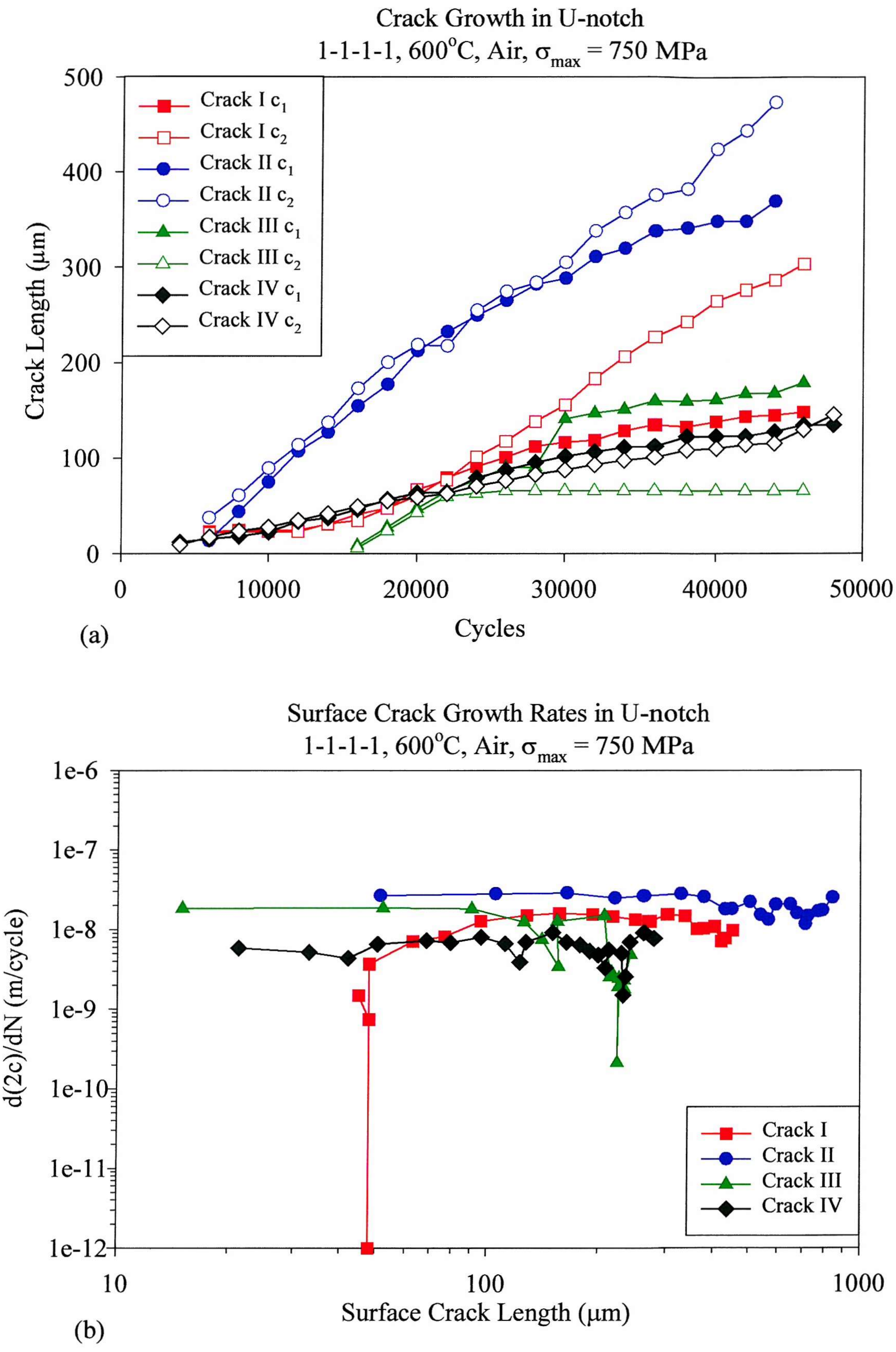

Figure 5.38: Growth of short cracks in U-notch root at 600°C in air, σ_{max} = 750 MPa. (Test A600-750-1-PR-01)

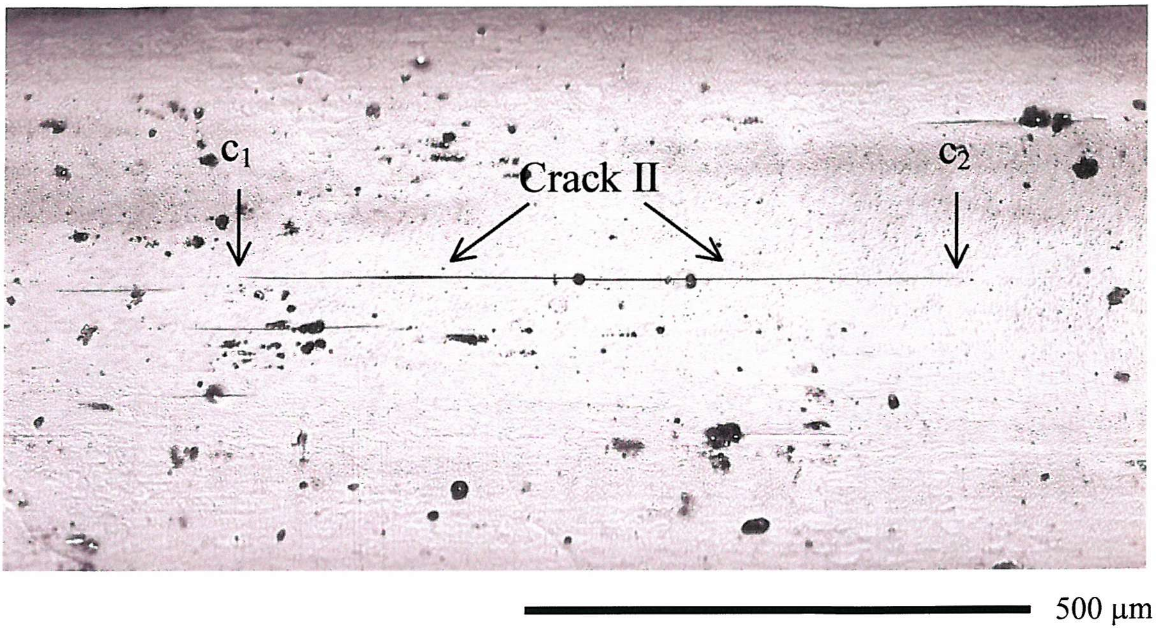

Figure 5.39: Optical image of replica taken from U-notch root. The image shows Crack II from test A600-750-1-PR-01 after 36000 cycles. Segment c_1 of the crack was retarded due to shielding by other cracks. Test conducted with σ_{max} = 750 MPa, R=0.1. The tensile axis is vertical.

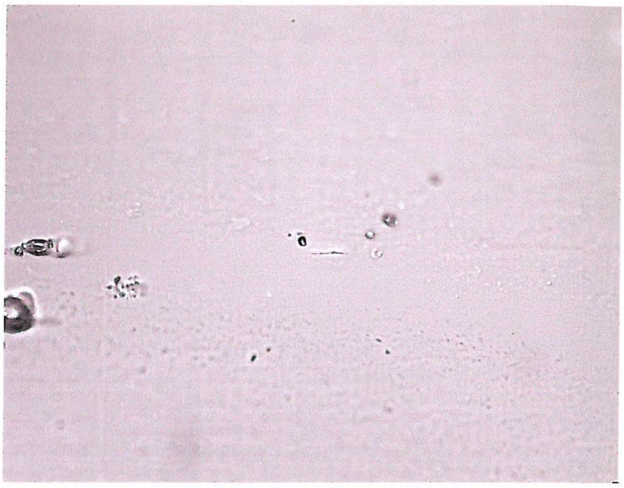

16000 cycles

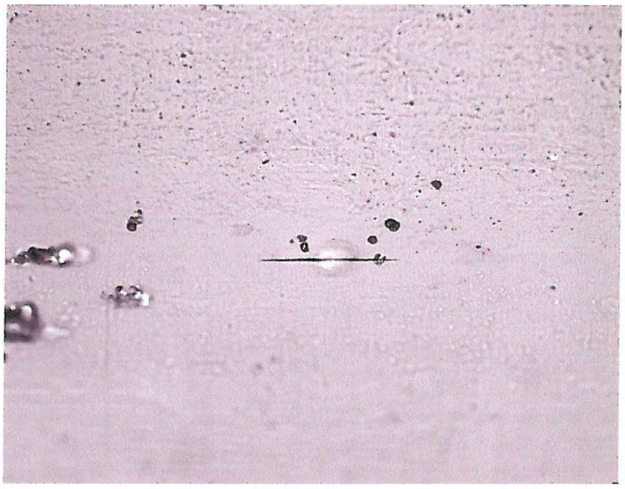

18000 cycles

20000 cycles

Figure 5.40: Sequence of optical micrographs from acetate replicas showing initiation of Crack III from test A600-750-1-PR-01. The development of bulge-like feature at the initiation site can be seen.

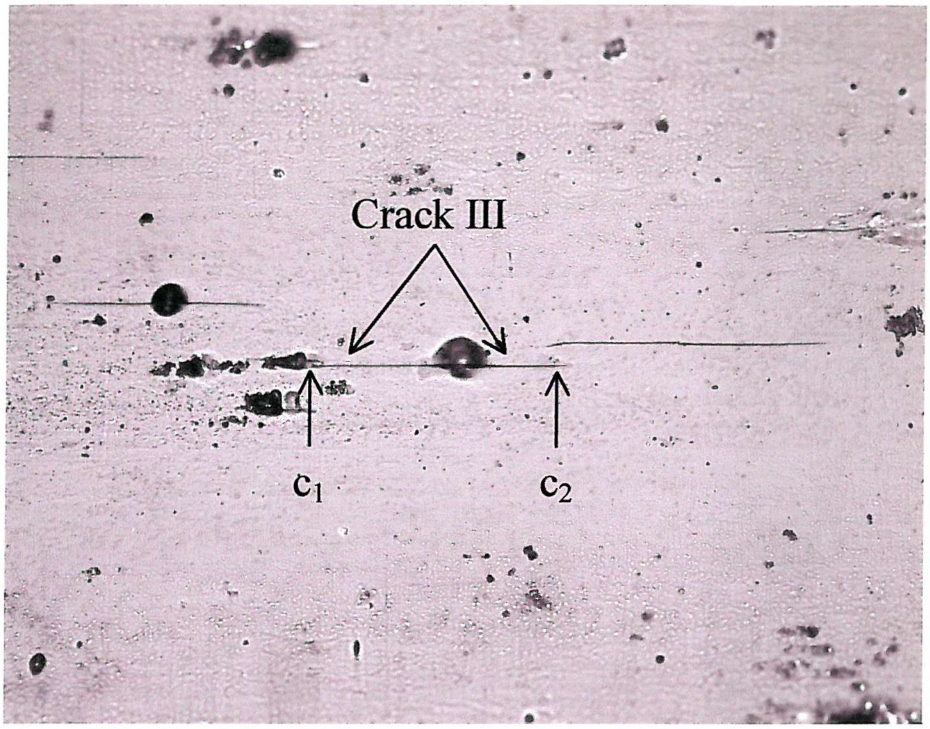

(a) 28000 cycles. 200 μm

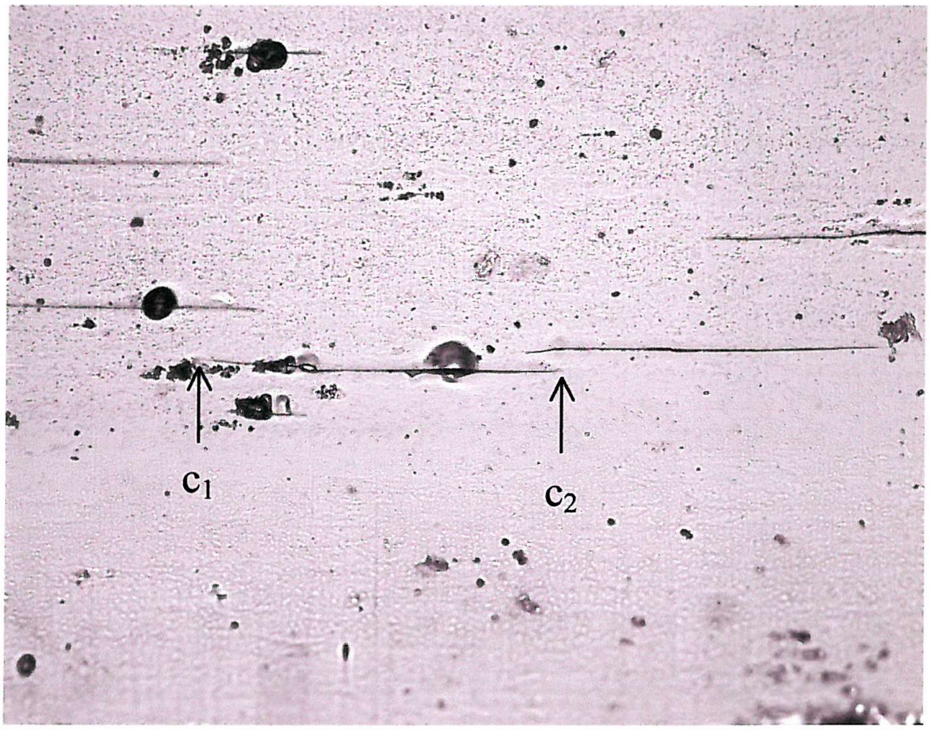

(b) 34000 cycles. 200 μm

Figure 5.41: Optical images from replicas showing arrest of one tip (c_2) of Crack III, while the other tip (c_1) continued to grow, assisted by coalescence. Note the bulge-like feature at the initiation site of Crack III. The tensile axis is vertical. (Test A600-750-1-PR-01).

(a) 48000 cycles

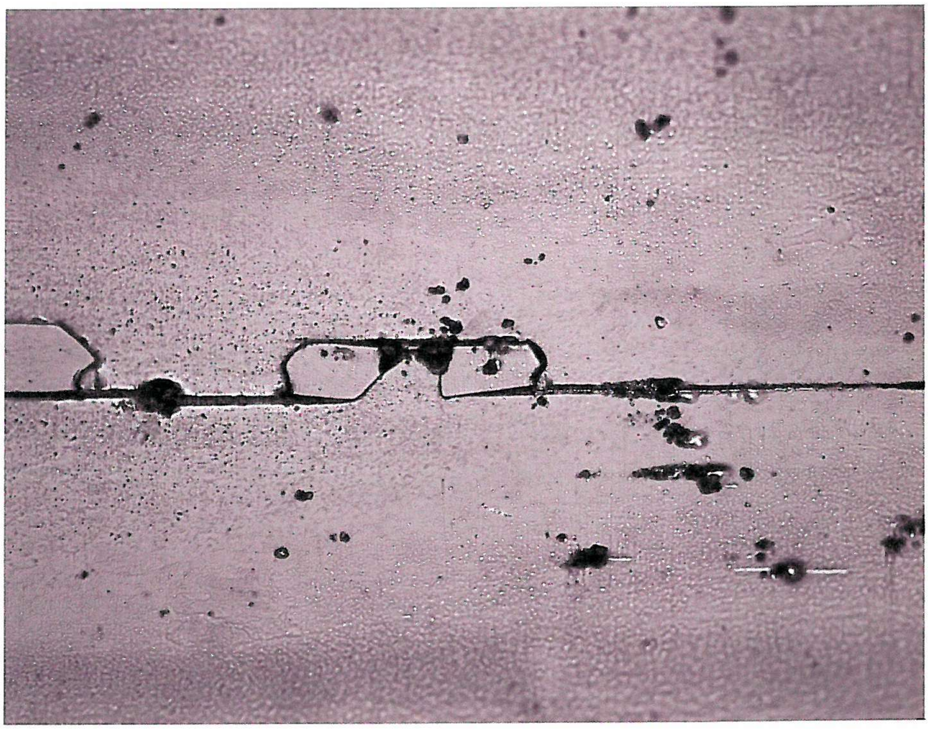

(b) 50000 cycles

Figure 5.42: Optical images from replicas showing rapid surface crack coalescence towards the end of the fatigue life. Test conducted with $\sigma_{max} = 750$ MPa, R=0.1.

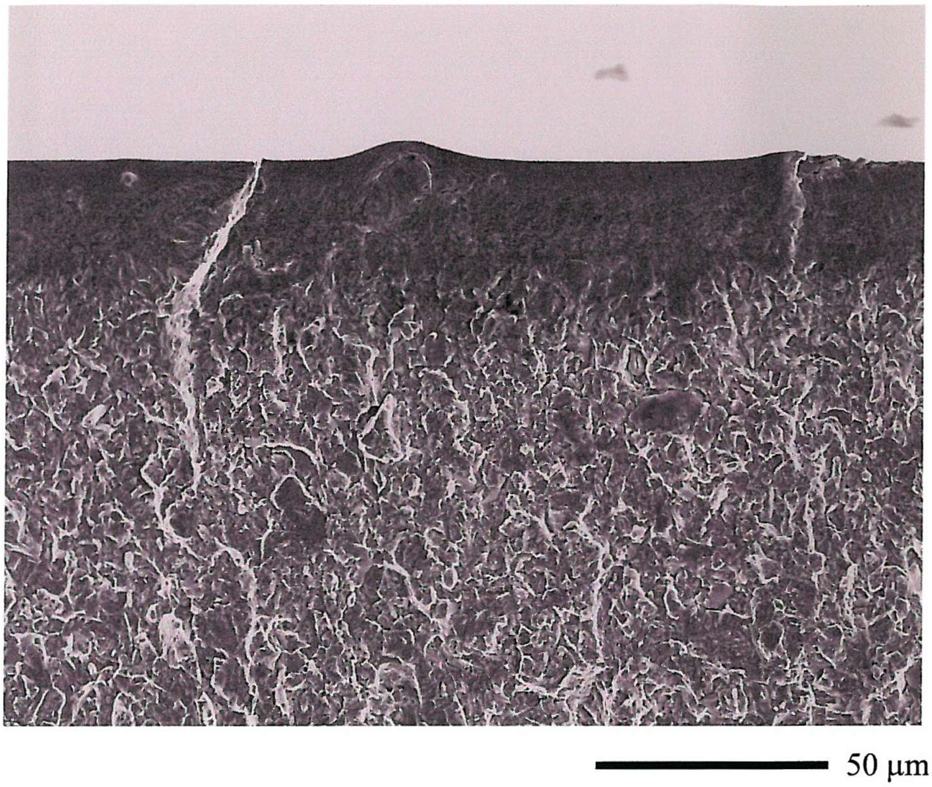

Figure 5.43: SEM image of fracture surface showing transition from very flat, transgranular fracture to mixed transgranular-intergranular fracture. Note the bulge above the (Nb,Ti)C particle at the crack initiation site.

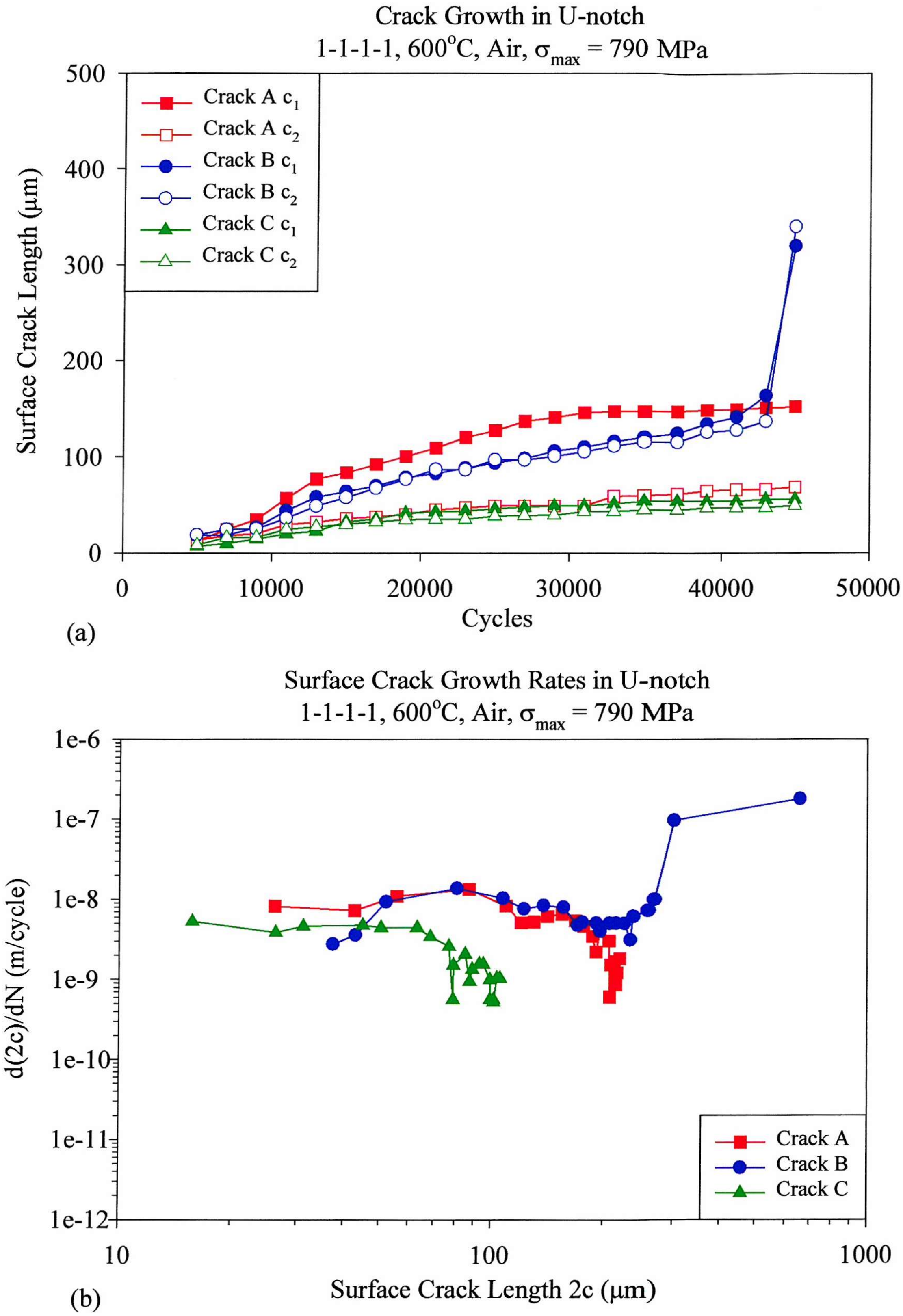

Figure 5.44: Growth of short cracks in U-notch root at 600°C in air, σ_{max} = 790 MPa. (Test A600-790-1-PR-01)

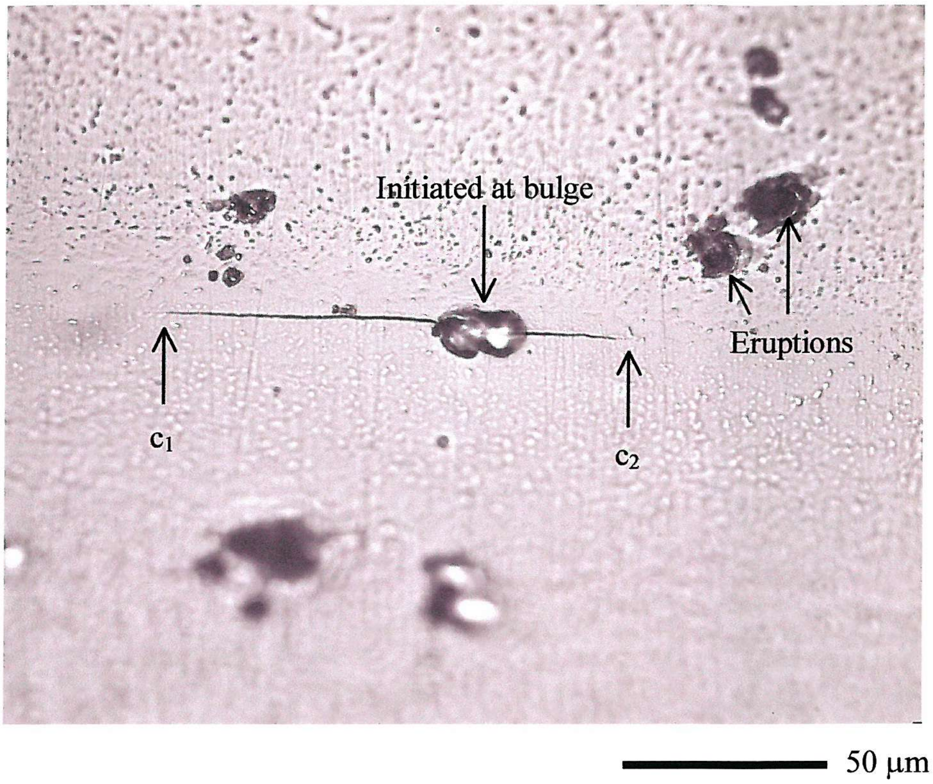

Figure 5.45: Crack A from test A600-790-1-PR-01 after 15000 cycles, showing asymmetry about the initiation point. (Optical).

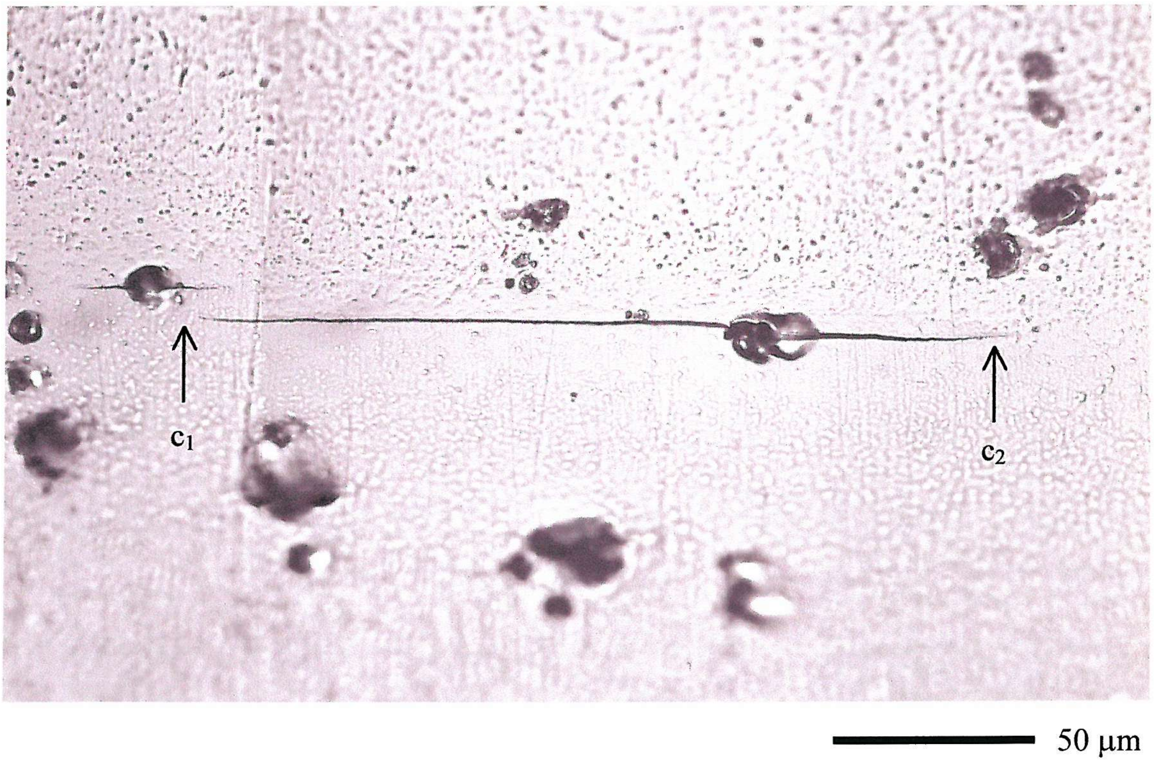

Figure 5.46: Crack A from test A600-790-PR-01 after 33000 cycles. Segment c_1 arrested due to interaction with adjacent small crack. (Optical).

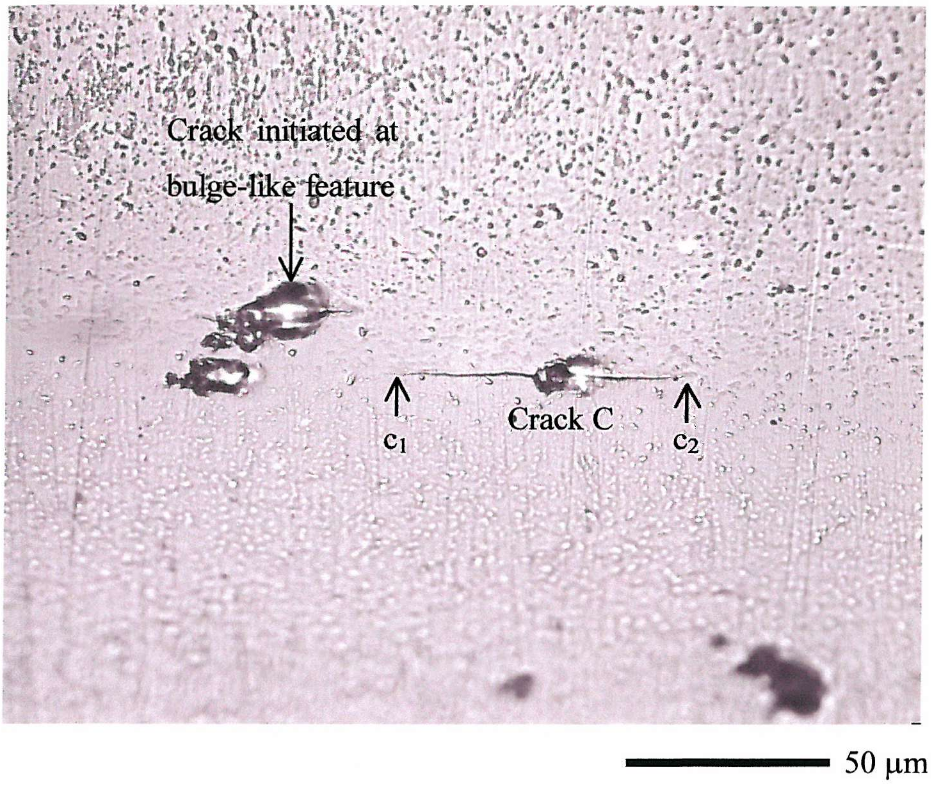

Figure 5.47: Crack C from test A600-790-PR-01 after 19000 cycles. Interaction with adjacent crack probably caused retardation of crack growth. The adjacent crack also initiated at a bulge-like feature. (Optical).

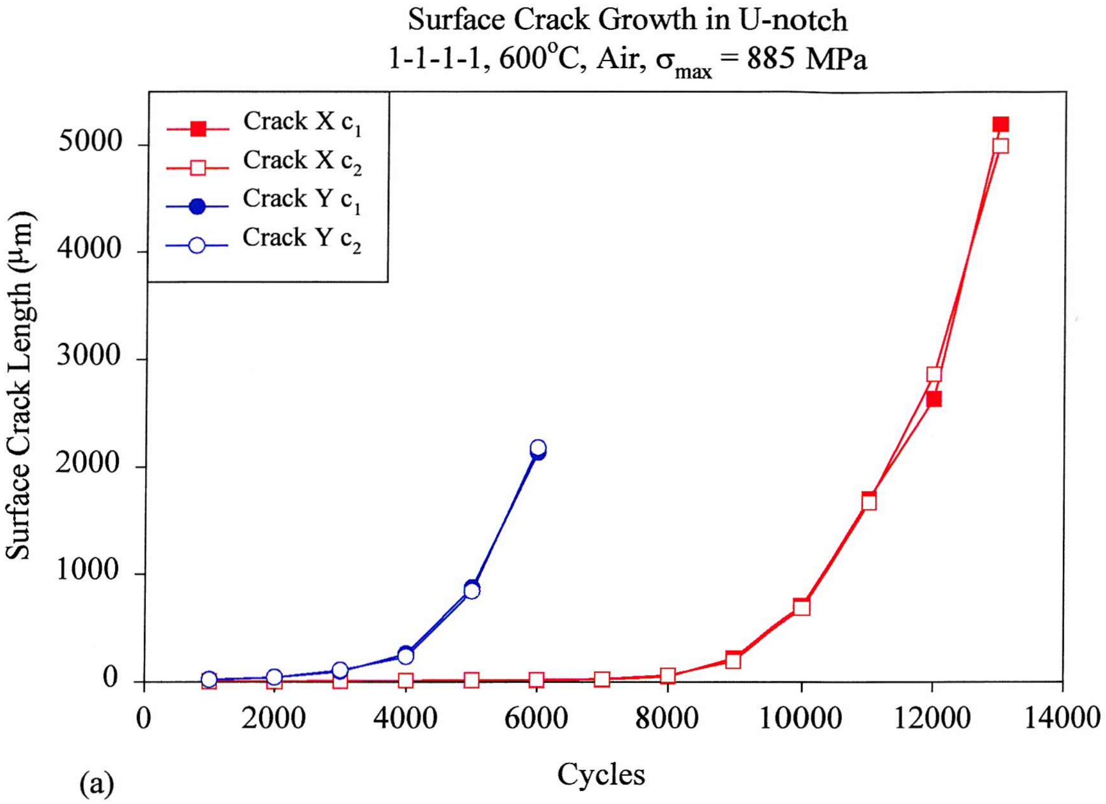

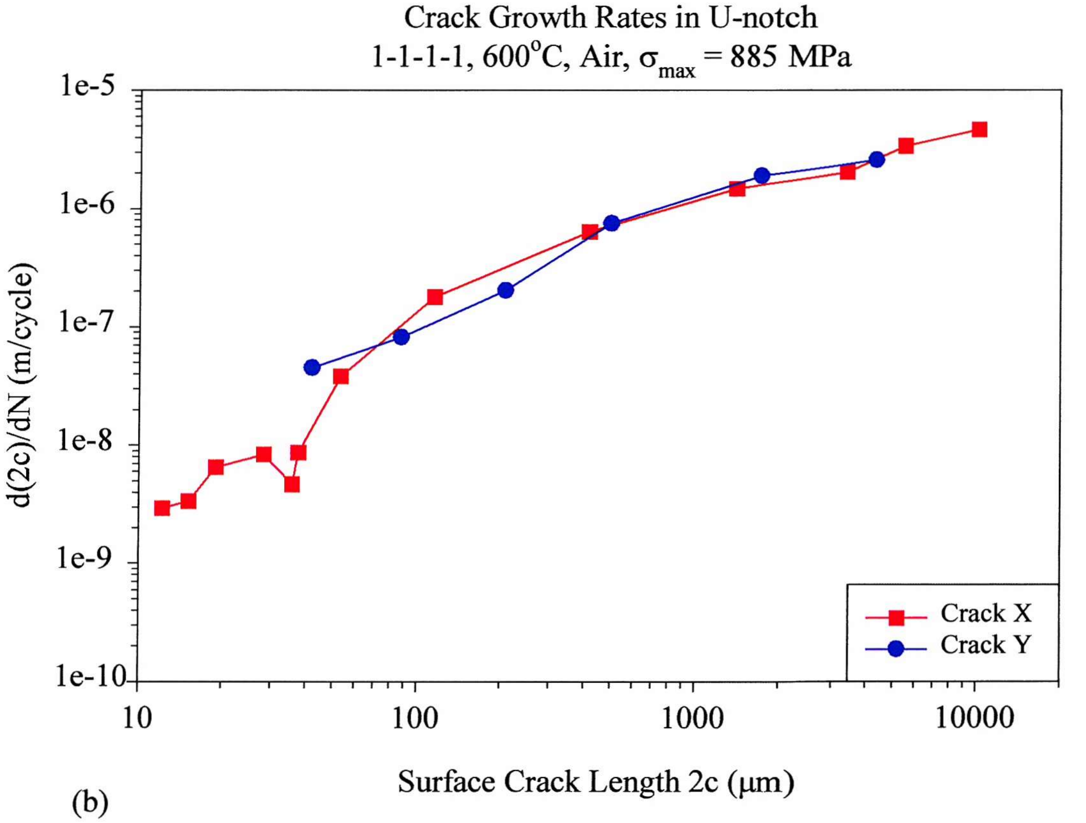

Figure 5.48: Growth of short cracks in U-notch root at 600°C in air, σ_{max} = 885 MPa. (Tests B600-885-1-PR-01 & B600-885-1-PR-02)

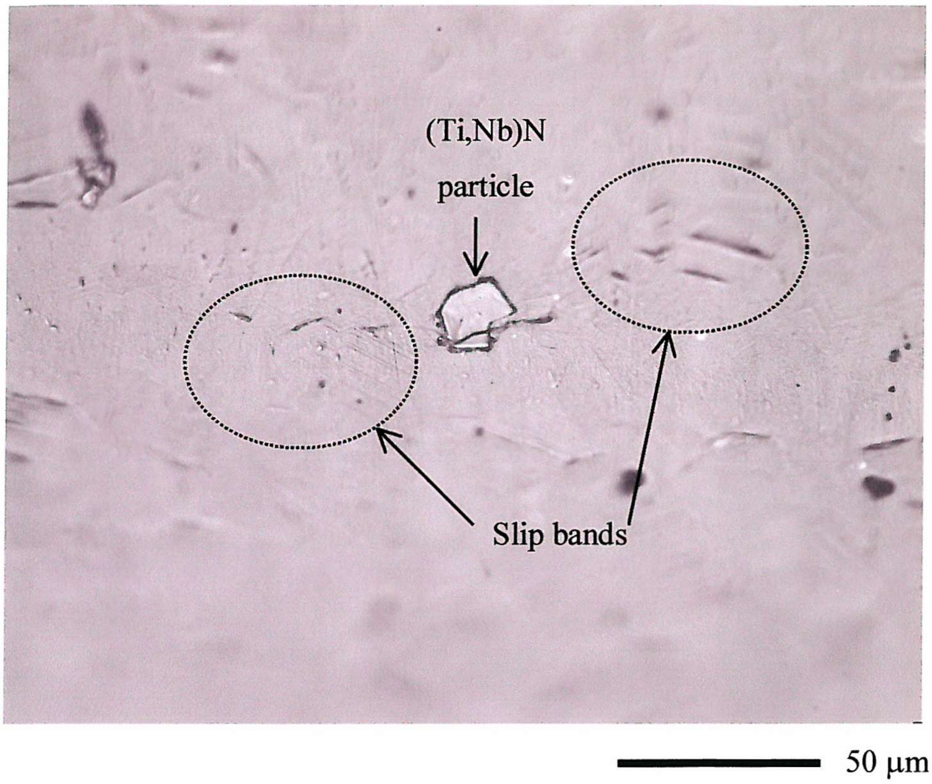

Figure 5.49: Crack Y from test B600-885-1-PR-02 after 1000 cycles, initiated at an (Ti,Nb)N particle. Some slip bands can also be seen. (Optical).

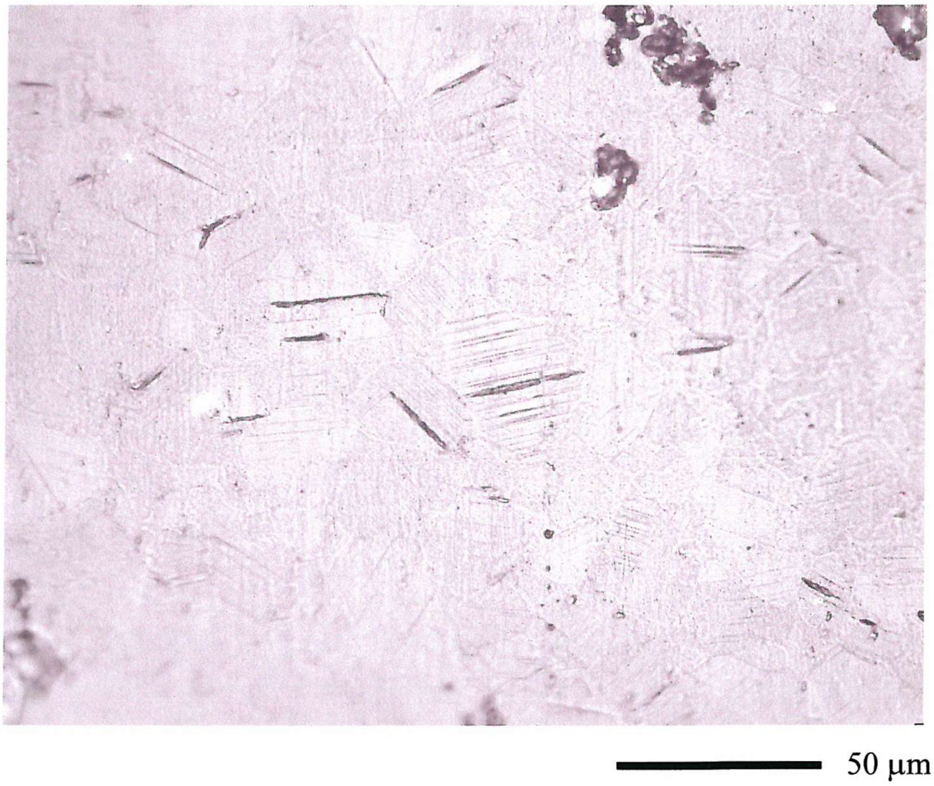

Figure 5.50: Slip bands on notch surface of test B600-885-1-PR-02 after 1000 cycles. The dark features at top right are eruptions of oxidised (Nb,Ti)C particles. (Optical).

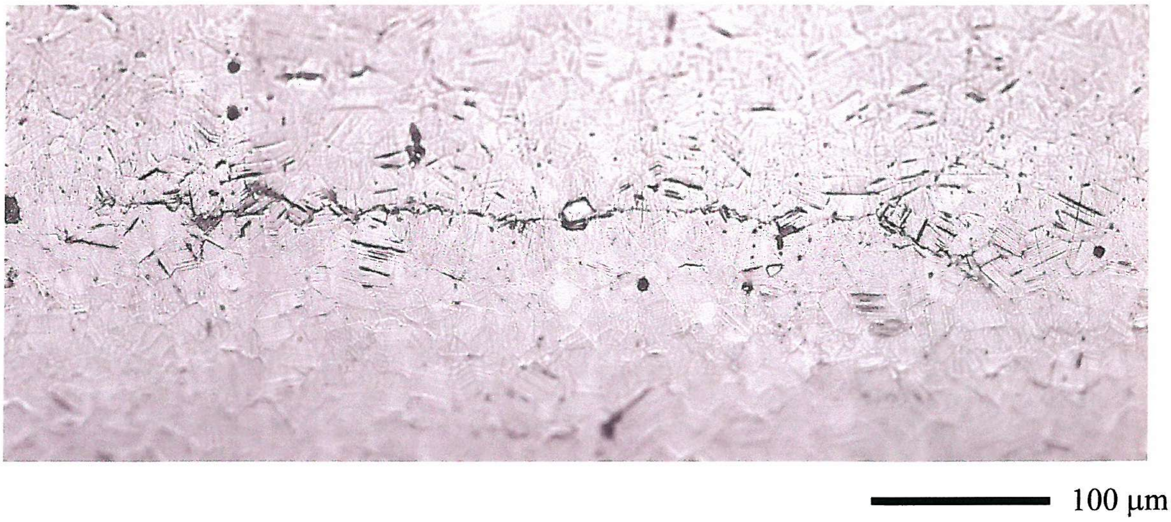

Figure 5.51: Crack Y from test B600-885-1-PR-02 after 4000 cycles, showing crack deflections. Crack propagation appeared to be mixed transgranular-intergranular. (Optical).

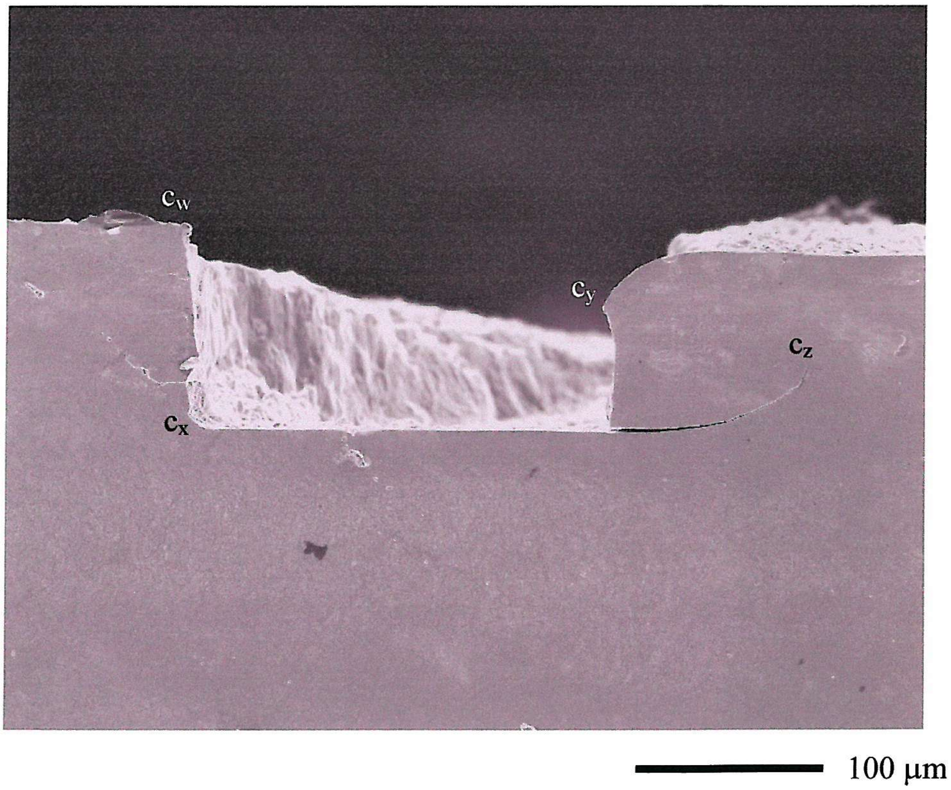

Figure 5.52: Plan view of notch root, test A600-750-1-PR-01, showing evidence of short crack coalescence behind the crack tips. Note the curved path taken by the cracks. (SEM, SEI).

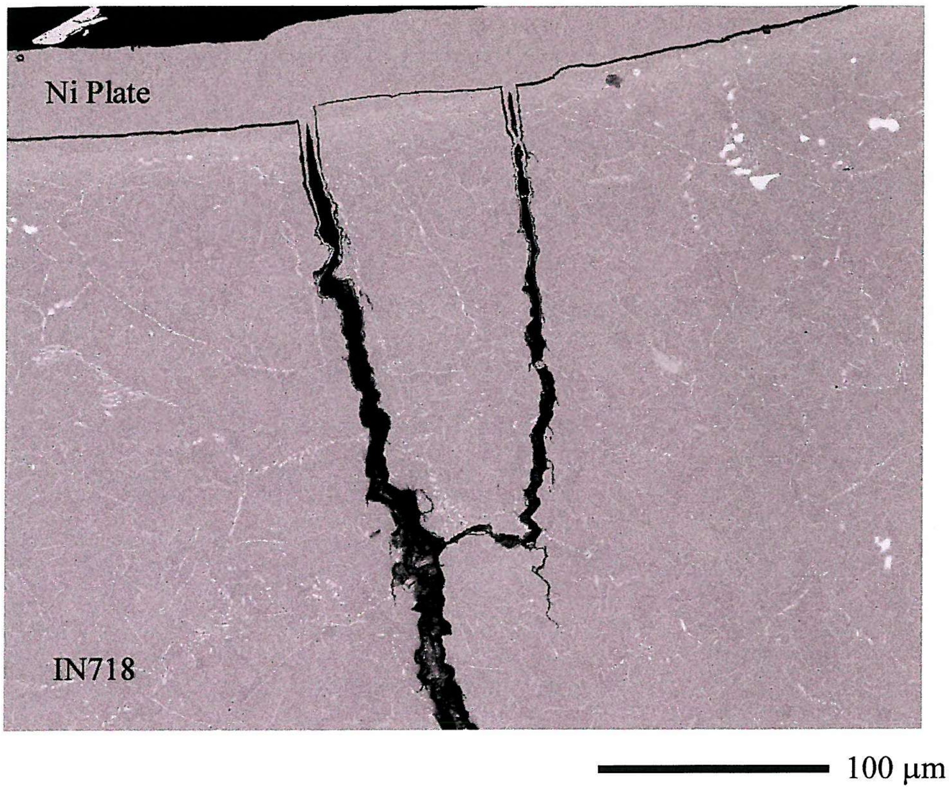

Figure 5.53: Cross-section through a fractured U-notch specimen (test A600-750-1-01), showing sub-surface coalescence of secondary cracks. (SEM, BEI)

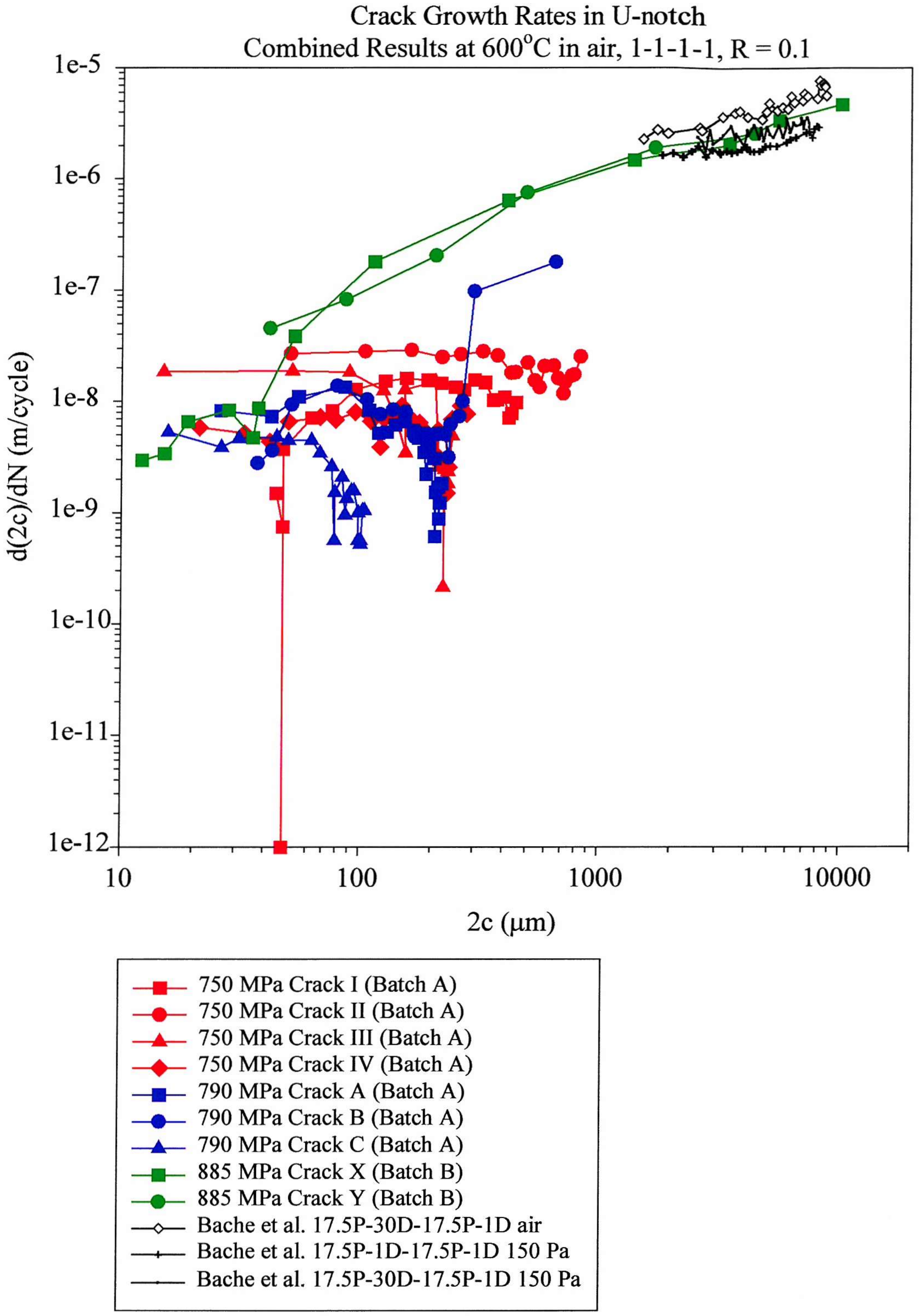

Figure 5.54: Combined plot of crack growth rates from the U-notch tests at different stress levels.

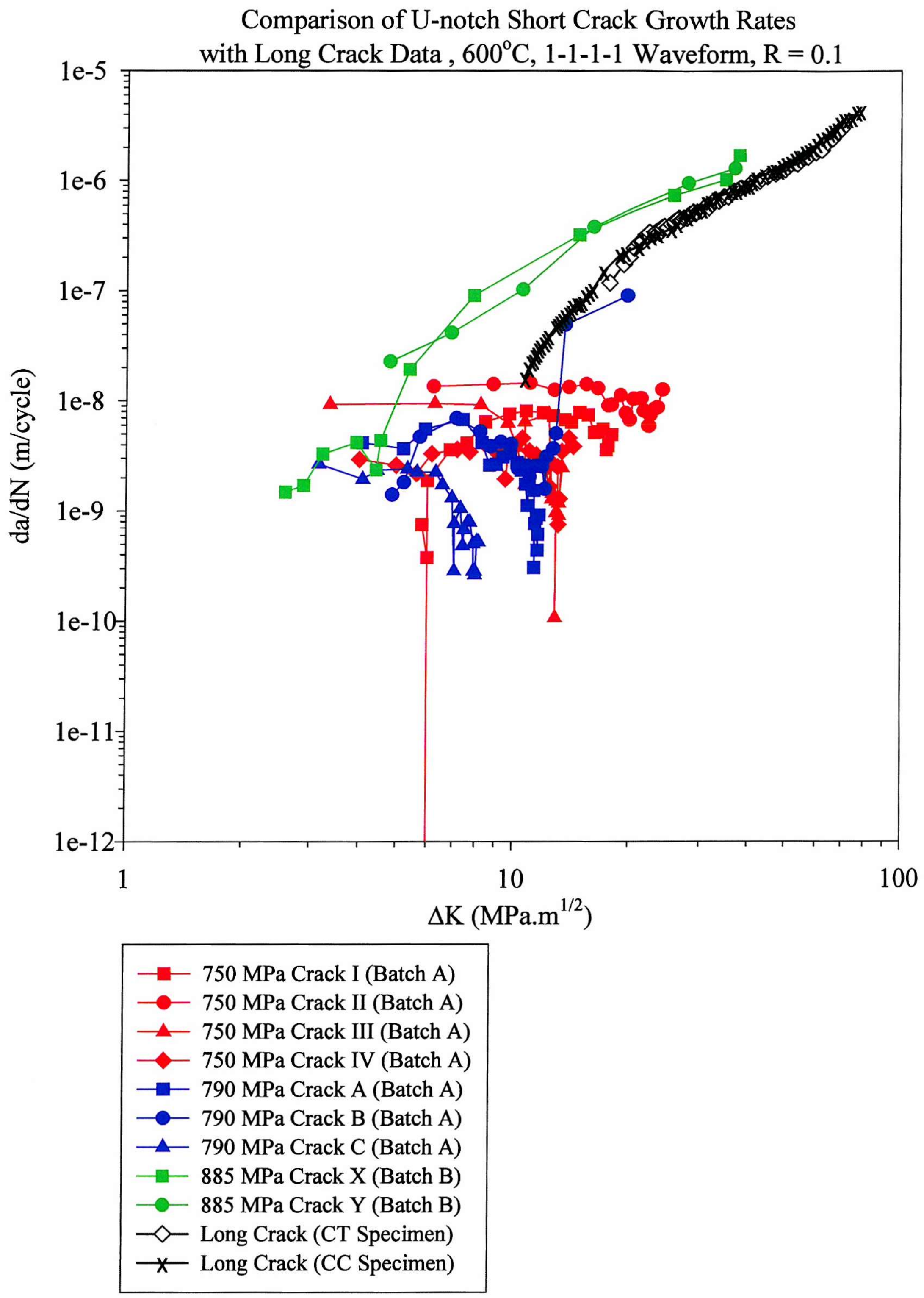

Figure 5.55: Comparison of short crack growth rates in U-notches with long crack data obtained at 600°C using a 1-1-1-1 waveform and $R = 0.1$.

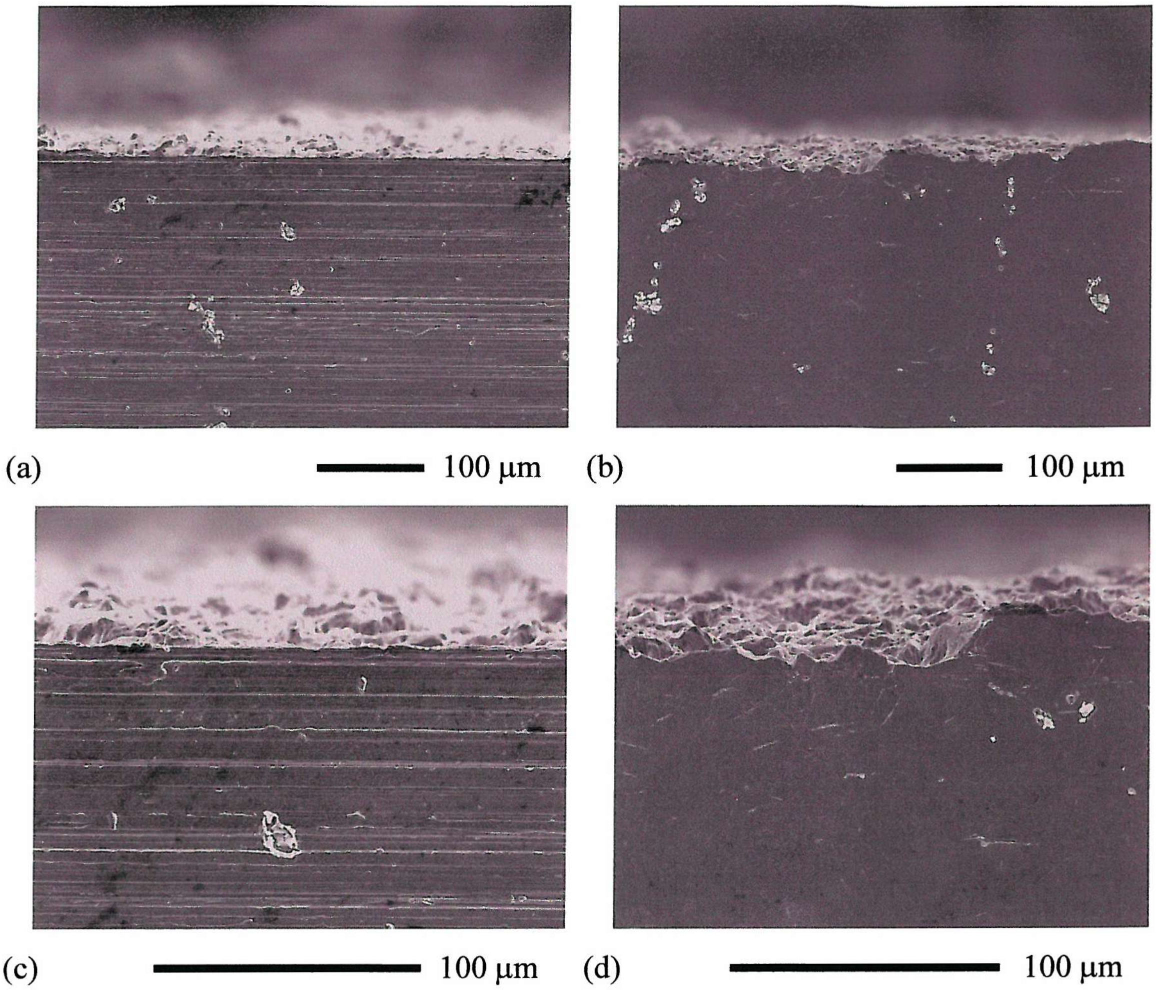

Figure 5.56: Comparison of surface crack fracture paths in notch root at σ_{max} = 885 MPa. Batch B specimens. (a) & (c) as-broached; (b) & (d) polished. (SEM, SEI).

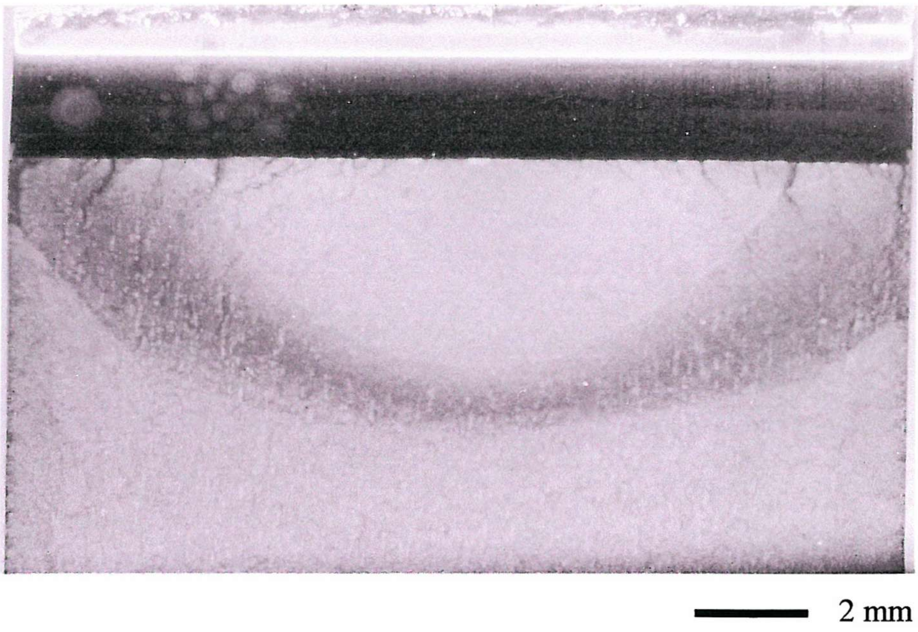

Figure 5.57: Macro photograph of fatigue fracture face, Test A600-790-1-PR-01. What became the dominant crack initiated near the notch centre, coalescing with numerous other small cracks to for the final defect.

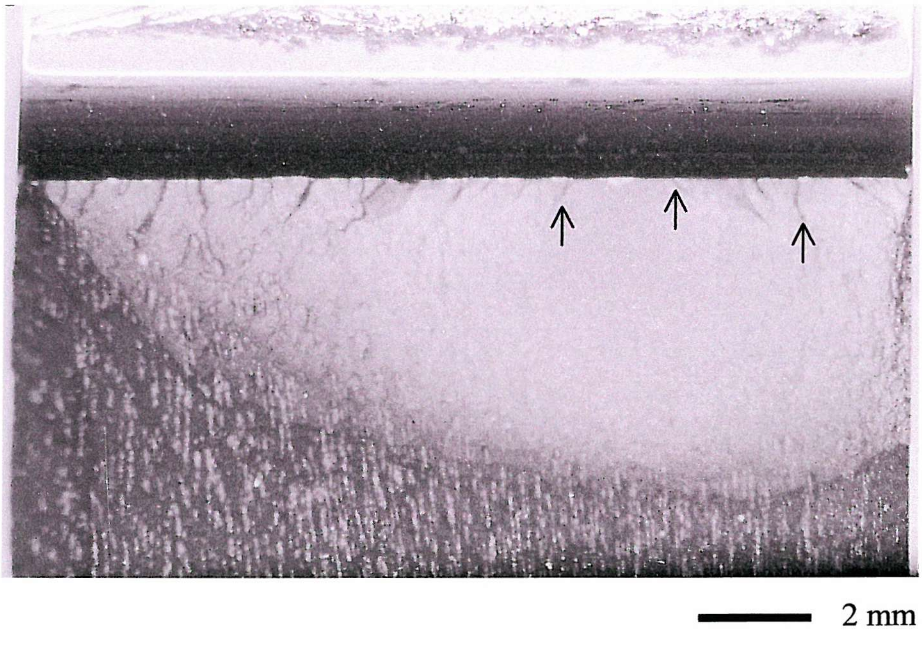

Figure 5.58: Macro photograph of fatigue fracture face, Test A600-790-1-P-03. The development of the dominant crack occurred from a point to the right of the notch centre in this image, resulting in the final fatigue crack having an asymmetric shape. Small steps on the fracture surface can be seen where some short cracks coalesced (some examples are arrowed).

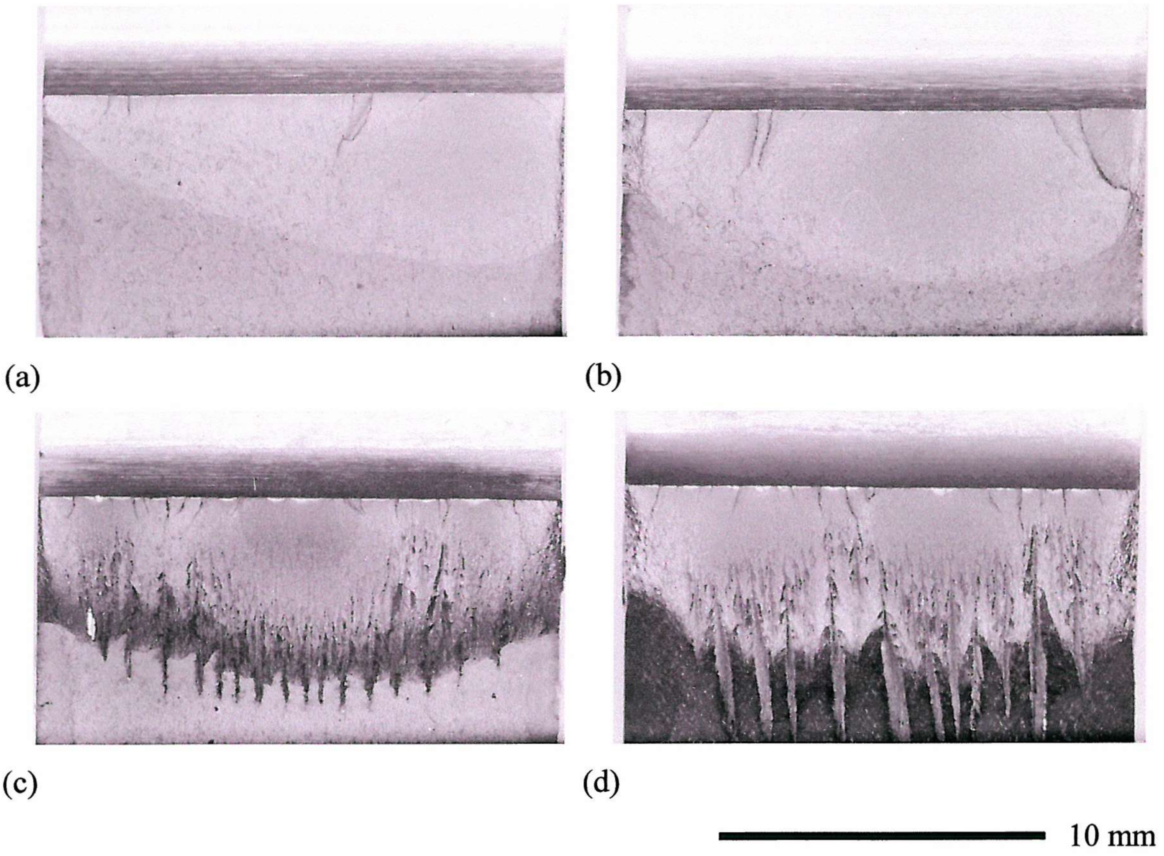

Figure 5.59: Macro photographs of fractured U-notch specimens. (a) Test B600-790-1-01; (b) Test B600-790-1-02; (c) Test A600-750-20-01 (20 second dwell); (d) Test A600-750-30-01 (30 second dwell).

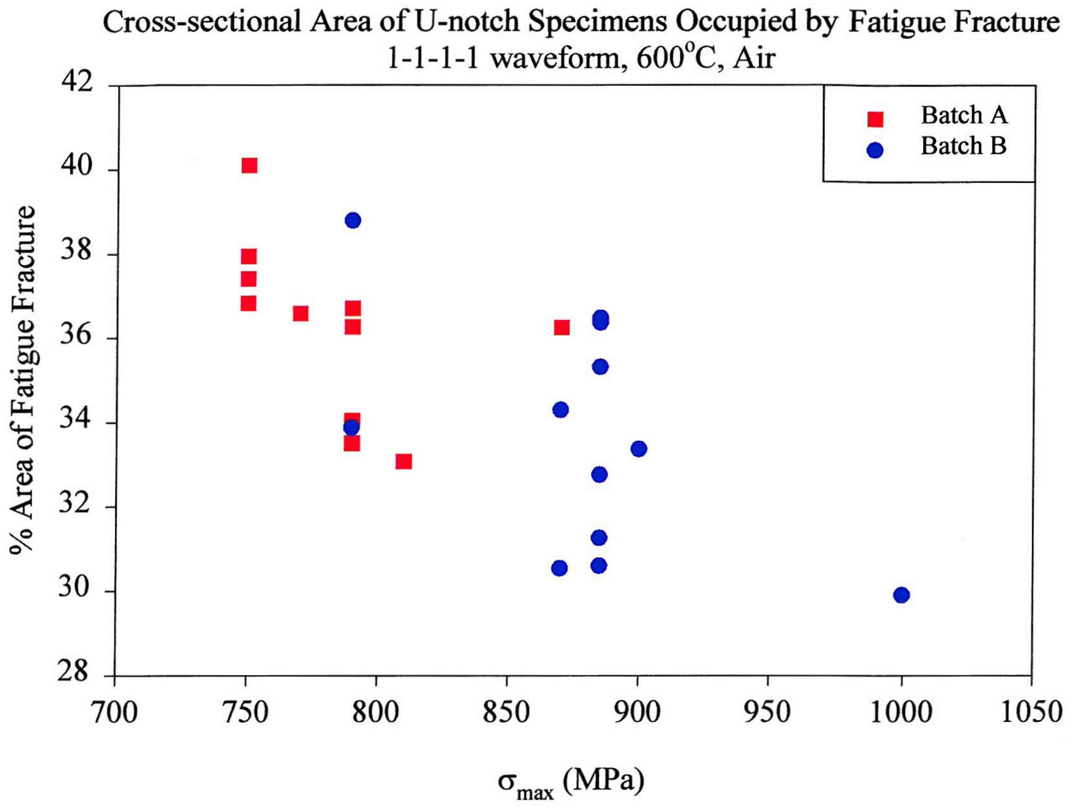

Figure 5.60: Effect of applied maximum stress on area of fatigue fracture.

5.11 References

[5.1] Andrieu A., Molins R., Ghonem H. & Pineau A. "Intergranular crack tip oxidation mechanism in a nickel-based superalloy" Mater. Sci. Engng. vol. A154 pp.21-28 (1992)

[5.2] Ghonem H. & Zheng D. "Oxidation-assisted fatigue crack growth behaviour in Alloy 718 - Part 1. Quantitative Modeling" Fatigue Fract. Engng. Mater. Struct. vol.14 No.7 pp.749-760 (1991)

[5.3] Scott P. M. & Thorpe T. W. "A critical review of crack-tip stress intensity factors for semi-elliptic cracks" Fatigue of Engng. Mater. & Struct. vol. 4 pp. 291-309 (1981)

[5.4] Mercer C., Soboyejo A. B. O. & Soboyejo W. O. "Micromechanisms of fatigue crack growth in a forged Inconel 718 nickel-based superalloy" Mater. Sci. Engng. A. vol. 270 pp. 308-322 (1999)

[5.5] Reed P. A. S., Hachette F. & Thakar D. "Pump-priming project on crack initiation in Inconel 718" University of Southampton Department of Engineering Materials Report No. PR/RA/FH,DT/98/01/244 (1998)

[5.6] ESDU 69020 "Elastic stress concentration factors. Geometric discontinuities in flat bars or strips of isotropic material" ESDU International, London pp. 8-10 (1993)

[5.7] Moss S. J., Unpublished data, ALSTOM Power, (1998)

[5.8] Reed P. A. S. Hachette F. Thakar D. Connolley T. & Starink M. J. "Creep-fatigue initiation and early crack growth in Inconel 718" Proc. 8th International Conference on Mechanical Behaviour of Materials (ICM8), Eds. Ellyin F. & Provan J. W., Fleming Printing Ltd. Victoria, BC, Canada, vol. 1 pp. 418-423 (1999)

[5.9] Vecchio R. S. & Hertzberg R. W. "A rationale for the 'apparent anomalous' growth behavior of short fatigue cracks" Engng. Fract. Mech. vol. 22 pp. 1049-1060 (1995)

[5.10] Bache M. R., Evans W. J. & Hardy M.C. "The effects of environment and loading waveform on fatigue crack growth in Inconel 718" Int. J. Fatigue vol. 21 Supp. pp. S69-S77 (1999)

6 DISCUSSION

This chapter discusses the experimental results presented in Chapter 5, beginning with some brief comments about the microstructure of the materials used and the differences in the two batches of U-notch specimens. There follows a detailed discussion and analysis of primary carbide oxidation, relating theoretical predictions of misfit due to oxidation to the features observed experimentally in thermal exposure and fatigue specimens. The results of fatigue experiments performed on plain bend bars are considered, before moving on to the main body of work which was the high temperature fatigue testing of U-notch specimens. Fatigue test results are analysed with reference to the FE modelling performed, the surface condition of the U-notch, loading, environmental conditions and discussions in the literature. A mechanism for crack initiation due to carbide oxidation is proposed, and throughout the discussion the differences in behaviour between the two batches of U-notch specimens are explored. The chapter is closed with a discussion of the relevance of the work to the in-service conditions experienced by turbine discs.

6.1 Microstructure

The use of U-notch specimens from two different disc forgings introduced the potential for differences in fatigue properties due to differences in microstructure. It was originally intended to obtain all specimens from a single disc (Batch A) but restrictions on material supply meant a second disc (Batch B) was used as well. Both discs were produced from the same cast of material at the same time using the same forging and heat treatment process, so one would expect a similar microstructure to result. This is borne out by the results of metallography on the two batches of specimens, showing them to have similar grain sizes, similar area fractions of primary carbides and nitrides and similar size distributions of primary carbides and nitrides. However, two differences between the as-received batches of U-notch specimens were surface roughness and the presence of what appeared to be a work-hardened deformation layer in the notch surface of Batch A specimens. These differences should be borne in mind during the discussion of fatigue results.

The extruded bar material used for some preliminary room temperature tests had a different microstructure to the disc material. The processing route for the extruded material is not known, but the fine grain size and globular δ phase morphology are signs that it may have been produced by a "Minigrain^{TM}" process [6.1] as described in Chapter 3 Section 3.2.7.

6.1.1 Volume fraction of Primary Carbides

The combined area fraction of primary carbides and nitrides in the IN718 disc materials measured by image analysis was 0.37% for Batch A and 0.33% for Batch B. For close-packed metallic materials such as the FCC matrix of IN718, the primary carbides and the primary nitrides, the number of atoms per unit volume is approximately the same. If all the carbon in the alloy is present solely in the primary carbides, the approximate volume fraction of primary carbide will be twice the atomic fraction of C, since each C atom takes up a metal atom (Nb or Ti) to form the carbide. Since the carbon content of the alloy was 0.15 at.%, a rough estimate of the volume fraction of primary carbides in the alloy is 0.3%. Similarly for the primary nitrides, their volume fraction will be approximately 0.05%, based on a nitrogen content in the alloy of 0.024 at.%. This yields a combined volume fraction of 0.35%, which agrees well with the area fraction results obtained by image analysis. A more rigorous analysis would use the atomic densities of (Nb,Ti)C and (Ti,Nb)N, but these are not known. What this simple estimate shows is that the volume fraction of primary carbides, which have a strong influence on crack initiation, is directly determined by the carbon content of the alloy.

6.2 Primary Carbide Oxidation

The results presented in Chapter 4 demonstrate that primary carbides at or close to the surface of IN718 oxidised at elevated temperatures, and there was a substantial volume expansion associated with oxidation. This was observed in unstressed specimens and U-notch fatigue specimens exposed at 550°C and 600°C in air. The Batch A U-notch tests in particular exhibited a link between primary carbide oxidation, localised matrix deformation and fatigue crack initiation. For this reason it is worthwhile considering which compounds formed when the primary carbides oxidised and how oxidation produced deformation in the surrounding matrix. Volume expansion and eruption formation by primary carbides was described by Sjoberg et al. [6.2], but the cause and magnitude of the volume expansion were not discussed in detail.

6.2.1 Phases Formed by Oxidation of Primary Carbides

The primary carbides present in the IN718 material used in this study were (Nb,Ti)C monocarbides. Nb was the majority metallic element with some substitution by Ti. It is therefore likely that the oxides formed were based on the oxides of niobium.

Niobium metal can form the monoxide NbO, the dioxide NbO_2 and the pentoxide Nb_2O_5. These oxides have been observed to form during the oxidation of pure NbC [6.3, 6.4].

Oxidation of NbC powder in the temperature range 420-600°C at an oxygen partial pressure of 4×10^3 Pa to 16×10^3 Pa was investigated by Shimada and Inagaki [6.3]. The final product of oxidation was determined by X-ray powder diffractometry to be Nb_2O_5, with some evidence for the formation of NbO as an intermediate step. Above 490°C, oxidation proceeded rapidly and during a thermogravimetry-differential thermal analysis (TG-DTA) experiment, a large exothermic peak was detected at 535°C [6.3]. This peak was attributed to the heat of crystallisation of Nb_2O_5. Another study by Miller et al. [6.4] on a thin synthetic film of NbC was performed in an X-ray photoelectron spectroscopy (XPS) instrument at 600-700°C using an oxygen partial pressure of 5×10^{-4} Pa. In this experiment NbO_x ($0 < x < 1$), NbO_2, NbO_x ($2 < x < 2.5$) and Nb_2O_5 were detected, with NbO_x ($0 < x < 1$) being the most abundant phase by area. These results suggest that NbC oxidises to gives NbO first, before formation of higher oxides. The formation of higher oxides like Nb_2O_5 could have been limited by the very low pressure of oxygen and the short exposure time (45 minutes) used by Miller et al. [6.4].

For oxidation of (Nb,Ti)C carbides in IN718 in air, it is possible that the lower oxides will form first, but that the final product of oxidation will be $(Nb,Ti)_2O_5$. During oxidation, the (Nb,Ti)C primary carbides will react with oxygen to give $(Nb,Ti)_2O_5$, with the evolution of CO or CO_2 gas.

$$4(Nb,Ti)C + 7O_2 \rightarrow 2\,(Nb,Ti)_2O_5 + 4CO \qquad \text{Eqn. 6.1}$$

$$4(Nb,Ti)C + 9O_2 \rightarrow 2(Nb,Ti)_2O_5 + 4CO_2 \qquad \text{Eqn. 6.2}$$

Experimental observation of eruptions and matrix deformation associated with oxidised primary carbides demonstrates that there was a substantial volume expansion when the particles oxidised. The volume expansion due to the transformation of NbC to Nb_2O_5 can be estimated using crystallographic data, although arriving at an estimate for the temperature range of interest (550-600°C) is complex, because Nb_2O_5 is polymorphic. It exists in several different crystal structures at different temperatures, for example the high temperature form H-Nb_2O_5 and the plate-like form B-Nb_2O_5. Amorphous Nb_2O_5 also exists and its density varies widely depending on the method of preparation. It is not known what form is adopted by the oxide eruptions in IN718, though a crystalline oxide form is considered to be more likely. For simplicity, just the oxidation of pure NbC to Nb_2O_5 will be considered. Using molar volume and density data for NbC [6.5] and Nb_2O_5 [6.6], estimates of the volume expansion factor can be calculated for the reaction:

$$4\mathrm{NbC} + 9\mathrm{O}_2 \rightarrow 2\mathrm{Nb}_2\mathrm{O}_5 + 4\mathrm{CO}_2 \qquad \text{Eqn. 6.3}$$

The volume expansion factor is given by the expression:

$$\delta_V = \frac{V_{Nb_2O_5}}{2V_{NbC}} \qquad \text{Eqn. 6.4}$$

where V_i is the molar volume of phase 'i'. Estimated volume expansion factors are listed in Table 6.1. The lower bound is 1.96, based on data for the B-form of Nb_2O_5, while the upper bound is 2.38, based on data for amorphous Nb_2O_5.

Phase	**Density ($\mathrm{g\ cm^{-3}}$)**	**Molar Volume ($\mathrm{cm^3\ mol^{-1}}$)**	**Estimated volume expansion factor**
NbC	8.18	12.83	n/a
H – Nb_2O_5	4.55	58.42	2.28
B – Nb_2O_5	5.29	50.2	1.96
Amorphous Nb_2O_5	4.36 to 5.12	51.9 to 61.0	2.02 to 2.38

Table 6.1: Estimated volume expansion factors for the oxidation of pure NbC to Nb_2O_5.

6.2.2 Misfit Calculations

Using calculations based on work by Starink et al. [6.7] and Lee et al. [6.8], the misfit stresses due to the difference in volume between NbC and Nb_2O_5 can be calculated for primary NbC carbides oxidising to Nb_2O_5 in a matrix of IN718.

For a spherical inclusion 'B' in a continuous matrix 'A', the misfit parameter ε_m is defined as:

$$\varepsilon_m = \frac{r_{oB} - r_{oA}}{r_{oA}} \qquad \text{Eqn. 6.5}$$

where r_{oB} and r_{oA} are the radii of the free undeformed particle 'B' and the empty undeformed cavity in the matrix 'A' respectively. In the case of thermal misfit due to a temperature change ΔT, the misfit parameter ε_m is:

$$\varepsilon_m = (\alpha_A - \alpha_B)\Delta T \qquad \text{Eqn. 6.6}$$

where α_A & α_B are the thermal expansion coefficients of 'A' and 'B'.

For a spherical particle of NbC oxidising to Nb_2O_5, the misfit parameter is defined as:

$$\varepsilon_m = \frac{r_{Nb_2O_5} - r_{NbC}}{r_{NbC}} \qquad \text{Eqn. 6.7}$$

Assuming a spherical particle of NbC of radius r_{NbC} oxidises completely to Nb_2O_5, then using the volume expansion factor calculated in Eqn. 6.4 gives:

$$\varepsilon_m = \sqrt[3]{\delta_V} - 1 \qquad \text{Eqn. 6.8}$$

For a positive misfit parameter in which $r_{oB} > r_{oA}$, formulae can be derived for the misfit stresses around the inclusion particle. Considering first the case of an elastically isotropic inclusion in an infinite, elastically isotropic matrix, the inclusion will be in hydrostatic compression. The pressure inside the inclusion for an infinitely small volume fraction of inclusions is given by [6.7]:

$$p_B = 3B_B(C-1)\varepsilon_m \qquad \text{Eqn. 6.9}$$

in which

$$C = \frac{3B_B}{3B_B + 4G_A} \qquad \text{Eqn. 6.10}$$

where G is the shear modulus and B is the bulk modulus.

Lee et al. [6.8] considered the case of a spherically misfitting inclusion in an infinite matrix, in which the matrix deforms plastically around the inclusion. Their model assumed that the matrix is a perfectly plastic material which obeys the von Mises yield criterion. The following expressions for the stress components (in polar co-ordinates) were obtained for a particle of radius r_B:

$$\sigma_r = \sigma_\theta = p_B \qquad r < r_B \qquad \text{Eqn. 6.11}$$

$$\sigma_r = \sigma_\theta - \sigma_y = 2\sigma_y \ln\left(\frac{r}{r_B}\right) + p_B \qquad r_B \le r \le r_p \qquad \text{Eqn. 6.12}$$

$$\sigma_r = -2\sigma_\theta = -\frac{2}{3}\sigma_y\left(\frac{r_p}{r}\right)^3 \qquad r > r_p \qquad \text{Eqn. 6.13}$$

where r_p is the plastic zone radius and r_B is the radius of the inclusion. Note these equations predict a discontinuity in σ_θ at $r = r_B$. Since the stresses at the boundary of the plastic zone must be continuous, the plastic zone radius is given by:

$$r_p = r_B \exp\left(-\frac{p_B}{2\sigma_y} - \frac{1}{3}\right) \qquad \text{Eqn. 6.14}$$

In this spherically symmetrical case, all the displacements are radial. Conditions of continuity of displacements and radial stresses at the particle/matrix interface give an expression from which p_B can be evaluated:

$$\frac{6\eta G_A \varepsilon_m}{\sigma_y}\left(1 + \frac{p_B}{3B_B\varepsilon_m} - \frac{p_B}{3B_A\varepsilon_m}\right) = \exp\left(-\frac{3p_B}{2\sigma_y} - 1\right) \qquad \text{Eqn. 6.15}$$

where :

$$\eta = \frac{(1+\upsilon_A)}{3(1-\upsilon_A)} \qquad \text{Eqn. 6.16}$$

and υ_A is Poisson's ratio for the matrix.

Equation 6.15 can be solved numerically for p_B and its value substituted in Equations 6.11 to 6.14 to give σ_r, σ_θ and r_p.

6.2.3 Oxidation Misfit

Considering the case of a spherical NbC particle transforming to Nb_2O_5 in an infinite IN718 matrix at 600°C, it was first assumed that there is no thermal expansion mis-match between the NbC particle and the matrix prior to oxidation. This is a reasonable assumption as any thermal expansion misfit strains resulting from the original processing will be negligible at 600°C compared to the magnitude of the oxidation mis-match. Thermal expansion mis-match is briefly discussed in Section 6.2.4. The mis-match parameter for complete transformation to Nb_2O_5 was calculated using Eqn. 6.4 and Eqn.

6.8. Using appropriate materials property data for IN718 and Nb_2O_5, Eqn. 6.15 was solved for p_B and substituted in Eqn. 6.11 to Eqn. 6.14 to give the predicted stresses and the plastic zone radius.

The available physical property data for IN718 and NbC are listed in Table 6.2 and Table 6.3. References from which the data were obtained are indicated in square brackets. Where data [6.9, 6.10] for the IN718 disc material used in this study are not available, typical values for wrought, precipitation hardened IN718 with a similar heat treatment history are quoted. Physical and mechanical property data for Nb_2O_5 were unobtainable in the open literature. Instead, estimated values are quoted in Table 6.4, based on typical data for some well-known metal oxides (Al_2O_3 and Fe_2O_3) [6.11].

Predicted misfit stresses are plotted in Figure 6.1 for the example of a fully constrained particle of H-Nb_2O_5. The model predicted a pressure inside the particle of -3.48 GPa. In the matrix, the predicted radial stress σ_r was compressive, decreasing in magnitude with increasing distance from the particle/matrix interface. The hoop stress σ_θ was compressive at the particle/matrix interface, gradually changing to a tensile stress with increasing distance. The maximum tensile value of σ_θ was 327 MPa at the boundary of the plastic zone in the matrix. Estimated plastic zone radii for the different forms of Nb_2O_5 are listed in Table 6.5. This idealised case produced estimates of the plastic zone size r_p of between 3.12 and 3.22 times the transformed particle radius.

Property	**Temperature**		
	20°C	**600°C**	**650°C**
E **(GPa)**	212.6 [6.10]	167.5 [6.10]	163 [6.12]
G **(GPa)**	77.2 [6.12]	65.5 [6.12]	63.4 [6.12]
B **(GPa)**	163 [a]	127 [a]	129 [a]
υ	0.294 [6.12]	0.276 [6.12]	0.283 [6.12]
σ_y **(MPa)**	1137 [6.9]	976 [b] [6.9, 6.10]	942 [6.9]
σ_{UTS} **(MPa)**	1411 [6.9]	1219 [6.10]	1149 [6.9]
α **(m/m/°C)** [c]	-	1.48×10^{-5} [6.13]	1.49×10^{-5} [6.13]

[a] Calculated from values of E and υ.

[b] Average of Batch A and Batch B data.

[c] Range from 20°C to specified temperature.

Table 6.2: Mechanical and physical property data for wrought IN718.

Property	Temperature		
	20°C	600°C	650°C
E (GPa)	437 [6.14] [a]	401 [6.14] [a]	399 [6.14] [a]
G (GPa)	178 [6.14] [a]	165 [6.14] [a]	164 [6.14] [a]
B (GPa)	251 [b]	230 [b]	229 [b]
υ	0.21 [6.14] [a]	0.21 [6.14] [a]	0.21 [6.14] [a]
σ_y (MPa)	-	-	-
σ_{UTS} (MPa)	-	-	-
α (m/m/°C)	6.7 x 10^{-6} [6.15] [c]	-	-

[a] Values are for hot-pressed NbC of 94% theoretical density.

[b] Calculated from values of E and υ.

[c] Applicable temperature range not known.

Table 6.3: Mechanical and physical property data for niobium carbide. References to the literature are given in square brackets.

Property	Temperature		
	20°C	600°C	650°C
E (GPa)	247	-	-
G (GPa)	102	-	-
B (GPa)	142	-	-
υ	0.21	-	-
σ_y (MPa)	-	-	-
σ_{UTS} (MPa)	-	-	-
α (m/m/°C)	7 x 10^{-6}	-	-

Table 6.4: Estimated mechanical and physical property data for niobium pentoxide.

Oxide Phase	r_p/r_{NbC}	$r_p/r_{Nb_2O_5}$
H-Nb_2O_5	4.22	3.21
B-Nb_2O_5	3.91	3.12
Amorphous Nb_2O_5	3.97 to 4.30	3.14 to 3.22

Table 6.5: Estimated plastic zone radii around an NbC particle which has transformed to Nb_2O_5.

Measurements were performed to see how the predicted plastic zone radius r_p compared with the extent of deformation observed experimentally. Measurements were made on images of bulges in thermal exposure specimens and bulges observed above oxidised primary carbides on U-notch fatigue fracture specimens. The maximum bulge height above the plane of the specimen surface was measured. Two points on the surface were established at 10% of the maximum bulge height, one each side of the bulge. A value of 10% was chosen as a compromise between measuring the total extent of deformation and choosing points which could be reliably identified from image to image. A straight line was drawn from the two surface points to the centre of gravity of the particle, as shown in Figure 6.2. Distances d_1, d_2, d_3 & d_4 shown in Figure 6.2 were measured. Measurements were performed using a Zeiss KS300 image analysis system. An estimate of the ratio of the plastic zone size r_p to the oxidised particle radius $r_{Nb_2O_5}$ was obtained by taking the mean value:

$$\frac{r_p}{r_{Nb_2O_5}} \approx \frac{\left\{\frac{d_1+d_2}{d_2}+\frac{d_3+d_4}{d_4}\right\}}{2} \qquad \text{Eqn. 6.17}$$

From these experimental observations, estimates of $r_p/r_{Nb_2O_5}$ ranging from 1.57 to 3.42 (mean 2.26) were obtained, compared to the theoretical predictions of 3.12 to 3.22.

This is not a rigorous comparison, bearing in mind the following caveats:

- The particles in real specimens were not spherical.
- The particles were close to the surface and hence the matrix was not infinite.
- The amount of matrix constraint will decrease the closer a particle is to the surface.

- In microsections and fracture faces there was no guarantee the plane of observation was through the exact centre of the particle.
- In fatigue specimens, the strain due to loading may have affected bulge formation.

However, the experimental observations confirm the theoretical prediction of a substantial volume expansion when primary carbides oxidise, with experimentally-derived estimates of plastic zone sizes roughly similar to the predicted values.

6.2.4 Thermal Expansion Misfit

Some of the high temperature fatigue tests performed on the IN718 specimens were interrupted in order to take replicas or make SEM observations. Hence, the possibility of thermal expansion mis-match between the matrix and oxidising primary carbides should be considered. Thermal expansion mis-match arising from processing can also create mis-match stresses around (Nb,Ti)C particles at room temperature. These stresses may affect room temperature crack initiation. Eqn. 6.6 can be used to determine the misfit parameter between an NbC particle and the IN718 matrix on cooling from 600°C to 20°C, assuming that there was no misfit at 600°C and that no relaxation occurred during cooling. Solving Eqn. 6.15 for p_B gave a predicted pressure within the particle of -980 MPa, much lower than that predicted for oxidation mis-match (-3.48 GPa). However, a maximum tensile hoop stress $\sigma_\theta = 379$ MPa was predicted, higher than the peak σ_θ predicted for oxidation mismatch. Eqn. 6.14 gave a predicted plastic zone radius of 1.1 times the NbC particle radius at room temperature. Similar magnitudes of σ_θ and r_p/r_{NbC} were predicted for cooling from the final heat treatment temperature of 650°C, which may affect room temperature fatigue behaviour. It was not possible to estimate the thermal expansion misfit between Nb_2O_5 and the matrix because the thermal expansion coefficient of Nb_2O_5 is not known. In the case of an NbC particle which has oxidised to Nb_2O_5, it is expected that the misfit will be dominated by volumetric expansion, though an additional contribution from thermal expansion mis-match upon cooling to room temperature is possible.

6.3 Eruption Formation on Thermal Exposure Specimens

The different oxide eruptions observed on thermal exposure specimens are intriguing features, whose formation can be discussed with regard to the oxidation of primary carbides and their resulting volume expansion. Three types of surface feature arising from primary carbide oxidation have been identified and these are shown schematically in Figure 6.3(a-c). These are the layered, tower-like eruptions seen on polished surfaces (Figure 6.3a), irregular shaped eruptions commonly seen on machined surfaces (Figure

6.3b) and the surface bulges observed in metallographic cross-sections and some fatigue specimens (Figure 6.3c).

It is not known how the layered structures depicted in Figure 6.3(a) formed, but it is possible that the layers are crystallographic in nature or the result of a lamellar oxidation process. For a crystallographic explanation, the layers may be caused by the difference in crystal structure between NbC and Nb_2O_5. NbC has a cubic sodium chloride-type structure, whereas Nb_2O_5 is either orthorhombic or monoclinic. This explanation assumes that the oxide is a specific crystalline phase and is not amorphous or a mixture of phases. Alternatively, a lamellar oxidation process may have proceeded as follows: Polishing of the samples produced a number of primary carbides with flat, exposed surfaces. This flat surface was easily oxidised during thermal exposure, resulting in a layer of niobium oxide on the surface with the remaining unoxidised particle underneath. Volume expansion due to oxidation raised the oxidised material proud of the surface. The oxide/carbide interface created then provided a preferential oxygen diffusion path for further oxidation. Another layer of oxide formed and expanded, forming another oxide/carbide interface. This process continued, building the observed tower-like structures. The layered surface eruptions on polished specimens were similar to those observed by Sjoberg et al. [6.2], but the authors did not comment directly on their morphology or offer a mechanism for their formation.

For a carbide only just exposed at the surface, like that shown in Figure 6.3(b), constraint by the matrix prevented free expansion of the oxide, resulting in a more irregular surface eruption and in some cases local matrix deformation. This scenario will also apply for the formation of eruptions on machined surfaces, where the primary carbides were partially exposed or covered by a very thin skin of matrix material.

The third scenario, shown in Figure 6.3(c), applies when a sub-surface carbide oxidised, and mis-match stresses due to the volume change between carbide and oxide were sufficiently high to cause matrix deformation. The fact that some carbides at the same depth below the surface did not oxidise suggests that a preferential diffusion path such as a grain boundary was required to produce sub-surface carbide oxidation.

6.4 Fatigue in Plain Bend Bars

6.4.1 Room Temperature Fatigue Testing

Room temperature tests were conducted to see if crack initiation occurred due to a micro-notch effect of pre-oxidised primary carbides. In fact, the results showed that pre-erupted carbides were not very effective crack initiators under cycle-dependent conditions at room temperature. Possibly, full eruption of the carbides reduced the potential for crack initiation by carbide cracking or separation of a carbide/matrix interface. As discussed in Section 6.2.4, residual stresses due to thermal expansion mis-match can develop around the primary carbides during cooling from the final heat-treatment temperature. Subsequent thermal exposure and oxidation of surface carbides may have helped to relieve those stresses, reducing the possibility of carbide/matrix interface separation. This may outweigh the potential for crack initiation at an erupted particle due to a micro-notch effect. Additionally, the fatigue tests were performed on specimens with surfaces polished prior to thermal exposure. Polishing more cleanly exposed some of the surface-intersecting primary carbides prior to oxidation, so that there was less constraint of the particles by the matrix and hence less matrix deformation as a result of volume expansion during oxidation. Minimising the matrix deformation associated with eruption formation may also help to reduce the tendency for crack initiation at eruptions during subsequent room temperature fatigue testing.

Short fatigue crack growth in the plain extruded bar specimens was as expected, exhibiting the so-called "anomalous" behaviour of short cracks when characterised using the LEFM parameter ΔK. Overall, there was little difference between the crack growth rates or fatigue lives of the specimens tested. In each case, cracks which initiated early on in the fatigue life (20000 - 40000 cycles, i.e. 15 - 30% N_f) were the ones which came to dominate the final fracture. The implication is that the fatigue life at room temperature was growth limited rather than initiation limited at the stress levels used.

6.4.2 High Temperature Testing

High temperature testing was performed on polished plain bend bars of Batch A disc material. As stated in Chapter 4, the aim of these tests was to provide back-up experiments in case study of crack growth in U-notch specimens proved unfeasible. In the event, substantial experimental work on U-notch specimens was performed, so study of plain bend bar specimens became a low priority in the test programme. Even so, the results will be discussed here because of some insights and lessons that may be obtained from them.

It is not certain what prevented crack initiation in the polished plain bend bar specimens at 600°C. The most likely cause is that the loads used were too low to give sufficient damage accumulation for crack initiation at slip bands or at stress concentrations where slip bands impinge on grain boundaries or particles. Test PB1 was performed with $\sigma_{max} = 930$ MPa, below the yield stress of 982 MPa at 600°C. In contrast, the FE model for the U-notch specimen after 10 cycles at a nominal $\sigma_{max} = 750$ MPa predicted a maximum von Mises stress of 1010 MPa, and a maximum tensile value of $\sigma_{xx} = 1170$ MPa, considerably higher than that used for test PB1. In test PB2, the applied σ_{max} in 3 point bend was increased in increments to 1180 MPa. In comparison with the maximum stresses in the U-notch, $\sigma_{max} = 1180$ MPa was a more realistic choice of load level for promoting crack initiation. However, most of the testing was performed at a frequency of 10 Hz. Testing at high frequencies is thought to produce more homogeneous slip in IN718 at elevated temperatures [6.16], reducing the tendency to form persistent slip bands. This may have reduced the probability of crack initiation in the plain bend bar test at 10 Hz. The FE model for the U-notch specimens was not available at the time the plain bend bar specimens were conducted. If plain bend bar tests at 600°C are to be considered for the future, then it would be useful to perform some elastic-plastic FE modelling of the plain bend bar specimens to identify load levels that would achieve a strain range similar to that obtained in the U-notch root.

Other, less important possible mechanisms for the prevention of crack initiation are stress relief due to creep relaxation, surface residual compressive stresses or the neutralisation of carbides as initiation sites due to carbide oxidation. Unlike the polished U-notch specimens, no crack initiation due to sub-surface oxidised carbides was observed. If there was insufficient slip band formation, this may have led to slower oxidation kinetics because there were fewer preferential paths along slip bands for stress-assisted oxygen diffusion.

The room temperature tests in the disc material were intended to establish if residual surface compressive stresses were preventing crack initiation. Both room temperature tests failed due to rapid propagation of a single crack initiated at one edge. Better bevelling of specimen edges to prevent edge initiation would have prevented this. However, replicas from test PB4 show that a short surface crack initiated at a carbide after 10000 cycles, suggesting that surface residual stress was not a factor in preventing crack initiation.

6.5 U-notch Stress-Strain Field

6.5.1 Stress Concentration & Cyclic Softening

FE modelling predicted an elastic stress concentration factor of 2.08 for the U-notch geometry. Tests were conducted with values of σ_{max} between 750 MPa and 1000 MPa, producing theoretical peak stresses in the notch root of 1560 MPa to 2080 MPa. These theoretical values are well above the uniaxial ultimate tensile stress of IN718 at 600°C, which as listed in Table 5.4 was 1219 MPa for the disc material used in this study. In reality, the material in the notch root yielded before such high stress levels were reached, producing a plastic zone in the notch root. Predicted plastic zone depths in the notch root increased with increasing applied stress, as expected. The zones were deepest at the notch centre, with a decrease in depth at the free surfaces at the specimen sides, shown in Figure 5.27.

Additionally, Inconel 718 is known to undergo cyclic softening at high temperatures [6.17, 6.18, 6.19]. At room temperature, there is some initial cyclic hardening, followed by cyclic softening [6.17, 6.20]. Cyclic softening means that for a constant applied strain amplitude, there is a reduction in the stress amplitude. Alternatively, for a constant applied stress amplitude, there is an increase in the resulting strain amplitude. This cyclic softening behaviour does not continue indefinitely. After an initial "shakedown" period, the material stress-strain response reaches an equilibrium [6.21]. This behaviour was incorporated into the material model used for FE modelling, which predicted a reduction in the local stress amplitude with cycling. This cyclic softening behaviour is shown in Figure 5.24. IN718 exhibits cyclic softening behaviour under fatigue loading because of its tendency to exhibit planar slip, as reviewed in Chapter 3 Section 3.2.8. The mechanism by which this occurs in IN718 is thought to be the shear dissolution of the γ'' strengthening precipitates [6.17, 6.20], though it has been pointed out [6.18] that the absence of γ'' in TEM images of slip bands in IN718 may be because the ordered DO_{22} structure of the particles was disrupted by shearing to give the same stacking sequence as the δ phase. Loss of order in the particle and a reduction in the mean particle area encountered by dislocations in their slip planes were proposed as alternative mechanisms of cyclic softening [6.18, 6.19]. The presence of a plastic zone and the development of cyclic softening in the notch root was expected to influence crack initiation and growth behaviour. Discussion of this influence is included in the following sections on crack initiation and growth in the U-notch specimens.

6.6 Crack Initiation Mechanisms in U-notch Specimens

6.6.1 Intrinsic Initiation

In this study, intrinsic initiation refers to crack initiation at sites where there was no surface or sub-surface particle or inclusion that could be identified as the cause of crack initiation. Intrinsic initiation was therefore that which occurred either along slip bands or at grain boundaries. The surface broaching marks may have influenced fatigue crack initiation via a micro-notch effect, though as will be discussed in Section 6.6.4, there was not a straightforward link between surface roughness and crack initiation.

Intense planar slip in Batch B specimens was evident from the slip bands visible on polished U-notch surfaces at σ_{max} = 790 MPa and σ_{max} = 885 MPa. Compared to Batch A specimens, a greater proportion of fatigue cracks initiated intrinsically, rather than at oxidised primary carbides. These observations are thought to be linked; if persistent slip bands develop in a material, then these can lead to crack initiation in a variety of ways. Compared to the surrounding matrix, slip bands are regions of high dislocation density and the interface between the slip band and the matrix can act as a preferred initiation site [6.21]. Formation of intense slip bands and crack initiation along them is promoted by cyclic softening, with dislocations preferentially gliding along the softer band rather than in the harder surrounding regions [6.17, 6.22]. As outlined in Chapter 3, in materials like IN718 which are sensitive to the environment at elevated temperatures, grain boundary embrittlement by oxidation can occur [6.23, 6.24, 6.25]. Impingement of slip bands on grain boundaries produces local stress concentrations at the boundary. The slip bands can also act as fast diffusion paths for diffusion of oxygen, accelerating grain boundary oxidation. Hence, stress concentrations at a grain boundary combined with grain boundary embrittlement may initiate cracks. In the case of the U-notch specimens, crack initiation appeared to be predominantly transgranular, so grain boundary embrittlement was not a major mechanism of crack initiation in this case. However, some intergranular crack propagation was observed on fracture surfaces, so the environment was affecting crack propagation paths.

A few bulges were observed at Batch B initiation sites which were found not to be associated with oxidised primary carbides. These features may have been an artefact of the broaching process, or small protrusions of material like those seen in specimens tested in vacuum. These protrusions are possible evidence of intense slip band formation and were of a similar scale to slip band extrusions observed elsewhere [6.21]. Note that in as-broached specimens the roughness of the U-notch masked the appearance of slip bands on the notch surface. Protrusions where slip bands intersect a free surface may act as crack initiators due to the local stress concentrating effect of the step formed.

Some intrinsic initiation was observed in Batch A specimens as well as in the Batch B specimens, though intense slip bands were not seen in the polished notch roots of Batch A specimens. However, there may still have been crack initiation in the Batch A notch roots along favourably oriented slip lines, and machining marks on as-broached specimens could also have acted as crack initiators.

6.6.2 Effect of Environment on Initiation

As expected, testing in vacuum suppressed the oxidation of primary carbides and the majority of crack initiation sites did not have a particle or other feature at the origin. Crack initiation was therefore intrinsic, probably enhanced by the micro-notch effect of the broaching marks in the notch root. The small bulges seen at three of the sites may have been extrusions of material where slip bands intersected the notch surface. Such extrusions can have a bulge-like appearance, such as the example shown in Figure 3.5 of Suresh [6.21]. Both vacuum tests were performed on Batch A U-notch specimens. Therefore it is not known what influence the surface deformation layer had on fatigue crack initiation behaviour in vacuum compared with Batch B specimens which did not have a deformation layer.

6.6.3 Initiation by Oxidised Primary Carbides

The bulges above oxidised carbides seen at crack initiation sites in the U-notch fatigue tests were very similar to the bulges observed in cross-sections through thermal exposure specimens. Both observations are evidence for extensive plastic deformation in the matrix around oxidising sub-surface primary carbides, as predicted by the misfit calculations in Section 6.2.3. For a mechanism of fatigue crack initiation in the U-notch specimens, it is proposed that the misfit strains due to carbide oxidation were superimposed on the elastic-plastic stress-strain field due to external loading. This created local strains high enough to cause fracture of the matrix in the vicinity of an oxidising particle, hence initiating a fatigue crack. The plastic deformation in the notch root and the formation of slip bands may have promoted stress-assisted oxygen diffusion, causing more rapid oxidation of the sub-surface primary carbides than that observed for unstressed thermal exposure specimens. Once a crack initiated, the crack itself provided another fast oxygen diffusion route to a sub-surface particle. The surface cracks observed experimentally at oxidised sub-surface carbides were very sharp, probably resulting in a high stress intensity at the crack tip which drove further propagation.

Matrix deformation was seen around some surface eruptions formed by oxidised (Nb,Ti)C carbide particles. It was originally thought that initiation at these surface oxide eruptions might be due to the micro-notch effect of a cavity beneath the erupted particle. However, the observation of matrix deformation associated with some surface eruptions in thermal exposure specimens and on the U-notch fatigue specimens suggests that it was the additional matrix strain caused by expansion mis-match which assisted crack initiation. Matrix deformation, combined with plastic strain accumulation from the fatigue loading could have caused initiation from those surface eruptions which produced sufficient misfit strains in the matrix. Initiation from surface eruptions was observed in Batch A and Batch B specimens, though many surface eruptions in both batches of material did not initiate cracks, so that only those eruptions which produced high enough misfit strains acted as crack initiators.

The high incidence of bulges at crack initiation sites in Batch A specimens suggests that expansion of oxidising sub-surface primary carbides was a significant mechanism of fatigue crack initiation in the notch root. Certainly for Batch A specimens, it was the oxidised sub-surface carbides, rather than oxide eruptions in general, that were the more numerous type of crack initiation site in U-notch specimens tested in air. This was not the case for Batch B specimens, in which initiation at oxidised sub-surface carbides was infrequent. The difference in crack initiation behaviour between the two batches of specimens when tested under the same conditions must arise from some difference in structure or mechanical properties in the notch root. There were two significant differences between the two batches of specimens; the roughness of the broached U-notch surfaces and the local microstructure in the notch root. The Batch B specimens had notch roots which where rougher than the Batch A specimens, while the Batch A specimens had a work hardened deformation layer in the notch root which was not present in Batch B specimens. Both these observations point to differences in the broaching process used to machine the U-notches. It is believed that the deformation layer in Batch A specimens arose from use of a blunt tool, causing local deformation of the material rather than cutting it cleanly.

6.6.4 Effect of Broaching on Initiation

Surface roughness will affect crack initiation behaviour. Generally, rougher surfaces result in earlier crack initiation and shorter fatigue lives due to the local stress concentration effect of surface features like scratches and machining marks. Despite the role of surface roughness in fatigue crack initiation and its relevance to real engineering components, little work has been done to quantify the effect of surface roughness on fatigue performance. In a study by Andrews et al. [6.26] on two microstructural variants of IN718, it was found that machining marks, rather than microstructure, were controlling crack initiation life in double edge notch specimens at 650°C. Taylor and Clancy [6.27] correlated the fatigue limit of En19 steel with the surface roughness parameters R_a and R_v for different surface finishes. Testing was performed under high cycle fatigue conditions at room temperature and it was found that polishing resulted in the highest fatigue limit. Even low roughness finishes like grinding and milling resulted in a distinctly different fatigue limit. Taylor and Clancy's data is reproduced in Table 6.6.

Surface	**R_a (μm)**	**R_v (μm)**	**Fatigue Limit (MPa)**
Polished (1μm diamond)	0.1-0.3	3-5	775
Ground	0.5-1.4	7-14	690
Milled (fine)	1.0-2.2	11-15	775
Milled (coarse)	1.1-1.8	26-34	733
Shaped (fine)	27-33	210-280	620
Shaped (coarse)	35-44	360-390	520

Table 6.6: Roughness data for different surfaces on En19 steel, from Taylor and Clancy (1991) [6.27].

By comparing theoretical LEFM predictions of threshold stress intensity with observed experimental results, the authors found that low roughness surfaces (ground, milled) were approximately described by a short crack approach, whereas for higher roughness (shaped surfaces) a notch approximation was better [6.27].

In the case of the U-notch specimens, if surface roughness was the critical factor one would expect the Batch B specimens to have a shorter fatigue life than the Batch A specimens under the same conditions. However, the opposite was observed, with as-broached Batch B specimens having longer lives, as shown in Figure 5.28. The as-broached Batch B specimens generally had fewer initiation sites than Batch A specimens tested under the same conditions. For polished Batch B specimens, the total number of initiation sites was also lower than in Batch A. Therefore, surface roughness alone cannot explain the difference in initiation behaviour between Batch A and Batch B.

The other difference between the notches in Batch A and Batch B was the presence of a deformation layer in the Batch A samples. This was up to 40 μm thick on the notch sides and approximately 10-16 μm thick in the notch root. The layer was not observed in Batch B specimens. Vickers microhardness measurements indicated that the surface deformation layer was approximately 15% harder than the bulk material in Batch A specimens, as described in Section 5.1.3 of Chapter 5. Cahoon et al. [6.28] related yield stress to hardness using the formula:

$$\sigma_y = 9.81\left(\frac{H_v}{3}\right)(Q)^{(n)} \qquad \text{Eqn. 6.18}$$

where:

σ_y = yield stress in MPa

H_v = Vickers hardness

Q = a constant

n = work hardening exponent

From Eqn. 6.18 it follows that providing n is constant, for a 15% increase in hardness a 15% increase in yield stress is predicted. This higher localised yield stress may have influenced crack initiation behaviour. Considering a purely continuum approach, it is possible to estimate how the higher local yield stress affected the local strain amplitude, and hence the strain-life characteristics of the Batch A specimens. Ideally, this should have been done by modifying the FE model to take into account a higher local yield stress at the notch surface, but this was not possible using the existing mesh or the user-defined constitutive model. Instead, a simplified approach was adopted, using the existing FE model outputs of elastic and plastic strain components at the notch root centre (node 222). A 15% increase in yield stress will increase the elastic strain before yielding occurs by the same factor, so the elastic components of strain in the notch root at σ_{max} were increased by a factor of 15% to reflect this. It was not possible to establish the effect of an increased yield stress on plastic strain components, so these were assumed to be unchanged. This assumption was considered reasonable, since most of the reversible strain in the notch root was due to the elastic contribution. The total strain amplitudes ε_{amp} for Batch A tests were then re-calculated using Eqn. 4.3 and Eqn. 4.4. The resulting adjusted strain-life curve for Batch A is compared with the original Batch B results in Figure 6.4. With total strain amplitudes adjusted to account for pre-existing cold work hardening in the notch root, the Batch A results now lie close to those obtained for Batch B specimens. Hence, an increased local yield stress and total strain amplitude in the notch root may explain the difference in the strain-life behaviour between Batch A and Batch B specimens.

Considering now a more microstructural explanation of the role of the surface layer, it is known that strain-life behaviour generally reflects the resistance of a material to crack initiation. The main crack initiation mechanism in Batch A specimens was matrix rupture caused by oxidation of sub-surface primary carbides. A higher yield stress will have led to greater stresses around mis-fitting particles, as predicted using Eqn. 6.11 to Eqn. 6.13. For example, with a 15% increase in σ_y, the maximum value of the hoop stress increased from 327 MPa to 376 MPa, though there was a reduction in the predicted plastic zone radius. For a carbide oxidising in the deformation layer of Batch A, these higher misfit stresses combined with the external loading may have enhanced crack initiation and early crack growth. This is consistent with the observation of many cracks initiating at oxidised carbides in Batch A, but only a few in Batch B. An additional effect on crack initiation and propagation in Batch A may have resulted from reduced ductility in the work-hardened layer.

6.6.5 Initiation at Primary Nitrides

In a few cases in Batch B, crack initiation at primary nitride particles was observed. This was probably due to slip band impingement on the particles, producing stress concentrations at the particle-matrix interface which resulted in crack initiation either by cracking of the particle or decohesion of the particle-matrix interface. This mechanism of crack initiation has been observed in other superalloys containing primary carbide and nitride particles, such as Incoloy 908 [6.29].

6.6.6 Quantification of Initiation Sites

The quantitative data for the number of crack initiation sites show that there were more initiation sites in Batch A specimens than in Batch B specimens tested under the same conditions. As already discussed in Sections 6.6.3 and 6.6.4, this may be linked to the deformation layer present in Batch A specimens.

Examining the post-fracture initiation site quantification data for the U-notch specimens in Tables 5.13 and 5.14 , there are some discrepancies between the number of sites counted on the left-hand and right-hand halves of the specimen. It is possible that some sites were overlooked during quantification, though considerable care was taken to ensure no sites were missed. An alternative explanation for the discrepancy can be offered by considering the relative positions of the short cracks which initiated in the notch root and the way they coalesced to form the dominant defect. This is illustrated schematically in Figure 6.5. During fatigue testing, a number of parallel but non-coplanar short cracks initiated in the notch root (see Figure 6.5a). As these short cracks grew, some of them overlapped before crack coalescence occurred (see Figure 6.5b). After coalescence, the dominant defect propagated until the specimen fractured. Note how coalescence behind the crack tips can result in the formation of an island of material. Some of the overlapping short cracks which contribute to the dominant defect only appeared on one half of the fractured specimen (Crack 1 in Figure 6.5d), hence leading to a discrepancy between the number of initiation sites counted on the left-hand and right-hand halves of fractured specimens. The coalescence of non-coplanar cracks resulted in the stepped appearance of the fracture surfaces in the notch root.

6.7 Crack Initiation Kinetics in U-notch Specimens

General observations on interrupted U-notch tests indicated that cracks first initiated within the first 25% of the overall fatigue life. More detailed crack initiation data was obtained from the interrupted replica tests on polished U-notch specimens, as shown in Figure 5.34 and Figure 5.36. Comparing these plots of number of cracks versus number of cycles, it can be seen that there were differences in initiation kinetics between the Batch A specimens tested at the lower stress levels σ_{max} = 750 MPa or σ_{max} = 790 MPa, and the high stress level Batch B tests at σ_{max} = 885 MPa. These will now be discussed.

6.7.1 Batch A Tests: σ_{max} = 750 MPa and σ_{max} = 790 MPa

For the Batch A tests at σ_{max} = 750 MPa and σ_{max} = 790 MPa, there was an initial incubation period at the start in which no cracks were observed. This incubation period was 2000 cycles at σ_{max} = 750 MPa and 5000 cycles at σ_{max} = 790 MPa. Given that replicas were taken every 2000 cycles, it is possible that crack initiation actually occurred earlier than this. However, the initially slow rate of crack nucleation in both tests is indicative of some form of incubation period necessary for crack initiation. Some of the first cracks observed initiated at bulges due to sub-surface primary carbide oxidation, so the incubation period for initiation is linked to the time required for oxidation of the particles. In terms of time at the test temperature of 600°C (including soak times), this period was approximately 2 hours 23 minutes for test A600-750-1-PR-01 and 5 hours 53 minutes for test A600-790-1-PR-01. This is considerably faster than the time required for sub-surface oxidation in unstressed thermal exposure samples, which was between 64 and 128 hours at 600°C. This implies a strong effect of fatigue cycling on the kinetics of oxidation, probably caused by enhanced oxygen transport along slip bands. The first particles to oxidise and initiate cracks may have been those favourably situated for fast oxygen diffusion to the particles, either being close to the surface or on a grain boundary. As already discussed, the deformation layer present in the notch root of Batch A specimens may have promoted faster diffusion. Following the initially slow rate of crack initiation, there was a transition to behaviour in which the number of cracks appearing increased at a steady rate, which was similar in both tests. The factors controlling this rate are thought to be the time required for oxidation of carbides in different parts of the specimen and the time required for accumulation of sufficient cyclic damage in the material to initiate further cracks. The number of primary carbides which are potential crack initiation sites will depend upon the number density of primary carbides in the material, their distribution relative to the notch surface and their distribution relative to preferential oxygen diffusion pathways such as grain boundaries. The local stress-strain environment around potential crack initiation sites will vary, depending on the position of the site in the notch root and shielding by cracks which have already initiated. The number of cracks initiated eventually reached a plateau, which can be attributed to a combination of exhaustion of potential crack initiation sites, reduction in the local strain at initiation sites due to shielding by neighbouring cracks, and crack coalescence.

6.7.2 Batch B Tests: σ_{max} = 885 MPa

In Batch B tests the development of crack initiation over time was significantly different from the Batch A tests performed at lower stress levels. Figure 5.36 shows that few cracks initiated until the latter stages of the fatigue life. As described in Section 5.6.2 of Chapter 5, the fatigue failure was controlled by initiation and growth of a single crack, with most of the other cracks initiating in the stress-strain field ahead of the tip of the growing crack or in the residual ligaments. One possible cause of the difference between Batch A and Batch B tests was the absence of a work-hardened surface layer in Batch B. This may have reduced the propensity for crack initiation at oxidised carbides compared to Batch A specimens. The effect of the deformation layer on crack initiation was discussed in Section 6.6.4. Another possible reason for reduced crack initiation was the much higher stress level used for Batch B. This led to a shorter fatigue life, allowing less time for sub-surface carbide oxidation and hence limited initiation by an oxidation mis-match strain mechanism. The formation of persistent slip bands was enhanced by the greater strain range in the notch root at $\sigma_{max} = 885$ MPa, and the absence of a surface deformation layer may also have promoted persistent slip band formation. This permitted rapid propagation of the dominant surface crack along slip bands or grain boundaries, reducing the potential for crack initiation elsewhere due to shielding by the main crack, except in the high stress regions ahead of the crack tips in the residual ligaments.

6.8 Short Crack Growth in U-notch Specimens

The failure of the LEFM parameter ΔK to adequately characterise short crack growth is expected, since ΔK is not valid for the material in the notch root, which underwent a considerable amount of plastic deformation. Characterisation of crack growth rates using alternative driving forces such as ΔJ or crack tip plastic strain range could be attempted, but it was considered beyond the scope of this investigation to undertake the additional FE modelling work required to calculate such parameters for individual cracks in the notch root. Such a characterisation could be further complicated by the presence of the deformation layer in Batch A specimens, which may have exerted an additional microstructural influence on crack propagation. However, it is worth qualitatively considering the approach to short crack fatigue proposed by Sadananda and Vasudevan [6.30, 6.31, 6.32, 6.33]. Briefly, their approach states that there are two driving forces, ΔK and K_{max}, which must be sufficient for cracks to grow. ΔK accounts for the accumulation of cyclic plasticity in the material and K_{max} (or its EPFM equivalent J_{max}), accounts for the forces required to break crack-tip bonds and cause crack advance. This leads to two crack growth thresholds, ΔK^* and K^*_{max} which must both be exceeded if a crack is to propagate. Experimentally, short crack propagation is affected by temperature, environment and microstructure. Sadananda and Vasudevan proposed [6.30, 6.30, 6.32, 6.33] that for short cracks it is the local crack tip environment that is crucial for determining crack propagation, and hence K_{max}, rather than ΔK is the important driving force for crack growth. If local forces due to external loading and internal stresses in the crack tip region fall below K^*_{max} then the crack will not propagate. For long cracks, the sensitivity to local crack tip conditions decreases and crack growth behaviour is controlled by ΔK. Sadananda and Vasudevan claimed [6.30] to be able to rationalise the "anomalous" behaviour of short cracks without invoking closure arguments. Indeed, their approach is attractive because it acknowledges that a material is not a continuum and that the local crack tip environment is important for determining short crack growth. The difficulty in using their approach for short cracks is in calculating the local value of K_{max} or J_{max} in specific cases.

6.8.1 Crack Propagation Rates

The two notable features of short crack propagation in the Batch A specimens at σ_{max} = 750 MPa and 790 MPa were the constant growth rate with increasing crack length and the very straight, transgranular path of the cracks along the notch root. The constant growth rate implies that the local crack tip driving force was constant for short cracks growing in isolation, except when it was reduced by crack shielding and interactions between the crack-tip stress fields of neighbouring cracks. This unusual behaviour of the surface cracks may have been partly due to the deformation layer present in the notch root, though the constant growth rate was observed for crack lengths at which the depth "*a*" was well beyond the observed extent of the deformation layer. For A600-750-1-PR-01 and A600-790-1-PR-01, the crack growth rates were 2 to 3 orders of magnitude smaller than the growth rates in the U-notch geometry studied by Bache et al. [6.34] (see Figure 5.54). Note that the rates were for much shorter cracks than those considered by Bache et al. [6.34], suggesting a change in propagation rate once cracks reached a critical size. This is supported by the rapid propagation of longest cracks in A600-750-1-PR-01 and A600-790-1-PR-01 towards the end of the tests. The change from steady to rapid crack growth at longer crack lengths in the Batch A tests suggests some form of critical crack length. In test A600-750-1-PR-01, assuming an *a:c* ratio of 1, the longest crack (Crack II) grew at a constant rate to a depth of approximately 0.42 mm. As well as being beyond the extent of the deformation layer, this was also beyond the predicted plastic zone depth in the notch root of approximately 0.185 mm (based on 0.2% plastic strain; see Figure 5.27). In test A600-790-1-PR-01, the longest crack (Crack B) grew stably to a length of 2c = 301 μm, beyond which there was very rapid growth and coalescence. Assuming an *a:c* ratio of 1, this represented a crack depth "*a*" of 150.5 mm, which is less than the predicted plastic zone depth of 240 μm (based on 0.2% plastic strain). Hence there does not appear to be a clear correlation between changes in crack propagation rate and the depth of either the deformation layer or the notch plastic zones in the Batch A tests.

Unlike the Batch A tests at σ_{max} = 750 MPa and σ_{max} = 790 MPa, the Batch B tests at σ_{max} = 885 MPa exhibited the more typical crack growth behaviour of increasing growth rate with increasing crack length, tending towards the Stage II crack growth behaviour expected for long cracks. Crack propagation rates reached the same order of magnitude to those reported by Bache et al. for similar crack lengths [6.34] (see Figure 5.54), bearing in mind that the experimental conditions were different. It could be that at σ_{max} = 885 MPa, local effects of microstructure and the notch plastic zone were less significant for crack propagation, and the growth was mainly driven by the externally applied stress amplitude. No deformation layer from broaching was present in the Batch B samples, which may also have altered the crack propagation behaviour relative to Batch A. There is some evidence for this in test B600-790-1-P-01 tested at σ_{max} = 790 MPa, in which slip bands were observed on the polished notch surface, but they were not observed in the equivalent tests performed on polished Batch A specimens.

6.8.2 Influence of Broaching Marks

One feature that may have affected crack propagation was the presence of broaching marks in the notch roots. The marks were straight and parallel to the notch axis and therefore favourably oriented to influence crack propagation. In Batch A specimens, cracks in the notch root were straight and parallel to the notch axis in both as-broached and polished specimens, so a conclusive link between broaching marks and crack propagation path was not apparent. In Batch B specimens, a clear difference between microscopic crack paths was apparent when as-broached and polished specimens tested under the same conditions were compared. For an as-broached notch, the surface crack path was essentially straight and parallel to the broaching marks, whereas in a polished notch the crack path deviated along slip bands or grain boundaries, as shown in Figure 5.56.

This difference may help to explain why polished specimens generally had longer fatigue lives than as-broached ones. In as-broached specimens, the broaching marks could have a micro-notch effect, providing a favourable pathway for surface crack growth parallel to the notch root, so that short crack growth rates were faster in as-broached specimens than in polished specimens. Using the arguments of Sadananda and Vasudevan [6.30] the broaching marks possibly enhanced the local value of the crack driving force K_{max} because of their stress concentrating effect. In the polished U-notch of Batch B specimens, persistent slip bands developed. Cracks were observed to propagate along slip bands or along grain boundaries. Some intergranular propagation in IN718 is expected at 600°C in air, because of oxidation embrittlement of grain boundaries [6.23, 6.24, 6.25]. In the Batch B U-notches, it is proposed that surface crack propagation of the crack along slip bands and grain boundaries produced a longer, more tortuous crack path, resulting in partial shielding of the crack from the applied stresses and hence a lower crack propagation rate. In Batch A specimens, removal of the broaching marks may have reduced the local crack driving force by eliminating the stress concentrating effect of the broaching marks, even though the actual crack path was unaffected. Removal of some of the surface work-hardened layer by polishing could also have acted to reduce surface crack propagation rates in Batch A.

Another experimental observation to consider is the absence of slip bands on polished notch surfaces of Batch A specimens. For example, at σ_{max} = 790 MPa at 600°C in air with a 1-1-1-1 waveform, slip bands were observed on the polished notch of a Batch B sample (Test B600-790-1-P-01), but not on Batch A samples (Tests A600-790-1-P-02 and A600-790-1-P-03). In Batch A samples, the surface cracks initiated were very straight, whereas in Batch B the surface cracks followed slip bands and grain boundaries. Metallographic cross-sections of notches showed that the deformation layer was still present in polished samples of Batch A specimens. The implication of these observations is that the deformation layer produced by broaching of the Batch A notches affected subsequent high temperature slip and fatigue behaviour. Ghonem et al. [6.24, 6.35] found that pre-straining IN718 room temperature produced more homogeneous slip during subsequent fatigue testing at 650°C in air. Though the authors were interested in the effects of pre-straining on long crack propagation rates, their result is relevant to the case of the U-notch roots because it demonstrates that prior deformation at room temperature can influence subsequent high temperature slip behaviour. Contrary to the observations of Ghonem et al. [6.24, 6.35], Kalluri et al. [6.36, 6.37] found that monotonic pre-straining of IN718 specimens resulted in more inhomogeneous slip during subsequent fatigue testing. The amount of slip inhomogeneity increased as the amount of pre-strain was increased from 2% to 10% [6.36]. However, unlike Ghonem et al. [6.24, 6.35], Kalluri et al. [6.36, 6.37] conducted their fatigue testing at 20°C under strain control. The fatigue life of samples pre-strained in tension was reduced relative to unstrained samples, suggesting that tensile pre-straining increased the susceptibility of the material to crack initiation along slip bands or at grain boundaries. The detrimental effect of pre-straining on fatigue life was most pronounced for low strain ranges, and decreased for higher strain ranges. There was little effect on fatigue life for specimens pre-strained in compression.

Neither the work of Ghonem et al. [6.24, 6.35] or Kalluri et al. [6.36, 6.37] provide sufficient insight into the absence of slip bands in the Batch A polished samples. If the deformation layer in Batch A did result in more homogeneous slip at 600°C, as suggested by the work of Ghonem et al. [6.24, 6.35], this would explain the absence of slip bands on polished notch surfaces. In the Batch A U-notch tests, surface cracks were straight and transgranular, which is consistent with the theory of Ghonem et al. [6.24, 6.35] that homogeneous slip reduces intergranular cracking. It was observed that below the notch surface, there was a transition to mixed transgranular-intergranular cracking of the material. The depth at which this occurred was 30-50 μm in the Batch A specimens, greater than the visible depth of the surface deformation layer, but perhaps at the boundary of the region of material in which homogeneous slip was enhanced. However, reduced fatigue lives in Batch A compared to Batch B are indicative of a detrimental effect of pre-straining, attributed by Kalluri et al. [6.36, 6.37] to greater slip inhomogeneity. Slip inhomogeneity implies the formation of intense slip bands, which were not observed in Batch A. An alternative explanation, independent of those proposed by other authors, is therefore proposed. The deformation layer in the Batch A specimens may have been work hardened to such an extent that substantial dislocation tangles or forest dislocations were generated. These dislocations would have been barriers to the co-operative glide of other dislocations, hence hindering the formation of visible slip bands. Substantial work hardening will also have reduced the ductility of the material within the deformation layer, reducing its resistance to crack initiation and propagation.

6.8.3 Surface Crack Coalescence

A detailed study of crack coalescence behaviour was beyond the scope of this work, but some of the experimental observations of coalescence behaviour are of general interest. Some aspects of crack coalescence were discussed in Section 6.6.6 to account for discrepancies between initiation site counts on the left hand and right hand halves of fractured specimens. As described in Section 5.7.1 and Section 5.7.4 of Chapter 5, short cracks in the notch root displayed some of the classic coalescence behaviour studied by Forsyth [6.38] and Soboyejo et al. [6.39]. Forsyth identified three different types of coalescence behaviour, depending upon crack offset and stress intensity factors:

(i) For steadily growing cracks approaching with a small offset under low ΔK conditions, crack tips can grow past one another, before deflecting towards one another at coalescence, producing islands of material such as that shown in Figure 5.42. A good example of crack tip deflection can be seen for crack tips c_y and c_z in Figure 5.52.

(ii) Cracks growing under high ΔK or K_{max} may deflect towards one another, coalescing by shear of the material between them before the tips overlap. This can be seen in Figure 5.52 for tips c_w and c_x. It was also observed on replicas during the final stages of fatigue life where local stresses would have been very high.

(iii) Fatigue cracks with large offsets may not deflect or coalesce, but they may affect propagation due to shielding effects [6.39].

The appearance of different crack coalescence behaviour in the same region of material, like that shown in Figure 5.52, suggests that crack coalescence behaviour is very sensitive to local stress-strain conditions. Forsyth [6.38] proposed that crack coalescence behaviour is related to crack tip plastic zone overlap. If the plastic zones overlap before the tips overlap, then breakthrough of the intervening material is more likely. If the crack tip plastic zones do not overlap, then bypass of the crack tips is possible. Complex stress-strain fields and mixed-mode loading develop in the vicinity of coalescing cracks. Crack tip deflection tends to occur in the local Mode I direction, as described by Forsyth [6.38] and Soboyejo et al. [6.39]. Apart from surface observations, it was found that cracks may coalesce at a depth position without this being apparent at the surface (see Figure 5.53). This was also observed by Soboyejo et al. [6.39].

6.8.4 Crack Propagation in the "*a*" Direction

In Batch A specimens, a transition in crack propagation mode was observed to occur at a depth of 30-50 μm below the notch surface. At the surface, propagation was transgranular, changing to mixed transgranular-intergranular in the depth direction. This may have occurred as cracks propagated beyond the influence of the surface deformation layer present in Batch A specimens. The depth of this deformation layer was observed to be approximately 15 μm in the notch root, so the transition was perhaps not solely related to the visible change in local microstructure. However, the region where localised slip characteristics were altered may have extended beyond the visible layer. Additionally, the state of plane stress at the surface is thought to favour transgranular propagation, as observed by Antunes et al. [6.40] in corner crack specimens of IN718 in air at 600°C.

Considering evolution of the crack shapes after coalescence, macroscopic examination of the fracture surfaces indicated that cracks tended towards a semi-elliptical shape, but the final crack profile which developed depended upon the position in the notch root from which the dominant crack or cracks initiated. This was briefly described in Section 5.9 of Chapter 5. In their studies, [6.39, 6.41, 6.42] Soboyejo et al. examined the evolution of the crack shapes after coalescence. Their work showed that crack aspect ratios *a:c* measured from beach marks were generally in the range 0.67 to 0.83. In this present study on U-notch specimens, the crack aspect ratio ranged from 0.62 to 1.55, with 60% of the cracks having an aspect ratio less than 1. As discussed by Soboyejo et al. [6.39], crack aspect ratios may be sensitive to specimen geometry and the specific interactions which occurred during crack coalescence. Crack aspect ratios greater than 1 are evidence of tunnelling, in which the propagation rate in the "*a*" (depth) direction was faster than in the "*c*" (surface) direction. This tunnelling may have been due to retardation of the cracks at the surface, either because of the state of stress in the notch root or shielding by other cracks. Antunes et al. [6.40] observed crack tunnelling in corner crack specimens of IN718 tested in air at 600°C. At the surface under plane stress conditions, transgranular fracture was favoured. At depth, plain strain conditions existed which were thought to increase crack propagation rates due to enhanced slip inhomogeneity and oxidation-assisted cracking. In the U-notch specimens used in this present study, some transgranular fracture was observed at the surface, consistent with the proposition of Antunes et al. [6.40] that plain stress conditions favour transgranular fracture. If oxidation-assisted propagation was occurring under plain strain in the specimen interior, tunnelling would be more evident for specimens subjected to a dwell at maximum load. This appeared to be the case for test B600-885-20-01, where an aspect ration of 1.55 was measured for one crack. In test A600-750-20-01, a crack aspect ratio of 1.15 was measured, and an aspect ratio of 1.09 was measured for a crack in test A600-750-30-01. However, a high crack aspect ratio of 1.3 was measured in test A600-790-1-P-02 with 1 second dwell, so the evidence for the effect of dwell on crack aspect ratio is not conclusive. As already discussed, the evolution of crack profiles may also be affected by where in the notch root the crack developed. Studies of crack shape evolution are generally easier with pre-initiated cracks, such as those performed by Bache et al. [6.34], or in the corner crack specimens used by Antunes et al. [6.40].

6.9 U-notch Lifetimes

The tests conducted indicate that crack initiation and growth in the U-notch specimens was a complex process, with the majority of the specimen life taken up by the initiation, growth and interaction of short fatigue cracks, until coalescence of several cracks generated a dominant defect which propagated rapidly to failure. Crack initiation and growth characteristics which affect fatigue life will be:

- The number of short cracks which initiate.
- The rate of crack initiation.
- The positions of short cracks relative to the notch axis and to each other.
- The rate of short crack growth.
- The degree to which cracks interact with one another via arrest or coalescence events.
- The rate of propagation of the final dominant defect.

Different experimental conditions such as temperature, environment, load level, waveform and notch surface condition, as well as microstructure may affect crack initiation and propagation behaviour, resulting in different overall fatigue lifetimes.

6.9.1 Effect of Environment on Lifetimes

The difference in fatigue lifetimes between the air and vacuum tests at 550°C (tests A550-750-1-01 and A550-750-1-V-01) was not as great as expected. It is possible that a temperature of 550°C was not sufficiently high to promote predominantly environment–dependent behaviour during crack propagation. Testing in air at 600°C (tests A600-750-1-01 and A600-750-1-02) produced a significant drop in fatigue life compared to vacuum (test A600-750-1-V-01), suggesting a much greater environmental dependency at the higher temperature. The greater environmental dependence at 600°C was probably due to faster oxidation kinetics for the primary carbides, resulting in faster crack initiation and a greater effect of oxidation embrittlement on fatigue crack propagation.

6.9.2 Effect of Dwell on Lifetimes

Tests performed on Batch A U-notch specimens at 600°C in air showed a beneficial effect of dwell times at maximum load. A 1-20-1-1 cycle at σ_{max} = 750 MPa (test A600-750-20-01) increased the fatigue life by a factor of 2 compared to a 1-1-1-1 cycle (tests A600-750-1-01 and A600-750-1-02) and a 1-30-1-1 cycle (test A600-750-30-01) increased the fatigue life by a factor of 3.1 compared to a 1-1-1-1 cycle. This is the same trend as that observed in a previous study of U-notch specimens manufactured from extruded bar material [6.43, 6.44], where a 1-30-1-1 cycle increased the fatigue life by a factor of 2.58 compared to a 1-1-1-1 cycle. Observations indicate that crack initiation occurred within the first 25% of the overall fatigue life, so that a significant proportion of life was taken up by short crack growth and coalescence. If this was the case, then a possible explanation for the increased lifetimes is that the dwell at maximum load retarded the growth of short cracks in the notch root. The retardation mechanism may be stress relaxation at the crack tips, or possibly oxide-induced crack closure, but closure seems unlikely for short cracks with a limited wake. Another factor to consider is the presence of a deformation layer in the Batch A specimens, which may have influenced the local slip characteristics. An apparently beneficial effect of dwell for short crack propagation in a notch geometry is surprising, given that dwell at maximum or minimum load is usually observed to enhance long crack growth rates [6.45, 6.46, 6.47, 6.48, 6.49, 6.50]. Little data for the effect of dwell on short cracks has been found in the literature, except for Bache et al.'s study of millimetre-sized cracks growing in a double-edged U-notch specimen [6.34]. The authors considered the effect of dwell at maximum load using a 17.5-x-17.5-1 waveform, where x = 1 or 30 seconds. Comparing a dwell of 1 second and 30 seconds at 600°C and a reduced air pressure of 150 Pa, the authors found that crack propagation was more rapid for the 30 second dwell than the 1 second dwell [6.34, 6.51]. Their results are consistent with observations of the effect of dwell in conventional long crack tests. (Note there is a mistake in the caption of Fig. 10 in reference [6.34]. To read correctly, the symbols for 1 second dwell and 30 second dwell should be interchanged, as confirmed in a private communication from Bache [6.51]).

A beneficial effect of dwell was not observed for Batch B U-notch specimens tested at the higher stress level of σ_{max} = 885 MPa (tests B600-885-20-01 and B600-885-20-02). The use of a higher stress level was intended to shorten the fatigue life relative to the Batch A experiments at σ_{max} = 750 MPa. This was done so that specimen fatigue lives were more representative of actual service experience, and to make it possible to perform interrupted tests with replicas to measure short crack growth rates. It was found that at 885 MPa in the Batch B specimens, a 20 second dwell reduced the fatigue life compared to a 1 second dwell, and it was decided not to perform replica studies. There was not sufficient experimental time available to assess the effect of dwell on Batch B specimens at σ_{max} = 750 MPa for direct comparison with the Batch A specimens.

The effect of a 20 second dwell on the Batch B lifetimes is consistent with the theory that dwell at maximum load enhances embrittlement of grain boundaries by oxidation, leading to higher crack propagation rates. It is possible that between σ_{max} = 750 MPa and σ_{max} = 885 MPa there was a transition in behaviour from a beneficial to a detrimental effect of dwell on specimen fatigue life. This could occur if creep processes are operating at 600°C. Stress-assisted oxidation will tend to accelerate crack propagation, while stress relaxation at crack tips due to creep will reduce crack propagation by reducing the local driving force. At σ_{max} = 750 MPa, stress relaxation may have been sufficient to counteract the effect of oxidation embrittlement during the dwell period. However, at σ_{max} = 885 MPa, enhanced oxidation embrittlement dominated over any stress relaxation at the crack tips. There may have been some oxidation-induced static load crack growth during the dwell period at σ_{max} = 885 MPa. Oxidation-induced static load intergranular cracking in the temperature range 550-650°C was recently observed in IN718 [6.52].

6.9.3 Effect of Stress Level and Broaching on Lifetimes

Not surprisingly, an increase in the value of σ_{max} while keeping other experimental conditions the same resulted in shorter fatigue lifetimes. It appears that notch surface condition, primarily the marks and/or deformation layer introduced by broaching influenced fatigue life as well. The influence of notch condition can be seen by the difference between the stress-life and strain-life curves for Batch A and Batch B in Figure 5.28 and Figure 5.31. Batch B specimens exhibited longer lifetimes than Batch A, despite Batch B having rougher notch surfaces.

Stress-life and strain-life curves are generally considered to be a representation of a material's resistance to crack initiation. This is consistent with the results for Batch A and Batch B, where Batch B samples generally had fewer initiation sites on the main fracture surface than Batch A. Interpretation of the results is complicated by the difference in behaviour between the two batches of U-notch specimens, possibly due to the deformation layer in Batch A. It appears that for Batch A specimens at σ_{max} = 750 MPa or 790 MPa, the life was controlled by the initiation, gradual growth and coalescence of a number of microscopic cracks, while in Batch B specimens at σ_{max} = 885 MPa a single, rapidly propagating crack controlled specimen life. Observations on interrupted tests and the replica records indicate that the first cracks appeared within the first 25% of total fatigue life, certainly within the first 10% of life on the polished specimens from which replicas were taken. The externally applied stress was not the only factor affecting crack initiation and propagation, and hence life. Instead, applied stress level combined with the local condition of the notch root, primarily the marks and/or deformation layer introduced by broaching were the factors which were influencing the fatigue life. As discussed in Section 6.8.2, broaching marks may have enhanced crack propagation rates, thereby shortening specimen lifetimes relative to polished specimens.

6.10 Relevance of Results to Real Turbine Discs

A concern when applying the result of laboratory tests to full scale components is ensuring the relevance of experimental work to performance under real service conditions. A case in point is the definition of crack initiation. In this study, initiation always refers to the first appearance of microscopic cracks. With the resolution of the replica techniques used to observe the cracks, they could be as small as 10-15 μm in length when first detected. However, from an engineering point of view, the crack initiation stage generally includes any crack growth below a depth of approximately 0.8 mm [6.53, 6.54]. The choice of a value of 0.8 mm was justified at the time on the basis of the limits of resolution of NDT techniques for finding cracks, and the inadequacy of LEFM crack growth laws in reliably predicting crack growth rates for shorter cracks [6.53]. Detection of a crack 0.75 mm deep was quoted [6.54] as an appropriate end point for laboratory-scale tests or full component testing. Substantial safety factors are applied to such life-to-first-crack measurements to declare the safe life of the disc. Extending the life of the component beyond the life to first crack was shown to carry a very high risk of failure, because the life to a first crack of around 0.75 mm depth was found to be very close to the burst life of test discs. The experimental results in this thesis bear out this out, with rapid crack propagation to failure once a crack reached a length of several hundred microns at σ_{max} = 750 MPa, and very rapid propagation at σ_{max} = 885 MPa. Very rapid propagation for millimetre-sized cracks was also observed in the work of Bache et al. [6.34] in double-edged U-notch specimens.

In damage tolerant design, it is assumed that components will contain defects of an initial size a_0 or c_0 and the application of crack growth laws is used to demonstrate that a component will have an adequate life as the defect propagates from its initial size to the critical size representing the end of component life. The results in this thesis show that microscopic cracks initiate early in the fatigue life of IN718 U-notch specimens and that an initial defect size of $2c$ = 10 - 15 μm can be detected using cellulose acetate replication. Features smaller than 10 μm could be resolved on the replicas, but 10 μm was considered to be the minimum resolution for crack detection. The growth rate data $d(2c)/dN$ for these cracks were typical of short cracks in that it was not possible to characterise them using the LEFM parameter ΔK. However, some useful crack growth rate versus crack length data were obtained at three different stress levels. The relatively constant crack growth rates observed for short cracks in Batch A specimens are significant, since they indicate that the driving force for crack growth in the notch roots is complex and highly localised. It must be borne in mind that the crack growth data was obtained for polished U-notches, and that fatigue lifetimes in polished specimens were longer than for as-broached specimens. Additionally, there is at present only limited test data available, so the statistical uncertainty of the results is high. The taking of replicas required numerous interruptions of the high temperature tests, so thermal cycling of the specimens may have influenced fatigue crack propagation, though steps were taken to minimise thermal fatigue effects.

The presence of a work-hardened deformation layer in the Batch A U-notch specimens which was not present in the Batch B specimens shows that the broaching process can produce microstructural changes in the material. Though the results are not conclusive, it appears that the presence of the deformation layer affected fatigue crack initiation and growth behaviour. The implication of this for real turbine discs containing hundreds of broached fir tree root fixings should not be ignored. Discs are designed, tested and certified with adequate safety factors to minimise the risk of disc failure and all discs are subject to rigorous process control. If inconsistencies in the quality of broaching are present then there is the possibility of in-disc and disc-to-disc variability in fatigue performance. It may therefore be worthwhile to investigate current broaching practices to see if process and quality control could be further improved.

In specimens with as-broached notch surfaces similar to those found in turbine discs, it was found that a significant mechanism of crack initiation was local matrix deformation caused by the oxidation of primary carbides. This was especially noticed for the Batch A specimens with a deformation layer in the notch root. Assuming that similar surface conditions may be present in turbine discs, crack initiation is likely to occur in conventionally wrought IN718 discs which contain a distribution of primary carbide particles. Though it might be tempting to try and improve the crack initiation resistance of IN718 by reducing the carbon content, previous work showed that this can have a detrimental effect on other properties such as stress-rupture life [6.55]. In addition, the development and qualification of a new alloy variant is costly and time consuming, and is only justified if a significant improvement in fatigue performance can be demonstrated. Instead, better understanding of the properties of existing alloys could assist in process control or damage modelling. For example, a disc with a higher than average number density of primary carbide particles might be expected to display a greater probability of fatigue crack initiation due to carbide oxidation.

6.11 Figures

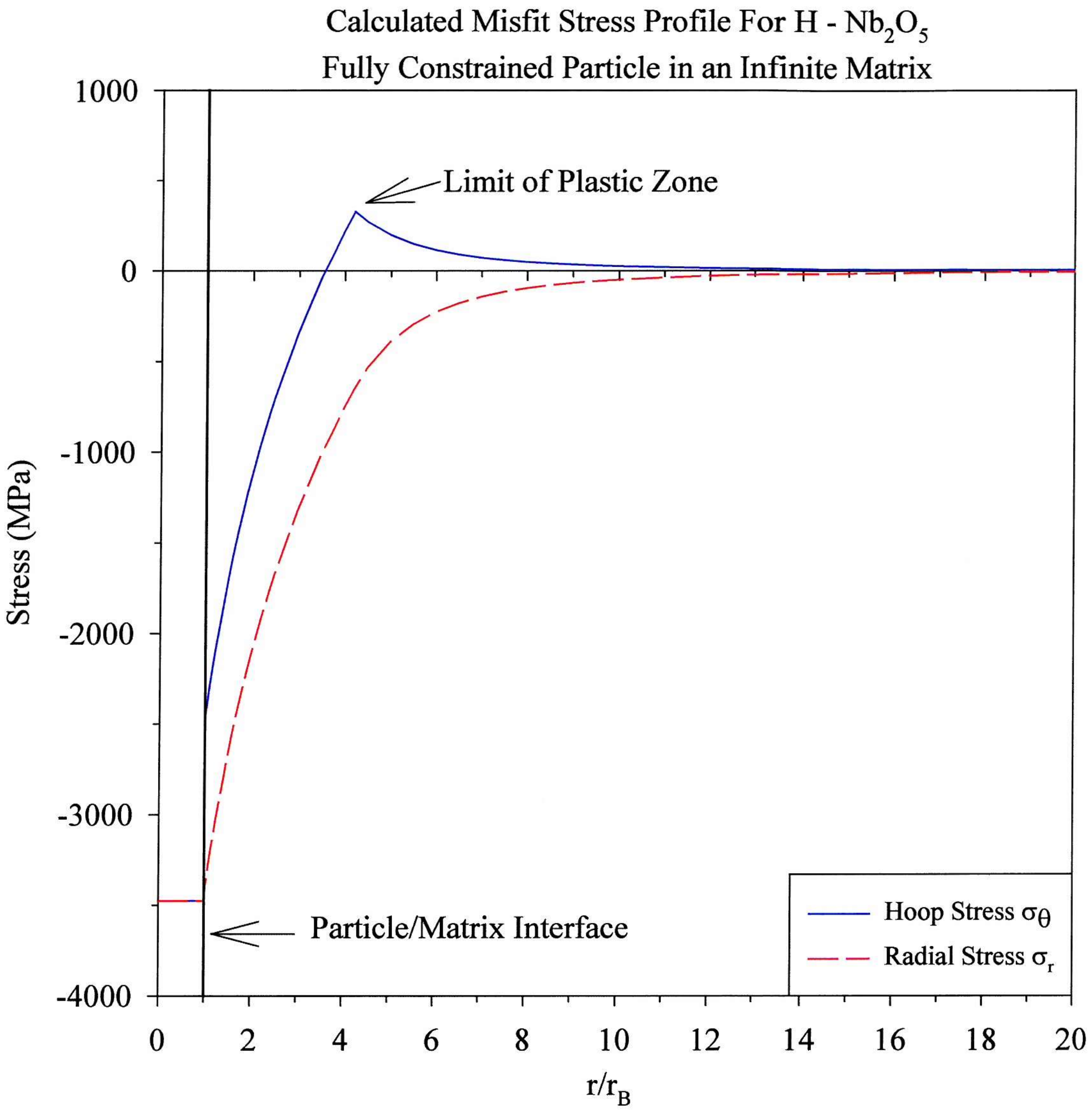

Figure 6.1: Predicted misfit stresses around a fully constrained particle of radius r_B in an infinite matrix, following oxidation of the particle from NbC to Nb_2O_5.

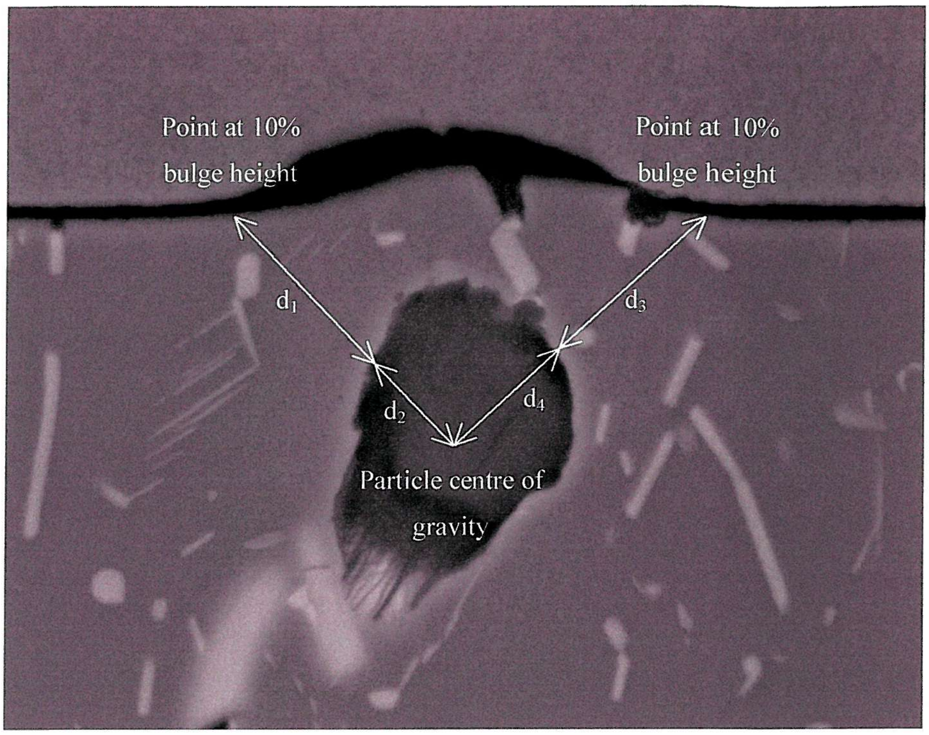

Figure 6.2: Measurements on images of bulges to determine the extent of deformation. A backscattered image from a thermal exposure specimen is used as an example.

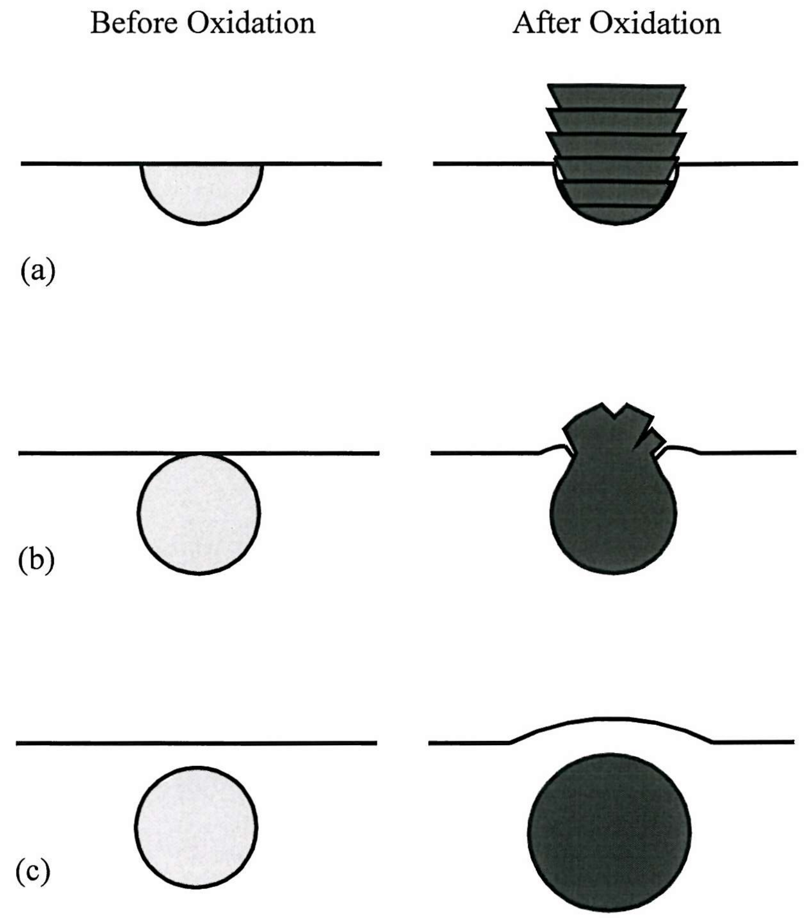

Figure 6.3: Different carbide oxidation scenarios. (a) Exposed carbide on polished surface; (b) Carbide just intersecting surface; (c) Sub-surface carbide causing matrix deformation.

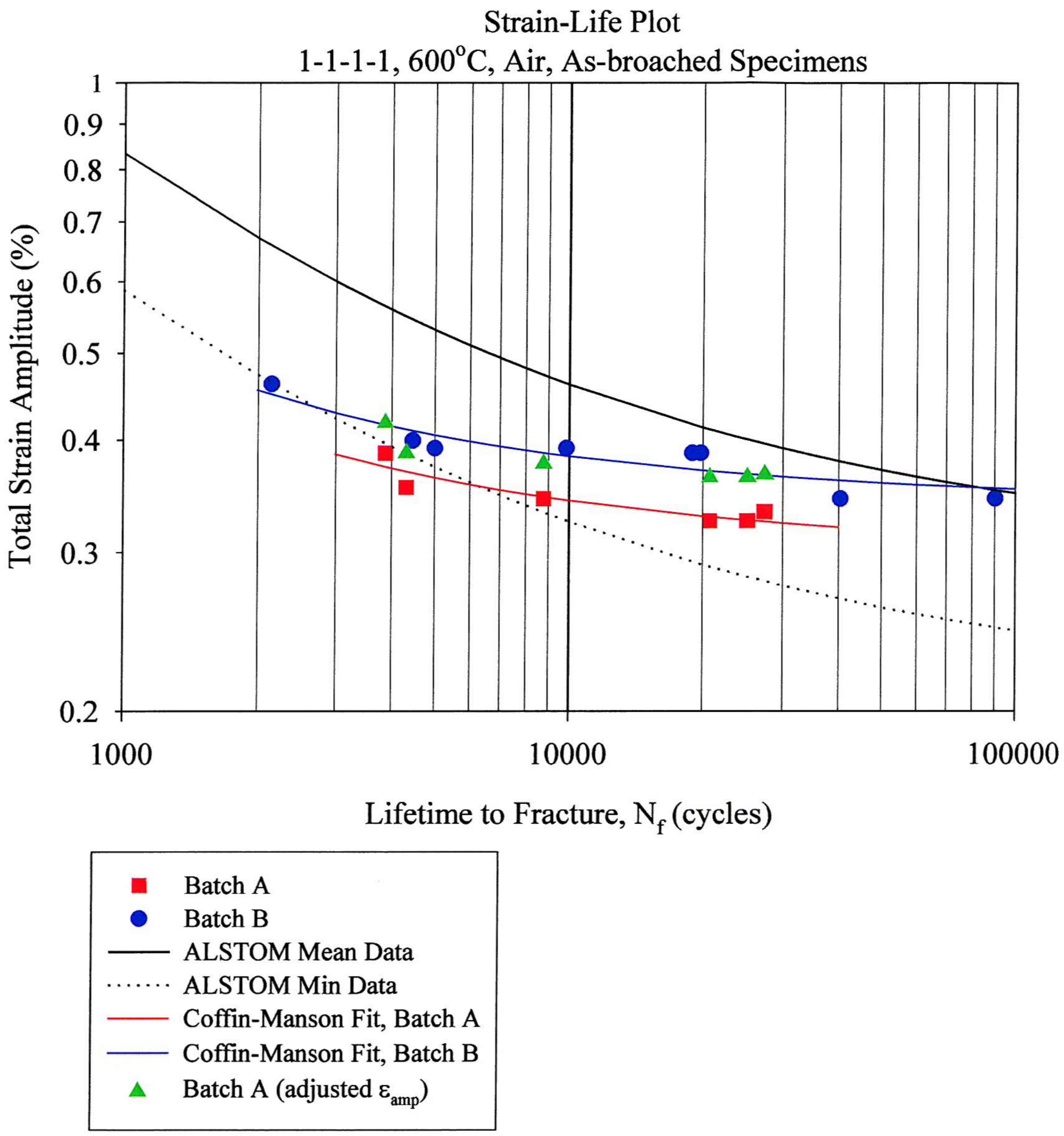

Figure 6.4: Modified Batch A strain-life curve for as-broached U-notch specimens, waveform 1-1-1-1, 600°C, air.

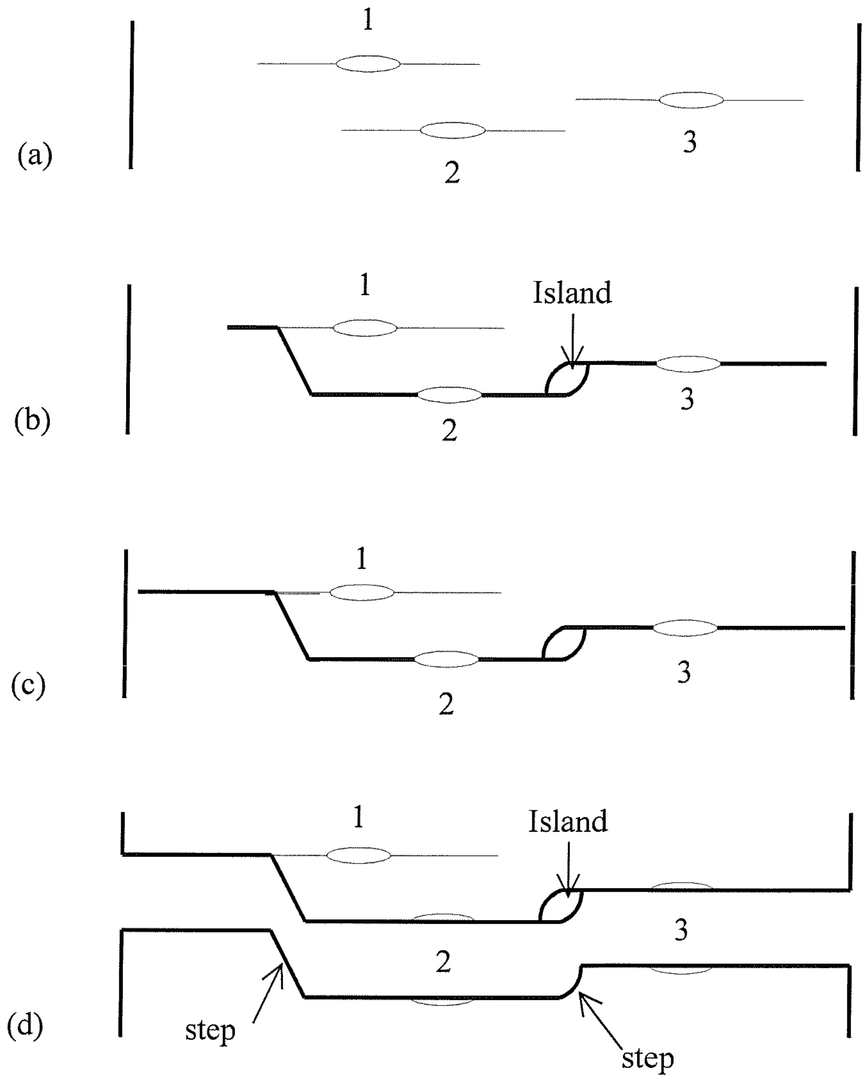

Figure 6.5: Schematic diagram in plan view of surface crack coalescence behaviour in U-notch specimens. (a) Individual short cracks propagating from initiation sites 1, 2 & 3; (b) cracks coalesce via short lateral segments - note coalescence behind crack tips forms an island of material; (c) dominant crack propagates to form through-thickness crack; (d) after fracture – note initiation site 1 is only present on one half of the fractured specimen.

6.12 References

[6.1] Brown E. E., Boettner R. C. & Ruckle D. L. "MINIGRAIN^{TM} Processing of Nickel Base Superalloys" Proc. 2nd. Int. Symp. on Superalloys, TMS, Warrendale, PA, pp. L1-L12 (1972)

[6.2] Sjoberg G., Ingesten N-G. & Carlson R.G. "Grain boundary δ phase morphologies, carbides and notch rupture sensitivity of cast Alloy 718" Proc. 2nd Int. Symp. Superalloy 718, 625 & Various Derivatives Ed. Loria E. A., TMS, Warrendale PA, USA, pp.603-620 (1991)

[6.3] Shimada S. & Inagaki M. "A kinetic study on oxidation of niobium carbide" Solid State Ionics vol. 63-65 pp.312-317 (1993)

[6.4] Miller C. F., Simmons G. W. & Wei R. P. "High temperature oxidation of Nb, NbC and Ni_3Nb and oxygen enhanced crack growth" Scripta Mater. vol. 42 pp. 227-232 (2000)

[6.5] Fletcher D. A., McMeeking R. F. & Parkin D. "The United Kingdom Chemical Database Service" J. Chem. Inf. Comput. Sci. vol. 36 pp. 746-749 (1996)

[6.6] Schafer H., Gruehn R. & Schulte F. "The Modifications of Niobium Pentoxide" Angew. Chem. Internat. Ed. vol. 5, pp. 40-52 (1966)

[6.7] Starink M. J., Van Mourik P. & Korevaar B. M. "Misfit Accommodation in a Quenched and Aged Al-Cu Alloy with Silicon Particles" Metall. Trans. A vol. 24 pp. 1723-1731 (1993)

[6.8] Lee J. K., Earmme Y. Y., Aaronson H. I. & Russell K. C. "Plastic Relaxation of the Transformation Strain Energy of a Misfitting Spherical Precipitate: Ideal Plastic Behavior" Metall. Trans. A vol. 11 pp. 1837-1847 (1980)

[6.9] Moss S. J. Unpublished Data, ALSTOM Power (1998)

[6.10] Jakeman, R. Unpublished Data, ALSTOM Power, (2001)

[6.11] Green D. J. An introduction to the mechanical properties of ceramics, Cambridge Solid State Science Series, Cambridge University Press, Cambridge, UK. ISBN 0-521-59913-X (1998)

[6.12] INCONEL alloy 718 Information Booklet IAI-19/4M/1994, INCO Alloys International, Fourth Edition, (1985)

[6.13] MIL Handbook 5H Section 6 pp. 51-76 (1998)

[6.14] Toth L. E., Monographs on Refractory Materials – No. 7 - Transition Metal Carbides and Nitrides, Ch. 5, Series Ed. Margrave J. L., Academic Press, New York (1971)

[6.15] Encyclopaedia of Chemical Technology, 3rd Edition, Wiley-Interscience, New York, vol. 4 p. 492 (1978)

[6.16] Clavel M. & Pineau A. "Frequency and wave-form effects on the fatigue crack growth behavior of alloy 718 at 298K and 823K" Metall. Trans A vol. 9 pp.471-480 (1978)

[6.17] Merrick H. F. "The low cycle fatigue of three wrought nickel-base alloys" Metall. Trans. vol. 5 (April 1974) pp.891-897 (1974)

[6.18] Fournier D. & Pineau A. "Low cycle fatigue behavior of Inconel 718 at 298K and 823K" Metall. Trans. A vol. 8A pp.1095-1105 (1977)

[6.19] Kalluri S., Rao K. B. S., Halford G. R. & McGaw M. A. "Deformation and damage mechanisms in Inconel 718 superalloy" Proc. 3rd. Int. Symp. Superalloys 718, 625, 706 & Various Derivatives, Ed. Loria E. A., TMS, Warrendale, PA, USA, pp. 593-606(1994)

[6.20] Worthem D. W., Robertson I. M., Leckie F. A., Socie D.F. & Altstetter C. J. "Inhomogeneous deformation of INCONEL 718 during monotonic and cyclic loadings" Metall. Trans. A vol. 21 pp.3215-3220 (1990)

[6.21] Suresh S. Fatigue of Materials Cambridge Solid State Science Series, Cambridge University Press, UK. ISBN 0-521-43763-6 (1991)

[6.22] Clark J. B. & McEvily A. J. "Interaction of dislocations and structures in cyclically strained aluminium alloys" Acta Met. vol. 12 p. 1359 (1964)

[6.23] Floreen S. & Kane R. H. "An investigation of the creep-fatigue-environment interaction in a Ni-base superalloy" Fat. Engng. Mater. Struct. vol. 2 pp. 401-412 (1980)

[6.24] Ghonem H. & Zheng D. "Frequency interactions in high-temperature fatigue crack growth in Superalloys" Metall. Trans. A vol. 23A pp. 3067-3072 (1992)

[6.25] Ghonem H., Nicholas T. & Pineau A. "Elevated temperature fatigue crack growth in alloy 718-Part II: Effects of environmental and material variables" Fatigue Fract. Engng. Mater. Struct. vol. 16 pp. 577-590 (1993)

[6.26] Andrews R. G., Koul A. K. & Au P. "Fatigue crack initiation in Alloy 718 at 650°C" Proc. 2nd Int. Symp. Superalloy 718, 625 & Various Derivatives Ed. Loria E. A., TMS, Warrendale PA, USA, pp.943-954 (1991)

[6.27] Taylor D. & Clancy O. M. "The Fatigue Performance of Machined Surfaces" Fatigue Fract. Engng. Mater. Struct. vol. 14, pp. 329-336 (1991)

[6.28] Cahoon J. R., Broughton W. H. & Kutzak A. R. "The determination of yield strength from hardness measurements" Metall. Trans. vol. 2 pp. 1979-1983 (1971)

[6.29] Mei Z. , Krenn C. R. & Morris J. W. "Initiation and growth of small fatigue cracks in a Ni-base superalloy" Metall. & Mater. Trans. A vol. 26A pp.2063-2073 (1995)

[6.30] Sadananda K. & Vasudevan A. K. "Short Crack Growth Behavior" Fatigue and Fracture Mechanics: Vol. 27, ASTM STP 1296, Eds. Piascik R. S., Newman J. C. & Dowling N. E., ASTM, USA pp. 301-316 (1997)

[6.31] Sadananda K. & Vasudevan A. K. "Short crack growth and internal stresses" Int. J. Fatigue vol. 19 Supp. No. 1 pp. S99-S108 (1997)

[6.32] Sadananda K. & Vasudevan A.K. "Analysis of high temperature fatigue crack growth behavior" Int. J. Fatigue vol. 19 Supp. No. 1 pp. S183-S189 (1997)

[6.33] Sadananda K. & Vasudevan A. K. "Analysis of small crack growth behavior using unified approach" Proc. Third International Conference Small Fatigue Cracks: Mechanics, Mechanisms & Applications, (Hawaii, Dec. 1998), Ed. Ravichandran K. S., Ritchie R. O. & Murakami Y. Elsevier Science, Oxford, UK, pp. 73-83 (1999)

[6.34] Bache M. R., Evans W. J. & Hardy M.C. "The effects of environment and loading waveform on fatigue crack growth in Inconel 718" Int. J. Fatigue vol. 21 Supp. pp. S69-S77 (1999)

[6.35] Zheng D., Rosenberger A. & Ghonem H. "Influence of prestraining on high temperature, low frequency, fatigue crack growth in superalloys" Mater. Sci. Engng. vol. A161 pp. 13-21 (1993)

[6.36] Kalluri S., Rao K. B. S., Halford G. R. & McGaw M. A. "Deformation and damage mechanisms in Inconel 718 superalloy" Proc. 3rd. Int. Symp. Superalloys 718, 625, 706 & Various Derivatives, Ed. Loria E. A. , TMS, Warrendale, PA, USA, pp. 593-606 (1994)

[6.37] Kalluri S., Halford G. R. & McGaw M. A. "Prestraining and its influence on subsequent fatigue life" Advances in Fatigue Lifetime Predictive Techniques: vol. 3, ASTM STP 1292, Eds. Mitchell M. R. & Landgraf R. W., ASTM, USA, pp. 328-341 (1996)

[6.38] Forsyth P. J. E. "A unified description of micro and macroscopic fatigue crack behaviour" Int. J. Fatigue vol. 5 pp. 3-14 (1983)

[6.39] Soboyejo W. O. & Knott J. F. "The propagation of non-coplanar semi-elliptical fatigue cracks" Fatigue Fract. Engng. Mater. Struct. vol. 14 pp. 37-49 (1991)

[6.40] Antunes F. V., Ferreira J. M., Branco C. M. & Byrne J. "Influence of stress state on high temperature fatigue crack growth in Inconel 718" Fatigue Fract. Engng. Mater. Struct. vol. 24, pp. 127-135 (2001)

[6.41] Soboyejo W. O., Kishimoto K., Smith R. A. & Knott J. F. "A study of the interaction and coalescence of two coplanar fatigue cracks in bending" Fatigue Fract. Engng. Mater. Struct. vol. 12 pp. 167-174 (1989)

[6.42] Soboyejo W. O., Knott J. F., Walsh M. J. & Cropper K. R. "Fatigue crack propagation of coplanar semi-elliptical cracks in pure bending" Engng. Fract. Mechanics. vol. 37 pp. 323-340 (1990)

[6.43] Reed P. A. S., Hachette F. & Thakar D. "Pump-priming project on crack initiation in Inconel 718" University of Southampton Department of Engineering Materials Report No. PR/RA/FH,DT/98/01/244 (1998)

[6.44] Reed P. A. S. Hachette F. Thakar D. Connolley T. & Starink M. J. "Creep-fatigue initiation and early crack growth in Inconel 718" Proc. 8th International Conference on Mechanical Behaviour of Materials (ICM8), Eds. Ellyin F. & Provan J.W., Fleming Printing Ltd. Victoria, BC, Canada, vol. 1 pp. 418-423 (1999)

[6.45] Ghonem H., Nicholas T. & Pineau A. "Elevated temperature fatigue crack growth in alloy 718-Part I: Effects of mechanical variables" Fatigue Fract. Engng. Mater. Struct. Vol.16 pp.565-576 (1993)

[6.46] Smith H. H. & Michel D. J. "Effect of environment on fatigue crack propagation behaviour of Alloy 718 at elevated temperatures" Metall. Trans. A vol. 17A pp.370-374 (1986)

[6.47] Pedron J. P. & Pineau A. "The effect of microstructure and environment on the crack growth behaviour of Inconel 718 alloy at 650C under fatigue, creep and combined loading" Mater. Sci. Engng. vol. 56 pp.143-156 (1982)

[6.48] Andrieu E., Cozar R. & Pineau A. "Effect of environment and microstructure on the high temperature behavior of Alloy 718" Proc. Superalloy 718 - Metallurgy & Applications Ed. Loria E. A., TMS, Warrendale PA, USA, pp.241-256 (1989)

[6.49] Diboine A. & Pineau A. "Creep crack initiation and growth in Inconel 718 alloy at 650°C" Fatigue Fract. Engng. Mater. Struct. vol. 10 pp.141-151 (1987)

[6.50] James L. A. "The effect of grain size upon the fatigue-crack propagation behavior of alloy 718 under hold-time cycling at elevated temperature" Engng. Fract. Mech. Vol. 25 pp. 305-314 (1986)

[6.51] Bache M., Personal Communication (2000)

[6.52] Pfaendtner J. A. & McMahon Jr. C. J. "Oxygen-induced intergranular cracking of a Ni-base alloy at elevated temperatures - an example of dynamic embrittlement" Acta Mater. vol. 49 pp. 3369-3377 (2001)

[6.53] Halford G. R., Meyer T. G., Nelson R. S., Nissley D. M. & Swanson G. A. "Fatigue life prediction modeling for turbine hot section materials" Trans. ASME J. Engineering for Gas Turbines & Power vol. 111 pp.279-285 (1989)

[6.54] Goswami T. K. "Hot section turbine disk lifing philosophies" Proc. International Gas Turbine and Aeroengine Congress and Exposition, ASME (Paper No. 93-GT-363) pp. 1-13 (1993)

[6.55] Banik T., Keefe P. W., Maurer G. E. & Petzold L. "Ultra fine grain/ ultra low carbon 718" Proc. 2nd Int. Symp. Superalloy 718, 625 & Various Derivatives Ed. Loria E.A., TMS, Warrendale, PA, USA, pp. 913-924 (1991)

7 CONCLUSIONS

7.1 Oxidation of Primary Carbides

Oxidation of (Nb,Ti)C primary carbides in IN718 readily occurred at temperatures of 550-600°C in air. The most likely product of oxidation was Nb_2O_5 and a substantial volume expansion accompanied oxidation. Theoretical calculations predicted a volume expansion factor of between 1.96 and 2.38 for the complete transformation of NbC to Nb_2O_5. This volume expansion explained the observation of surface eruptions of oxidised material seen on thermal exposure and fatigue specimens. Sub-surface oxidation of primary carbides was also observed, though a preferential oxygen diffusion path such as a grain boundary may be necessary for this. Calculations of the misfit between an oxidised primary carbide and the surrounding matrix predicted that the misfit strains were high enough to cause localised plastic deformation of the matrix. Direct evidence of such plastic deformation was observed in cross-sections through thermally exposed specimens and during SEM observations of U-notch fatigue specimens, where bulge-like crack initiation sites associated with oxidised sub-surface primary carbides were frequently seen.

7.2 Fatigue Testing of Plain Bend Bars

7.2.1 Testing at Room Temperature

Room temperature fatigue testing was performed on plain bend bar samples of extruded IN718. Comparisons were made between as-received material and specimens thermally exposed at 600°C to promote the oxidation of primary carbides. Short crack growth rates were similar in both as-received and exposed material. Cracks which initiated early on in the fatigue life (20000-40000 cycles; 15 - 30% N_f) were the ones which came to dominate the final fracture. The implication is that the fatigue life at room temperature is growth limited rather than initiation limited at the stress levels used. In unexposed material, the majority of cracks initiated at primary carbides and nitrides, whereas in exposed material the majority of cracks initiated intrinsically. It therefore appeared that pre-erupted carbides were not effective crack initiators under cycle-dependent conditions at room temperature. Possibly, full eruption of the carbides reduces the potential for crack initiation by carbide cracking or separation of a carbide/matrix interface, instead of raising the potential for crack initiation due to a micro-notch effect.

7.2.2 Testing at 600°C

Limited high temperature fatigue testing on plain bend bars of IN718 disc material did not result in any crack initiation. The probable cause of this was that the loads used were too low to give sufficient damage accumulation for crack initiation. Most of the testing was performed at a frequency of 10 Hz. Testing at high frequencies is thought to produce more homogeneous slip in IN718 at elevated temperatures, reducing the tendency to form persistent slip bands. This may also have reduced the probability of crack initiation in the plain bend bar tests.

7.3 Fatigue Testing of U-notch Specimens

7.3.1 Batch Variability

The fatigue behaviour of IN718 U-notch specimens was found to be different in the two batches of specimens supplied. Both batches had similar microstructures in terms of grain size, primary carbide content and the presence of grain boundary δ phase. However, Batch A specimens were found to have a work-hardened deformation layer in the broached notch, while Batch B specimens did not. The Batch A specimens had lower notch surface roughness than Batch B. The difference between the batches was clearly seen in strain-life plots, with Batch B specimens exhibiting longer lifetimes than Batch A under the same experimental conditions. It was shown that an increase in yield stress in the Batch A deformation layer could account for the difference in strain-life behaviour between the two batches.

7.3.2 Fatigue Crack Initiation

Crack initiation commenced early on in the fatigue life of the U-notch specimens, so that much of the life was taken up by further initiation, short crack growth and coalescence. For Batch A specimens, it was the oxidised sub-surface carbides, rather than oxide eruptions in general, that were the more numerous type of crack initiation site in U-notch specimens tested in air. This was not the case for Batch B specimens, in which initiation at oxidised sub-surface carbides was infrequent. Additionally, Batch B specimens generally had fewer initiation sites than Batch A specimens tested under the same conditions, despite the Batch B specimens having rougher notches. It was therefore thought that the deformation layer present in Batch A specimens affected crack initiation and propagation behaviour, possibly by influencing the degree of slip inhomogeneity. Slip bands were not observed on the surface of polished notches in Batch A, but they were observed in Batch B specimens, suggesting more inhomogeneous slip in Batch B. This appears to be counterintuitive, since inhomogeneous slip is generally considered to be detrimental to resistance to crack initiation and propagation.

Crack initiation kinetics varied with applied stress. At the lower stress levels of σ_{max} = 750 MPa or 790 MPa in Batch A, there was an initial incubation period at the start in which no cracks were observed. Following the initially slow rate of crack initiation, there was a transition to behaviour in which the number of cracks appearing increased at a steady rate. The factors controlling this rate are thought to be the time required for oxidation of carbides in different parts of the specimen and the time required for accumulation of sufficient cyclic damage in the material to initiate further cracks. The number of cracks initiated eventually reached a plateau, attributed to a combination of exhaustion of potential crack initiation sites, reduction in the local strain at initiation sites due to shielding by neighbouring cracks, and crack coalescence. At σ_{max} = 885 MPa in Batch B specimens, fatigue failure was controlled by initiation and growth of a single crack, with most of the other cracks initiating in the stress-strain field ahead of the tip of the growing crack or in the residual ligaments. One possible cause of the difference between Batch A and Batch B tests was the much higher stress level used for Batch B. This led to a shorter fatigue life, allowing less time for initiation by primary carbide oxidation. In addition, slip band formation was enhanced by the greater strain range in the notch root at σ_{max} = 885 MPa. This permitted rapid propagation of the dominant surface crack along slip bands or grain boundaries, possibly shielding other potential initiation sites from the applied stresses. However, crack initiation in the later stages of tests was observed in the localised high stress regions ahead of the crack tips.

7.3.3 Fatigue Crack Growth

In Batch A specimens at of σ_{max} = 750 MPa or 790 MPa, the propagation of short surface cracks in the U-notch root was observed to be approximately constant across a wide range of crack lengths. This is in contrast to the usual trend of increasing growth rate with increasing crack length observed for long crack tests. A constant propagation rate implies that the local crack tip driving force was constant for short cracks growing in isolation. This cannot be characterised using global continuum approaches such as LEFM.

In Batch A specimens the surface cracks in the U-notches were all remarkably straight, with no deflections except those occurring during crack coalescence. This transgranular propagation may have been due to the presence of the deformation layer in the notch root of Batch A specimens. A transition to mixed transgranular-intergranular propagation into the depth of the specimen was observed to occur at a depth of approximately 30-50 μm, which may have occurred as the cracks propagated beyond the influence of the surface deformation layer.

Unlike the Batch A tests at σ_{max} = 750 MPa and σ_{max} = 790 MPa, the Batch B tests at σ_{max} = 885 MPa exhibited the more typical crack growth behaviour of increasing growth rate with increasing crack length. It is possible that the local effects of microstructure and the notch plasticity were less significant for crack propagation, and the growth was mainly driven by the externally applied stress amplitude. No deformation layer from broaching was present in the Batch B samples, which may also have altered the crack propagation behaviour relative to Batch A. Some evidence for this was found by performing a test on a polished specimen at σ_{max} = 790 MPa. Slip bands were observed on the polished notch surface, but they were not observed in the equivalent tests performed on polished Batch A specimens. The absence of slip bands in Batch A specimens may have been due to extensive work hardening in the surface deformation layer, which prevented easy dislocation glide and the formation of slip bands.

Some evidence was found of crack tunnelling with crack a:c ratios greater than 1. This was possibly enhanced by the introduction of 20 second or 30 second dwells at maximum load.

7.3.4 Fatigue Crack Coalescence

Various examples of crack coalescence behaviour were observed. In some cases, crack tips can grew past one another, before deflecting towards one another at coalescence, producing islands of material. This is typical of cracks where the local driving force is low and crack tip plastic zones do not overlap. In other cases, coalescence occurred before crack tips overlapped, indicating higher local driving forces and possibly some crack tip plastic zone overlap. Both types of coalescence were observed in the same specimen, suggesting crack coalescence behaviour was very sensitive to the local driving force under the same nominal external loading conditions. Evidence of sub-surface coalescence without apparent coalescence at the surface was also found.

7.3.5 U-notch Fatigue Lifetimes

The tests conducted indicated that crack initiation and growth in the U-notch specimens was a complex process, with the majority of the specimen life taken up by the initiation, growth and interaction of short fatigue cracks, until coalescence of several cracks generated a dominant defect which propagates rapidly to failure.

A beneficial effect of dwell at maximum stress was observed for Batch A tests conducted in air at 600°C. A 1-20-1-1 cycle increased the fatigue life by a factor of 2 compared to a 1-1-1-1 cycle and a 1-30-1-1 cycle increased the fatigue life by a factor of 3. This is the same trend as that observed in a previous study of U-notch specimens manufactured from extruded IN718 bar. However, no such beneficial effect of dwell was observed for Batch B specimens tested at a substantially higher load level of σ_{max} = 885 MPa.

Polishing U-notches to remove broaching marks generally resulted in an increase in fatigue life for a 1-1-1-1 cycle at 600°C in air. A similar trend was observed in previously reported work on extruded IN718, using a 10 Hz sawtooth waveform in air at 600°C. Removal of the broaching marks may reduce crack initiation due to micro-notch effects, though cracks still initiated early in the fatigue life due to carbide oxidation. An alternative possibility was that the broaching marks enhanced surface crack propagation by increasing the local crack driving force due to a micro-notch effect. The marks were favourably oriented for crack growth parallel to the notch root axis and hence perpendicular to the tensile axis.

8 FURTHER WORK

8.1 U-notch Fatigue Tests

8.1.1 Batch Variability due to Broaching

The two batches of U-notch specimens had notch root surface roughness and microstructure that were not the same. Batch A had smoother notches than Batch B, but Batch A had a surface deformation layer that was not present in Batch B. Results from the two batches of disc material tested showed a difference in fatigue crack initiation and growth behaviour that was probably caused by these differences in notch surface condition. This difference in broaching quality is interesting because it may arise in production discs, with consequences for in-service fatigue performance. It is recommended that for future work on new batches of U-notch specimens, metallography is performed to check the microstructural condition of the notch root. It may also be possible to retrospectively check for broaching deformation in the specimens of extruded IN718 from a previous study [8.1] performed at Southampton. FE modelling incorporating a work-hardened surface layer would help to clarify the effect on predicted strain amplitudes of the deformation layer observed in Batch A specimens.

8.1.2 Vacuum Testing

Vacuum testing was only performed on Batch A U-notch specimens Lifetimes and crack initiation behaviour in vacuum may have been influenced by the presence of the deformation layer observed in the notch roots. Some vacuum testing on specimens without a deformation layer would be of interest. It would also be interesting to study the behaviour in vacuum of a specimen with a polished U-notch, for example to examine differences in surface crack propagation path compared to an air test.

8.1.3 Alternative Crack Growth Measurement Technique

The acetate replication technique used in this study yielded good information on surface short crack lengths and crack propagation behaviour, but it required the use of polished specimens and the tests had to be interrupted, resulting in long test durations. There was also some concern that repeated thermal cycling may have affected crack propagation. As an alternative, a DC potential drop technique could be used to monitor crack growth without interrupting the test. A four point probe technique, such as that used by Coffin [8.2] should be considered, as this eliminates drift effects which can be a problem during high temperature testing. One disadvantage of using a potential drop technique is that the resolution is generally inferior to the replica technique, and some development work will be required to calibrate the system. Computer modelling of the potential field in the notch root may be required to cope with multi-site initiation and the development of semi-elliptical crack shapes. Coffin [8.2] reported that the resolution of the potential drop technique was sensitive to notch geometry, and the existing U-notch specimen may not be optimised for crack growth measurements using potential drop. Rather than monitoring crack growth, it will be easier to use a potential drop technique to monitor initiation of a crack of a given size, for example the 0.8 mm depth quoted [8.3] as the end point for turbine disc component testing.

8.1.4 Effect of Dwell

For Batch A specimens, the results of this study demonstrated a beneficial effect on fatigue life of 20 second and 30 second dwells at σ_{max} = 750 MPa, R=0.1. A similar effect was reported in a previous study on U-notch samples of extruded IN718. No such effect was observed at σ_{max} = 885 MPa for Batch B specimens. There may be a transition in behaviour with increasing stress level, so it is recommended to study the effect of dwell at different stress levels on a single batch of specimens. As a preliminary test, running two of the remaining Batch B specimens at σ_{max} = 790 MPa with a 1-20-1-1 would enable comparison with existing data for a 1-1-1-1 cycle at the same stress level. For a more detailed investigation of dwell, two sets of tests are of interest:

- Effect of increasing σ_{max} in the range 750 MPa to 885 MPa, keeping the dwell time constant.
- Effect of increasing dwell times in the range 1-20 seconds, keeping σ_{max} constant.

In the present study, all dwell tests were performed on as-broached samples. It would be of interest to establish the effect of dwell on polished samples as well, particularly if a replica technique is to be used to monitor short crack growth rates. Once the effect of dwell on fatigue life has been characterised, short crack growth rate measurements are proposed to determine if dwell influences short crack propagation rates in the notch root. This may be performed on interrupted tests by taking replicas from polished specimens, or by a potential-drop technique. More detailed fractography should be performed to look for evidence of static load crack growth.

8.2 Long Crack Testing

Having obtained short crack growth rates from the U-notch specimens, it is desirable to have long crack growth rate data from the same material, so that short and long crack growth rates can be compared directly. The long crack tests would provide useful information on the time dependent nature of long crack growth in IN718 disc material for comparison with existing published data. Tests with 1 second and 20 second dwells at maximum load performed in air and vacuum could be used to investigate the effect of dwell and environment on crack propagation. Comparing the air and vacuum test results will confirm whether time-dependent crack growth is dominated by environmental effects or whether there is some contribution from creep processes as well.

8.3 References

[8.1] Reed P. A. S., Hachette F. & Thakar D. "Pump-priming project on crack initiation in Inconel 718" University of Southampton Department of Engineering Materials Report No. PR/RA/FH,DT/98/01/244 (1998)

[8.2] Coffin L. F. "Notch fatigue crack initiation studies in a high strength nickel base superalloy" Engng. Fract. Mech. vol. 28 pp. 485-503 (1987)

[8.3]Goswami T. K. "Hot section turbine disk lifing philosophies" American Society of Mechanical Engineers (Paper number: 93-GT-363) Presented at International Gas Turbine & Aeroengine Congress and Exposition ASME, New York pp. 1-13 (1993)

INTELLECTUAL PROPERTY AGREEMENT FOR THE IN718 MATERIAL CONSTITUTIVE MODEL PROVIDED BY ABB ALSTOM POWER (NOW ALSTOM POWER)

The source code of the material model for IN718 is released to Thomas Connolley on the 7.1.2000 for the duration of his PhD studentship, supported by ABB ALSTOM POWER, at Southampton University, Southampton, UK. The subroutines that comprise the material model are only to be used in conjunction with Thomas Connolley's research work on IN718, in collaboration with ABB ALSTOM POWER. The subroutines may not be used or communicated, either in part or as a whole, to any other person or organisation outside of Southampton University's staff or students, who are legitimately involved in Thomas Connolley's research work, in conjunction with ABB ALSTOM POWER. In receiving this material model, Thomas Connolley accepts these conditions of use and agrees to ensure that Southampton University will maintain no permanent record of the model (electronic or otherwise) after the end of his studentship. Prior permission to publish any details of the model or information from it must be obtained from ABB ALSTOM POWER.